

Towards an Embeddable Structural Health Monitoring Sensor: Design and Optimization of MEMS Piezoelectric Vibration Energy Harvesters

by

Anna Marie Mracek

S.B. Aeronautics and Astronautics
Massachusetts Institute of Technology (2004)

Submitted to the Department of Aeronautics and Astronautics
in Partial Fulfillment of the Requirements for the Degree of

Master of Science in Aeronautics and Astronautics

at the

MASSACHUSETTS INSTITUTE OF TECHNOLOGY

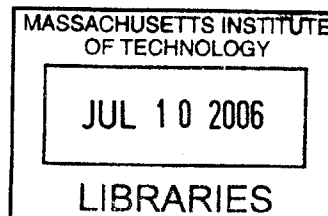
May 2006

© 2006 Massachusetts Institute of Technology. All Rights Reserved.

Signature of Author.....
Department of Aeronautics and Astronautics
May 26, 2006

Certified by.....
Brian L. Wardle
Boeing Assistant Professor of Aeronautics and Astronautics
Thesis Supervisor

Accepted by.....
Jaime Peraire
Professor of Aeronautics and Astronautics
Chair, Committee on Graduate Students



AERO

Towards an Embeddable Structural Health Monitoring Sensor: Design and Optimization of MEMS Piezoelectric Vibration Energy Harvesters

by

Anna Marie Mracek

Submitted to the Department of Aeronautics and Astronautics on May 26, 2006 in Partial Fulfillment of the Requirements for the Degree of Master of Science in Aeronautics and Astronautics

ABSTRACT

Wireless structural health monitoring (SHM) has gained considerable interest as a potential method of reducing aircraft maintenance costs while increasing safety. Distributed power supplies for the sensing nodes are needed for a practical implementation of this technique. Vibrational energy harvesting using MEMS piezoelectric resonant devices is an appealing solution to this challenge due to their relatively high potential for power generation (compared to other harvesting techniques) and capacity to be integrated into the microfabrication procedure of the remainder of the SHM node. A comprehensive review of energy harvesting devices, particularly piezoelectric harvesters, is presented, including characterization of previous devices in terms of key power performance metrics. An existing coupled electromechanical model is presented and modified for use in optimization studies with both {3-1} Mode and {3-3} Mode piezoelectric cantilevered beam configurations. The modified model accurately represents published experimental results. A series of design optimization studies is presented for four devices operating in an aircraft vibration environment. Untapered bimorph {3-1} Mode and unimorph {3-3} Mode MEMS devices with large proof masses, as well as tapered unimorph devices (both with and without proof masses) are studied and a 2- or 3-parameter geometric optimization is performed. Optimization objectives include power output, operating power density, static power density, and specific power with very different optimum device configurations favored for the different objectives. A {3-3} Mode MEMS unimorph device optimized for static power density is conservatively predicted to generate 1.9 mW/cm^3 of electrical power. This optimization is presented graphically and the predicted performance of the optimum {3-3} Mode unimorph devices with proof masses is detailed. It is found that the optima occur within the micro-scale design space studied, suggesting that MEMS devices are the best choice for distributed aircraft vibrational energy harvesting. The optimization results presented are for one potential SHM vibration environment using cantilevered beam harvesters, however, the technique presented can be extended to other environments and other harvester geometries.

Thesis Supervisor: Brian L. Wardle

Title: Boeing Assistant Professor of Aeronautics and Astronautics

Acknowledgements

I would like to thank Prof. John Dugundji for his support and guidance throughout this project. Truly instrumental to the development of the results presented here, his involvement went far beyond the call of duty. His experience, as well as his genuine love of both students and the work itself, were key components of my graduate experience and will be remembered fondly.

Additionally, this work would not have come together without the effort and patience of my advisor, Prof. Brian Wardle, the MIT Microsystems Technology Lab (MTL) staff, or any number of others who offered insight and advice along the way. Gratitude is also extended to the National Science Foundation, which supported me during this process.

Lastly, but most importantly, my family and fiancé, Carl Dietrich, deserve much of the credit for their unfailing love and tireless support. It is my pleasure and honor to share my past, and my future, with each of you. Without your love and God's Grace, I would not be where I am. Thank you for everything.

Contents

1	Introduction	17
1.1	Selected Applications for Harvested Power	17
1.2	Advantages of Piezoelectric Harvesting of Mechanical Vibrations	18
1.3	Specific Motivation of this Work	19
1.3.1	Aircraft Structural Monitoring and Proposed Solution.....	20
1.3.2	Vibration Environment of Aircraft Empennage.....	20
1.4	Overview and Contribution of this Thesis.....	21
2	The Energy Harvesting Landscape	25
2.1	Introduction to Energy Harvesting	25
2.1.1	Piezoelectric Energy Harvesting.....	25
2.1.2	Other Types of Energy Harvesting	27
2.2	A Discussion of Comparison Metrics and Examples	27
2.2.1	Explanation of Useful Energy Harvesting Metrics	28
2.2.2	An Exploration of Harvesting Efficiency	29
2.3	A Survey of Existing Piezoelectric Vibration Harvesters	31
2.4	A Brief Survey of Other Energy Harvesting Devices	34
2.4.1	Capacitive Harvesting Devices	34
2.4.2	Thermal Harvesting Devices.....	35
2.4.3	Other MEMS Harvesting Devices of Interest	35
2.5	Review of Text and Work by Roundy et al.	36
2.5.1	Derivation of Beam Governing Equations.....	36
2.5.2	Results and Discussion	41
2.6	An Introduction to Supporting Electronics for Energy Harvesting	42
2.6.1	Power Management Techniques and Circuitry	43
2.6.2	Energy Storage Options	44
3	Modeling and Optimization of Uniform Beam Harvesters	47
3.1	Previous Modeling.....	47
3.2	The {3-1} and {3-3} Electrical Modes.....	52
3.3	Impact of Microfabrication on Harvester Design	56
3.4	Modeling for Optimization: The Uniform Beam.....	57

3.4.1	Model Example for Aircraft Vibration Harvesting.....	58
3.4.2	Uniform {3-3} Mode Harvester: Model Validation	63
3.4.3	Uniform {3-1} Mode Harvester: Model Verification.....	64
3.5	Untapered (Uniform) Beam Optimization Results	70
3.5.1	Challenges to Optimization.....	70
3.5.2	Resulting Tools for Uniform Beam {3-3} Mode Optimization.....	71
3.5.3	Resulting Tools for Uniform Beam {3-1} Mode Optimization.....	81
3.5.4	Uniform Beam Optimization Results and Conclusions	89
4	Modeling and Optimization of Tapered Beam Harvesters.....	93
4.1	Tapered {3-3} Mode Beam without a Proof Mass	93
4.2	Tapered {3-3} Mode Beam with a Proof Mass	103
4.3	Tapered Beam Optimization Results and Conclusions	114
5	Conclusions and Recommendations	118
5.1	Conclusions and Contributions.....	118
5.2	Recommendations for Future Work	121
6	References	123
7	Appendix A: Optimization Harvester Models: MATLAB Code	129
A.1	Untapered {3-3} Mode Harvester Model with Proof Mass.....	129
A.2	Untapered {3-1} Mode Harvester Model with Proof Mass.....	139
A.3	Tapered {3-3} Mode Harvester Model without Proof Mass	149
A.4	Tapered {3-3} Mode Harvester Model with Proof Mass	161
A.5	Piezoelectric Material Library File.....	173

List of Figures

Figure 1.1: Comparison of Power Sources from du Toit [3].	19
Figure 1.2: Jet aircraft vibration exposure, from: MIL-STD 810F, Figure 514.5C-8 [50].	21
Figure 2.1: 1D Representative Device from du Toit [3].	30
Figure 2.2: Power Input and Dissipation in 1D Device Efficiency Example	31
Figure 2.3: Schematic of Beam Geometry	37
Figure 3.1: Beam with Proof Mass from du Toit [3]	49
Figure 3.2: Bimorph ($\{3-1\}$ Mode) Harvester Schematic with Two Pairs of Electrodes	53
Figure 3.3: Unimorph ($\{3-3\}$ Mode) Harvester Schematic with Interdigitated Electrodes	53
Figure 3.4: Side and Top Views of a $\{3-3\}$ Mode Cantilevered Device	58
Figure 3.5: Example Carpet Plot for $\{3-3\}$ Mode Untapered Device Operating Power Density with Example Point Marked	59
Figure 3.6: Close-Up View of Example Point on Operating Power Density Carpet Plot from Figure 3.5	60
Figure 3.7: First Mode Shape and Curvature of the First Mode for $\{3-3\}$ Mode Example Case	61
Figure 3.8: $\{3-3\}$ Mode Micro-Scale Unimorph Model Validation for Tip Displacement, Maximum Relative Tip Displacement [μm] vs. Base Displacement [nm]	64
Figure 3.9: $\{3-1\}$ Mode Macro-Scale Bimorph Power Production Model Verification: Device Power vs. Normalized Frequency, Ω	66
Figure 3.10: $\{3-1\}$ Mode Macro-Scale Bimorph Resonance and Off-Resonance Power Production Model Verification, Power [μW] vs. Load Resistance [$\text{k}\Omega$]	67
Figure 3.11: $\{3-1\}$ Mode Macro-Scale Bimorph Resonance and Off-Resonance Power Production Model Verification, Voltage [V] vs. Load Resistance [$\text{k}\Omega$]	68
Figure 3.12: $\{3-1\}$ Mode Macro-Scale Bimorph Resonance and Off-Resonance Power Production Model Verification, Tip Displacement [μm] vs. Load Resistance [$\text{k}\Omega$]	69
Figure 3.13: Anti-Resonant Frequency Contours for a Untapered $\{3-3\}$ Mode Unimorph Device	72
Figure 3.14: Device Power Output Contours for a Untapered $\{3-3\}$ Mode Unimorph Device	72
Figure 3.15: Close-Up of Device Power Output Contours for a Untapered $\{3-3\}$ Mode Unimorph Device	73
Figure 3.16: Dual Operating Peaks and Optimum Load Resistance for Untapered $\{3-3\}$ Mode Device	74
Figure 3.17: Maximum Device Power Output for an Untapered $\{3-3\}$ Mode Unimorph Device Shown Against L and L_0 along Maximum Power Output Contour	74

Figure 3.18: Maximum Device Power Output for an Untapered {3-3} Mode Unimorph Device Shown Against L and L ₀ Across the Entire Design Space	75
Figure 3.19: Operating Power Density Contours for an Untapered {3-3} Mode Unimorph Device.....	76
Figure 3.20: Close-Up of Operating Power Density Contours for an Untapered {3-3} Mode Unimorph Device	76
Figure 3.21: Maximum Operating Power Density for an Untapered {3-3} Mode Unimorph Device Shown Against L and L ₀ Across the Entire Design Space.....	77
Figure 3.22: Static Power Density Contours for an Untapered {3-3} Mode Unimorph Device.....	78
Figure 3.23: Close-Up of Static Power Density Contours for an Untapered {3-3} Mode Unimorph Device	78
Figure 3.24: Maximum Static Power Density for an Untapered {3-3} Mode Unimorph Device Shown Against L and L ₀ Across the Entire Design Space.....	79
Figure 3.25: Specific Power Contours for an Untapered {3-3} Mode Unimorph Device	79
Figure 3.26: Close-Up of Specific Power Contours for an Untapered {3-3} Mode Unimorph Device	80
Figure 3.27: Maximum Specific Power for a Uniform {3-3} Mode Unimorph Device Shown Against L and L ₀ Across the Entire Design Space.....	80
Figure 3.28: Anti-Resonant Frequency Contours for a Untapered {3-1} Mode Bimorph Device	82
Figure 3.29: Device Power Output Contours for an Untapered {3-1} Mode Bimorph Device.....	83
Figure 3.30: Close-Up of Device Power Output Contours for an Untapered {3-1} Mode Bimorph Device	83
Figure 3.31: Maximum Device Power Output for an Untapered {3-1} Mode Bimorph Device Shown Against L and L ₀ Across the Entire Design Space.....	84
Figure 3.32: Operating Power Density Contours for an Untapered {3-1} Mode Bimorph Device.....	84
Figure 3.33: Close-Up of Operating Power Density for an Untapered {3-1} Mode Bimorph Device.....	85
Figure 3.34: Maximum Operating Power Density for an Untapered {3-1} Mode Bimorph Device Shown Against L and L ₀ Across the Entire Design Space.....	85
Figure 3.35: Static Power Density Contours for an Untapered {3-1} Mode Bimorph Device.....	86
Figure 3.36: Close-Up of Static Power Density Contours for an Untapered {3-1} Mode Bimorph Device	86
Figure 3.37: Maximum Static Power Density for an Untapered {3-1} Mode Bimorph Device Shown Against L and L ₀ Across the Entire Design Space.....	87
Figure 3.38: Specific Power Contours for an Untapered {3-1} Mode Bimorph Device	87
Figure 3.39: Close-Up of Specific Power Contours for an Untapered {3-1} Mode Bimorph Device.....	88

Figure 3.40: Maximum Specific Power for an Untapered {3-1} Mode Bimorph Device Shown Against L and L_0 Across the Entire Design Space.....	88
Figure 4.1: Rayleigh-Ritz Results for Tapered Beam without a Proof Mass.....	94
Figure 4.2: Anti-Resonant Frequency Contours for a Tapered {3-3} Unimorph Device, no Proof Mass..	95
Figure 4.3: Device Power Output Contours for a Tapered {3-3} Mode Unimorph Device, no Proof Mass	96
Figure 4.4: Close-Up of Power Output for a Tapered {3-3} Mode Unimorph Device, no Proof Mass	96
Figure 4.5: Maximum Device Power Output for a Tapered {3-3} Mode Unimorph Device Shown Against Length and Raper Ratio Across the Design Space.....	97
Figure 4.6: Operating Power Density Contours for a Tapered {3-3} Mode Unimorph Device, no Proof Mass	98
Figure 4.7: Close-Up of Operating Power Density for a Tapered {3-3} Mode Unimorph Device, no Proof Mass	99
Figure 4.8: Maximum Operating Power Density for a Tapered {3-3} Mode Unimorph Device Shown Against Length and Raper Ratio Across the Design Space	99
Figure 4.9: Static Power Density Contours for a Tapered {3-3} Mode Unimorph Device, no Proof Mass	100
Figure 4.10: Close-Up of Static Power Density Contours for a Tapered {3-3} Mode Unimorph Device, no Proof Mass	100
Figure 4.11: Maximum Static Power Density for a Tapered {3-3} Mode Unimorph Device Shown Against Length and Taper Ratio Across the Design Space.....	101
Figure 4.12: Specific Power Contours for a Tapered {3-3} Mode Unimorph Device, no Proof Mass	102
Figure 4.13: Close-Up of Specific Power Contours for a Tapered {3-3} Mode Unimorph Device, no Proof Mass	102
Figure 4.14: Maximum Specific Power for a Tapered {3-3} Mode Unimorph Device Shown Against Length and Raper Ratio Across the Design Space.....	103
Figure 4.15: Tapered Beam Geometry with Proof Mass	104
Figure 4.16: Mode Shapes for Rayleigh-Ritz Analysis of a Tapered Beam with a Proof Mass.....	105
Figure 4.17: Curvature of R-R Mode Shape for Tapered Beam with Proof Mass, varying Taper	105
Figure 4.18: Curvature of R-R Mode Shape for Tapered Beam with Proof Mass, varying L_0	105
Figure 4.19: Anti-Resonant Frequency Contours for a Tapered {3-3} Unimorph Device with a Proof Mass and $L=0.5\text{mm}$	106
Figure 4.20: Device Power Output Contours for a Tapered {3-3} Mode Unimorph Device, with Proof Mass, $L=0.5\text{mm}$	107

Figure 4.21: Close-Up of Device Power Output Contours for a Tapered {3-3} Mode Unimorph Device with Proof Mass	107
Figure 4.22: Device Power Output Contours for a Tapered {3-3} Mode Unimorph Device, with Proof Mass, L=0.3mm	108
Figure 4.23: Maximum Device Power Output for a Tapered {3-3} Mode Unimorph Device Shown Against Proof Mass and Taper Ratio along Maximum Power Contour.....	108
Figure 4.24: Operating Power Density Contours for a Tapered {3-3} Mode Unimorph Device, with a Proof Mass, L = 0.5mm.....	109
Figure 4.25: Close-Up of Device Power Output Contours for a Tapered {3-3} Mode Unimorph Device, with Proof Mass, L=0.5mm.....	109
Figure 4.26: Maximum Operating Power Density for a Tapered {3-3} Mode Unimorph Device Shown Against Proof Mass and Taper Ratio along Maximum Power Contour.....	110
Figure 4.27: Static Power Density Contours for a Tapered {3-3} Mode Unimorph Device, with a Proof Mass, L = 0.5mm	111
Figure 4.28: Close-Up of Static Power Density Contours for a Tapered {3-3} Mode Unimorph Device with a Proof Mass, L=0.5mm.....	111
Figure 4.29: Maximum Static Power Density for a Tapered {3-3} Mode Unimorph Device Shown Against Proof Mass and Taper Ratio along Maximum Power Contour.....	112
Figure 4.30: Specific Power Contours for a Tapered {3-3} Mode Unimorph Device, with a Proof Mass, L = 0.5mm	113
Figure 4.31: Close-Up of Specific Power Contours for a Tapered {3-3} Mode Unimorph Device, with Proof Mass, L = 0.5mm.....	113
Figure 4.32: Maximum Specific Power for a Tapered {3-3} Mode Unimorph Device Shown Against Proof Mass and Taper Ratio along Maximum Power Contour	114

List of Tables

Table 2.1: Key Metrics for Energy Harvesting Device Comparison	29
Table 2.2: Existing Piezoelectric Vibration Energy Harvesting Devices.....	32
Table 2.3: Device Parameters from Roundy <i>et al.</i> [1]	41
Table 2.4: Piezoelectric Coupling Factors and Corresponding Open-Circuit Frequency Ratios.....	42
Table 3.1: Constitutive Coefficients for {3-1} Mode Piezoelectrc Material	55
Table 3.2: Constitutive Coefficients for {3-3} Mode Piezoelectric Material	55
Table 3.3: PZT 5A Material Properties.....	56
Table 3.4: Example {3-3} Device Layer Properties	59
Table 3.5: Model Predictions for {3-3} Example Case	62
Table 3.6: {3-1} Mode Bimorph Device Layers and Properties:.....	82
Table 3.7: Untapered Harvesting Device Optimization Summary	90
Table 3.8: Performance Metrics for {3-3} Mode Untapered Unimorph Optimized Devices	91
Table 4.1: Cantilevered Beam Mode Shape Constants for Eq 4-1.....	93
Table 4.2: Tapered Harvesting Device Optimization [†] Summary.....	116
Table 4.3: Performance Metrics for {3-3} Mode Tapered Unimorph Optimized [†] Devices	117

Nomenclature

Variable	Description	Units
A_p	Piezoelectric material cross section	[m ²]
B_f	Input coefficient	[kg]
C	Capacitance	[C/V]
C	Mechanical damping coefficient	[N/m/s]
C_p	Piezo capacitance	[F]
C^E	Modulus of elasticity	[GPa]
D	Electric displacement	[C/m ²]
E	Electric field	[V/m]
H_0	Height of proof mass	[m]
I	Current	[A]
J_0	Mass moment of inertia around center of proof-mass	[kg-m ²]
J_{yy}	Mass moment of inertia around center of proof-mass	[kg-m ²]
K	Device spring constant	[N/m]
K_{ij}	Device spring constant in Rayleigh-Ritz Analysis	[N/m]
L	Length of active beam	[m]
L_0	Length of proof mass	[m]
M	Mass coefficient	[kg]
M_{ij}	Mass coefficient in Rayleigh-Ritz Analysis	[kg]
M_0	Mass of proof-mass	[kg]
P	Power output	[W]
P_{op}	Operating power density	[μW/cm ³]
P_{out}	Device power output	[W/kg]
P_{st}	Static power density	[μW/cm ³]
R	Resistance	[Ω]
R_l	Load resistance	[Ω]
R_{le}	Effective load resistance	[Ω]
$R_{l,opt}$	Optimal load resistance for power generation	[Ω]
S	Strain	-
S_0	Moment imposed on beam by proof-mass	[N-m]
T	Stress	[kPa]
T_k	Kinetic energy	[J]
U	Internal strain energy	[J]
V	Voltage	[V]
V_{out}	Device voltage output	[V]
V_p	Piezoelectric Volume	[m ³]
V_s	Structural (nonpiezoelectric) Volume	[m ³]
W	External work	[J]
W_0	Total acceleration spectral density	[g ² /Hz]
W_A	Aerodynamic vibrational excitation	[g ² /Hz]
W_J	Engine vibrational excitation	[g ² /Hz]
W_e	Electrical energy	[J]
a	Electrode width	[m]
b	Width of active beam	[m]
b_0	Width of beam tip	[m]

c_m	Structural damping coefficient	[N/m/s]
c_e	Electrical damping coefficient	[N/m/s]
\mathbf{c}^E	Piezoelectric material stiffness	[GPa]
\mathbf{e}	PZT coupling coefficient	[C/m ²]
\mathbf{f}_k	Point load at position x_k	[N]
m	Mass	[kg]
m	Mass per unit length of beam	[kg/m]
m_0	Mass per unit length of proof-mass	[kg/m]
p	Electrode pitch (spacing)	[m]
q_j	Charge extracted at x_j	[C]
r	Magnitude of Relative displacement	[m]
t_t	Thickness of beam	[m]
t_p	Thickness of piezoelectric layer	[m]
\mathbf{u}	Base displacement	[m]
v	Magnitude of voltage	[V]
v_{op}	Operating volume	[cm ³]
v_{st}	Static volume	[cm ³]
$w(x)$	Relative beam displacement at position x	[m]
w_{tip}	Relative beam displacement at end of structure	[μ m]
w_B	Input base displacement	[m]
\ddot{w}_B	Input base acceleration	[m]
x	Distance along beam	[m]
Θ	Coupling coefficient	[N/m/s]
Ω	Frequency ratio (input/resonant)	-
Ω_{oc}	Open circuit frequency ratio	-
Ω_{sc}	Short circuit frequency ratio	-
α	ωRC , Non-dimensional Resistance	-
ϵ^S	Dielectric constant	[F/m]
η	Harvesting efficiency	-
κ^2	Θ^2/KCp , Non-dimensional Coupling Term	-
ψ_{rN}	Beam mode shape for N th mode	-
ψ_{vN}	Electrical mode shape for N th mode	-
$\varphi(x)$	Rotation of beam axis at position x	[rad]
φ_j	Scalar electrical potential at j th electrode	[V]
ρ	Density	[kg/m ³]
ω	Input excitation frequency of device	[Hz]
ω_{ar}	Anti-resonant frequency of device	[Hz]
ω_N	Natural frequency of N th mode of beam	[Hz]
$\omega_r = \omega_1$	Resonant frequency	[Hz]
ζ_m	Non-dimensional mechanical damping coefficient	-

1 Introduction

As microelectronics have gained popularity, energy harvesting has received increasing amounts of attention in the literature. The miniaturization of components such as processors, sensors, receivers and transmitters has made distributed, embedded or implanted devices – often referred to as nodes – appealing for applications ranging from wild animal tagging and tracking to civil structural health monitoring to *in vivo* medical devices. Of particular interest in this body of work is the structural health monitoring of metallic and composite structures now being used in primary aircraft structures. The inaccessibility of nodes after their initial deployment – due to either wide geographic distribution or physical implantation in either a structure or a living organism – discourages use of traditional sources of power such as batteries or other chemical sources as at some point the device either runs out of power (the battery is drained or the fuel is exhausted) requiring that it must either be reclaimed (usually at great expense and/or difficulty) or considered lost. Hard-wire connections of these devices to a central power source – even in the isolated instances where this would be possible, such as on a civil or aircraft structure – is prohibitive as the installation cost and weight of wiring negate the benefit of existing wireless data transfer technologies.

1.1 Selected Applications for Harvested Power

The following applications were selected from the literature to give a sense of current work that is particularly interesting and/or relevant to the efforts of this work. They are by no means to be seen as an exhaustive review of the potential applications available for a piezoelectric vibration energy harvesting device. Rather, the selected applications serve as complements to the work presented here and as a context for the goal of distributed wireless sensors for aircraft structural health monitoring that is driving this body of work.

Bai *et al.* [40] present a description of a wireless sensing network architecture for an aircraft engine. Temperature and other sensors would be paired with communication and control circuitry that would allow increased engine performance and early identification of engine health issues. Vibrational energy harvesting is one of the top power supply choices presented for this system. This basic system architecture could be extensible to the health monitoring of a larger aircraft structure as discussed in following sections.

Lynch *et al.* [42] present a piezoresistive MEMS-based accelerometer designed to be used within a wireless sensing network for civil structural health monitoring. The Tsing Ma Suspension Bridge health monitoring project in Hong Kong is cited as an example of a wired sensing system, with a total price tag of \$8M, 25% of which was installation cost. The installation of wires accounted for 75% of the required labor. The proposed MEMS alternative could be easily coupled with wireless transmission technology and energy harvesting to present a virtually maintenance-free solution that would have offered a savings of \$1.5M or 18% for the Tsing Ma project based on installation labor savings alone. There is also potential for great manufacturing efficiency if the MEMS piezoelectric accelerometer presented could be designed for simultaneous fabrication with a MEMS piezoelectric vibration energy harvester. A similar small-scale accelerometer is presented by Park *et al.* [41].

Perhaps most relevant, a variety of MEMS strain sensors were embedded in composite plates and tested by Hautamaki *et al.* [35], demonstrating that such devices can successfully function in both uniaxial and bending loading conditions. While piezoelectric strain sensors were discounted in favor of doped polysilicon piezoresistive-based strain sensors due to the problem of charge dissipation over time, satisfactory sensitivity and repeatability were obtained from the sensors tested. At unpackaged thicknesses of 1-2 μm , these sensors could potentially be successfully embedded in aircraft composite structures as a typical ply thickness is roughly 150 μm . Their work also presents a set of metrics that can be used to compare various strain sensors.

1.2 Advantages of Piezoelectric Harvesting of Mechanical Vibrations

Piezoelectric vibration energy harvesting falls into a broader category known as fixed power generation sources which, as opposed to fixed energy sources, can produce a given power level for an indefinite period of time. Advantageous over fixed energy density sources (such as batteries) due to their nominally infinite life, power harvesting devices are particularly desirable for applications in which access is difficult or impossible and longevity is important. (The embedded aircraft composite strain sensor network discussed in the next section is just such an application.) du Toit [3] presents a recent and thorough review of both fixed energy density and fixed power generation sources. A summary chart from this comparison is reproduced in Figure 1.1 below. It should be noted that the axial flow generator is only applicable to situations where fluid flow is available and that solar energy is not an option for embedded power generation devices such as those needed for the composite health monitoring application at hand, leaving piezoelectric vibration energy harvesting as the highest power density option. The difference in life span between fixed power and fixed energy density devices can be seen by comparing the 1 Year and 10 Year power density levels for each set of devices.

The conclusion that piezoelectric devices present the best option for vibration energy harvesting is also found in the text book [1] and other work of Roundy *et al.* [2], after a comparison of piezoelectric and electro-static vibration energy harvesting devices. Because of the potential simplicity and flexibility of a cantilevered beam piezoelectric harvester, a wide range of vibration sources can be targeted for power generation. Another advantage to using piezoelectric devices is that their behavior as actuators (in which an electric charge is applied to cause a deformation) is fairly well understood and offers a basis for extension to energy harvesting (using a deformation to generate a charge or current).

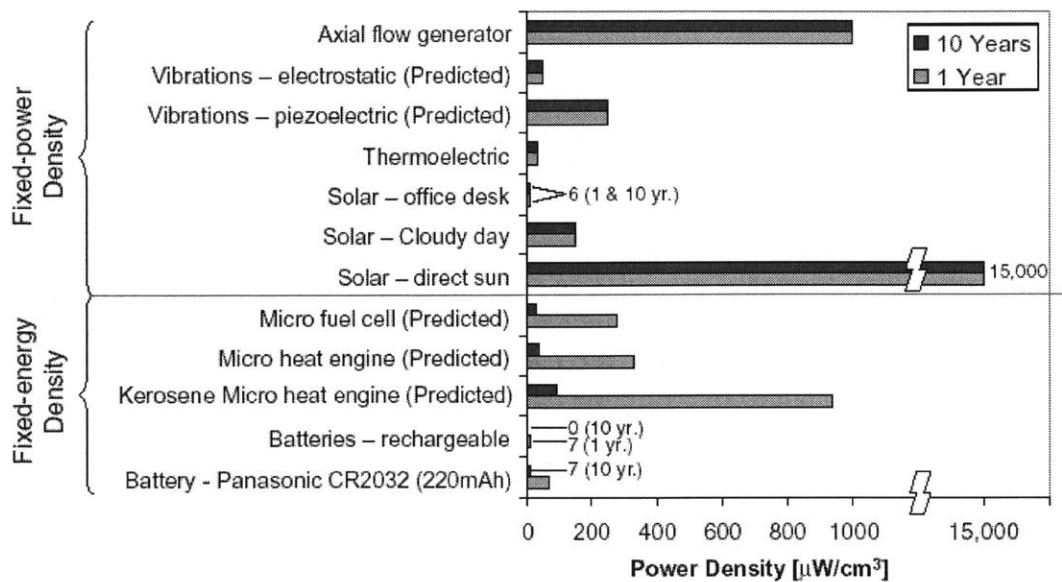


Figure 1.1: Comparison of Power Sources from du Toit [3].

1.3 Specific Motivation of this Work

While all of the applications mentioned in this section would benefit from the successful development of a MEMS piezoelectric vibrational energy harvester, the particular application that has motivated this work is that of health management in aircraft structures, particularly composite structures. While composite structures can offer significant advantages in terms of strength and weight, additional care relative to metal structures must be taken to ensure damage tolerance and durability. Furthermore, composites are the material of choice for military and commercial aircraft (as well as space craft) now, and increasingly so. Ensuring safe structures can end up being quite costly in terms of both aircraft time out of service and maintenance expenses. Boller [50] presents data indicating that approximately 70% of the damage discovered on aircraft components after inspection are due to fatigue cracking. (While this study was not limited to composite structures, it does serve to indicate the magnitude of this problem.) The difficulty in predicting these cracks results in inspection costs for a given component being roughly half of its total life cycle cost (LCC). NASA/CR-2000-209848 [48] puts structural health monitoring into the larger framework of aircraft operations and provides an economic justification for SHM systems.

The development of a health-monitoring package that can be seamlessly integrated into the airframe without the extra complexity, weight and expense of cables or wires would pave the way for significant savings throughout an aircraft's life, as well as increased safety.

The current maintenance issues associated with fatigue and damage tolerance in aircraft, as well as the particular vibration environment selected for investigation in this work, are outlined in the following subsections.

1.3.1 Aircraft Structural Monitoring and Proposed Solution

Current tools for fatigue monitoring are reviewed by Molent [53] and include flight hour or flight/landing cycle counting, fatigue metering, range pair counters, multi-channel recorders, and strain gauges. Of these choices, strain gauges have the advantages of being able to capture a time history that directly reflects principle load components at points of interest during both normal operation and abrupt loading from maneuvering, gusts and buffet. Strain gauge data is also advantageous because it is more directly comparable to fatigue test data and accounts not only for aircraft operation but also changing weight over any given flight. The primary drawbacks to strain gauge implementation include difficulty in placement, installation and maintenance, and cumbersome connections for data transmission and power supply. These drawbacks are significant enough to overrule the benefits of strain gauge fatigue monitoring for aircraft such as the F/A-18, which currently employs cycle counting as its primary means of fatigue damage tracking, despite the significant potential for inaccuracy due to gross assumptions intrinsic to this technique.

One method of strain gauge integration into the airframe that was developed by F-K Chang [51], and also presented by Boller [50], is that of a “smart layer” to be included in the composite lay-up. The “smart layer” would sandwich piezoelectric strain sensing fibers between Kapton foil and then embed this layer into the composite or apply it as a sticker onto the outside of the skin. Boller forecasts that such a strain monitoring device could extend the life of the Canadian Air Force’s F/A-18 fleet by 12 years and save over 400M Canadian dollars (~\$345M USD), even though the “smart layer” is still a wired device. The end goal of the larger body of work that this thesis is part of is to develop similar embedded plies or externally applicable patches that do not require physical contact with the outside world and do not have the potential to degrade the integrity of the structure they will be monitoring. By incorporating strain gauges and wireless data transmission technology with MEMS vibrational energy harvesting components, a system could be developed that offers the benefits of strain gauge fatigue monitoring without the majority of their drawbacks. Such a system would allow maintenance efforts to be driven by actual aircraft loading instead of set schedules or assumption of what the aircraft may have experienced over a given mission.

1.3.2 Vibration Environment of Aircraft Empennage

For a military aircraft, after the main landing gear, the components with the highest LCC are the empennage skin and control surfaces [50]. Because of the composite construction being employed in the empennage skins of F/A-18 aircraft and their identification as a critical component, the vibration environment found in this area of the airplane skin was used as the basis for device design in this work. The vibration exposure found on the aircraft’s empennage can be calculated through the use of data found in the Military Standard 810F, Annex C, Method 514.5 [47]. The acceleration spectral density given in MIL-STD 810F and reproduced here as Figure 1.2 was used in conjunction with Table 514.5C-III, also found in MIL-STD 810F, to obtain the operating point of 1000Hz at 3.89 m/s^2 . The vibration level presented in the Standard is the vibration that a component on the aircraft must be able to withstand, it is likely an upper bound for what can be expected in practice. While an upper bound in one sense, due to the

inclusion of only aerodynamic (and not engine) vibration, as discussed below, this vibration level is considered a good design point.

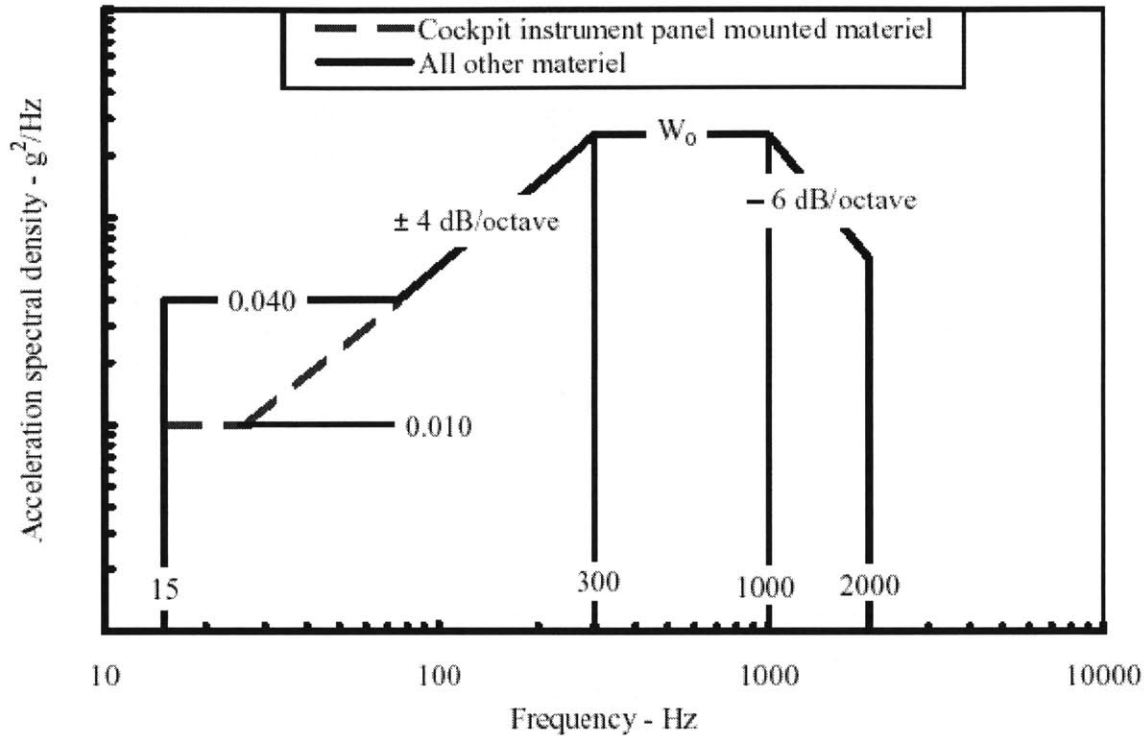


Figure 1.2: Jet aircraft vibration exposure, from: MIL-STD 810F, Figure 514.5C-8 [47].

The operating frequency selected as the input excitation for this work of 1000Hz was selected as it is the upper bound for the region of highest acceleration spectral density as seen in Figure 1.2. The value for W_0 was obtained through the process outlined in Method 514.5, which is based on a combination of both aerodynamic (W_A) and engine (W_J) vibrational excitation. The aerodynamic excitation, W_A , was based on a device weighing less than 36kg that is mounted away from surface discontinuities and for subsonic flight conditions. This gives a moderately conservative value compared to the other options present in the table. A value for the engine excitation contribution, W_J , was attempted based on information about a GE F-404 jet engine from Jane's Aero-Engines [49], but due to a high level of uncertainty about many of the parameters required by Table 514.5C-III the decision was made to go with the more reliable (and conservative) estimate based on aerodynamic vibration alone. For this case, $W_0 = W_A = 1.579e-4 g^2/Hz$, giving the acceleration of $3.8991 m/s^2$ at 1000Hz that is used throughout. If in the future a device is being designed for a particular field trial on an aircraft, W_A and W_J should be calculated based on the specifics of that environment and the resulting vibration input used.

1.4 Overview and Contribution of this Thesis

To date, all (except one) of the piezoelectric vibration harvesting devices that have been built have been on the macro scale, not the MEMS scale that would be required for integration of an

energy harvester into a wireless MEMS sensor package. This thesis will bridge the gap between existing macro scale work and the design of an optimized MEMS prototype device. The first of these gaps hinges on the fabrication process itself. Despite previous work done by Sood [11] and others at MIT on fabrication, a reliable, repeatable piezoelectric deposition process does not exist at MIT. Thin film micro fabrication of active materials such as lead zirconium titanate, $\text{PbZr}_x\text{Ti}_{(1-x)}\text{O}_2$ (PZT) is an active area of research in the materials community around the world. Though fabrication efforts and lessons learned today are described later in this work in the context of optimization constraints, establishing the process for device fabrication is left for future work.

The other issues that are addressed in this work are also necessary for realization of application-specific MEMS energy harvesters. Identification and definition of key performance parameters is addressed in Chapter 2. Design tool development and optimization for maximization of different performance metrics is also detailed in this work. Other design questions which are currently left open-ended in the literature that are addressed here include the potential benefit of tapering the beam geometry, the choice of piezoelectric operating mode (31 vs. 33) and the effects of coupled piezoelectric material properties on power generation. All of these questions need to be addressed before piezoelectric vibration harvesting devices can be incorporated as the primary energy source for devices in embedded, distributed, MEMS-scale wireless sensors.

To summarize, the main contributions of this work take the form of the following:

- Definition and standardization of relevant performance metrics for energy scavenging devices to enable comparison between device types and across devices.
- Initial investigation into the necessary power electronics and energy storage mechanisms that would be used in conjunction with a vibrational energy harvesting device to provide power for a wireless sensor node.
- Review of the single existing published text on the topic of MEMS energy harvesting, that of Roundy *et al.* [1] and comparison of piezoelectric (and other) energy harvesting devices.
- Multi-variable design optimization for various performance metrics including specific power, operating power density, static power density, and absolute device power output.
- Modeling of a tapered beam configuration and investigation into whether such a design possesses significant benefits over a uniform width device.
- Exploration of the performance differences between {31} and {33} Mode piezoelectric beam harvester operation.

The approach that is taken throughout is analytical, utilizing a model based on previous work by du Toit [3 and 5] that is derived from energy principles and recast for use within a design space

sweep for optimization. This model was validated and verified by comparison to existing {3-3} and {3-1} Mode [4] piezoelectric harvester data.

2 The Energy Harvesting Landscape

In this chapter, current work on energy harvesting is reviewed. While energy harvesting is currently the recipient of a good amount of attention, there is a lack of consistency in the approach and often results are published without enough information to facilitate comparison between projects. Thus, a framework within which these various efforts can be compared is established here by looking at device performance metrics, such as overall conversion efficiency and power normalizations. In addition, attention is given to the accompanying power electronics that would need to be implemented with an energy harvesting device to enable wireless structural health monitoring. While piezoelectric materials are the focus of this work, other options for energy harvesting are also briefly mentioned.

2.1 Introduction to Energy Harvesting

Due to the rising need for a self-contained, continuous (*i.e.* not life-limited) power supply for distributed microelectronics, a large variety of techniques are currently being explored in the literature for harnessing ambient energy. Ambient energy sources that are commonly available to a device are light, thermal gradients, and mechanical energy. Of particular interest here are those devices that harness the mechanical energy of ambient vibration by straining a piezoelectric material. The text and other work of Roundy, Wright and Rabaey, [1 and 2], is given extra attention here as theirs is currently the only published text on the subject. In the following sections, an overview of other piezoelectric-based and assorted energy harvesters is given. Useful comparison and performance metrics are defined and applied to several existing devices. Other necessary accompanying technologies such as power electronics and energy storage devices are briefly considered at the end of this chapter.

2.1.1 Piezoelectric Energy Harvesting

A piezoelectric material is defined as any material that can transform electrical energy into mechanical strain energy or, conversely, mechanical strain energy into electrical charge [8]. Piezoelectric materials can be formed by aligning the electric dipoles that are found naturally in a subclass of materials known as ferroelectrics through the process of poling. Poling is achieved by applying a strong electric field to align the dipoles in the material, typically at an elevated temperature still below the Curie temperature. After a poled ferroelectric is cooled, it will maintain its (strong) piezoelectric qualities that are captured in a set of coupled constitutive equations between mechanical and electrical energy. These equations take many forms. They were expressed by Sodano *et al.* [6] in the form reproduced below:

$$\begin{bmatrix} \mathbf{T} \\ \mathbf{D} \end{bmatrix} = \begin{bmatrix} \mathbf{c}^E & -\mathbf{e}^t \\ \mathbf{e} & \boldsymbol{\varepsilon}^S \end{bmatrix} \begin{bmatrix} \mathbf{S} \\ \mathbf{E} \end{bmatrix} \quad \text{Eq 2-1}$$

where \mathbf{c} is the modulus of elasticity, ϵ is the dielectric constant, \mathbf{e} is the PZT coupling coefficient, \mathbf{T} , \mathbf{D} , \mathbf{S} , and \mathbf{E} represent stress, electric displacement (charge per unit area), strain and electric field respectively. The superscript indicates that the parameter that was held constant during the measurement of the quantity being modified, except for t which indicates transpose.

Electromechanical coupling allows both actuation, which has been a popular use of piezoelectric materials for some time now, and sensing (or energy harvesting), which will be explored further here. By introduction of a strain to the piezoelectric material a charge separation forms. This charge can then be removed from the device as useable power through appropriate power electronics including a load resistance. Strain can be induced by a number of different means. Mechanical vibration is the source that is of most interest here as it is prevalent in the aircraft environment of interest described in the Introduction, but it is certainly not the only potential source of mechanical excitation. Piezoelectric devices have also shown significant promise in harnessing the energy that is lost during the course of the human gait – as much as 7W of power from the heel strike of a 154-lb person taking one step a second – and even the rib motion of respiration [8 and 15].

Whereas impact-driven energy conversion such as from a heel strike relies on the high-rate compression of a piezoelectric stack, vibrational energy is best harvested through the use of a piezoelectric resonator, usually taking the form of a cantilevered beam. The beam geometry gives the designer the choice of two different operating modes of the piezoelectric material, {31} and {33}. In both cases, the direction of poling is taken to be in the 3 direction. In {31} Mode operation, the strain is generated perpendicular to the electric field; this is accomplished by utilizing plate electrodes above and below the piezoelectric layer of the beam. In {33} Mode operation, the strain and electric field are in the same direction. This can also be accomplished with a cantilevered beam structure through the use of interdigitated electrodes which lay like meshed fingers across only the top surface of the beam structure. Both modes of operation are considered in the design modeling and optimization work that is presented later in this thesis. (These modes are discussed further in Section 3.2.)

Regardless of the mode of operation of the piezoelectric material, the cantilever can be designed to resonate at the frequency of its input excitation. As was explored in some depth in du Toit's work [3], and neglected entirely in Roundy *et al.* [1], there exists both a resonant and an anti-resonant frequency for a piezoelectric device due to the nature of the electrical and mechanical coupling. When operated at their optimum resistances, each frequency yields equal power output (P), but anti-resonant operation gives a higher voltage output (V) and resonant operation a higher current (I) via $P=IV$. As voltage can be critical for electrical applications, it is the anti-resonant frequency that is the focus in this work. Fortunately, as shown by Sodano *et al.*, even when the resonant or anti-resonant frequency of the device cannot be matched exactly to the source, (*i.e.* the source is random with an average frequency around resonance or antiresonance) it is still possible to use a vibrational energy harvester to charge a battery, though at over twice the required time as if operated at optimum [6].

2.1.2 Other Types of Energy Harvesting

Though currently the most promising option for vibrational energy harvesting, piezoelectric materials are certainly not the only energy harvesting option. Vibration can be harvested through the use of capacitive devices as in Roundy *et al.* [1 and 2] and Meninger *et al.* [14], but at a reduced power generation level. MEMS scale capacitive harvesting devices could potentially be easier to fabricate with traditional silicon wafer microfabrication techniques, however. Vibration can also be harvested through electromagnetic generators and a spring-mass system such as is common in wrist watches [15]; magnets scale down poorly, however, as device size shrinks.

In addition to vibration, ambient radio energy, temperature gradients, light, airflow and impact are all potential sources of energy that could be scavenged by a remotely placed device. Paradiso and Starner [15] present a broad comparison of the potential performance of these different types of devices. Unfortunately, their information is missing many of the metrics discussed in the following section, so it is still difficult to make direct comparisons between these different potential energy sources. Some general statements were still made about each potential energy source: Ambient radio energy is attractive in that it is pervasive in today's world, however due to its extremely low energy content, less than a microwatt per square centimeter is predicted to be available. Light energy has the potential to be quite intensely available, but this is dependent highly on location and time of day. Additionally, photovoltaic energy is not available for *in vivo* or embedded structural devices. Ambient airflow has been demonstrated to be harvestable by a microelectromechanical turbine to 1 mW/cm^2 , but even more so than with light energy, this type of energy harvesting has limited applicability. Impact, such as from a heel strike or button push can gather as much as 7 W from walking or $50 \text{ } \mu\text{J/N}$ from a push button, but these piezoelectric devices show little promise in terms of miniaturization or incorporation into a completely self-sufficient sensor/transmitter package.

While new, creative, and interesting methods of garnering energy from a device's surroundings continue to be explored, and may be ideal for other applications, piezoelectric vibrational energy harvesting will be explored in depth in this work due to its potential for high power density MEMS scale devices tailored to power generation from machine or airplane skin vibrations in the kHz range.

2.2 A Discussion of Comparison Metrics and Examples

A standardization of comparison metrics is clearly lacking throughout the open literature. Many devices are described in terms of their maximum power output without mention of their size or mass. Most typically, power per unit volume or area is reported, with the volume or area being only that of the static device (thus exaggerating power production). The energy sources that are being scavenged for power are also quite varied, covering frequency ranges from a few Hertz to a several thousand Hertz and energy densities that are equally varied. As power output is directly dependent on the available power input, it is thus difficult to make even the most basic comparisons between the different devices in the literature. While the broad variety of potential applications makes it difficult, if not impossible, to assert that there is one crucial performance metric, by providing basic information on electrical output and the dimensions and mass of the

device, authors can give system designers the tools to determine which type of device holds the most promise for their application.

2.2.1 Explanation of Useful Energy Harvesting Metrics

Before continuing further with an effort at comparison, a few popular performance metrics will be described and their key differences called out. The most obvious characteristic is simply device power output, measured in Watts (W) or microwatts (μW). If the application of interest is insensitive to device size or weight, then this metric is useful. If, however, there are other constraints on the system in terms of volume or mass, other metrics become more valuable. Additionally, various input vibrations contain different levels of available power, thus an efficiency term will more accurately compare devices operating in different environments.

The two most popular other absolute (*i.e.* not related to efficiency) performance metrics are often confused in the literature. They are specific power and power density. Specific power has units of power per device mass ($\mu\text{W}/\text{kg}$) and is particularly useful for weight-constrained applications. Power density has units of power per device volume ($\mu\text{W}/\text{cm}^3$) and is sensitive to the definition of the volume used in its calculation. Operating power density is the most telling metric for volume-constrained devices (*i.e.* those being designed for implantation or structural embedding). The operating volume is defined as the volume that is used by the device while in operation (*e.g.*, the volume swept out by the tip displacement of a resonating cantilever structure) and is usually much larger than the device static volume. The static volume, however, is more commonly given in literature (perhaps because of the higher static power density value that it yields) and is simply the volume of the device when not undergoing any excitation or power harvesting. It is the opinion of the author that operating power density is by far the most telling for device comparison as it is this operating volume that would actually be required for device implementation into a structure or organism. Packaging will scale with operating volume as well. As will be seen later, the operating power density is perhaps the most intriguing metric for design, as there is a trade to be considered between the increased strain (and thus power generation) and the increased operating volume that high tip displacement causes.

These absolute metrics, however, do not reflect the efficiency with which the device converts ambient energy into useable electric power. To capture this characteristic, a power harvesting efficiency must be calculated as power harvested over power available, or input ($P_{\text{out}}/P_{\text{available}}$). Some attention was given to increasing the efficiency of a piezoelectric vibration harvester by Richards *et al* [7] without utilizing a specific source or device design. In many cases, however, it is the power output, specific power, or power density that is of critical importance rather than the device efficiency. However, even if the decision is made to sacrifice harvesting efficiency of a device, such a metric would allow much more straightforward comparison between various devices presented in the literature. These five metrics are presented with their representative symbols and units in Table 2.1.

Voltage is also included in Table 2.1 as a key metric for two reasons. First, some electronics that one would wish to power using a vibrational harvesting device require a minimum voltage output. Secondly, by choosing the operating point of the piezoelectric harvester device, either high voltage or high current can be produced while maintaining nearly constant output power.

Thus, required voltage is something that should be kept in mind when designing a piezoelectric vibrational energy harvesting device.

One final note about device comparison centers on the packaging for the device. When final device designs are eventually considered for energy harvesting, it will be the total package size and mass that matters – the harvester itself as well as all of the power electronics and energy storage devices necessary to provide the necessary power for the device at hand. However, as the devices that are currently being developed are often early in the prototyping phase, and as power electronics and energy harvesting devices are often being developed separately, such an inclusive approach is unrealistic at this point. As such, the masses and volumes used for comparison here, and used later in this work for design, are only those of the harvesting devices themselves.

In short, to enable broad device comparison and application-specific device selection, the characteristics of a device as shown in Table 2.1 should be published when describing its operation.

Table 2.1: Key Metrics for Energy Harvesting Device Comparison

Characteristic	Symbol	Units
Target Frequency	ω	Hz
Harvesting Efficiency	η	$P_{out}/P_{available}$
Device Power Output	P_{out}	μW
Operating Power Density	P_{out}/v_{op}	$\mu W/cm^3$
Static Power Density	P_{out}/v_{st}	$\mu W/cm^3$
Specific Power	P_{out}/m	W/kg
Device Voltage Output	V_{out}	V

The static volume (v_{st}) and operating volume (v_{op}) needed to calculate operating and static volumes are as follows:

$$v_{st} = (L + L_0)(b_m)(H_0 + t_t) \quad \text{Eq 2-2}$$

$$v_{op} = (L + L_0)*(b_m)*(2w(L) + H_0 \cos(\varphi(L)) + L_0 \sin(\varphi(L))) \quad \text{Eq 2-3}$$

where $w(L)$ is the maximum displacement of the end of the active beam section, $\varphi(L)$ is the rotation at the end of the active beam, L and b_m are the length and maximum width of the active beam, L_0 and H_0 are the length and height of the proof mass, and t_t is the total thickness of the active beam. The last term in the expression for v_{op} is simply the total height that is swept out by the combination of beam and proof mass during operation.

2.2.2 An Exploration of Harvesting Efficiency

As mentioned in the previous section, Harvesting Efficiency, η , is a useful metric for device comparison and an example case is shown here. The 1-dimensional device that was used as

model exploration by du Toit (Figure 2.1) was employed here to determine an efficiency calculation. The mass of the proof mass in this example device is 0.01 kg, the structural damping coefficient (c_m) is 0.05 N/m/s, and the device was assumed to be operating at a resonance frequency of 1053 Hz with an input base acceleration of 1 m/s². The electrical damping (c_e) was calculated based on the applied load resistance using the following formula as presented by Roundy *et al* [2]:

$$c_e = \frac{k_{33}^2 \omega}{\sqrt{\omega^2 + 1/(RC)^2}} \tag{Eq 2-4}$$

Where k_{33} ($k_{33}^2 = 0.56$ in this example) is the piezoelectric coupling metric of the material, R and C are the resistance and capacitance of the device respectively, and ω is the input frequency. For the example case worked in this section here, $c_e = 0.0434$ N/m/s. In the power-optimal configuration, the electrical damping would equal the structural damping. This case would result in the maximum overall Harvesting Efficiency that can be obtained with this type of device, $\eta = 0.50$, meaning that half of the energy available to the device is lost to structural damping while half is captured as electrical power.

An effective device spring constant, K , as shown in Figure 2.1, is also defined:

$$K = \frac{c_{33}^E A_p}{t_p} \tag{Eq 2-5}$$

Where c_{33}^E is the piezoelectric material stiffness, A_p is the cross-sectional area of the piezoelectric material and t_p is the thickness of the piezoelectric material. In the example case at hand, $K = 11,100$ N/m.

If desired, an additional damping term due to the air drag force can be included as well, but this term impacts the total Harvesting Efficiency by about 1% and is not included here. More information on drag force damping can be found in du Toit [3].

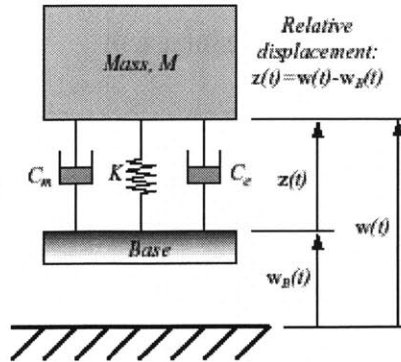


Figure 2.1: 1D Representative Device from du Toit [3].

Power available to the device was calculated by summing the power dissipated through all of the prominent mechanisms: electrical harvesting and mechanical damping of the structure. The power that goes to mechanical damping is lost, while the power dissipated through the load resistor as useable power is what is represented as P_{out} . The total power available and the power dissipated by each of the described mechanisms over two periods of excitation are shown in Figure 2.2. On average, this sample device had an efficiency of 46.5%. This is less than the theoretical maximum of 50% efficiency because the resistance is not optimized. In general, η will be less than 50% if $c_e \neq c_m$. This is true regardless of whether $c_e > c_m$ or $c_e < c_m$. In practice, c_e can be tuned to equal c_m by changing the electrical load resistance (which is a design variable of the system).

The MATLAB script that was used to run this sample case is included for reference in the Appendix A. It should be noted that in order to determine η for a given device, in addition to information about the piezoelectric material, the mass and structural damping coefficients of the device must be known. A surprising number of devices are published without including all of the information required to generate a harvesting efficiency estimate. It is the recommendation of the author that this metric – or at least a complete set of information needed to calculate it- be included in future work on this topic.

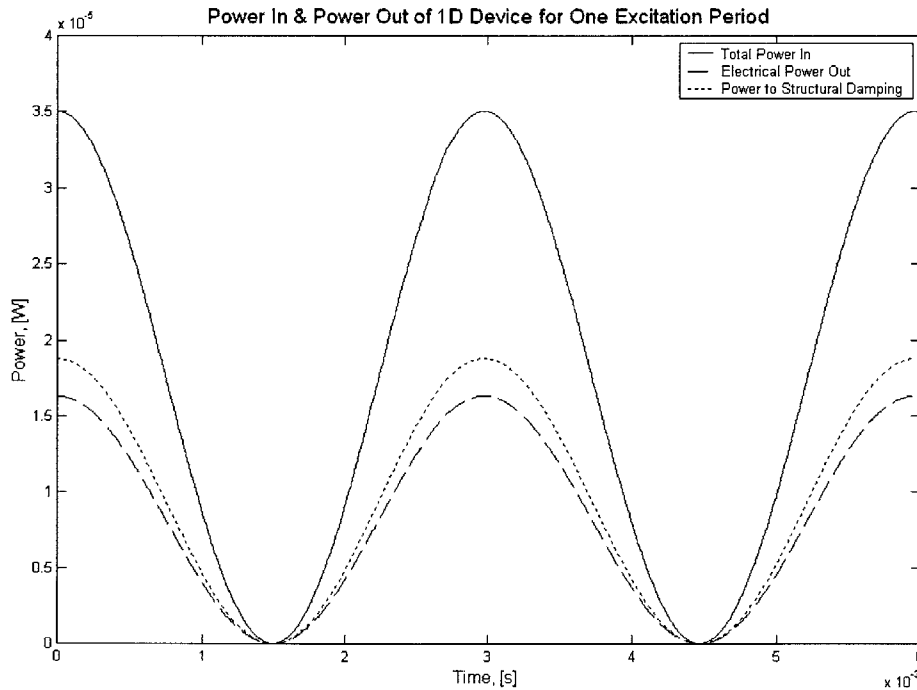


Figure 2.2: Power Input and Dissipation in 1D Device Efficiency Example

2.3 A Survey of Existing Piezoelectric Vibration Harvesters

The characteristics listed in Table 2.1 (as available) are collected in Table 2.2 below for various published devices. One of the difficulties with the current literature is the lack of documentation

for many published devices. More information and explanation as available follows the table for each device listed.

Table 2.2: Existing Piezoelectric Vibration Energy Harvesting Devices

Device	ω [Hz]	η	P_{out} [μ W]	P_{out}/v_{op} [μ W/cm ³]	P_{out}/v_{st} [μ W/cm ³]	P_{out}/m [W/kg]	V_{out} [V]
Umeda <i>et al.</i> ball drop, [13]	843	N/A	.3W	N/A	N/A	N/A	1.2 - 95
Sodano <i>et al.</i> 1 st piezo, [6]	30	N/A	900	N/A	462	0.095	3
Sodano <i>et al.</i> MFC [9]	64	N/A	11.7	N/A	37.2	N/A	N/A
Sodano <i>et al.</i> QP10ni [9]	64	N/A	29.5	N/A	60.0	N/A	N/A
Sodano <i>et al.</i> QP10n [9]	64	N/A	137	N/A	279	N/A	N/A
Roundy <i>et al.</i> cant. Beam, [1, 2]	100	N/A	215	N/A	227	N/A	6
Glynne-Jones <i>et al.</i> tapered beam, [10]	80.1	N/A	2.2	1.86	9.45	N/A	1.25
du Toit, Bi-morph harvester [3]	113	0.4	550	263	397	0.052	9
Sood, {33} Mode IDE MEMS harvester [11]	14,000	N/A	1	250,000	500,000	N/A	2.4

The Umeda *et al.* device [13] is often cited as the pioneering work in piezoelectric mechanical to electrical energy conversion. The device was powered simply by the impact of a steel ball onto a plate that had a piezoelectric element on the back. It was not designed for continuous power harvesting but was an early proof-of-concept for piezoelectric-based energy harvesting. The frequency listed is for the first mode of the plate. The second mode, which was also observed, was at 3.24kHz. The power generation from this device was the result of all plate vibrations after the impact. The initial voltage spikes observed upon initial impact varied greatly across the range of tests performed. No information about the device volume or mass is available. The added complications of the ball and drop height make operational and static volumes less applicable.

The Sodano *et al.* first piezoelectric device [6] used an existing commercially available piezoelectric device, the Quick Pack QP40N (Midé Technology Corporation, Medford, MA, USA), as their generator. This generator was operated as a stand-alone vibration harvester utilizing the {31} Mode of piezo excitation. The volume that is used in Table 2.2 is the entire device static volume. The operating volume is not given. Though the power characteristics given are for the test case of 30 Hz and 10k Ω resistance, a range of 25-150Hz was tested and the voltage output ranged from near zero to 6.8V in the best case.

The Sodano *et al.* devices discussed in [8] were all affixed to the same larger aluminum beam structure to standardize the strain input that each device was receiving. The Micro-Fiber Composite (MFC) device was of interest as the fiber structure of the piezoelectric material (which is then embedded in a flexible epoxy matrix) makes it far less brittle and therefore easier to use. The MFC device utilizes the {33} Mode of operation with interdigitated electrodes (IDE). The second device listed, the Quick Pack IDE (model QP10ni) utilizes the {33} Mode of operation but with a monolithic piezoelectric structure instead of the fibrous composite of the MFC. The third device compared was the Quick Pack model QP10n, a monolithic piezoelectric structure that utilizes the {31} Mode of operation with a standard electrode pattern (as did the QP40N tested in [6]). The volumes used for power normalization in [9] are those of the active piezoelectric component only, however for ease of comparison, the volumes used in Table 2.2 for these devices were the total device volumes (including the aluminum beam but not including supplemental electronics). Voltage outputs for the devices in [9] were not given, nor were the device masses. Frequencies explored included the first 12 modes of the aluminum host beam, covering frequencies from 3.78 to 1401.0 Hz. The frequency of 64 Hz given in Table 2.2 corresponds to the 3rd mode of the host beam, which resulted in the highest power output for each device. Though it is not specifically addressed in the paper, it is likely that the 3rd beam mode resulted the highest power production due to higher strains in the beam under the harvesters for this mode than for the others.

As discussed in depth later in this chapter (Section 2.5), there have been some issues related to the Roundy *et al.* work as presented in [1] and [2]. The data given in Table 2.2 was gleaned in part from the figures in their work, but a complete, reproducible picture of their results was not captured in either source.

Glynne-Jones *et al.* [10] used a tapered bimorph device that activated the PZT in the {31} Mode with plate electrodes. The device consisted of a triangular shim of 316 stainless steel with electrodes and piezoelectric material printed and fired onto both sides in a trapezoidal stack. It is not clear how the authors arrived at the tapered geometry of the device, though it is stated that it was motivated by a desire to have a uniform strain distribution in the piezoelectric material. Concerns are mentioned about the complicating component of edge effects in a device of this geometry. The frequency given in Table 2.2 is the experimentally determined anti-resonant frequency of the device. The power characteristics were taken from the maximum observed power output, occurring at resonance with an experimentally determined optimum resistance of 333k Ω . The operating volume was calculated roughly from a given tip displacement at maximum excitation of 0.9mm.

du Toit [3] utilized a commercially available bimorph device, the T226-A4-503X from Piezo Systems, Inc. The device had no proof mass and had dimensions of 63.5 x 31.8 x 0.686 mm. Tests were done that successfully verified the model presented in du Toit's work [3] at off-resonance conditions (it was shown that the model underestimated the power and voltage generated at resonances) and demonstrated a peak power production of 550 μ W at 113 Hz. The power and voltage outputs given in Table 2.2 were from an anti-resonant operating point of 113 Hz with 170 k Ω resistance. The maximum tip deflection of 175 μ m was used to calculate the operating power density. Operating at 60 k Ω resistance and at resonance (107 Hz) gives a slightly higher power output of nearly 600 μ W but a decreased output voltage of only 3.6 V

(compared to 9.3 V), demonstrating the trade between available voltage and current that can be leveraged due to the difference in anti-resonant and resonant operating conditions. The efficiency of 0.4 that is shown is based on resonant operation and was calculated as per the technique described in Section 2.2.2.

Sood *et al.* [11] built and tested a MEMS-scale device that was reported to have excellent power output characteristics. The processing technique that is recorded in the work by Sood *et al.* has proven to not be a reliable approach to guarantee successful PZT deposition. While the work presented by Sood *et al.* can be taken as an encouraging step towards a MEMS-scale device, it may not be conclusive. The unusually high power densities reported in Table 2.1 seem questionable.

In summary, macro scale devices have been successfully tested, demonstrating electrical power harvesting from a vibration source using a piezoelectric structure. Such structures are even available commercially. However, none of the devices listed in Table 2.2 (with the possible exception of the Sood [11] device which was discussed above) would be adequate as a device power supply due to their large size and/or low power outputs. Smaller devices, like the micro-scale designs investigated in this work, are naturally better suited to higher-frequency applications due to both their smaller size and higher resonance and anti-resonant frequencies. The lack of published operational volumes and power conversion efficiencies with can easily be seen by the large number of unknown quantities in Table 2.2 is a serious impediment to device comparison and should be rectified by those working in the field.

2.4 A Brief Survey of Other Energy Harvesting Devices

Piezoelectric materials are one way of many that are currently being explored around the world in which ambient vibrational energy can be transformed into useful power. This section touches briefly on examples of other work that is being undertaken in the energy harvesting field without attempting to be a universal comparison, or completely inclusive sampling of the literature.

2.4.1 Capacitive Harvesting Devices

Capacitive harvesting devices are easily manufactured using MEMS technology and can also be used to generate power from ambient vibration. Roundy *et al.* looked at capacitive devices in their text [1] in addition to piezoelectric devices, in which piezoelectrics were considered superior for sensor node applications. Capacitive harvesting work has been done by Meninger *et al.* [14] as well.

In both designs the plates of the harvester are charged with an external power supply and their relative motion changes the capacitance of the device. This in turn can be tapped as useful power. In the gap-closing design, as presented by Roundy *et al.*, the overlapping fingers moved transversely to each other. In the pure overlap design presented by Meninger *et al.*, the fingers slide in and out of each other. Roundy *et al.* [2] preferred the in-plane harvester as being less sensitive to in-plane torsional instabilities that could be excited by off-axis vibration and cause the fingers to touch. These devices are not necessarily tuned to resonance, but rather to a

frequency ratio, $\Omega = \omega/\omega_n$, that gives the optimal travel of the device relative to the stationary fingers.

While capacitive harvesters have the potential to be quite simple and can be fabricated using existing MEMS technology, Roundy *et al.* [2] concluded that it was possible to obtain a higher power density with a piezoelectric device.

2.4.2 Thermal Harvesting Devices

Thermal energy harvesting devices operate with the Carnot cycle in which useful work can be obtained from a temperature difference. This is the same cycle that allows large-scale power generation from geothermal sites. While there are several devices in the literature that operate using this principle, the efficiency with which they can harness the energy available is directly related to the difference in temperature between the hot and cold ends of the device. For most commonly available temperature differences, say between body temperature and room temperature, the resulting efficiency is only around 5%. Even at these low efficiencies, some useful power has been reported.

As part of his survey of energy harvesting devices (which is focused on energy that can be harvested from the human body), Paradiso [15] describes Applied Digital Solutions' Thermo Life device as being 0.5 cm^2 and being able to produce $30 \mu\text{W}$ of power from a 5°C thermal gradient. Richards *et al.* [38] are working on a micro heat engine that they are coupling with a piezoelectric membrane harvester to generate energy from the thermal cycling generated by an external heat source. Stordeur and Stark [37] are developing a thermoelectric generator designed for MEMS applications and driven by a 20°C thermal gradient that has been shown to produce about $20\mu\text{W}$ of power.

In summary, thermal electric generation is a useful energy harvesting methodology for environments where significant thermal gradients can be maintained. For the case of aircraft skin vibration that is explored as an example in this work however, such a gradient is not present.

2.4.3 Other MEMS Harvesting Devices of Interest

In addition to the piezoelectric, capacitive, and thermo-electric devices that were discussed in this section, energy is available from many other sources. Solar, biological, nuclear, electromagnetic and even evaporative energy are all potential sources. Scherrer *et al.* [55] presents a macro-scale electromagnetic device that is predicted to produce 7mW of power (equivalent to a static power density of $778\mu\text{W}/\text{cm}^3$) with a 35Hz excitation. Vibrational amplitude is not given and testing was underway at the time of this writing. Moving away from vibrational excitation, Borno *et al.* [46] present a MEMS device based on Young-Laplace capillary forces. In a $300\mu\text{m}$ long arc, the curvature changes, straining the device as water evaporates from its fern-like channels. No power was generated from this device, but such a device could be built with a piezoelectric layer for power generation.

2.5 Review of Text and Work by Roundy *et al.*

The analysis presented in the book and journal articles by Roundy, Wright and Rabaey [1] and [2] on power generation using a vibrating piezoelectric beam was examined in some detail as part of this body of work. The findings of this examination highlight a key effect of the piezoelectric material's electromechanical coupling behavior while raising concerns about some oversimplifications in the Roundy *et al.* work. While the governing equations from which Roundy *et al.* began are correct, a critical oversight is made in their application to derive the resulting displacement, voltage and power. Roundy *et al.* assume that the operating frequency is constant at the natural frequency of the structure. This neglects a second, higher frequency, optimal power operating point that occurs at antiresonance (about 1.5 times the natural frequency in the case analyzed in their book) which results from the open circuit coupled behavior of the piezo material. Similarly, the assumption of a single optimal load resistance for the system is shown to omit significant power generation potential compared to an optimum load resistance that is allowed to vary with frequency. In actuality, as no special efforts to electrically short circuit the device during testing were reported, it is likely that any frequency observed as resonance was actually the anti-resonant frequency of the device. Note that the notation used in this section is consistent with that of the book by Roundy *et al.*, and is not necessarily the same as that used elsewhere in this work, and does not appear in the nomenclature section of this work.

2.5.1 Derivation of Beam Governing Equations

The state space model for a vibrating bimorph piezoelectric beam resonator with a proof mass (see Figure 2.3) developed by Roundy *et al.* is given in their Appendix A of the book as equation A.33 and repeated as Roundy A.33 below.

$$\begin{bmatrix} \dot{\delta} \\ \ddot{\delta} \\ \dot{V} \end{bmatrix} = \begin{bmatrix} 0 & 1 & 0 \\ -\frac{k_{sp}}{m} & -\frac{b_m b^{**}}{m} & \frac{k_{sp} d a}{2 m t_c} \\ 0 & -\frac{2 d Y_c t_c}{a \varepsilon} & \frac{-1}{R C_p} \end{bmatrix} \begin{bmatrix} \delta \\ \dot{\delta} \\ V \end{bmatrix} + \begin{bmatrix} 0 \\ b^* \\ 0 \end{bmatrix} \dot{y} \quad \text{(Roundy A.33)}$$

Where δ is average piezoelectric strain in the beam, V is voltage, y is the base displacement, k_{sp} is the effective spring constant for a tip load, m is the proof mass, $b_m = 2\zeta\omega_n m / b^{**}$ is the mechanical damping coefficient, b^{**} relates the average stress to vertical force applied at the center of the proof mass, b^* relates average strain to vertical tip displacement, d is the piezoelectric strain coefficient, Y_c is the Young's Modulus of the piezo material¹, t_c is the

¹ It is not specified whether this is the short- or open-circuit modulus.

thickness of the piezo ceramic layer, ϵ is the dielectric constant of the piezoelectric material, R is the resistance of the system, C_p is the effective capacitance of the piezoelectric device ($C_p = a^2 \epsilon \omega l_e / 2t_c$), where a is a constant and equals 1 if the layers are wired in series and 2 if they are wired in parallel. The overhead dot represents the derivative with respect to time. The average stress and strain of interest are the average axial stress and strain in the region of the piezoelectric material covered by the electrode. The average stress is defined in Roundy A.2 as:

$$\sigma = \frac{1}{l_e} \int_0^{l_e} \frac{M(x)b}{I} dx \quad (\text{Roundy A.2})$$

where b is the distance between the neutral axis (center of the shim) and the center of the piezo layer. Thus, this stress is both a length and through-thickness average: $\sigma = Y_c \delta$. The relationships between average stress and force and average strain and displacement are as follows from beam theory (ignoring the mass of the beam and using other unaddressed simplifying assumptions) and can be found as equations A.5 and A.13 respectively.

$$b^{**} = \frac{2I}{b(2l_b + l_m - l_e)} \quad (\text{Roundy A.5})$$

$$b^* = \frac{3b}{l_b^2} \frac{(2l_b + l_m - l_e)}{(2l_b + \frac{3}{2}l_m)} \quad (\text{Roundy A.13})$$

Where I is the moment of inertia of the cross section (not modulus-weighted), l_b is the length of the beam up to the proof mass, l_m is the length of the proof mass, l_e is the length of the electrode. Due to the geometry of the Roundy *et al.* device, $l_e \leq l_b$. A schematic of the beam geometry is given below as Figure 2.3. The cross section of the beam is vertically symmetric with a center shim and piezo material layers on both sides. The piezo layers are poled in series in the {3-1} Mode (see [1] Figure 4.2).

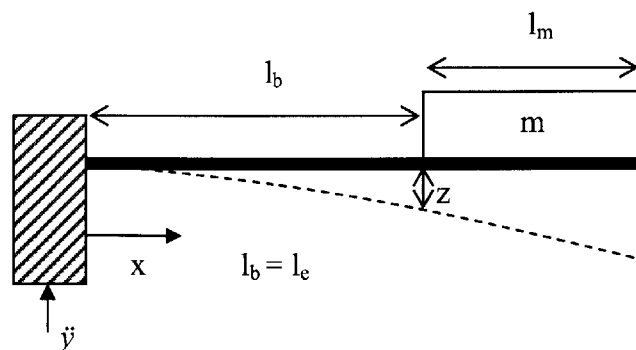


Figure 2.3: Schematic of Beam Geometry

There is concern over the applicability of the above model to the beam and proof mass structures analyzed due to the large size of the proof mass in comparison to the beam. For example, Design 1 described in Roundy Table 4.4 gives the length of the beam (l_b) as 6.5mm and the length of the proof mass (l_m) as 8.5mm. Representing a large proof mass as a point force is an oversimplification that leads to model error, however, it is sufficient at this point to further investigate the application of this model ignoring the oversimplifications. (A modal analysis of a beam and proof mass was conducted by duToit and Wardle [3] and is implemented here in Chapter 3.) There is additional concern that the actual geometry of the resonator is more closely approximated by a plate than a beam, but that issue has not been explored at this time.

The state space model given by Roundy *et al.* as A.33 is rewritten into two equations, coupling voltage (V) and average strain (δ). The Laplace Transform of these equations is taken with $\bar{V} = L(V)$ and $\bar{\delta} = L(\delta)$ and the resulting two equations are written in matrix form:

$$\begin{bmatrix} s^2 + 2\zeta\omega_n s + \omega_n^2 & -\omega_n^2 \frac{ad}{2t_c} \\ \frac{2k^2 t_c}{ad} s & s + \frac{1}{RC_p} \end{bmatrix} \begin{bmatrix} \bar{\delta} \\ \bar{V} \end{bmatrix} = \begin{bmatrix} b^* \ddot{y} \\ 0 \end{bmatrix} \quad \text{Eq 2-6}$$

using the following substitutions: $\omega_n^2 = \frac{k_{sp}}{m}$, $2\zeta\omega_n = \frac{b_m b^{**}}{m}$, and $k^2 = \frac{d^2 Y_c}{\varepsilon}$, where k^2 is the piezoelectric coupling factor². Note that taking $\omega_n^2 = \frac{k_{sp}}{m}$ is a significant approximation. The factor a equalling 1 or 2 depending on whether the piezoelectric operation is in parallel or series. This re-written set of governing equations is subsequently taken through the same process that was applied to the governing equations used in the modeling presented in this work (see Section 3.1) in an effort to more fully understand the Roundy *et al.* results.

Proceeding to solving Eq 2-6, the determinant is:

$$\det = s^3 + \left(2\zeta\omega_n + \frac{1}{RC_p} \right) s^2 + \left(\omega_n^2 + \frac{2\zeta\omega_n}{RC_p} + \omega_n^2 k^2 \right) s + \frac{\omega_n^2}{RC_p} \quad \text{Eq 2-7}$$

and the average strain is found in terms of s to be

² As with modulus, it is not specified whether these properties are open- or short-circuit values. The macro-scale devices tested in Roundy *et al.* were operated in {3-1} Mode.

$$\bar{\delta} = \begin{vmatrix} b^* \ddot{y} & -\omega_n^2 \frac{ad}{2t_c} \\ 0 & s + \frac{1}{RC_p} \end{vmatrix} \frac{1}{\det} \quad \text{Eq 2-8}$$

which gives:

$$\frac{\bar{\delta}}{\ddot{y}} = \frac{b^* \left(s + \frac{1}{RC_p} \right)}{s^3 + \left(2\zeta\omega_n + \frac{1}{RC_p} \right) s^2 + \left(\omega_n^2 + \frac{2\zeta\omega_n}{RC_p} + \omega_n^2 k^2 \right) s + \frac{\omega_n^2}{RC_p}} \quad \text{Eq 2-9}$$

where \ddot{y} is the input base acceleration. (Note that Roundy *et al.* use A_{in} to denote the input acceleration.)

By the same process, an expression for voltage, \bar{V} , in terms of s is found to be

$$\frac{\bar{V}}{\ddot{y}} = \frac{-s \frac{2k^2 t_c}{ad} b^*}{s^3 + \left(2\zeta\omega_n + \frac{1}{RC_p} \right) s^2 + \left(\omega_n^2 + \frac{2\zeta\omega_n}{RC_p} + \omega_n^2 k^2 \right) s + \frac{\omega_n^2}{RC_p}} \quad \text{Eq 2-10}$$

This expression correlates with the expression for voltage given in Roundy *et al.* A.37.

The inverse Laplace transform is taken by substituting $s=j\omega$ into equations 2-9 and 2-10. The expressions for the magnitude of strain and voltage are found by setting

$$\left| \frac{\delta}{\ddot{y}} \right| = \sqrt{\frac{\delta(j\omega) \delta(-j\omega)}{\ddot{y} \ddot{y}}} \quad \text{Eq 2-11}$$

and similarly for V/\ddot{y} . Relative displacement can be found as $z = \frac{\delta}{b^*}$. The magnitude of the power is equal to V^2/R . Putting together all these gives:

$$\frac{\bar{\delta}}{\ddot{y}} = \frac{\sqrt{1 + (RC_p)^2 \omega^2}}{\sqrt{\left[(\omega_n^2 - \omega^2) - 2\zeta\omega_n RC_p \omega^2 \right]^2 + \left[(\omega RC_p) \left(\omega_n^2 (1 + k^2) - \omega^2 \right) + 2\zeta\omega_n \omega \right]^2}} \quad \text{Eq 2-12}$$

$$\frac{\bar{V}}{\ddot{y}} = \frac{\omega RC_p \frac{2k^2 t_c}{ad} b^*}{\sqrt{\left[(\omega_n^2 - \omega^2) - 2\zeta\omega_n RC_p \omega^2 \right]^2 + \left[(\omega RC_p) \left\{ \omega_n^2 (1 + k^2) - \omega^2 \right\} + 2\zeta\omega_n \omega \right]^2}} \quad \text{Eq 2-13}$$

$$\left| \frac{P}{\ddot{y}^2} \right| = \frac{1}{R} \left| \frac{V}{\ddot{y}} \right|^2 = \frac{\omega^2 RC_p^2 \left(\frac{2k^2 t_c}{ad} b^* \right)^2}{\left[(\omega_n^2 - \omega^2) - 2\zeta\omega_n RC_p \omega^2 \right]^2 + \left[(\omega RC_p) \left\{ \omega_n^2 (1 + k^2) - \omega^2 \right\} + 2\zeta\omega_n \omega \right]^2} \quad \text{Eq 2-14}$$

(Note that equations 2-12 to 2-14 can be written in a much more useful form, particularly the denominator, as done in this work in Section 3.1.)

Between equations A.37 (voltage as a function of $j\omega$) and A.38 (voltage in terms of $\omega = \omega_n$), Roundy *et al.* make a critical oversimplifying assumption: the driving frequency ω is set equal to the natural frequency of the system, ω_n . This is the same as setting $\omega = \omega_n$ in the above equations. The problem with this assumption is that it captures only one mode of operation for the piezoelectric material and neglects the effect of the electromechanical coupling on the natural frequency of the device. These two frequencies can be seen by looking at what happens to the magnitude of z as the load resistance R tends to 0 and to infinity in equation 2-12. When the piezoelectric is operating in short-circuit conditions ($R \rightarrow 0$), the peak displacement (and therefore peak power) occurs at $\Omega_{SC} = \omega/\omega_n = 1$ as assumed by Roundy *et al.* However, when the piezo is operating in open-circuit conditions ($R \rightarrow \infty$), it can be shown that a local maximum displacement and power response occurs when $\Omega_{OC} = \omega/\omega_n = \sqrt{1 + k^2}$.

It is worth noting that in general, when a piezoelectric material is part of a structure, the rest of the structure also has an effect on the open circuit antiresonance frequency of the device. Only the material properties of the piezo are present in the expression for Ω_{OC} above as the effect of the rest of the structure is simplified via $\omega_n^2 = k_{sp}/m$ in Roundy *et al.*'s analysis. This is why k^2 is used in the expression for Ω_{OC} instead of κ^2 (which includes structural parameters as well as the material), as will be used throughout the rest of this thesis.

The effect of these two peak operating frequencies can be seen in the graphs that follow. According to the material properties and device geometries given for the devices tested by Roundy *et al.*, the piezo coupling coefficient was small enough that Ω_{SC} and Ω_{OC} were close enough to make the two operating peaks almost indistinguishable. (This is the same effect that is seen if the piezo elements are a small part of the structure.) However, if a coupling coefficient typical of the {3-3} mode of operation is assumed instead of that for the {3-1} mode of operation, two peaks do become visible. It is intuitive that as the coupling approaches zero (or as less and less of the structure is comprised of piezo material), the coupling is removed and the two peaks become only one, located at $\Omega = \omega/\omega_n = 1$.

An additional consequence of setting $\omega = \omega_n$ is that the optimal value for resistance that was found in A.40 is not a function of frequency. Using this value of R_{opt} gives significantly lower

power output than that obtained by allowing R_{opt} to vary as a function of Ω (as much as 6mW vs 3mW for high coupling coefficients).

The optimal resistance as a function of frequency is:

$$R_{opt} = \sqrt{\frac{\omega_n^4 + (4\zeta^2 - 2)\omega_n^2\omega^2 + \omega^4}{C_p^2\omega_n^2[(1+k^2)^2\omega_n^4 - 2(1+k^2 - 2\zeta^2)\omega_n^2\omega^2 + \omega^4]}} \quad \text{Eq 2-15}$$

which is found by differentiating the expression for power, Eq. 2-14, with respect to resistance and solving for the resistance at the maximum. This is in contrast with the optimal resistance given by Roundy (and repeated below), which was found by the same technique but after the operating frequency was fixed at $\Omega=1$ and is thus not a function of operating frequency.

$$R_{opt} = \frac{1}{\omega_n C_p} \frac{2\zeta}{\sqrt{4\zeta^2 + k^4}} \quad \text{(Roundy A.40)}$$

Equation Roundy A.40 can be obtained by setting $\omega = \omega_n$ in Eq 2-15.

2.5.2 Results and Discussion

The parameter values given in Chapter 4 of Roundy *et al.* [1] for Design 1 (Table 4.4) were used to generate plots of the above equations. They are

Table 2.3: Device Parameters from Roundy *et al.* [1]

ω_n	120 Hz	l_b	6.5 mm
d	320e-12 m/V	l_m	8.5 mm
t_c	0.139 mm	l_e	6.5 mm
t_{sh}	0.102 mm	b	0.1205 mm
w_m	6.7 mm	h_m	7.7 mm
w_b	3.0 mm	a	1
C_p	9.4e-9 Farads	ζ	0.025
k_{31}	0.32		

The k used in the expressions in Eq 2-12 through Eq 2-15 and Roundy A.40 is the piezo coupling coefficient (see Eq 2-6). (A structural spring constant, k_{sp} , is used early in the equations but is normalized by mass, m , and replaced with ω_n). The input acceleration was taken to be 2.25 m/s². Using the dimensions above with the material properties in Table 4.1 (on page 55 of Roundy *et al.* [1]), and the definition of moment of inertia found in Roundy A.1, $I=8.71e-11$ m⁴.

Using this information and plotting predicted displacement, z , voltage and power output of the device, it was shown that the over-simplified equations (with Ω set to 1) do not reveal the dual operating peaks that can be seen when Ω is allowed to vary and resistance is optimized as a function of frequency.

The larger the piezoelectric coupling, the more prominently these dual operating peaks appear. Investigations were done using either $k_{31} = 0.32$ or $k_{33} = 0.75$, which are typical piezoelectric coupling coefficient values. However, there appears to be some confusion in Roundy *et al.* in section 4.5 (p. 63) in the discussion of possible values for k . It is possible that they were confusing the material property of the piezoelectric coupling with the overall structural coupling. To mitigate this possibility, power was plotted for three different values of k , the k_{31} and k_{33} given above and a second $k_{31} = 0.18$ as used at various points in Chapter 4 of Roundy *et al.* [1]. The open-circuit frequencies (Ω_{OC}) are given for each value of stiffness in Table 2.4 below, where Ω_{SC} is taken as 1 in all cases.

Table 2.4: Piezoelectric Coupling Factors and Corresponding Open-Circuit Frequency Ratios

k_{31}	Ω_{OC}
0.18	1.017
0.32	1.050
0.75	1.250

As can be seen, for low values of k , given as k_{31} , the open circuit frequency becomes closer and closer to the short circuit frequency. This is easily understood by realizing that the presence of these dual operating peaks is due to the effect that the electrical behavior of the piezoelectric has on the overall structural stiffness (and thus on the resonant frequency of the structure). The more pronounced that electrical-mechanical interaction is (*i.e.* the larger the value of k), the larger the effect that electrical conditions can have on the overall structural properties and resonance.

Further concern arose when this author attempted unsuccessfully to reproduce the data and model comparisons that are included in Chapter 5 of Roundy *et al.* [1]. The equations that are given as the plotted models do not reproduce the plots shown with the input conditions and material properties listed in the supporting text. A root cause of this discrepancy was not determined.

Finally, Chapter 3 of Roundy *et al.*, “Comparison of Methods”, which looks at piezoelectric vs. electrostatic and electromagnetic conversion relative to one another, misses both scaling and thin-film realities of microscale (MEMS) harvesters. The conclusion that piezoelectrics are better than, or comparable to, the other two methods does however seem to hold. Section 4.2 in Roundy *et al.*, Material Selection for piezoelectric harvesters, is similarly overly simplistic.

2.6 An Introduction to Supporting Electronics for Energy Harvesting

In addition to the power supply itself, a micro-scale sensing node will need to be designed for efficient use of the available energy. This concern is valid regardless of the source of the node’s power: even though ambient harvesting power supplies are not life-limited, they are still power-limited. Particularly if the energy source is intermittent, conservation of the energy that is harvested is critical. Efficient energy usage can be accomplished through the design of the power electronics themselves or through implementation of dynamic power management schemes that take advantage of “down-time” in the device’s operation to reduce overall power consumption. The possibility of intermittent power generation, or similarly of intermittent high

power usage, makes the need for an energy storage mechanism, such as rechargeable batteries or a capacitor, clear as well.

2.6.1 Power Management Techniques and Circuitry

Much of the power management schemes that have been developed have been investigated for use with battery powered devices, but their applicability extends to systems powered with harvested ambient energy. The MIT μ AMPS project led by Anantha Chandrakasan has done a significant amount of work on energy-efficient support technologies for distributed wireless sensor networks [14, 18, 19, 20, 21, 23 & 32]. The basic idea behind power-aware system management is to shut down, or sleep devices when not needed and wake them as necessary [18]. This is particularly applicable to systems in the node such as the transmitter and processor. If there are times when no energy needs to be transmitted, or peak processing performance is not required, these devices can be placed into a low-energy consumption sleep state and reactivated either based on a set schedule or an event trigger. An example given by the μ AMPS group for their μ AMPS-1 prototype acoustic sensor node shows that out of a total peak power consumption of just under 1W, 450mW can be saved by sleeping the processor and an additional 300mW can be conserved by shutting down the radio transmitter [19]. Thus, real savings can be realized from implementing this type of dynamic power management.

This basic concept is not quite as simple to implement as it might seem, however. Due to potentially large power overheads associated with shutting down and reinitializing components, it can actually be more energy-expensive to sleep a component for a short time than to allow it to operate. Additionally if data transmission is required, larger buffering capability is required if the transmission packets are to be separated by longer periods of time [19]. Transmission energy per bit can also be traded against transmission accuracy [19]. There is also a trade to be negotiated between energy consumed and the probability that a desired event will be missed. The μ AMPS group has shown that there is a nearly linear relationship between these two characteristics, allowing the designer to tailor the balance of sensitivity and power consumption to a given application [18 & 19].

As communication is one of the largest power drains on a device, it makes sense that energy efficient communication schemes have also been investigated. The μ AMPS group developed a communication protocol, LEACH (Low-Energy Adaptive Clustering Hierarchy), which can result in up to an 8x reduction in power required by dividing nodes into clusters to distribute the communication energy load more evenly among the nodes in the sensing network [23]. By combining efficient compression and data routing energy, the LEACH scheme trades-off the quality of the output and the amount of compression achieved to lower the overall system power consumption. As with the power management schemes described early, the system designer would have to evaluate this trade in the context of any given application, but it is important to realize that such potential is available.

A number of power management schemes (many of which are similar to those developed by the μ AMPS group and described briefly above) were incorporated into the WiseNET wireless system design developed by Enz *et al.* [22]. From a system perspective, WiseNET seeks to eliminate several common sources of wasted communications-related power due to idle listening, emitting without a ready receiver, overhearing data meant for another node and data transmission

collisions. Through software and hardware design, the WiseNET scheme is modeled as needing between 10 and 600 μ W average node power consumption depending on the operating requirements. This would bring the power required by a wireless node into a range that could be supplied with a small ($\sim 1\text{cm}^3$) vibrational energy harvesting device such as those investigated in this work. Currently, however, the device prototype consumes 31.5mW in transmit mode and 1.8mW in receiving mode, both of which are currently above the range of *continuous* power generation of micro-scale vibrational energy harvesters.

Another interesting power management technique was proposed for use with energy harvesting chips by Torres *et al.* [16]. It involves a “boost-buck” regulator that more seamlessly handles the variations in power produced by a number of different power harvesting devices by allowing power levels produced both below and above the design point of the system to be efficiently used or stored.

2.6.2 Energy Storage Options

Due to the intermittent nature of both the power source and the power demand of the sensor node, a MEMS scale energy storage technique is needed for successful implementation of self-powered sensor node. One of the simplest techniques is to couple the energy harvesting device with a rechargeable battery. A more complicated, but potentially more beneficial technique is presented by Lakeman *et al.* [30], in which a microsupercapacitor is coupled in parallel with a rechargeable microbattery for optimal power dispensation. With this hybrid power source, a sudden load on the power supply does not result in the sharp drop in available voltage seen with only a battery, but rather the capacitor steps in more quickly and mitigates the demand, giving a higher delivered power for a given footprint.

Promising work has also been done on developing micro scale rechargeable batteries that could be coupled (alone or in parallel with a capacitor as described above) with a piezoelectric vibration energy harvesting device. Ryan *et al.* [24] presented work on various small scale batteries, including lithium, nickel and zinc combinations which were tested in packages with footprints of 0.25cm^2 as well as in micro scale packages of $750\mu\text{m} \times 750\mu\text{m} \times 25\mu\text{m}$. This micro scale device was tested in over a dozen cycles with densities of up to $5.1\text{mA}/\text{cm}^2$. A $50\mu\text{m}$ square device had been built but not tested at the time of the article’s publication. Microfabrication techniques were also demonstrated for many of the thin films and components that would be necessary to mass produce these types of batteries. Additionally, rechargeable lithium microbatteries are the subject of a substantial set of literature [25 26 27 28]. Sadoway and Mayes [26] indicate that lithium solid polymer electrolyte (Li-SPE) batteries are currently the leaders in the microbattery field with a nominal voltage of 3.1V, and specific energies of 1440 kJ/kg.

It has also been shown that a piezoelectric vibration energy harvesting device is capable of charging a battery similar to those described above by Sodano *et al.* [29]. Testing of both a monolithic piezoelectric device and a Macro Fiber Composite (MFC) device – both macro scale – highlighted a key requirement on the power harvesting device. The current produced by the harvester must be at least one-tenth of the battery’s capacity to enable charging in their scheme. The monolithic piezoelectric device was capable of producing such a current but the MFC device was not. Using the monolithic device, it was shown that both a random and a resonant input

vibration signal could be used to charge batteries of sizes ranging from 40mAh to 1000mAh. The larger the battery's capacity, the greater the disparity was in time-to-charge for resonant and random signals, with both resonant and random signals requiring 1.6 hours to charge the smallest battery while the 1000mAh battery requiring 22 hours at resonance and 32 hours with a random signal. This is an encouraging result as it is difficult to guarantee exactly what the input vibration will be for any given harvesting device.

3 Modeling and Optimization of Uniform Beam Harvesters

A modeling approach and design methodology for piezoelectric untapered (or uniform) beam vibration energy harvesters is presented in this chapter. The modeling used in this work is based on work done previously by du Toit [3 and 5]. Beginning with an explanation of the modeling approach used, piezoelectric operating modes and MEMS device fabrication constraints are discussed before comparing the models used to data for both {3-1} and {3-3} Mode harvesters. Graphical optimization results and sample design recommendations and performance predictions or devices operating in an aircraft vibrational environment are presented in the second half of this chapter. Together, this chapter provides a basis that can be extended to any application for which the vibration environment and device performance metrics are known.

3.1 Previous Modeling

The governing equations that were adapted and used in the design and optimization tools for this work were originally presented by du Toit [3] and will be explained but not re-derived here. Beginning with first principles and conservation of total energy including components of kinetic energy (T_k), internal strain energy (U), electrical energy (W_e), and external work (W) – both in the structure and in the piezoelectric material – the result of this previous analysis is a pair of governing equations that demonstrate the coupling of structural displacement and charge generated in the piezoelectric material. The originating conservation equation and individual energy terms are reproduced below:

$$\int_{t_1}^{t_2} [\delta(T_k - U + W_e) + \delta W] dt = 0 \quad \text{Eq 3-1}$$

Where δ indicates the first variation of the function and the integral is taken over the time t_2-t_1 . The individual terms are:

$$T_k = \frac{1}{2} \int_{V_s} \rho_s \dot{\mathbf{u}}^t \dot{\mathbf{u}} dV_s + \frac{1}{2} \int_{V_p} \rho_p \dot{\mathbf{u}}^t \dot{\mathbf{u}} dV_p \quad \text{Eq 3-2}$$

$$U = \frac{1}{2} \int_{V_s} \mathbf{S}^t \mathbf{T} dV_s + \frac{1}{2} \int_{V_p} \mathbf{S}^t \mathbf{T} dV_p \quad \text{Eq 3-3}$$

$$W_e = \frac{1}{2} \int_{V_p} \mathbf{E}^t \mathbf{D} dV_p \quad \text{Eq 3-4}$$

$$\delta W = \sum_{k=1}^{nf} \delta \mathbf{u}_k \mathbf{f}_k(t) + \sum_{j=1}^{ng} \delta \varphi_j q_j \quad \text{Eq 3-5}$$

Where the subscript p represents the piezoelectric material and the subscript s indicates the rest of the structure. Relative displacement (of the beam relative to the base displacement input) is represented by \mathbf{u} , density is ρ , \mathbf{S} is strain, \mathbf{T} is stress, \mathbf{E} is electric field and \mathbf{D} is electric displacement. In the external work term, $\varphi_j = \varphi(x_j, t)$ represents the scalar electrical potential at the j^{th} electrode, $\mathbf{f}_k(t)$ are point loads at discrete positions x_k , and q_j are the charges extracted from the electrodes at x_j . (Throughout, a superscript E indicates that the quantity was measured at constant electric field; S indicates constant strain.) The mechanical mode shapes [3, 54] of the beam are given by:

$$\psi_{rN} = c \sinh \lambda_N x + d \cosh \lambda_N x + e \sin \lambda_N x + f \cos \lambda_N x \quad \text{Eq 3-6}$$

Where the subscript r denotes that it is a mechanical mode shape (subscript v denotes electrical) and N is the mode number. (The coefficients c , d , e , and f are determined by enforcing the boundary conditions of the beam and are defined for the case of a cantilevered beam with a proof mass shortly.) For the analysis here, N is taken to be 1 and dropped from following expressions. The relative transverse displacement of the beam (see Figure 3.1), w , can be considered to be a function of both time and position along the beam, $w = r(t)\psi_r$, and similarly for the voltage, v , across the piezoelectric: $v = v(t)\psi_v$ (only one mode shape is taken for the voltage, such that ψ_{v1} is referred to as ψ_v , as was done for the mechanical mode shape). For convenience, $\lambda_N^4 = m\omega^2 / (cI)_e$ was defined where $(cI)_e$ is the effective bending stiffness of the beam.

Proceeding with the governing equation derivation, these quantities can be simplified to represent the particular case of interest. The reader is referred to du Toit's work for the detail that takes these energy equations to the beam governing equations. The original derivation in [3] deals with the full matrix coefficients, which allow for the inclusion of multiple modes in the governing equations. As this work is focused on the practical application of these equations to design and optimization of piezoelectric devices, this level of complexity will be eliminated as only the first structural vibration mode, ψ_{r1} , and a single electrical mode, ψ_{v1} , will be considered from here on. These single modes have been shown to capture the response of experimentally tested beam harvesters [4]. The scalar governing equations are:

$$M\ddot{r} + C\dot{r} + Kr - \Theta v = -B_f \ddot{w}_B \quad \text{Eq 3-7}$$

$$\Theta \dot{r} + C_p \dot{v} + \frac{1}{R_l} v = 0 \quad \text{Eq 3-8}$$

Where r represents the amplitude of the relative displacement (w), and v represents the amplitude of the voltage and the other coefficients are defined below. The first governing equation above is the mechanical governing equation showing the electrical coupling through the term Θv . The second governing equation is the electrical governing equation, showing the mechanical coupling also through the Θ term. The effective load resistance, R_{le} , includes both the internal piezoelectric resistance and the electrical circuit load in parallel, but as the internal

resistance is much larger, R_{le} is dominated by the load resistance and R_{le} is referred to as R_l throughout.

The scalar coefficients are defined below.

$$M = \int_{V_s} \psi_r^2 \rho_s dV_s + \int_{V_p} \psi_r^2 \rho_p dV_p \quad \text{Eq 3-9}$$

$$K = \int_{V_s} (-z \psi_r'')^2 c_s dV_s + \int_{V_p} (-z \psi_r'')^2 c^E dV_p \quad \text{Eq 3-10}$$

$$C = 2\zeta_m \omega M \quad \text{Eq 3-11}$$

$$\Theta = \int_{V_p} (z \psi_r'') e(-\nabla \psi_v) dV_p \quad \text{Eq 3-12}$$

$$C_p = \int_{V_p} (\nabla \psi_v)^2 \varepsilon^S dV_p \quad \text{Eq 3-13}$$

$$B_f = \int_0^L m \psi_r dx \quad \text{Eq 3-14}$$

The mass coefficient, M , and the input coefficient, B_f , given above are for the case when the beam does not have a proof mass. In Figure 3.1, reproduced from du Toit [3] with variable names adapted to the current terminology, is an illustration of a beam with a large proof mass – which is the situation for many of the MEMS designs investigated in this work.

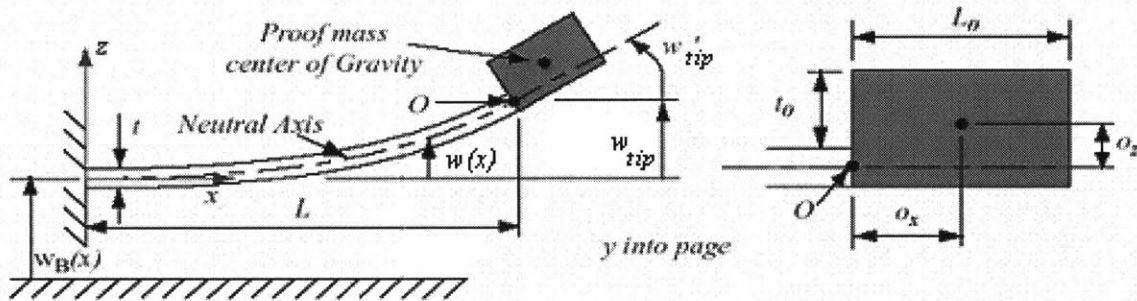


Figure 3.1: Beam with Proof Mass from du Toit [3]

When a large proof mass is present, the expressions for M and B_f given above should be replaced with the following:

$$M = \int_{V_s} \psi_r(x)^2 \rho_s dV_s + \int_{V_p} \psi_r(x)^2 \rho_p dV_p + M_0(\psi_r(L))^2 + 2S_0(\psi_r(L))\psi_r'(L) + J_0(\psi_r'(L))^2 \quad \text{Eq 3-15}$$

and

$$B_f = m \int_0^L \psi_r(x) dx + m_0 \psi_r(L) \int_L^{L+L_0} dx + m_0 \psi_r'(L) \int_L^{L+L_0} x dx \quad \text{Eq 3-16}$$

where M_0 is the mass of the proof mass, S_0 is the moment the proof mass imposes on the beam, I_0 is the mass moment of inertia around the center of the proof mass. L is the length of the beam, L_0 is the length of the proof mass, m and m_0 are the mass per unit length of the beam and proof mass, respectively, and x is the distance along the length of the beam. No modifications to the other coefficients are needed.

The mechanical mode shapes for this configuration, rewritten from Eq 3-6 above, can be found analytically to be:

$$\psi_{rN} = f \left[(\cosh \lambda_N x - \cos \lambda_N x) - \frac{A_{12}}{A_{11}} (\sinh \lambda_N x - \sin \lambda_N x) \right] \quad \text{Eq 3-17}$$

Where the coefficients A_{11} and A_{12} are found from:

$$\begin{aligned} A_{11} &= (\sinh \bar{\lambda}_N + \sin \bar{\lambda}_N) + \bar{\lambda}_N^3 \bar{J}_0 (-\cosh \bar{\lambda}_N + \cos \bar{\lambda}_N) + \bar{\lambda}_N^2 \bar{S}_0 (-\sinh \bar{\lambda}_N + \sin \bar{\lambda}_N) \\ A_{12} &= (\cosh \bar{\lambda}_N + \cos \bar{\lambda}_N) + \bar{\lambda}_N^3 \bar{J}_0 (-\sinh \bar{\lambda}_N + \sin \bar{\lambda}_N) + \bar{\lambda}_N^2 \bar{S}_0 (-\cosh \bar{\lambda}_N + \cos \bar{\lambda}_N) \\ A_{21} &= (\cosh \bar{\lambda}_N + \cos \bar{\lambda}_N) + \bar{\lambda}_N \bar{M}_0 (\sinh \bar{\lambda}_N - \sin \bar{\lambda}_N) + \bar{\lambda}_N^2 \bar{S}_0 (\cosh \bar{\lambda}_N - \cos \bar{\lambda}_N) \\ A_{22} &= (\sinh \bar{\lambda}_N - \sin \bar{\lambda}_N) + \bar{\lambda}_N \bar{M}_0 (\cosh \bar{\lambda}_N - \cos \bar{\lambda}_N) + \bar{\lambda}_N^2 \bar{S}_0 (\sinh \bar{\lambda}_N + \sin \bar{\lambda}_N) \end{aligned} \quad \text{Eq 3-18}$$

Where $\bar{\lambda}_N = \lambda_N L$, $\bar{M}_0 = \frac{M_0}{mL}$, $\bar{S}_0 = \frac{S_0}{mL^2}$, and $\bar{J}_0 = \frac{J_0}{mL^3}$. The moment induced by the proof mass is $M_0 = m_0 L$, $S_0 = M_0 o_x$ accounts for the displacement of the center of gravity of the mass from the end of the beam while $J_0 = J_{yy} + M_0(o_x^2 + o_z^2)$ accounts for the inertia of the center of gravity above the beam neutral axis. J_{yy} is the mass moment of inertia of the proof mass around its own center of gravity. The frequencies, ω_N for each Nth mode can then be found with

$$\omega_N = \bar{\lambda}_N^2 \sqrt{(cI)_e / mL^4}.$$

The particular modes are found by solving for the $\bar{\lambda}_N$ such that $\begin{vmatrix} A_{11} & A_{12} \\ A_{21} & A_{22} \end{vmatrix} = 0$. Each successive value of $\bar{\lambda}_N$ that satisfies the above represents a successive mode of the structure. For the analysis presented here, only the first mode is again considered. For the case without a proof mass, the above reduces to the familiar coefficients for the cantilevered beam mode shapes [54].

The electrical mode shapes depend on whether the device is operating in the {3-3} or {3-1} piezoelectric Mode. These shapes and the differences between these modes will be discussed in the next section.

By substituting the appropriate mode shapes into the coefficients defined in Eq 3-9 through Eq 3-14, and applying the governing equations (Eq 3-7 and 3-8), the following normalized equations for relative displacement, voltage and power output can be obtained:

$$\left| \frac{r}{B_f \ddot{w}_B} \right| = \frac{1}{K} \frac{\sqrt{1 + (\alpha\Omega)^2}}{\sqrt{\left[\{1 - \Omega^2\} - 2\zeta_m \Omega^2 \alpha \right]^2 + \left[\{1 + \kappa^2\} - \Omega^2 \right] \alpha \Omega + 2\zeta_m \Omega^2}^2} \quad \text{Eq 3-19}$$

$$\left| \frac{v}{B_f \ddot{w}_B} \right| = \frac{1}{|\Theta|} \frac{\alpha \kappa^2 \Omega}{\sqrt{\left[\{1 - \Omega^2\} - 2\zeta_m \Omega^2 \alpha \right]^2 + \left[\{1 + \kappa^2\} - \Omega^2 \right] \alpha \Omega + 2\zeta_m \Omega^2}^2} \quad \text{Eq 3-20}$$

$$\left| \frac{P_{out}}{(B_f \ddot{w}_B)^2} \right| = \frac{\omega_1}{K} \frac{\alpha \kappa^2 \Omega^2}{\left[\{1 - \Omega^2\} - 2\zeta_m \Omega^2 \alpha \right]^2 + \left[\{1 + \kappa^2\} - \Omega^2 \right] \alpha \Omega + 2\zeta_m \Omega^2}^2} \quad \text{Eq 3-21}$$

where $\alpha = \omega_1 R_1 C_p$, $\kappa^2 = \Theta^2 / KC_p$, $\Omega = \omega / \omega_1$, and ω_1 is the first modal frequency (resonant, short circuit, frequency) of the device. The frequency ratio, Ω is the ratio of input frequency to natural frequency, ζ_m , is the mechanical damping ratio, and K and C_p are the stiffness and capacitance as defined above. It should be noted that unlike the nondimensional material piezoelectric coupling coefficients of k_{33} or k_e , κ is a nondimensional structure/system electromechanical coupling coefficient. It is important to remember that the above is intended only as a summary of the basic equations on which the design tools demonstrated in this work were based; the reader is directed to [3] for the details for the derivation.

The last piece of du Toit's modeling that will be repeated here in summary is that of the optimal load resistance for power generation, $R_{l,opt}$, as a function of frequency. Presented in the long form used later in modeling, this optimum resistance is:

$$R_{l,opt} = \frac{\alpha_{opt}}{C_p \omega_1} \quad \text{Eq 3-22}$$

Where ω_1 is the resonant (or first natural) frequency of the device and the nondimensional resistance at power-optimum, α_{opt} , is:

$$\alpha_{opt}^2 = \frac{1}{\Omega^2} \frac{(1 - \Omega^2)^2 + (2\zeta_m \Omega)^2}{([1 + \kappa^2] - \Omega^2)^2 + (2\zeta_m \Omega)^2} \quad \text{Eq 3-23}$$

For the many cases where $2\zeta_m/\kappa^2 \ll 1$, this results in the optimum value, $\alpha_R = 2\zeta_m/\kappa^2$ and $\alpha_{AR} = \kappa^2/2\zeta_m(1 + \kappa^2)$ for the resonance frequency, $\Omega_R = \Omega_{SC} = 1$, and anti-resonance frequency, $\Omega_{AR} = \Omega_{OC} = \sqrt{1 + \kappa^2}$, respectively.

3.2 The {3-1} and {3-3} Electrical Modes

As mentioned in the previous section, there are multiple structural and mechanical coupling relationships that can be employed when using a piezoelectric material. The two that are considered here are the {3-1} and {3-3} Modes of operation for a beam. The numbers refer to the numbered axes in a Cartesian coordinate system where the 3-direction is the direction of poling (by convention) in the piezoelectric material and the others follow the right hand rule. Thus, in the {3-1} Mode, the mechanical excitation (imposed strain in the 1-direction) is perpendicular to the electric field established in the piezoelectric (in the 3-direction). This corresponds to a beam configuration where the electrodes sandwich the piezoelectric elements of the beam – which can incorporate two layers of piezoelectric, one above and one below a structural layer, creating a bimorph harvester. A unimorph harvester can also be created in the {3-1} Mode, but a bimorph was modeled here for more direct comparison to the experimental work done by du Toit [3]. In the second mode, the {3-3} Mode, the strain and the electric field are parallel to each other (in the 3-direction). This is accomplished by having interdigitated electrodes on the top of a single layer of piezoelectric, forming a unimorph harvester. A bimorph {3-1} Mode harvester is illustrated in Figure 3.2; a unimorph {3-3} Mode device is represented in Figure 3.3. In both figures, local material (piezoelectric) coordinates are shown.

Three key dimensions for electric mode definition are marked in Figure 3.2 and Figure 3.3: the thickness of the piezoelectric layer, t_p , in both cases, and the width, a , of the electrodes and the spacing between the centers of the electrodes (or pitch), p , in the {3-3} Mode unimorph configuration. Additional information on these two piezoelectric modes can be found in du Toit [3], but the key differences are summarized here.

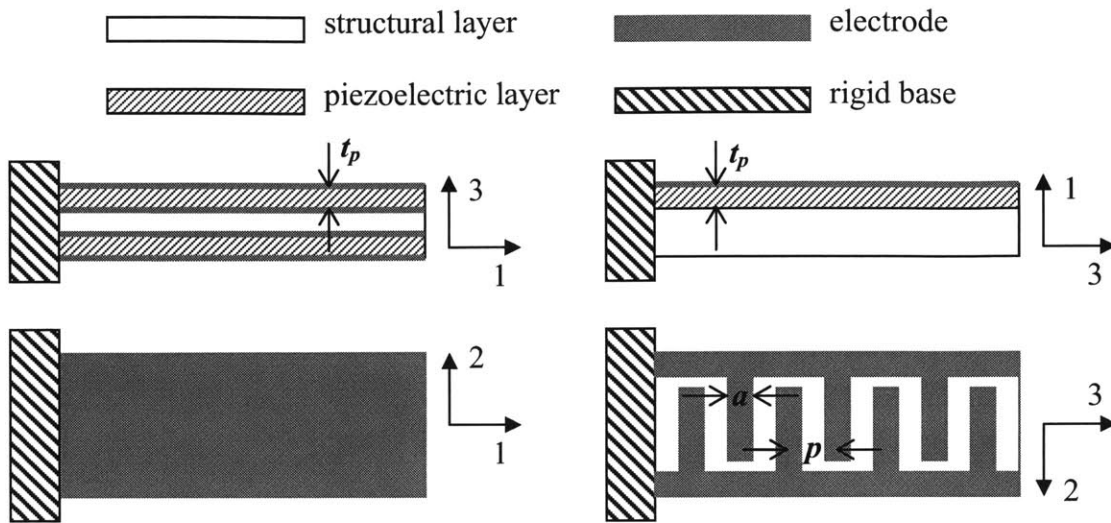


Figure 3.2: Bimorph ({3-1} Mode) Harvester Schematic with Two Pairs of Electrodes

Figure 3.3: Unimorph ({3-3} Mode) Harvester Schematic with Interdigitated Electrodes

The electric mode shape for the {3-1} Mode structure shown in Figure 3.2 is:

$$\psi_v = \frac{-z + t_p}{t_p} \quad \text{Eq 3-24}$$

Where z is the distance through the thickness of the piezoelectric material and t_p is the thickness of the piezoelectric layer. The electric field is linear through the thickness of each piezoelectric layer. When this is substituted into Θ (Eq 3-12) and used to find voltage (Eq 3-20), it can be seen that in {3-1} Mode piezoelectric operation, developed voltage is dependent on the thickness of the piezoelectric layer. As it is this voltage that is measured (or used) experimentally, to maximize the signal-to-noise ratio the layers are connected in series. Appendix C of du Toit [3] discusses these inter-element connections in detail.

The electric mode shape for the {3-3} Mode structure shown in Figure 3.3 is:

$$\psi_v = \frac{-x_i + (p - a/2)}{p - a} \quad \text{Eq 3-25}$$

Where x_i is the distance along the beam between the i^{th} pair of interdigitated electrodes and p and a are the pitch and electrode width as defined above. In this mode, the electric field is linear between the interdigitated electrodes, not through the thickness of the piezoelectric layer. The definition of this mode shape is one of the key modeling assumptions that was used: it was assumed that the electric field between the electrodes was uniform and that there was no electric

field under the electrodes. This likely over-predicts the field in the region between the electrodes, but this is compensated by the under prediction in the area directly underneath the electrodes. By following the same process as for the {3-1} Mode case, it can be seen that in {3-3} Mode operation, the voltage produced by the device depends on the interdigitated electrode spacing.

In addition to the difference in electrical mode shapes for the two operating modes, there is a difference in the material constitutive relationships between the {3-1} and {3-3} Modes. The full three-dimensional constitutive matrix equation relating strain, \mathbf{S} , stress, \mathbf{T} , electric displacement, \mathbf{D} , and electric field, \mathbf{E} , is given by du Toit [3] and simplified by using the assumption that in the global coordinate system, stresses $T_3 = T_4 = T_5 = 0$ in the piezoelectric layer, and the reduced {3-1} Mode constitutive relation is:

$$\begin{Bmatrix} T_1 \\ T_2 \\ T_6 \\ D_3 \end{Bmatrix} = \begin{bmatrix} c_{11}^E * & c_{12}^E * & 0 & -e_{31} * \\ c_{21}^E * & c_{11}^E * & 0 & -e_{31} * \\ 0 & 0 & c_{66}^E * & 0 \\ e_{31} * & e_{31} * & 0 & \epsilon_{33}^S * \end{bmatrix} \begin{Bmatrix} S_1 \\ S_2 \\ S_6 \\ E_3 \end{Bmatrix} \quad \text{Eq 3-26}$$

The star indicates that the constants included are the reduced piezoelectric material constants and are defined below for both the {3-1} and {3-3} Modes. (In the work presented here and that of du Toit [3], the material coefficients for the beam configuration were used as insufficient information was available about the piezoelectric material to calculate the plate coefficients.) Not equal to the full 3-D constants, these values are obtained by inverting the 2-D stiffness matrix that can be obtained through measurements done under constant electric field conditions. Recall that a superscript E indicates that the property was measured at constant electric field, S , at constant strain. By considering a beam configuration, the further simplification that $T_2 = T_6 = 0$ can be made. This allows the constitutive matrix equation for the {3-1} Mode to be written as:

$$\begin{Bmatrix} T_1 \\ D_3 \end{Bmatrix} = \begin{bmatrix} c_{11}^E * & -e_{31} * \\ e_{31} * & \epsilon_{33}^S * \end{bmatrix} \begin{Bmatrix} S_1 \\ E_3 \end{Bmatrix} \quad \text{Eq 3-27}$$

The terms for this reduced constitutive relationship for both the beam and plate geometry are given in Table 3.1.

Table 3.1: Constitutive Coefficients for {3-1} Mode Piezoelectric Material

Beam Configuration	Plate Configuration
$c_{11}^{E*} = \frac{1}{s_{11}^E}$	$c_{11}^{E*} = \frac{s_{11}^E}{(s_{11}^E)^2 - (s_{12}^E)^2}$
$e_{31}^{*} = \frac{d_{31}}{s_{11}^E}$	$e_{31}^{*} = \frac{d_{31}}{s_{11}^E + s_{12}^E}$
$\varepsilon_{33}^{S*} = \varepsilon_{33}^T - \frac{d_{31}^2}{s_{11}^E}$	$\varepsilon_{33}^{S*} = \varepsilon_{33}^T - \frac{2d_{31}^2}{s_{11}^E + s_{12}^E}$

A similar matrix reduction and simplification procedure can be followed for the {3-3} Mode, and a similar set of coefficients is obtained and presented below:

$$\begin{Bmatrix} T_3 \\ D_3 \end{Bmatrix} = \begin{bmatrix} c_{33}^{E*} & -e_{33}^{*} \\ e_{33}^{*} & \varepsilon_{33}^{S*} \end{bmatrix} \begin{Bmatrix} S_3 \\ E_3 \end{Bmatrix} \quad \text{Eq 3-28}$$

The terms for both the beam and plate geometric configurations are listed in Table 3.2:

Table 3.2: Constitutive Coefficients for {3-3} Mode Piezoelectric Material

Beam Configuration	Plate Configuration
$c_{33}^{E*} = \frac{1}{s_{33}^E}$	$c_{33}^{E*} = \frac{s_{11}^E}{s_{11}^E s_{33}^E - (s_{13}^E)^2}$
$e_{31}^{*} = \frac{d_{33}}{s_{33}^E}$	$e_{31}^{*} = e_{33}^{*} = \frac{s_{11}^E d_{33} - s_{13}^E d_{31}}{s_{11}^E s_{33}^E - (s_{13}^E)^2}$
$\varepsilon_{33}^{S*} = \varepsilon_{33}^T - \frac{d_{33}^2}{s_{33}^E}$	$\varepsilon_{33}^{S*} = \varepsilon_{33}^T - \frac{1}{s_{11}^E s_{33}^E - (s_{13}^E)^2} (s_{33}^E d_{31}^2 - 2s_{12}^E d_{31} d_{33} + s_{11}^E d_{33}^2)$

The complete set of PZT-5A piezoelectric material properties as obtained by du Toit [3] from the manufacturer, Morgan Electro Ceramics for the macro-scale device discussed in Section 3.4.3, are presented in Table 3.3.

Table 3.3: PZT 5A Material Properties

Permittivity:		Compliance:		Piezoelectric Constants:	
ϵ_0	8.854e-12	s_{11}^E	16.4e-12	d_{31}	-171e-12
	[F/m]		[1/Pa]		[m/V]
ϵ_{33}^T	1700* ϵ_0	s_{33}^E	18.8e-12	d_{33}	374e-12
ϵ_{11}^T	1730* ϵ_0	s_{44}^E	47.5e-12	d_{15}	584e-12
ϵ_{33}^S	830* ϵ_0	s_{66}^E	44.3e-12	e_{31}	-5.4 [C/m ²]
ϵ_{11}^S	916* ϵ_0	s_{12}^E	-5.74e-12	e_{33}	15.8
Density: 7750		s_{13}^E	-7.22e-12	e_{15}	12.3
	[kg/m ³]				
				Coupling:	
				k_{31}	0.334
				k_{33}	0.705

3.3 Impact of Microfabrication on Harvester Design

The design decision between utilizing the {3-1} or {3-3} Mode can be significantly affected by device manufacturing considerations. As was seen in the preceding electrical mode shape equations, in {3-1} Mode the possible voltage developed is a function of the piezoelectric layer thickness while in {3-3} Mode, it is controlled by the size and spacing of the interdigitated electrodes on the top of the device. This latter configuration capitalizes on the flexibility available through mask design for MEMS processing. The designer can choose the pitch, p , and electrode width, a , at will with the only limitation being the achievable resolution of the mask developing and transfer process. Currently, this feature resolution limit is approximately 4 μ m. The MEMS device recently prototyped by Sood [11] utilizes this operational mode due to similar fabrication considerations.

Designing a device to precise voltage requirements in {3-1} Mode is more difficult as the determining dimension is that of the piezoelectric thickness. The manufacturing technique currently employed for piezoelectric (PZT) deposition is spin coating a wafer with sol-gel and then heating the wafer to crystallize/anneal the PZT. The thickness of the resulting PZT layer is controlled through the speed at which the wafer is spun during the coating process, but this process has been shown to be inexact. There have also been significant difficulties across many research groups in generating thicker layers of PZT (>1 μ m) without serious cracking. This combination of fabrication difficulties has focused MIT-based fabrication efforts on the {3-3} Mode piezoelectric operation. There is however the potential to increase the power generation of a single device by creating a bimorph harvester with two layers of piezoelectric material each operating in the {3-1} Mode. Currently, efforts are underway to prototype a basic {3-1} Mode bimorph device with a Si structural layer and determine the feasibility of micro-scale fabrication of devices utilizing this operational mode.

Several other manufacturing constraints also play a role in harvester device design, and were used to bound the design and optimization study that follows later in this and the next chapter. Following from the {3-1} Mode discussion above, the maximum PZT thickness that has been obtained successfully (though not repeatedly) with the Mitsubishi sol-gel spin-coat process is 0.48 μ m. An overall thickness of 0.5 μ m was used as the thickness in the design optimization

studies as this is what should be obtained by a successful execution of the process used by Sood [11], and in all cases thicker PZT generates more power.

The structural layers themselves are also dictated by fabrication constraints, particularly inter-layer bonding and residual stress considerations. The Sood device consisted of a layer of SiN_x and of SiO_2 . Their thicknesses were determined by the desire to minimize the curvature of the released beam structure. The presence of the SiO_2 was deemed necessary due to adhesion concerns with a supporting layer for the PZT: ZrO_2 was deposited on the SiO_2 with a spin-coat process very much like that for the PZT as a base layer and diffusion barrier and adheres better to the SiO_2 than to the SiN_x . Adhesion concerns also drove the metal choices for the electrodes – a thin Ti adhesion layer was deposited before the Pt electrode layer.

The last key structural influence on the device design that will be discussed here is that of the obtainable proof mass height and composition. With the e-beam deposition techniques currently available in MIT's Microsystem Technology Laboratory (MTL), a maximum metal height of $\sim 3\mu\text{m}$ can be obtained. The un-tapered devices considered in this chapter (that have a proof mass) were constrained to have a Pt proof mass of $3\mu\text{m}$ in height (the maximum). Preliminary investigations showed that from a volumetric – or power density – perspective, a dense, taller shape was more desirable than a less dense, longer one for the same total mass. Platinum was chosen for the proof mass both for its high density and also because it is the top electrode layer, thus simplifying fabrication.

In short, when designing a MEMS harvesting device, one must take into account four main factors: mask image resolution, obtainable layer thicknesses, inter-layer adhesion, and residual stress management. The numerical constraints imposed in this work are based on the experience of Sood [11] and the MTL technical staff – a future designer should investigate their current manufacturing capabilities and take into account any additional constraints or process improvements.

3.4 Modeling for Optimization: The Uniform Beam

The initial modeling that was done by du Toit [3 and 5], summarized above, was expanded and recast to allow application of the governing equations as a design and performance investigation tool. While du Toit had looked at the impact of operating in both modes on the governing equations, only the {3-1} Mode model had been implemented. For the current effort, a {3-3} Mode model was implemented and the results were compared to {3-3} Mode published data [11] in Section 3.4.2 below. The goal of this modeling effort was to develop tools that could be used over a wide range of input vibrations and MEMS device geometries for design optimization and as a tool to understand the performance of MEMS piezoelectric vibration energy harvesting devices. The end result of this tool for the designer is a set of carpet plots showing the parameter of interest over the design space with the input vibration that is being considered. An optimal design that takes into account the manufacturing constraints described earlier can then be selected for fabrication using these carpet plots. An example of how this type of plot is generated follows; full sets of plots relevant to the originally motivating aircraft skin application are included at the end of this chapter for both {3-3} and {3-1} Mode devices.

In this chapter, un-tapered beams with uniform cross-sections and a tip proof mass are considered as this is the type of device for which experimental data is available for validation. The following chapter expands this model to allow for a tapered beam (*i.e.* varying the width of the cross-section along the beam length) but is conceptually very similar to the models explained in detail here. Due to the similarity of the structure of the {3-3} and {3-1} Mode models, only the {3-3} Mode model will be discussed in detail. Similarities and differences of the {3-1} Mode model to the {3-3} Model will be addressed in Section 3.5.3.

3.4.1 Model Example for Aircraft Vibration Harvesting

In this section, an example case that was chosen as typical of devices for the aircraft structural health monitoring MEMS space is presented. This device is not presented as an optimum, but as an example of the structure and usage of the modeling technique used. A {3-3} Mode device is considered here, but the basic steps are the same for either operating mode. As mentioned earlier the basic design considered here was an un-tapered cantilevered beam of active length L with a proof mass of length L_0 attached at the tip. The basic device geometry is shown in Figure 3.4, as are the layers and their properties as given in Table 3.4.

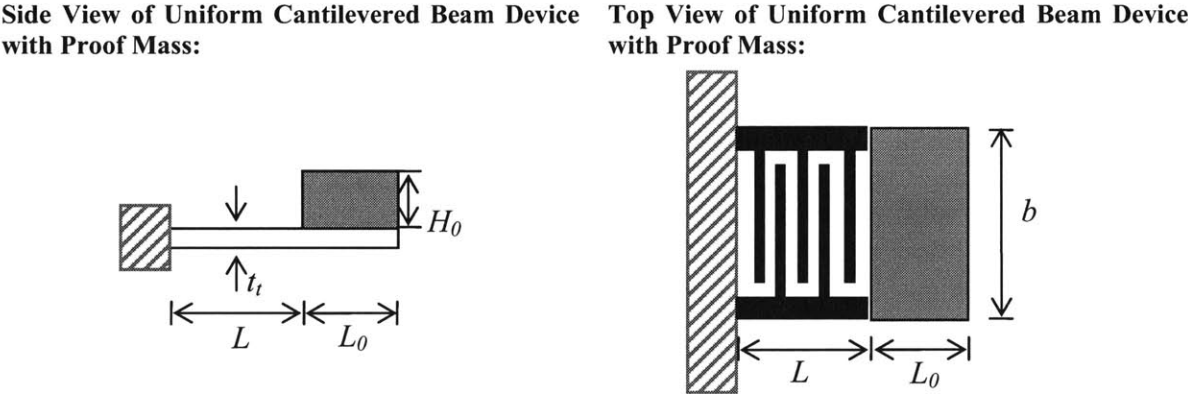


Figure 3.4: Side and Top Views of a {3-3} Mode Cantilevered Device

For the example device – a {3-3} Mode untapered unimorph – shown here, $L = 0.2652\text{mm}$, $L_0 = 0.3398\text{mm}$, $b=1\text{mm}$, $H_0 = 3\mu\text{m}$, and the layer thicknesses and properties are as shown in Table 3.4, starting with the interdigitated electrode layers on top and going down through the device. In the model, the piezoelectric layer beneath the proof mass is neglected with respect to power generation (the entire proof mass region of the beam is considered to be rigid) and an effective proof mass of length L_0 is defined. This is shown in Figure 3.4, as opposed to the representation in Figure 3.1, where the proof mass does not sit on top of the other beam layers. The point from which these beam and proof mass lengths were obtained is shown in the context of the entire design space carpet plot in Figure 3.5.

Table 3.4: Example {3-3} Device Layer Properties

Layer Material	thickness, [μm]	density, [kg/m ³]	modulus, [GPa]	plate modulus, [GPa]
Pt	0.20	21440	170.0	200.5
Ti	0.02	4510	110.0	124.4
PZT	0.50	7750	64.01	64.01*
ZrO ₂	0.05	6000	244.0	263.2
SiO ₂	0.10	2300	69.00	70.59
SiN _x	0.40	3000	313.0	344.0

* Note that the modulus for PZT was calculated from the full constitutive relationships using the 2D formulas presented earlier based on available manufacturer's information. (The value shown for the PZT modulus is c_{33}^{E*} , as defined in Table 3.2 for a beam)

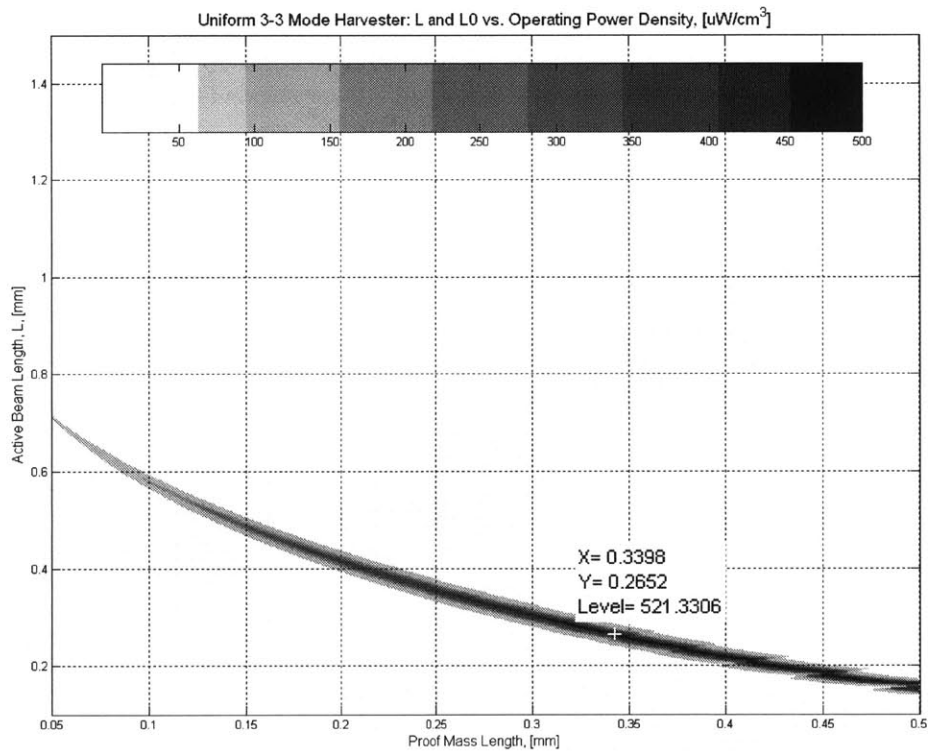


Figure 3.5: Example Carpet Plot for {3-3} Mode Untapered Device Operating Power Density with Example Point Marked

A closer view of the example point is shown in Figure 3.6. The horizontal axis displays L_0 , the length of the proof mass; the vertical axis, L , the active beam length. The point that is marked represents a proof mass length of 0.3398mm and a beam length of 0.2652mm which is predicted to achieve an operating power density of 521.3 $\mu\text{W}/\text{cm}^3$. This point will be carried through as an example of how the model calculates the various quantities of interest for device design and modeling are calculated in the model. Additional carpet plots and commentary on their structure follow at the end of this chapter.

For all of the length and proof mass length combinations investigated, the layer thicknesses shown in Table 3.4 and 1mm beam width were held constant. Additionally, the proof mass was considered to be a 3 μm thick layer of Pt deposited on top of the other beam layers. The proof mass and the layered portion under it were considered to be rigid. The beam modulus was used for the piezoelectric material as insufficient material data was available to calculate the plate modulus. The aspect ratio of the beams considered are rather small however, as for the other layers in the beam the plate modulus was used.

The electrode pattern is that shown for an interdigitated electrode in Figure 3.3 with a pitch, p , of 16 μm and a “finger” width, a , of 4 μm . As was originally assumed by Sood [11], the electrodes were assumed to cover only 50% of the top surface of the device in moment and stiffness calculations.

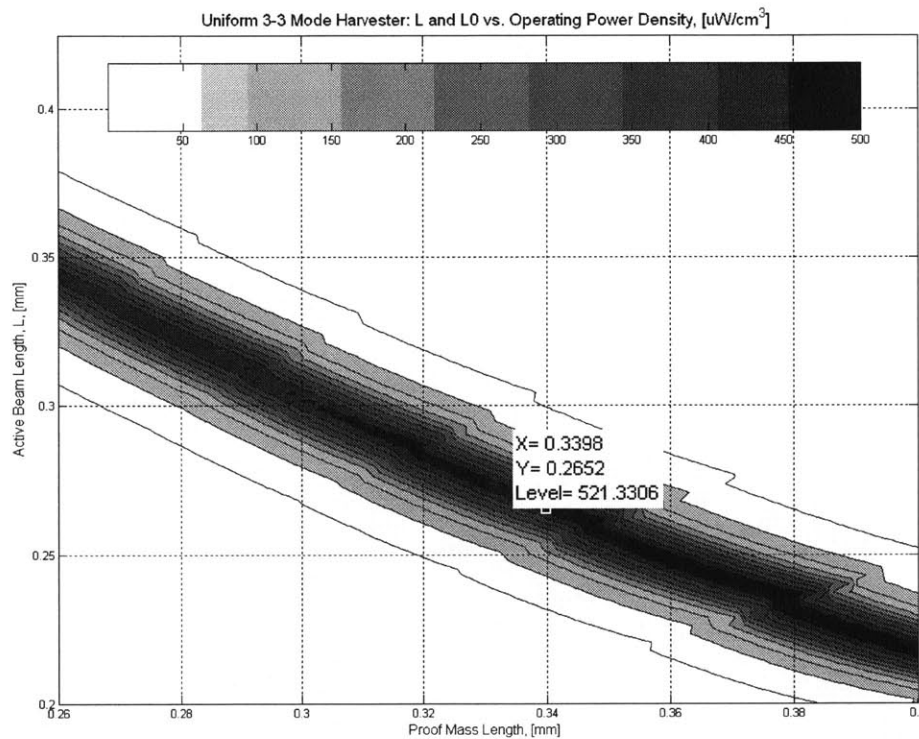


Figure 3.6: Close-Up View of Example Point on Operating Power Density Carpet Plot from Figure 3.5

The vibrational input to the device was held constant at a point which could be expected from an aircraft empennage skin (see discussion in Section 1.3.2) [47]: 1000Hz at 3.8982 m/s^2 . The device modeled was developed to operate at the anti-resonant frequency and the load resistance was set to the local optimum value for power generation at each point in the carpet plot.

After setting the input conditions and device geometry, the model calculates the modulus-weighted neutral axis of the beam structure. This is the reference point that is used throughout the remainder of the calculations for the beam – a point that is especially important when considering unimorph beam geometry as this allows the asymmetry due to the single layer of PZT on the structure to be accommodated. For this example, the neutral axis is at 0.485 μm from

the bottom of the beam in the SiO₂ structural layer. Once the modulus-weighted neutral axis has been determined, the moment of inertia for each layer is determined using the parallel axis theorem. The electrode layers are weighted with the fractional area coverage mentioned earlier. This weighting can have as much as 200Hz difference in the resulting natural frequency and is an important consideration for {3-3} Mode devices.

This layer structure results in a structural beam bending stiffness of $EI = 2.678e-11 \text{ N/m}^2$ (taking into account the partial area coverage of the electrodes on the top of the beam), a neutral axis location, z_{NA} , of $0.485\mu\text{m}$ above the bottom of the beam, and a mass per unit length of active beam, m , of $9.932e-6 \text{ kg/m}$.

Up to this point, the model has carried out the calculations on a layer-by-layer basis. The moments and moduli for each layer are now combined to produce an effective bending modulus. (For all of the optimization models, wherever possible, parameters are calculated as a function of x , along the beam length, to facilitate the introduction of a taper in Chapter 4.)

Next, the proof mass is considered. Using the technique implemented by du Toit and explained in Section 3.1, the center of mass, moment and moment of inertia for the effective proof mass, which includes the platinum mass added to the beam as well as the rigid portion of the beam under the platinum, are calculated. For the case being discussed here, the center of mass is 0.1699 mm from the end of the active beam section and $1.978\mu\text{m}$ above the modulus-weighted neutral axis (or $0.708\mu\text{m}$ above the top of the active beam structure).

Applying Eq 3-17, the resulting mode shape and mode shape curvature are obtained and shown for the active beam length in Figure 3.7 below. Note that because of the effect of the proof mass, the curvature (and thus the moment in the beam) does not go to zero at the end of the active beam section.

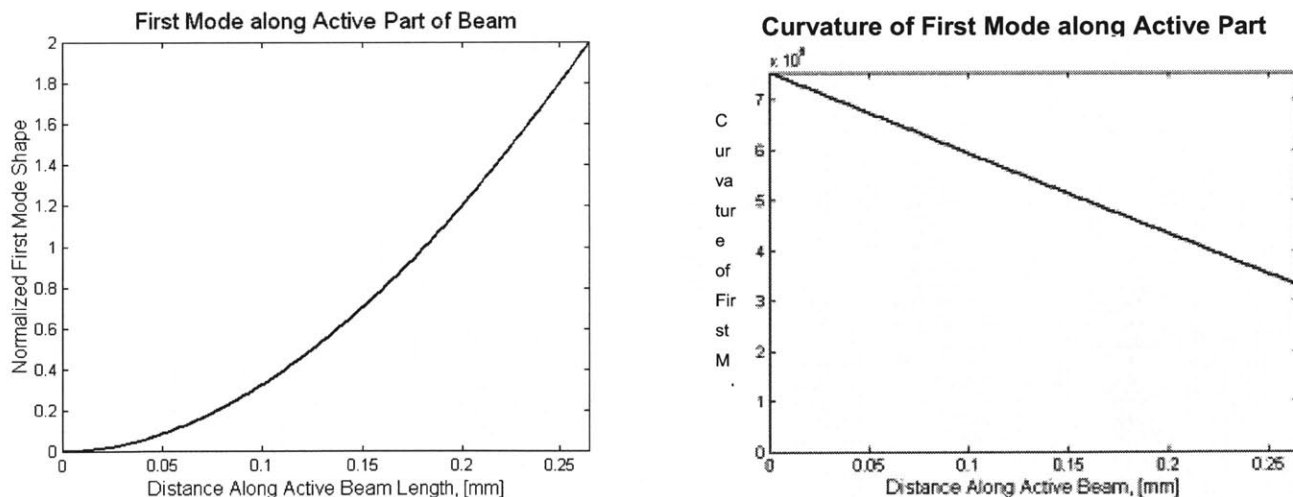


Figure 3.7: First Mode Shape and Curvature of the First Mode for {3-3} Mode Example Case

All of the components are now in place to calculate the mass, M , stiffness, K , coupling, Θ , capacitance, C_p , and input, B_f , coefficients for the first mode as given in Eq 3-9 through 3-14. These coefficients for the example case are: $M = 5.86 \times 10^{-9}$ kg, $K = 0.2216$ N/m, $\Theta = 3.64 \times 10^{-7}$ C/m, $C_p = 7.03 \times 10^{-12}$ F and $B_f = 2.143 \times 10^{-8}$ kg. The mechanical damping ratio was taken as $\zeta_m = 0.005$. The resonant frequency of the device can now be computed as $\omega_n = \sqrt{K/M}$. In this case, $\omega_n = 6148.8$ rad/s = 978 Hz. To determine the anti-resonant frequency, Ω_{oc} is calculated by:

$$\Omega_{oc} = \sqrt{1 + \kappa^2} \quad \text{Eq 3-29}$$

where $\kappa^2 = \Theta^2 / KC_p$ and $\Omega_{oc} = \omega_{ar} / \omega_n$, is the ratio of the anti-resonant (or open circuit) frequency of the device to the resonant (or short circuit) frequency ($\Omega_{sc} = 1$). Another important frequency ratio is that of the input frequency to the resonant frequency, $\Omega = \omega / \omega_n$. In this case, $\Omega_{oc} = 1.0417$ and $\Omega = 1.0220$. The fact that the frequency ratio for this example device is between open and short circuit frequency ratios is typical of a device with high operating power density. Operating between these power peaks allows the device to hit a compromise between power generation and the volume required for the larger tip displacement that would result from being directly aligned with either peak power generation points. (Recall from Chapter 2 that operating power density is obtained by dividing the total device power output by the rectangular volume required for device operation, roughly: $(L + L_0) * b * 2 * w_{tip}$.) This point will be discussed more subsequently when the entire set of carpet plots is examined.

Continuing towards the calculations of power and tip displacement, the optimum resistance is calculated using Eqs 3-22 and 3-23 given in Section 3.1 to be 2.7 MOhms. Using this load condition and the equations for power, voltage and tip displacement that are also given at the beginning of this chapter, the performance predictions in Table 3.5 for this example device are obtained. Maximum strain in the device is calculated to ensure that the device is not exceeding the limit for fatigue damage which was set conservatively at 500 micro strain.

Table 3.5: Model Predictions for {3-3} Example Case

Parameter	Prediction for Example Device
Device Power Output	0.0030 μ W
Operating Power Density	522.2 μ W/cm ³
Static Power Density	1154.3 μ W/cm ³
Specific Power	0.1085 W/kg
Voltage Produced	0.2716 V
Maximum PZT Strain	30.5 $\mu\epsilon$
Tip Displacement, w_{tip}	1.5417 μ m
ω_r	978 Hz
ω_{ar}	1019 Hz
Ω_{opt}	1.02

This model and optimization allows the user to vary the device geometry and input conditions over any range of interest to investigate a specific geometry or to determine what the design space for a given application looks like. The validation of this model follows and an example design space investigation for this and {3-1} Mode operation for aircraft usage conclude the chapter.

3.4.2 Uniform {3-3} Mode Harvester: Model Validation

The {3-3} Mode version of the un-tapered beam harvester model was compared to data collected by Sood [11] for a micro-scale unimorph harvesting device (properties as in Table 3.4). Unfortunately, while this data is potentially the most complete data set available for this operating mode, there is a good bit of uncertainty associated with the recorded observed power data (see Table 2.2). The tip displacement data and resonant and anti-resonant frequencies have been deemed reliable.

The Sood device was a MEMS unimorph device whose structural layer consisted of 0.4 μm of SiN_x and 0.1 μm of SiO_2 . The piezoelectric layer was 0.48 μm of spin-coated PZT over 0.05 μm of ZrO_2 with 0.02 μm of Ti and 0.2 μm of Pt making up the interdigitated electrodes on the top surface of the device. The resonant frequency observed for this device was 13.7 kHz; the model used here predicted 13.65kHz (0.36% difference); the observed anti-resonant frequency was 13.9 kHz, as compared to the modeled 14.0 kHz (0.71% difference).

The experiments conducted with the Sood device to measure relative tip displacement were done by varying the base displacement at a constant frequency input at the resonant (short circuit) frequency. As seen in Figure 3.8 below, the data shows a non-linearity at high base acceleration, but the linear model compares favorably at low acceleration. This low acceleration ($<10\text{m/s}^2$) is the area of application for the model for harvesting energy from most aerospace vibration sources. Also shown in Figure 3.8 is the effect of small changes in the damping coefficient, ζ_m , used in the model on the predicted tip displacement.

In addition to tip displacement, voltage and power predictions were also compared to the published Sood data (See Table 2.2). For these quantities however, only the trends were considered due to the uncertainty surrounding the measured data. In this respect, the model performed well, and overall predicted much more reasonable values for these quantities.

Though only partial due to the lack of a complete and reliable data set, the comparisons done in this section indicate that the {3-3} Mode un-tapered unimorph cantilevered beam energy harvesting model can be used with confidence for optimization.

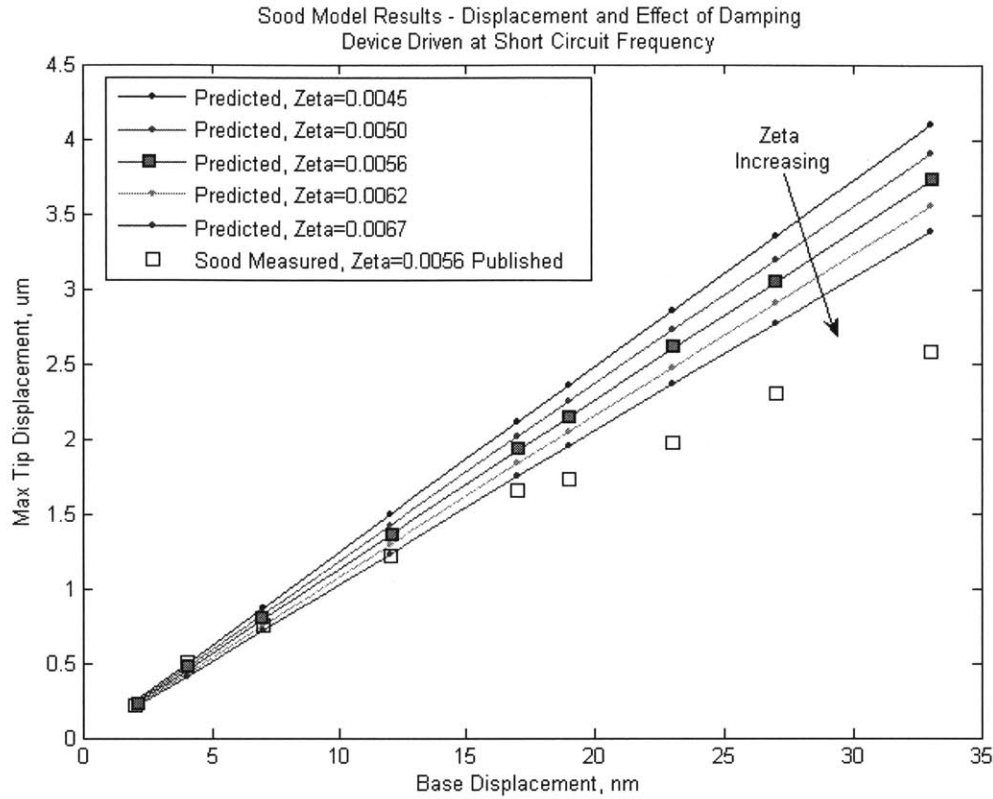


Figure 3.8: {3-3} Mode Micro-Scale Unimorph Model Validation for Tip Displacement, Maximum Relative Tip Displacement [μm] vs. Base Displacement [nm]

3.4.3 Uniform {3-1} Mode Harvester: Model Verification

The {3-1} Mode version of the un-tapered beam harvester model was compared to data collected by du Toit [3] for a macro-scale bimorph harvesting device. (No micro-scale data is available in the literature.) A similar comparison had been previously done by du Toit to verify the original application of the governing equations with positive results. The device that was tested was a bimorph with an active length, L , of 55.0 mm, total thickness, $t_t = 0.686$ mm, and width, $b = 31.8$ mm and was acquired from Piezoelectric Systems, Inc. (the T226-A4-503X). The bimorph consisted of two piezoelectric layers with thickness $t_p = 270 \mu\text{m}$ surrounding a brass structural shim of thickness $t_s = 140 \mu\text{m}$ (accurate to within $\pm 5 \mu\text{m}$). This device did not have a proof mass. In all cases, the device was tested with a base input acceleration of 2.5 m/s^2 . The natural frequency of the device was determined experimentally to be 107 Hz; the anti-resonant frequency was found to be 113 Hz.

A few of the key non-dimensional parameters from the analysis presented at the beginning of the chapter as calculated for this device at anti-resonance (113 Hz) are presented here for reference: $\zeta_m = 0.0178$, $\alpha = 2.9874$, $\kappa^2 = 0.1077$, $\Omega_{oc} = 1.0525$.

The new implementation of these equations retains their original accuracy over a wide range of load resistance and normalized input frequency ($\Omega = \omega/\omega_n$) as shown in Figures 3.9 through Figure 3.12.

As can be seen in Figure 3.9, the model predicts the location of the resonant peak well but consistently under predicts the power generation at resonance. It has been suggested that this overly conservative result at resonance is due to the fact that non-linearities in the electrical coupling are not included in the model [4 and 5 **Error! Reference source not found.**]. For further {3-1} Mode model validation, performance off-resonance is compared to the macro-scale data in the following figures where the load resistance is varied while keeping frequency and input acceleration (still 2.5 m/s^2) constant.

In Figure 3.10 and Figure 3.12, the sharp shift in optimal resistance for maximum power and tip displacement that results from going from the resonance to the antiresonance frequencies (107 Hz to 113 Hz in this experiment) should be noted. A similar shift in resistance is shown later in Figure 3.16 for an example within the design space considered in this thesis. The model predicts this shift in resistance as noted in the discussion that follows Eq 3-23.

The differences in the predicted vs. measured power are small enough to give confidence in the performance of the model at these conditions. (Recall that the resonant frequency was 107 Hz; the anti-resonant frequency – also tested above – was 113 Hz.) In Figure 3.10 the presence of an optimal resistance for each operating frequency is also clearly visible in both the modeled and measured data.

Power output is a key piece of the model, but it is not the only quantity of interest. A comparison of Voltage predictions to the du Toit macro-scale data is shown in Figure 11, and tip deflection under the same test conditions as power output above is shown in Figure 3.12. For both quantities, the model results compare favorably to the measured data.

Comparison of Model Results to du Toit Data for Bimorph Harvester

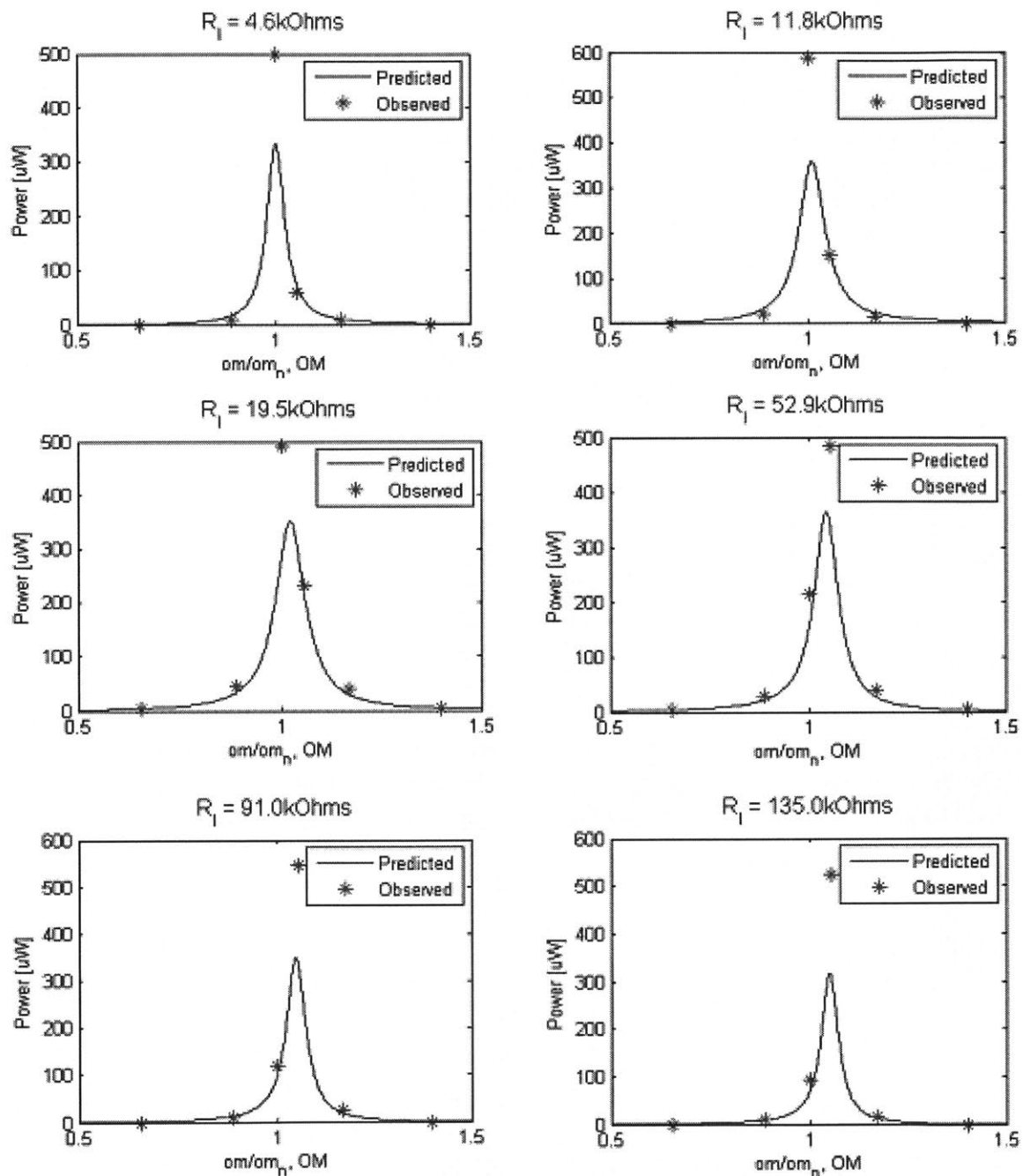


Figure 3.9: {3-1} Mode Macro-Scale Bimorph Power Production Model Verification: Device Power vs. Normalized Frequency, Ω

Comparison of Model Results to du Toit Data for Bimorph Harvester

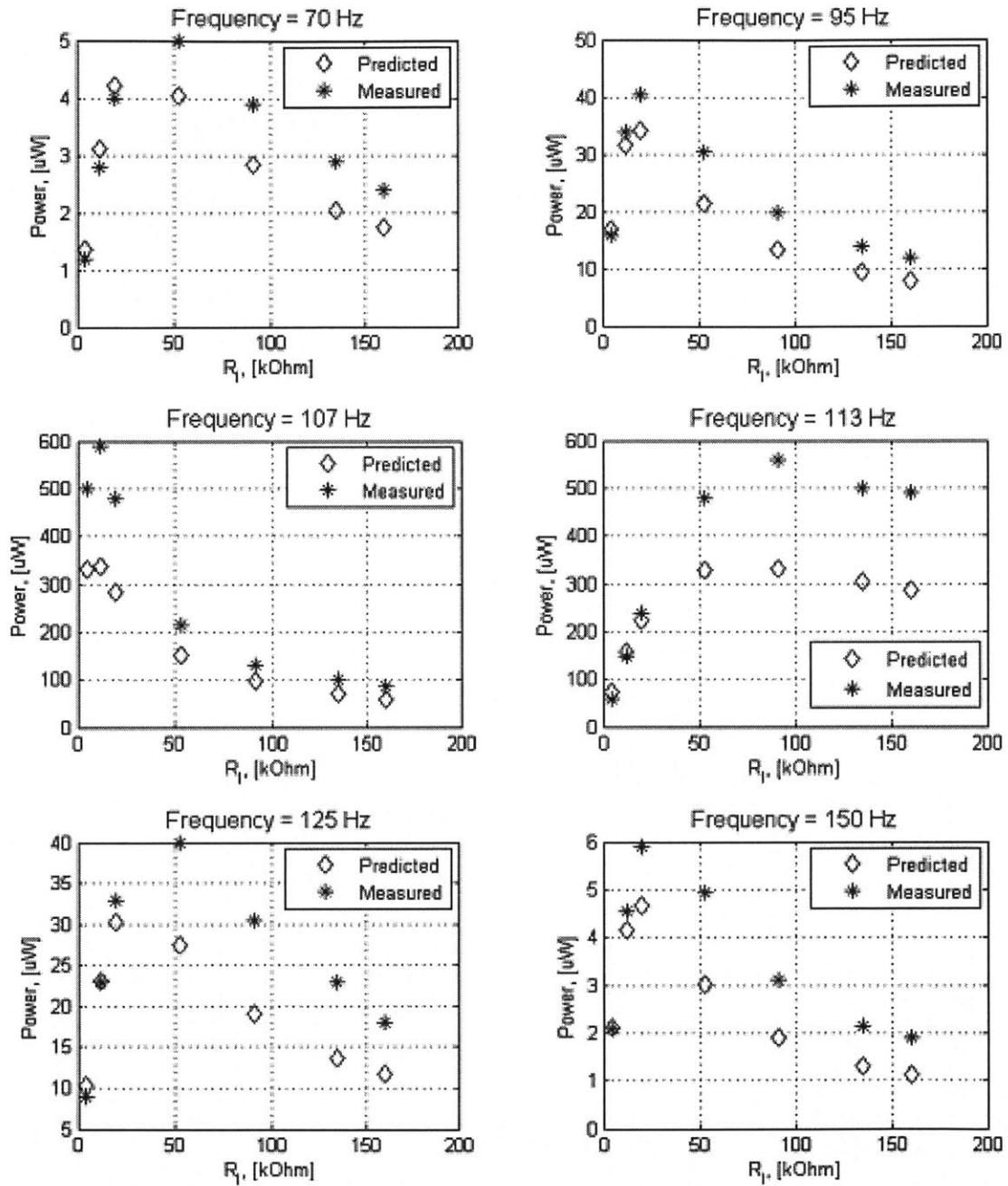


Figure 3.10: {3-1} Mode Macro-Scale Bimorph Resonance and Off-Resonance Power Production Model Verification, Power [µW] vs. Load Resistance [kOhms]

Comparison of Model Results to du Toit Data for Bimorph Harvester

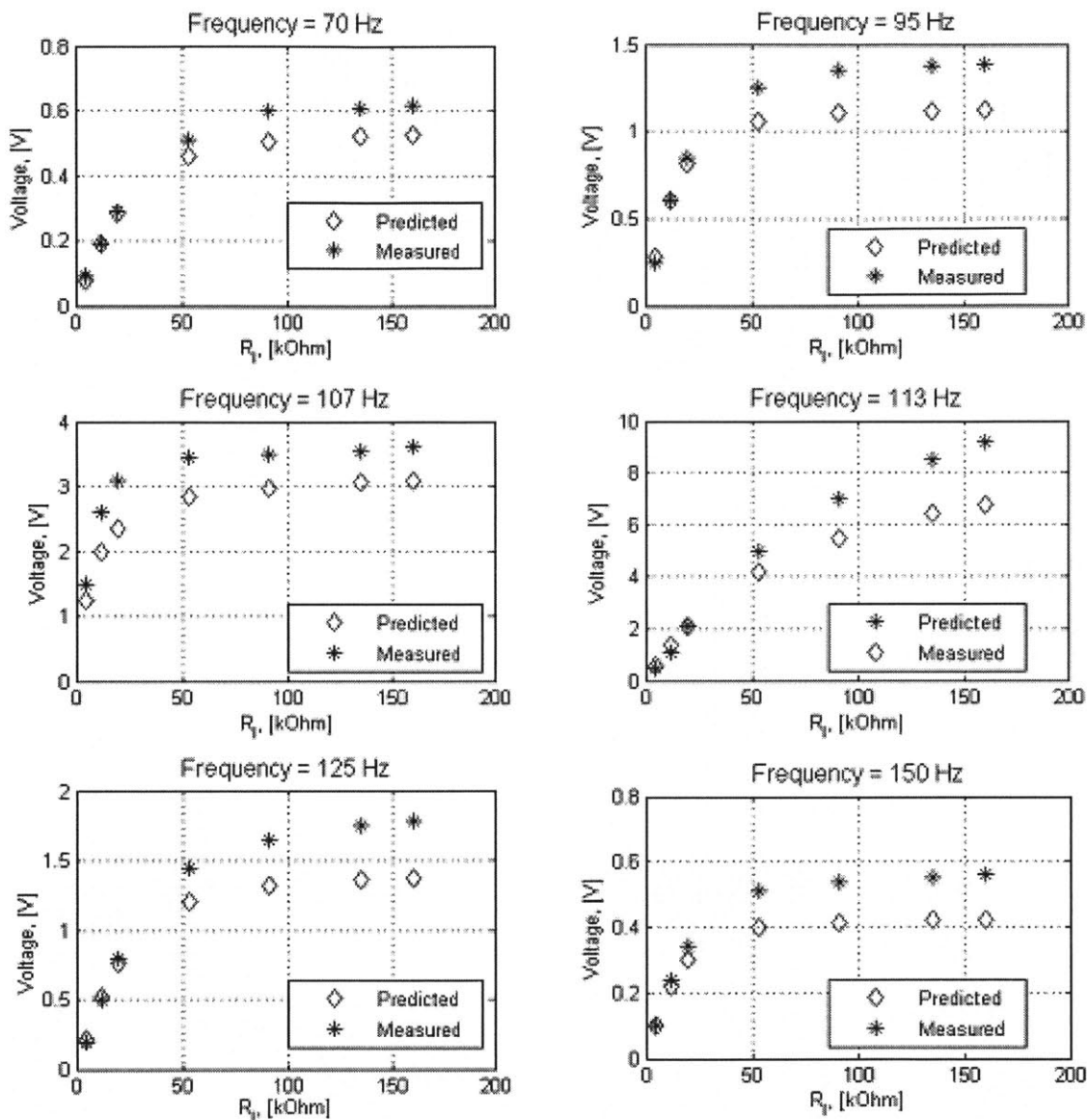


Figure 3.11: {3-1} Mode Macro-Scale Bimorph Resonance and Off-Resonance Power Production Model Verification, Voltage [V] vs. Load Resistance [kOhms]

Comparison of Model Results to du Toit Data for Bimorph Harvester

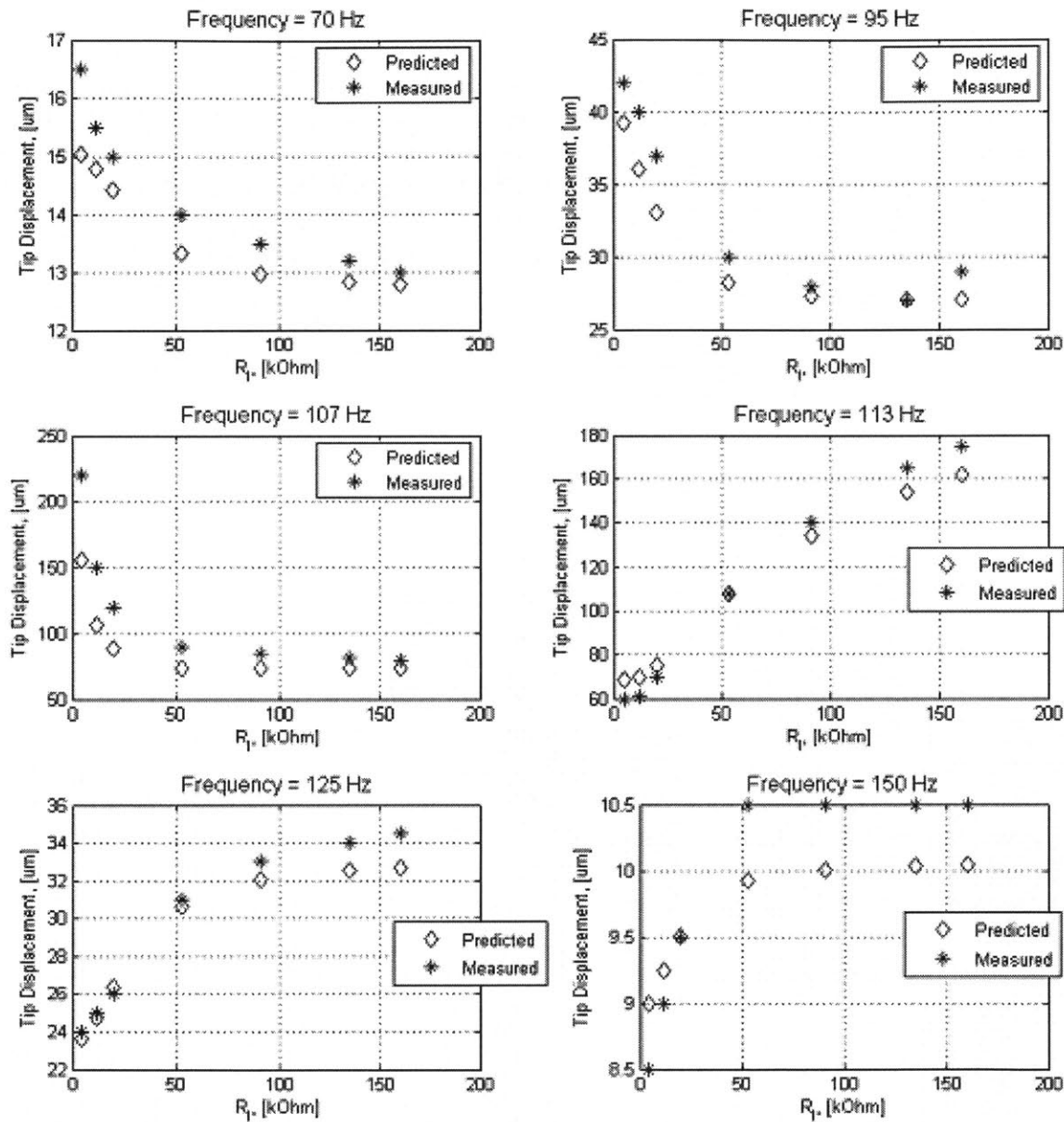


Figure 3.12: {3-1} Mode Macro-Scale Bimorph Resonance and Off-Resonance Power Production Model Verification, Tip Displacement [μm] vs. Load Resistance [kOhms]

Based on this comparison, the {3-1} Mode un-tapered bimorph cantilevered beam energy harvesting model can be used with confidence for optimization as presented in the next section knowing that at resonance and anti-resonance the model predictions are conservative re. power generation.

3.5 Untapered (Uniform) Beam Optimization Results

The models described earlier in this chapter are particularly useful for investigation of various device geometries and designs when considering the wide variety of potential applications for piezoelectric energy scavenging devices. The application considered in this section is that of aircraft structural health monitoring by wireless sensors in or on the skin of a jet fighter aircraft's tail. Both {3-3} and {3-1} Mode results are shown with the geometries varying over the following ranges: active beam length was varied from 0.1mm to 1.5mm and proof mass length was varied from 0.05mm to 0.5mm resulting in a maximum possible device length of 2.0mm. As seen in the following plots however, a device of this maximum length was not favored for the objective functions considered here. All geometries considered had the same layers – those detailed in the {3-3} Mode example in Section 3.4.1 and the same proof mass height, 3 μ m of platinum. The input, as mentioned in the example case, was 1000 Hz vibration with a base acceleration of 3.8982 m/s², a value determined to be realistic but conservative for a skin-mounted device based on the vibration spectrum presented in MIL-STD 810F [47] and examined earlier in Section 1.3.2.

The last general note on the optimization technique is that of the discretization used in the numerical modeling of the design space. Not only were the ranges of the geometric quantities of interest (L and L₀ in this chapter) discretized, the length of the beam itself was divided to facilitate numeric integration. Additionally, when determining the mode shapes in the case of a proof mass, a discrete determinate search method is used to identify the frequency coefficients for each configuration. For reference, the full design space was discretized into geometric steps of 1 μ m. (Close-up plots increase resolution to 0.1 μ m.) The active length of the beam was divided into 100 segments for numerical integration. The resolution in looking for the determinate needed for the beam mode was 0.001, but noticeable accuracy improvements can be seen up to two orders of magnitude finer resolution. The numerical error introduced in these discretizations, and the difficulty of handling an extremely large proof mass caused some numeric instability at the edges of the design space. If this particular region is of interest, a tighter design space with closer tolerances and smaller step sizes could be investigated to mitigate this inaccuracy. The close-up carpet plots that are given in this and the next chapter to show the structure of the plots were generated from just such a tighter, more finely discretized modeling effort.

3.5.1 Challenges to Optimization

As can be seen in the following carpet plots, there are many local minima and maxima in the design space for these devices. Multiple geometry combinations result in the device having a favorable resonant (or anti-resonant) frequency. This local minima/maxima issue was compounded by the existence of dual operating peaks (anti-resonance and resonance) that have comparable power outputs. Due to this, a standard gradient search method for optimization is ineffective. Following the failure of this type of technique, such as MATLAB's `fmincon` and `fminsearch` functions, the decision was made to generate carpet plots that could be used as a tool by device designers with their complete application constraint space in mind instead of generating one absolute "best" solution. While the plots shown below cover the beam and proof mass length space, a designer could use this same technique with the code included in the

appendices to generate similar plots for any two of the geometric, or material, variables of interest.

It is also worth noting here that different performance metrics (objective functions) result in different optimal device configurations. The criteria that are considered to be of the most interest here are device power output, or the output power produced by one device, operating power density, which is power produced normalized by the volume swept out by the beam and proof mass during operation, static power density, which is power normalized by the much smaller stationary volume of the device, and specific power, in which power is normalized by the total device mass. It should be noted that for packaging considerations, static power is of little use as the beam must move to generate power. It is presented here merely for comparison to the literature as it is a popular metric elsewhere. It should also be noted that the volumes and masses used in these results are for the piezoelectric beam and proof mass only – not the surrounding power electronics and packaging that will be required to make a functional harvester. In future work, as these external components are defined, their size and mass will be taken into account as well.

3.5.2 Resulting Tools for Uniform Beam {3-3} Mode Optimization

By looking at combinations of active beam length, L , between 0.1mm and 1.5mm (on the vertical axis) and proof mass length, L_0 , between 0.05mm and 0.5mm (on the horizontal axis) carpet plots of the resulting beam operating parameters are created, yielding design tools for a MEMS aircraft structural health monitoring power harvesting device. The details of the un-tapered {3-3} Mode unimorph device geometry are given in the example case shown in Section 3.4.1.

The anti-resonant frequency contours are shown below. Due to the higher voltage production possible in this operational mode, all of the devices were considered to be operating at anti-resonance. At this condition, the piezoelectric coupling results in a structural resonant frequency higher than that observed if the device is shorted. For all cases shown here it is assumed that the resistance is tuned to the optimum for power production following Equations 3-22 and 3-23.

Due to the strong relationship between power production and the ability of a device to capture the input vibration frequency as its anti-resonant (or resonant) frequency, the following plots for power production, operating and static power density and specific power all reflect the 1000kHz frequency contour shape observed in Figure 3.13. (While the full ranges of proof mass length and beam lengths stated earlier were considered for each objective function, the plotting area is reduced to show more detail.)

The power output falls off very quickly as the device anti-resonant frequency gets away from the input frequency. The geometric trade between the effect of beam length and proof mass size on the device's resonant frequency can be seen: for small proof masses, longer active beam lengths are favored while for longer active beam lengths, a smaller proof mass is needed to match the input frequency.

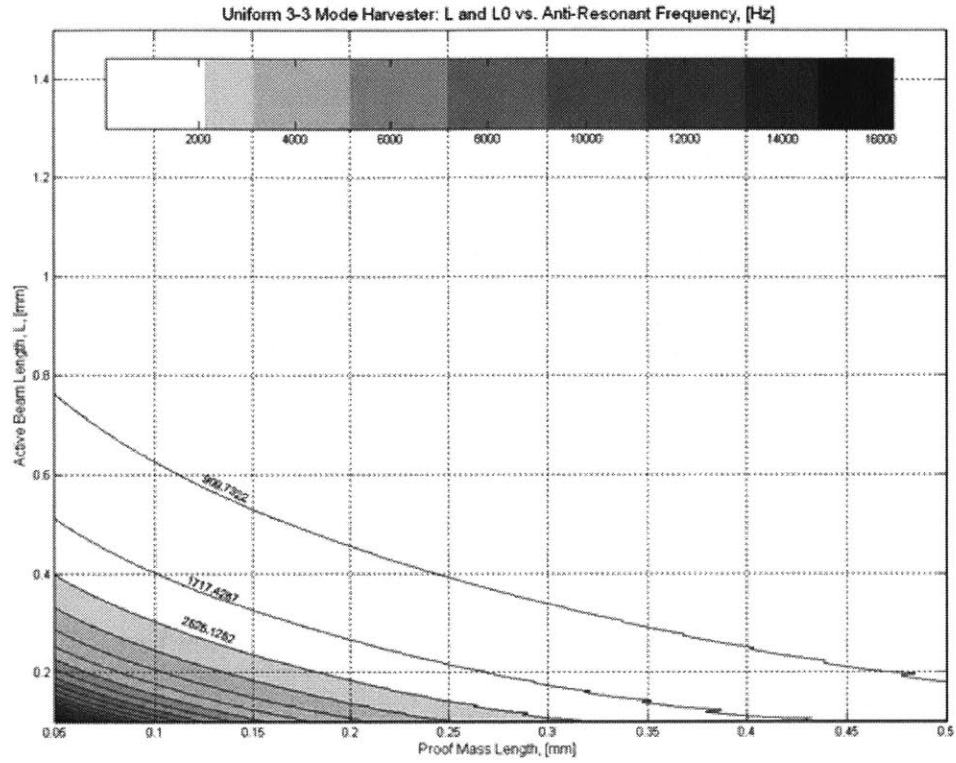


Figure 3.13: Anti-Resonant Frequency Contours for a Untapered {3-3} Mode Unimorph Device

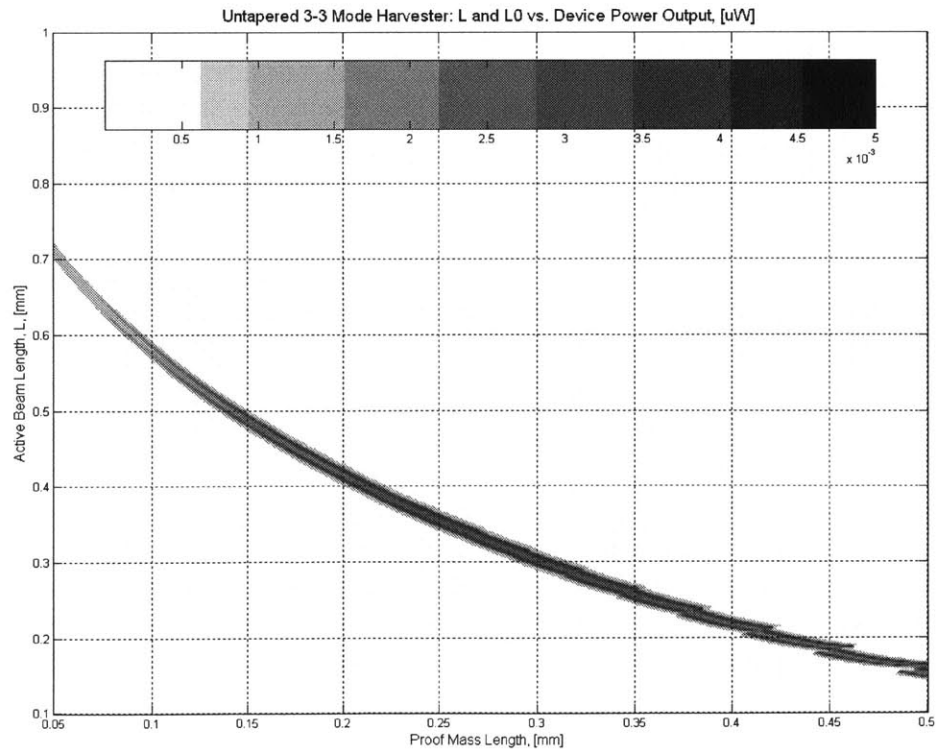


Figure 3.14: Device Power Output Contours for a Untapered {3-3} Mode Unimorph Device

A close-up of a portion of the contour in Figure 3.14 is shown in Figure 3.15. Note the dual operating peak structure by optimizing the load resistance for power production as a function of frequency for each design in the space. To illustrate these dual operating peaks in more detail, a cross-section of the carpet plot shown in Figure 3.15 is taken at a proof mass length of $L_0 = 0.3\text{mm}$. Power output and optimal load resistance are plotted along this cross-section in Figure 3.16. Note that due to the difference in the natural frequency of the device at the two peaks, the optimal resistance is quite different. This difference – and the key impact that it has on device performance – highlights the importance of the accompanying power electronics in future work. The difference in height of the two peaks in Figure 3.16 is due to the difference in active beam length at each peak. The beam with the larger length (area) produces more power. If power were plotted against Ω , there would be no difference in the height of the peaks that would be seen in that representation.

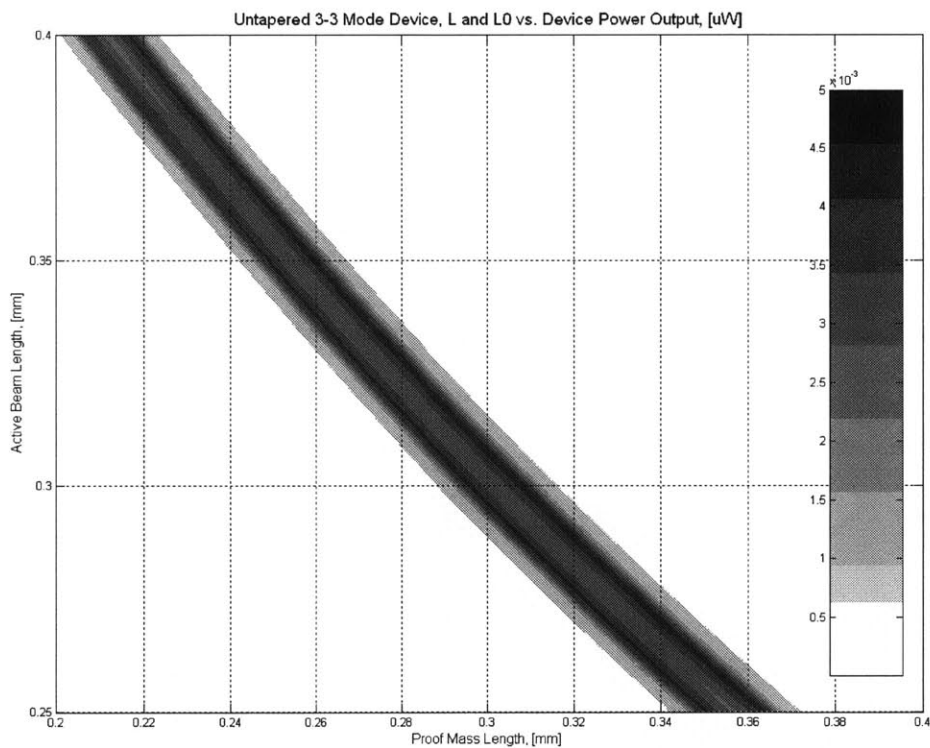


Figure 3.15: Close-Up of Device Power Output Contours for an Untapered {3-3} Mode Unimorph Device

By looking at the power output achieved at different points along the contour shown in Figure 3.14 as a function of active beam length or proof mass length (letting it be assumed that the other parameter that is required to achieve the desired anti-resonant frequency), more can be learned about the effects of each of these geometric parameters on device performance. At very short beam lengths, where the proof mass is very large, the structure behaves more like a hinge than a cantilevered beam and the model results are not as dependable (far right of the full carpet plots). At these extreme cases the model is also particularly sensitive to the discretization across the design space (and mentioned at the beginning of this section). The result of this is that there are numerical discontinuities and oscillation that would not be present in a physical system (as seen at the far right of the power vs. L_0 plot in Figure 3.17). Overall, for the majority of the points in

the design space, the discretization is fine enough that these numerical errors are not significant. Even at the extremes of the model where they become apparent, the observed trends are still applicable.

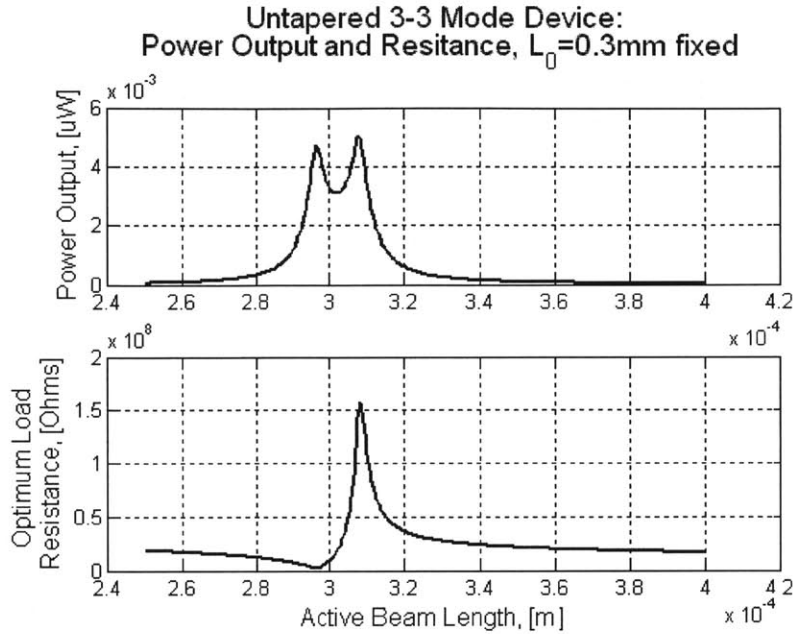


Figure 3.16: Dual Operating Peaks and Optimum Load Resistance for Untapered {3-3} Mode Device

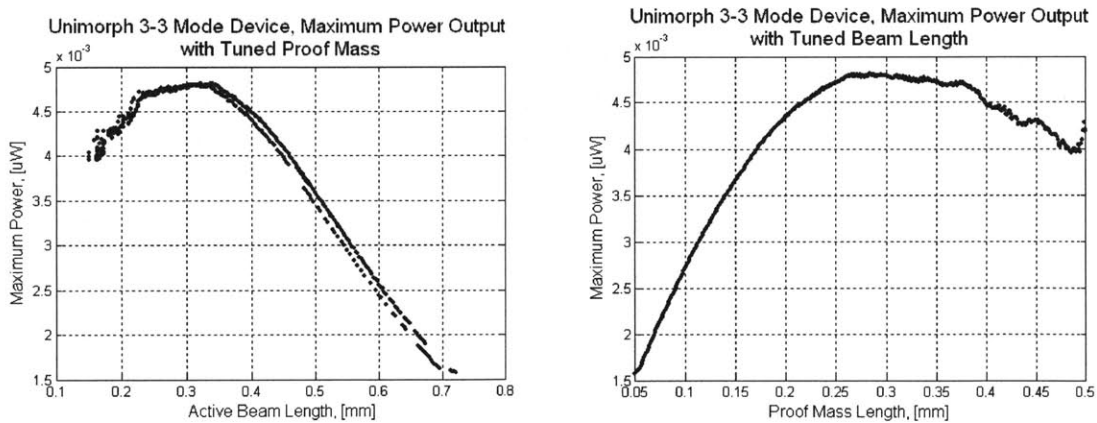


Figure 3.17: Maximum Device Power Output for an Untapered {3-3} Mode Unimorph Device Shown Against L and L_0 along Maximum Power Output Contour

By parametrically tracing the two-peak contour shown in Figure 3.14 along L (on the left of Figure 3.17), the two operating peaks are seen as an effective dual line for part of the graph. If instead, the entire design space is considered, the drop-off in power production away from the resonant frequency is more clearly visible as shown in Figure 3.18.

If an application's primary concern was maximizing power output, Figure 3.17 and Figure 3.18 would guide design towards a device with roughly $\sim 0.35\text{mm}$ of active beam length and $\sim 0.25\text{mm}$ of proof mass (from the peaks in Figure 3.17 and Figure 3.18), given these input conditions and the rest of the device geometry. The overall maximum device power output predicted within this space is $0.0051\mu\text{W}$ per device. (While this is a small power amount, due to the advantages of MEMS fabrication, many devices could be manufactured on the same wafer and used together to generate larger power levels that when coupled with appropriate power electronics could be of useful levels.)

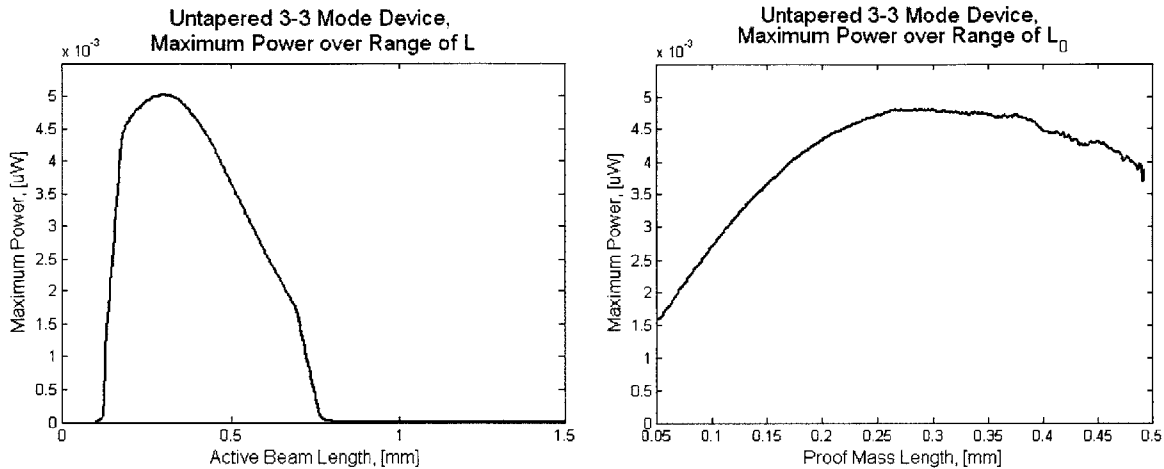


Figure 3.18: Maximum Device Power Output for an Untapered {3-3} Mode Unimorph Device Shown Against L and L_0 Across the Entire Design Space

Other performance parameters could lead to different device geometries. In Figures 3.19 and 3.20, the same design space but a different objective function, operating power density, is explored.

An interesting difference can be seen by comparing the close-up views of the power output and operating power density plots shown above. For power output alone, there is no penalty associated with large tip motion, so the best device is one that matches the anti-resonant (or resonant) frequency of the input base excitation. However, for operating power density, a large tip displacement is detrimental as it requires more operating volume. Thus, the dual operating peaks are not observed and instead the optimum device is one that operates in the trough between these two peaks. This represents the best compromise between the power gain to be had from being near anti-resonance and the increased volume required to operate at either the resonant or anti-resonant power peak.

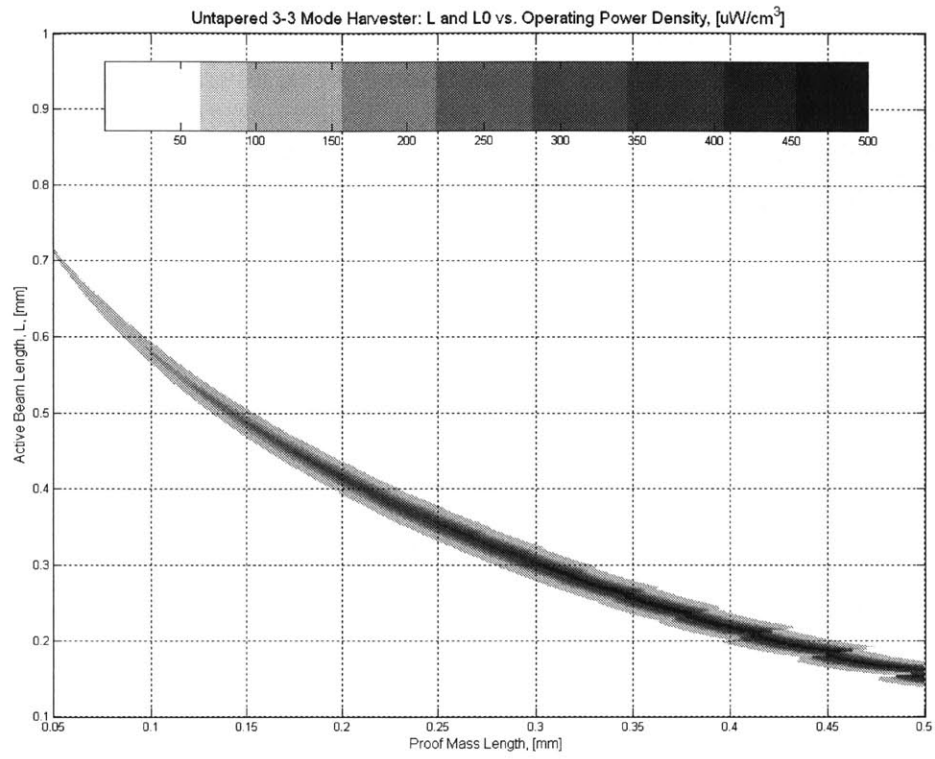


Figure 3.19: Operating Power Density Contours for an Untapered {3-3} Mode Unimorph Device

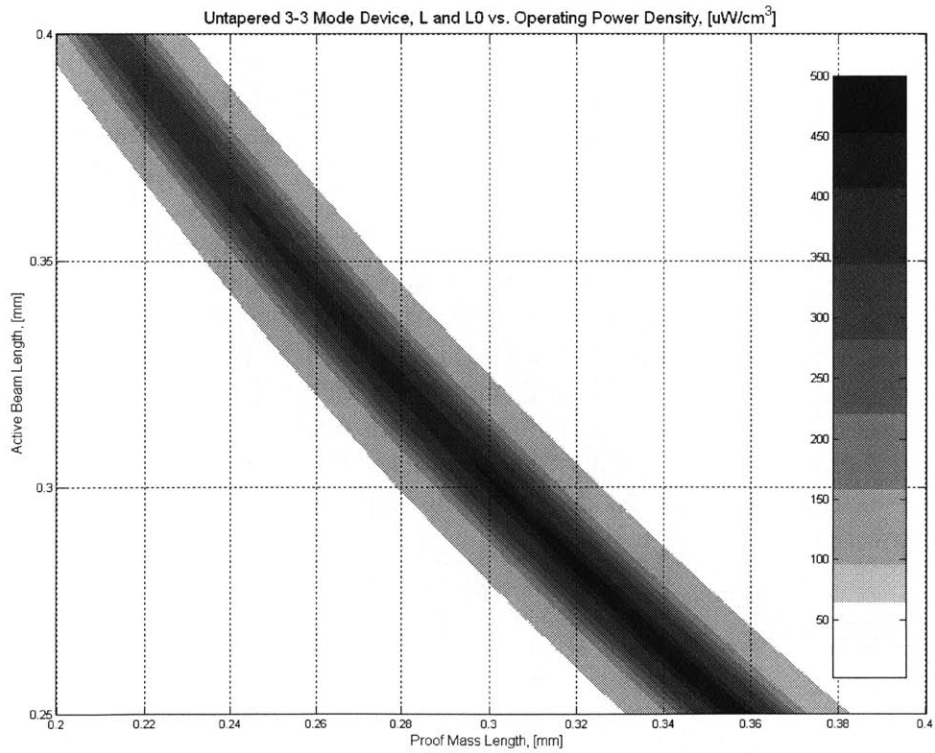


Figure 3.20: Close-Up of Operating Power Density Contours for an Untapered {3-3} Mode Unimorph Device

As was shown for power output, the charts in Figure 3.21 trace the optimum operating power density over the design space against active beam length and proof mass length.

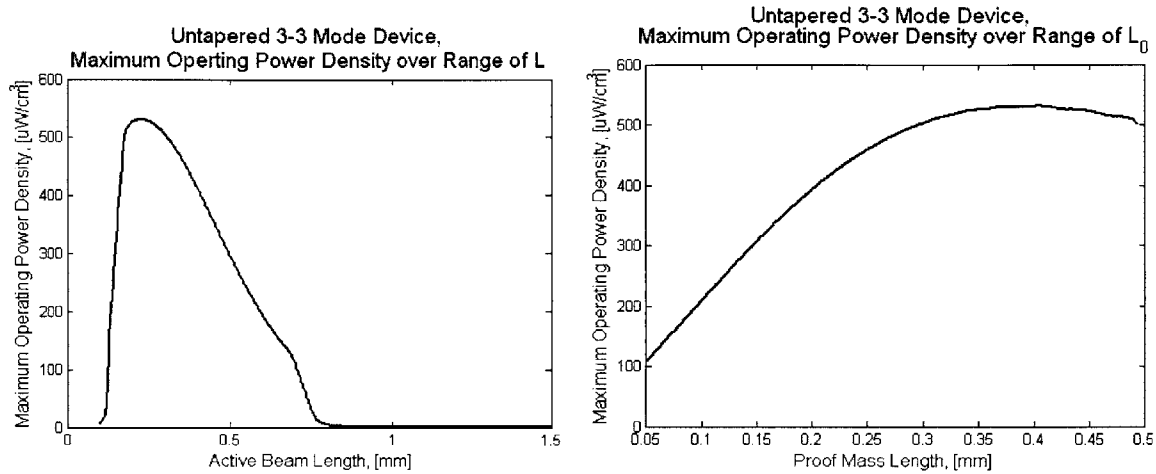


Figure 3.21: Maximum Operating Power Density for an Untapered {3-3} Mode Unimorph Device Shown Against L and L_0 Across the Entire Design Space

Unlike a device optimized for pure output power, which was roughly dimensioned with $L = 0.3\text{mm}$ and $L_0 = 0.25\text{mm}$, Figure 3.21 indicates that the best design for operating power density has an active beam length, L of about $\sim 0.25\text{mm}$ and a proof mass, L_0 , of about $\sim 0.375\text{mm}$. The maximum operating power density that was predicted from a device in this space is $536 \mu\text{W}/\text{cm}^3$.

A set of plots for static power density is included in Figures 3.21 through 3.24 for completeness, but since the volume penalty of increasing the length of a stationary device is not nearly as pronounced as the effect of on-resonant tip deflection, the trends for static power density are the same as those for pure device power output. As with pure device power output, the dual operating peaks can be seen in the close up and trace plots of static power density. The best device for static power density – as seen from the peaks in Figure 3.24 – is also very similar to that for power output, with an overall maximum static power density of $1935 \mu\text{W}/\text{cm}^3$.

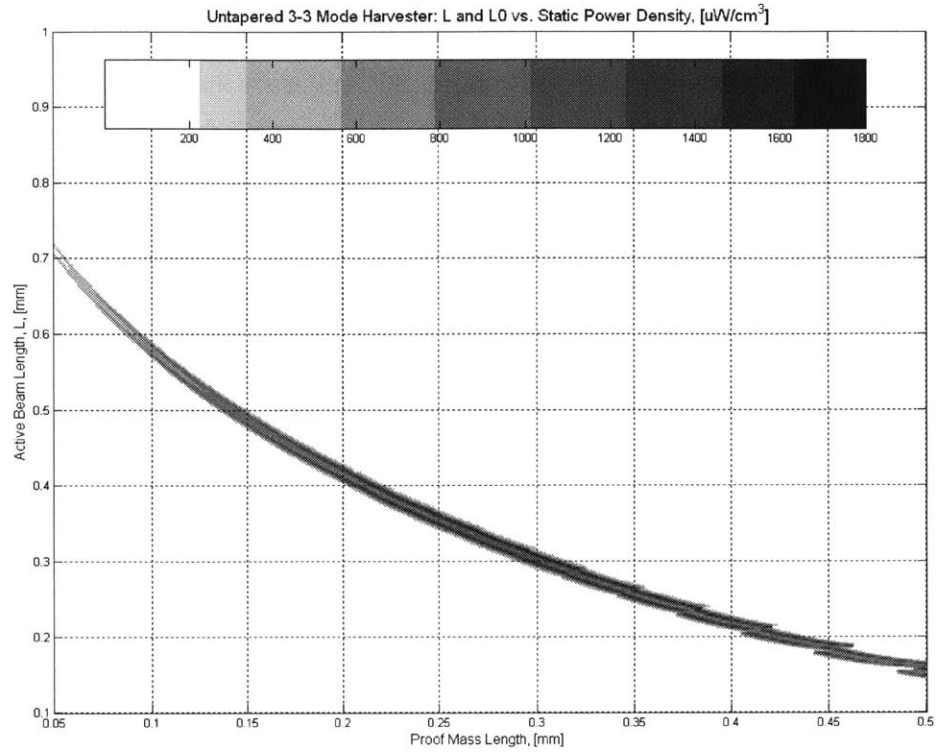


Figure 3.22: Static Power Density Contours for an Untapered {3-3} Mode Unimorph Device

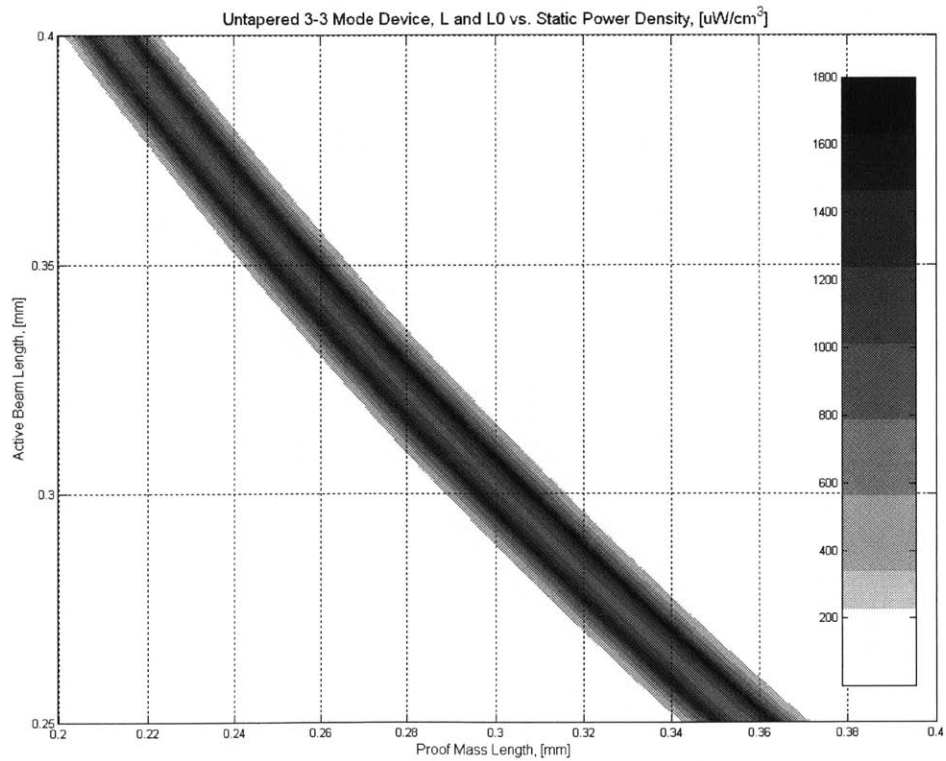


Figure 3.23: Close-Up of Static Power Density Contours for an Untapered {3-3} Mode Unimorph Device

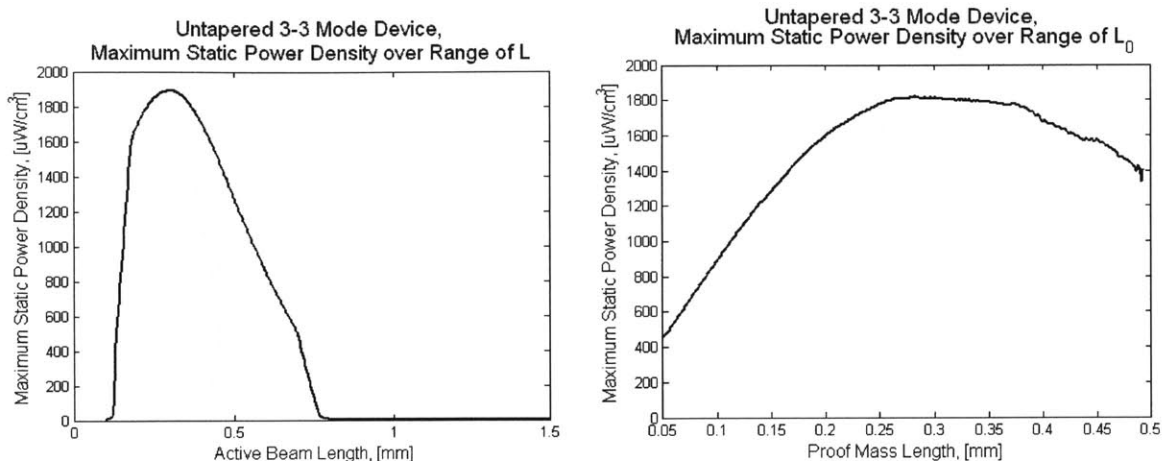


Figure 3.24: Maximum Static Power Density for an Untapered {3-3} Mode Unimorph Device Shown Against L and L_0 Across the Entire Design Space

The last metric of interest is specific power, or device power normalized by the harvester’s mass. Specific power contours and maximums are presented in Figure 3.25, Figure 3.26, and Figure 3.27 over the same design space.

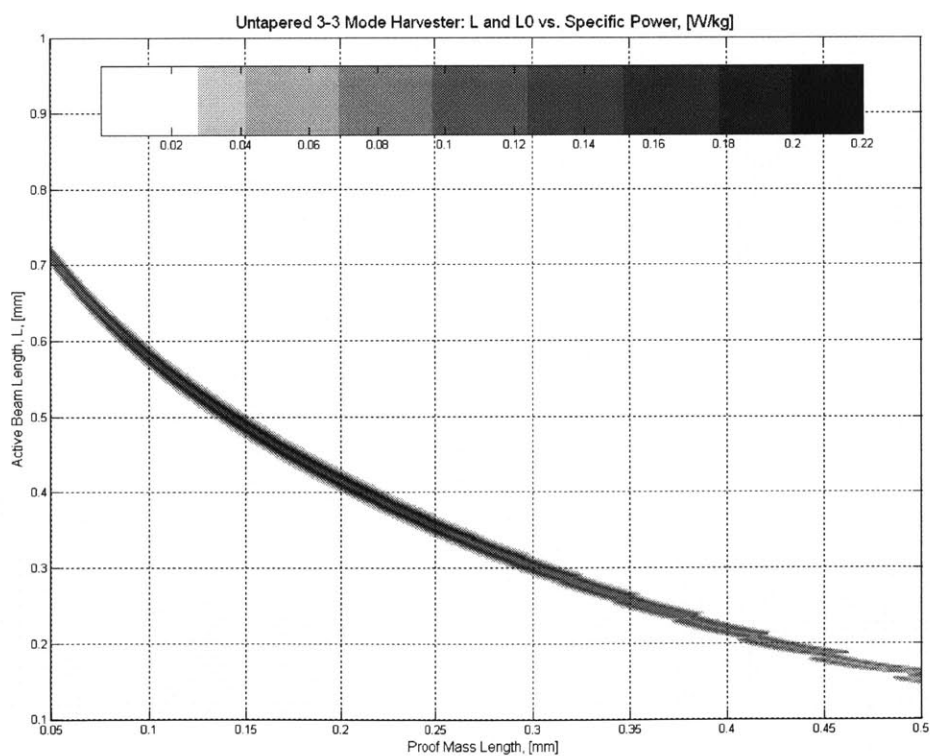


Figure 3.25: Specific Power Contours for an Untapered {3-3} Mode Unimorph Device

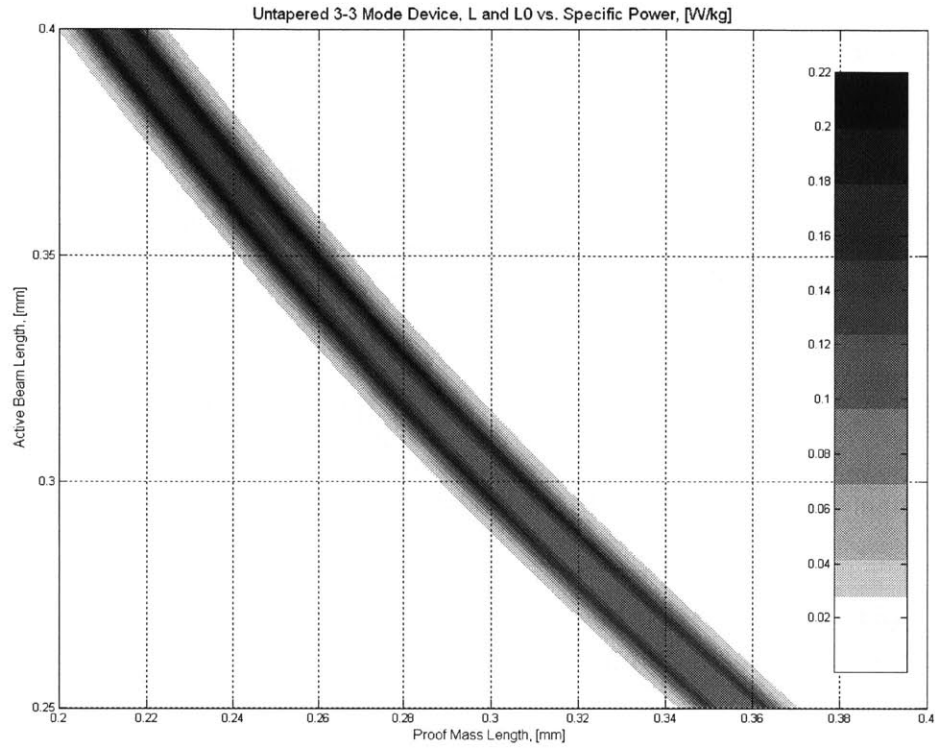


Figure 3.26: Close-Up of Specific Power Contours for an Untapered {3-3} Mode Unimorph Device

Again, the dual operating peaks are seen in Figure 3.26 as in power output and static power density. Designing for specific power leads to a third basic device geometry.

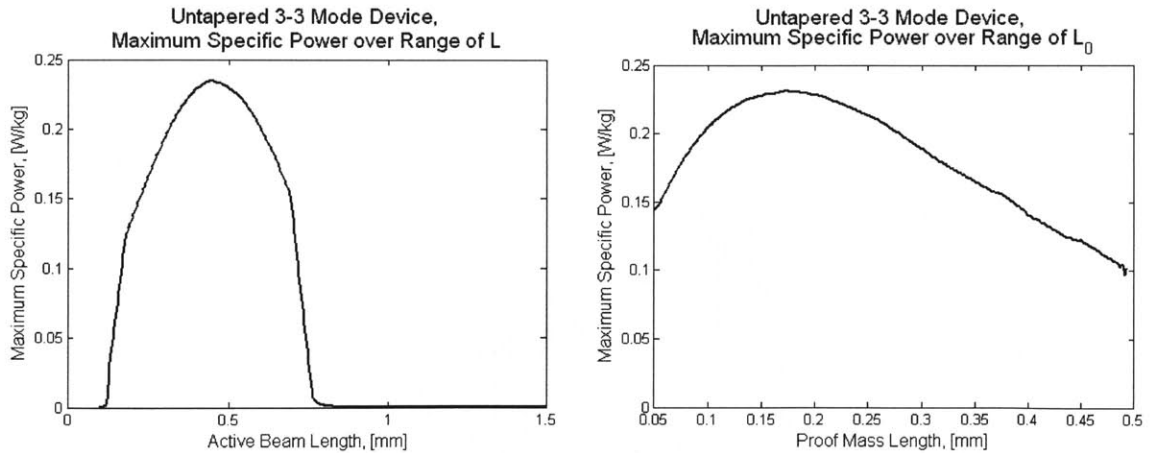


Figure 3.27: Maximum Specific Power for a Uniform {3-3} Mode Unimorph Device Shown Against L and L_0 Across the Entire Design Space

As can be seen in the plots of specific power along the maximum contour in Figure 3.27, the ideal device for maximizing specific power has an active beam length, L , of about ~ 0.45 mm and a proof mass length, L_0 , of about ~ 0.175 mm where the maximum specific power generated is

0.24 W/kg. This geometry makes sense as the proof mass has a much higher linear density than the beam structure itself but the additional tip displacement of a device of this geometry is not penalized by this metric.

As a final assessment of these devices, the maximum strain generated across the design space was determined. This is important as it help to determine durability of the device. It has been conservatively proposed that a recurring strain of greater than 500 micro-strain will lead to eventual damage in the piezoelectric structure. Across the entire design space considered in this section, the maximum strain predicted is $84\mu\epsilon$, well below the conservative limit of $500\mu\epsilon$. This means that any of the proposed device geometries are likely sufficiently fatigue tolerant to be practical in a real world airframe application.

A summary chart of the designs resulting from the four objective functions discussed in this section is presented at the end of this chapter along with the results from the {3-1} Mode Untapered Bimorph design study that follows in the next section.

3.5.3 Resulting Tools for Uniform Beam {3-1} Mode Optimization

In this section, the resulting design tools for a un-tapered {3-1} Mode bimorph beam over an expanded design space ($0.1 \leq L \leq 1.5\text{mm}$ and $0.05 \leq L_0 \leq 0.75\text{ mm}$) are presented. Overall, the trends from the {3-3} case discussed above are also applicable. Due to the fact that there is a higher percentage of PZT in the {3-1} Mode structure, the effects of anti-resonance vs. resonance are more pronounced (a larger fraction of the structure is changing its material properties based on electrical effects). Additionally, due to the increased thickness of the bimorph device, a larger (longer) device is required to match the same input conditions than for the {3-3} Mode device geometry shown in the previous section. This increased thickness drives the natural frequency of the device up, requiring a larger proof mass to accommodate the input excitation of 1000 Hz. As in the {3-3} Mode unimorph case, the proof mass is $3\ \mu\text{m}$ thick platinum, and is designed (power-optimal resistance) for anti-resonant operation. The beam is composed of two layers of PZT each sandwiched by electrodes with a purely structural element in the center. The thicknesses, densities and moduli of the layers are given in Table 3.6. The total bimorph active beam thickness is $2.48\ \mu\text{m}$.

The carpet plots for anti-resonant frequency, power output, operational power density and static power density are presented in this section in the same matter as in Section 3.5.1. As in the previous section, the plot for anti-resonant frequency (Figure 3.28) covers the entire design space while the plots for each power objective function are cropped to show more detail in the peak areas of interest here.

Table 3.6: {3-1} Mode Bimorph Device Layers and Properties:

Layer Material	thickness, [μm]	density, [kg/m ³]	modulus, [GPa]	plate modulus, [GPa]
Pt	0.20	21440	170.0	200.5
Ti	0.02	4510	110.0	124.4
PZT	0.50	7750	66.0 (c_{11}^{E*})	66.0*
Ti	0.02	4510	110.0	124.4
Pt	0.20	21440	170.0	200.5
SiO ₂	0.10	2300	69.00	70.59
SiN _x	0.40	3000	313.0	344.0
SiO ₂	0.10	2300	69.00	70.59
Pt	0.20	21440	170.0	200.5
Ti	0.02	4510	110.0	124.4
PZT	0.50	7750	66.0 (c_{11}^{E*})	66.0*
Ti	0.02	4510	110.0	124.4
Pt	0.20	21440	170.0	200.5

* Note that the modulus for PZT was calculated from the full constitutive relationships using the 2D formulas presented earlier based on available manufacturer's information. (The value shown for the PZT modulus is c_{33}^{E*} , as defined in Table 3.2 for a beam)

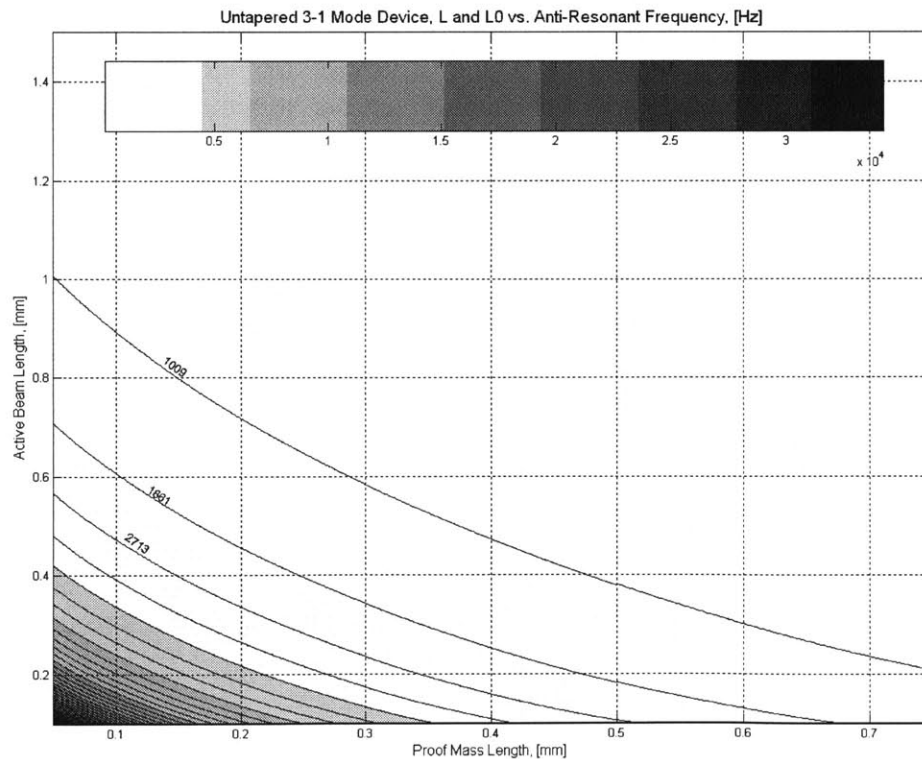


Figure 3.28: Anti-Resonant Frequency Contours for a Untapered {3-1} Mode Bimorph Device

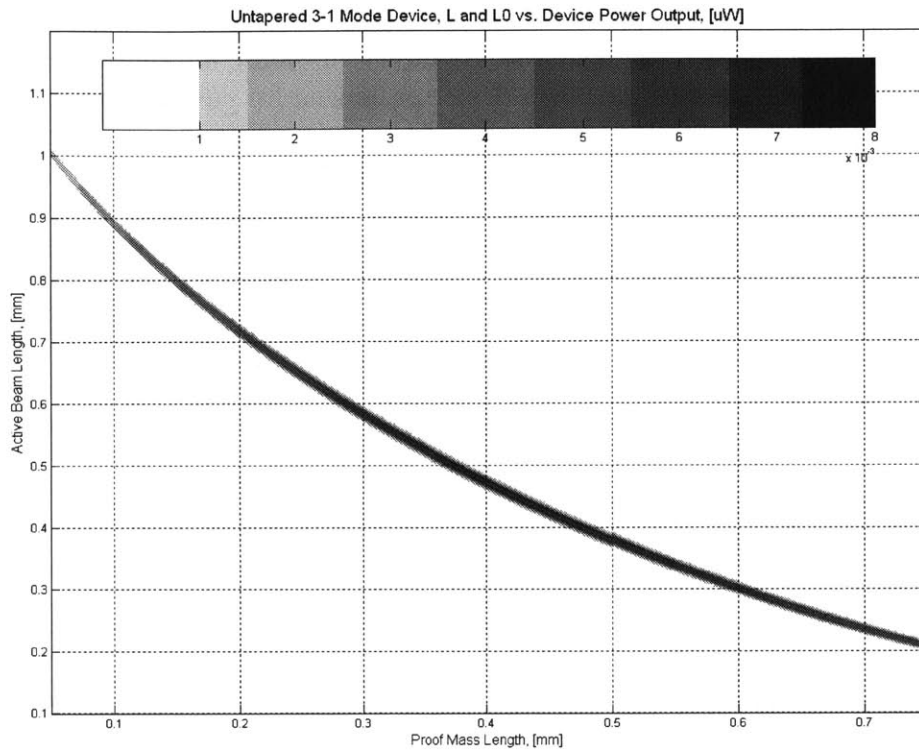


Figure 3.29: Device Power Output Contours for an Untapered {3-1} Mode Bimorph Device

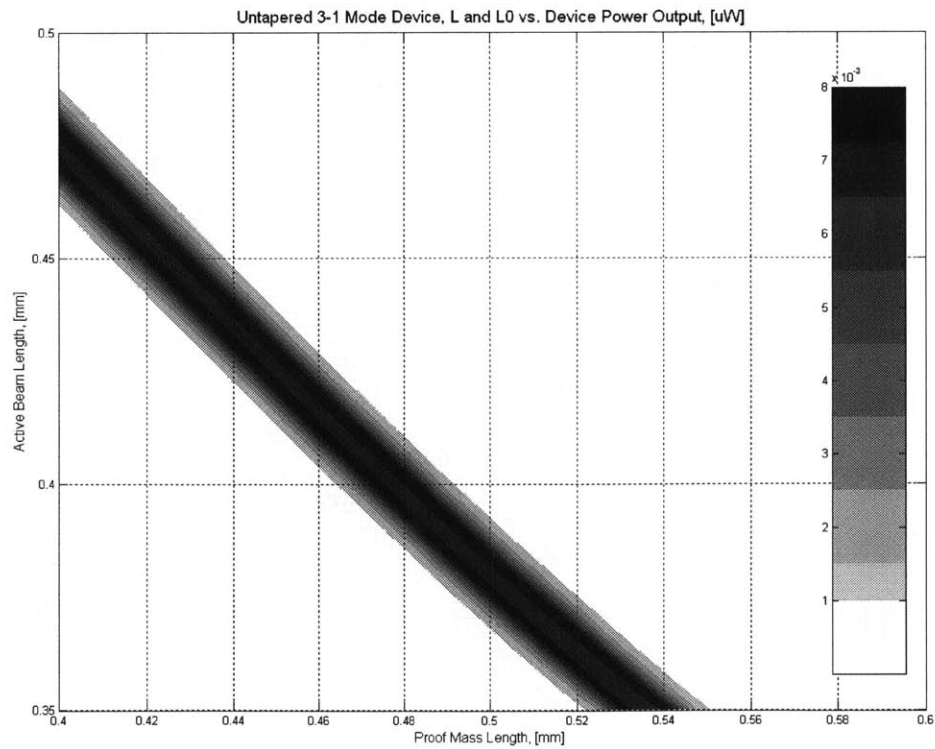


Figure 3.30: Close-Up of Device Power Output Contours for an Untapered {3-1} Mode Bimorph Device

As with the {3-3} Mode device, in close-up (Figure 3.30), the dual power peaks can be seen.

Looking at power output across the design space shown in Figure 3.29 and 3.30 against active beam length, L , and proof mass length, L_0 , a device optimized for power output alone is roughly $L \approx 0.45$ mm and $L_0 \approx 0.425$ mm (see Figure 3.31). The maximum predicted device power output for a {3-1} Mode bimorph device in this space is $0.0089 \mu\text{W}$.

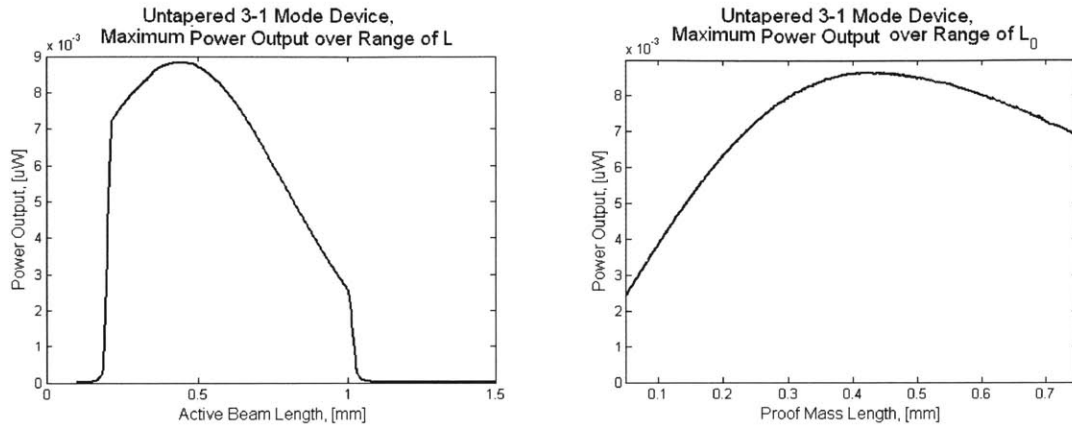


Figure 3.31: Maximum Device Power Output for an Untapered {3-1} Mode Bimorph Device Shown Against L and L_0 Across the Entire Design Space

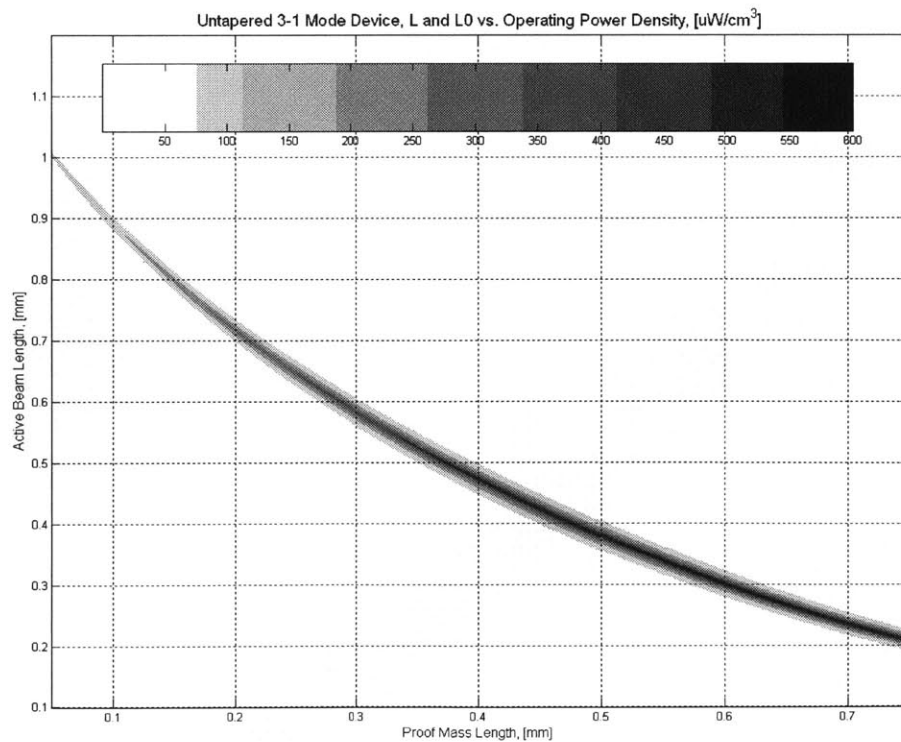


Figure 3.32: Operating Power Density Contours for an Untapered {3-1} Mode Bimorph Device

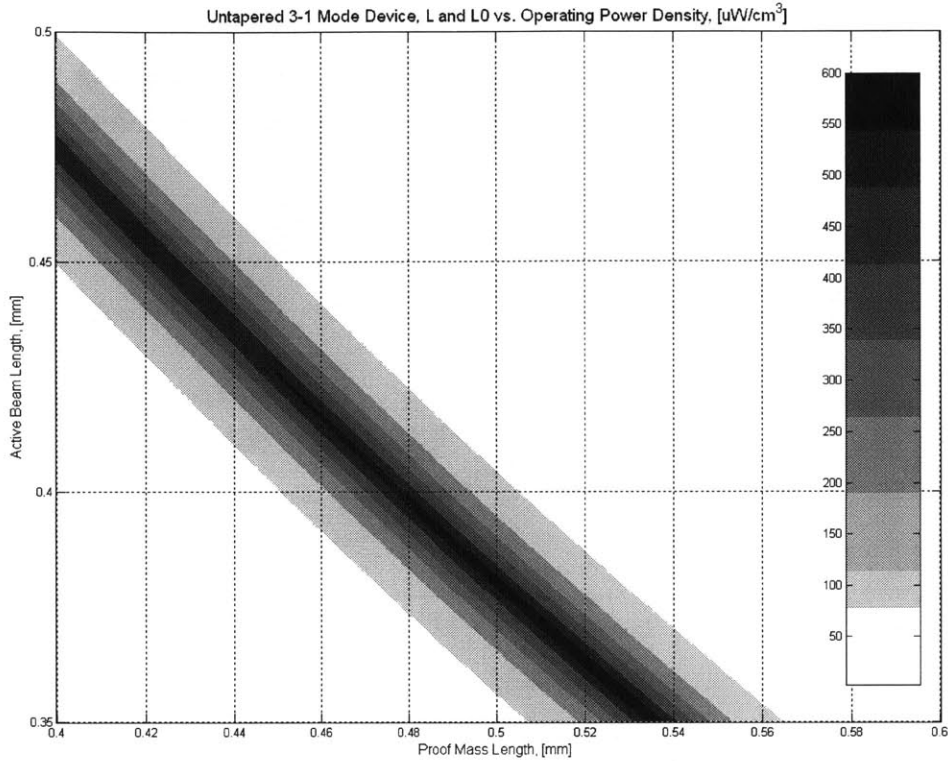


Figure 3.33: Close-Up of Operating Power Density for an Untapered {3-1} Mode Bimorph Device

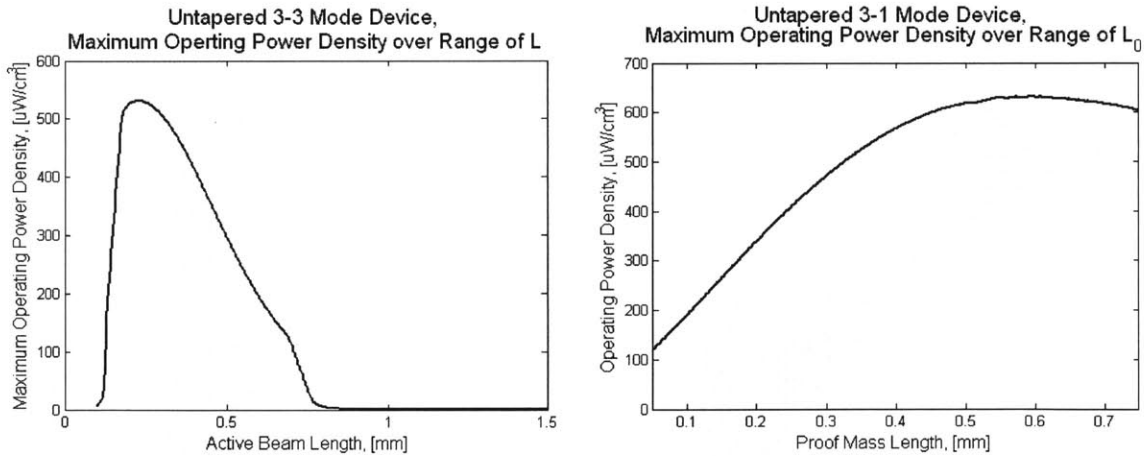


Figure 3.34: Maximum Operating Power Density for an Untapered {3-1} Mode Bimorph Device Shown Against L and L_0 Across the Entire Design Space

The maximum operating power density predicted for a {3-1} Mode bimorph device in this design space is $624 \mu\text{W}/\text{cm}^3$, with a geometry of roughly $L \approx 0.35 \text{ mm}$ and $L_0 \approx 0.5 \text{ mm}$, as seen in Figure 3.34.

As for the {3-3} Mode devices examined in the previous section, static power density is not necessarily a practical design metric, but as it is a popular one, it is also included below as Figure 3.35 through 3.37 for a {3-1} Mode bimorph device.

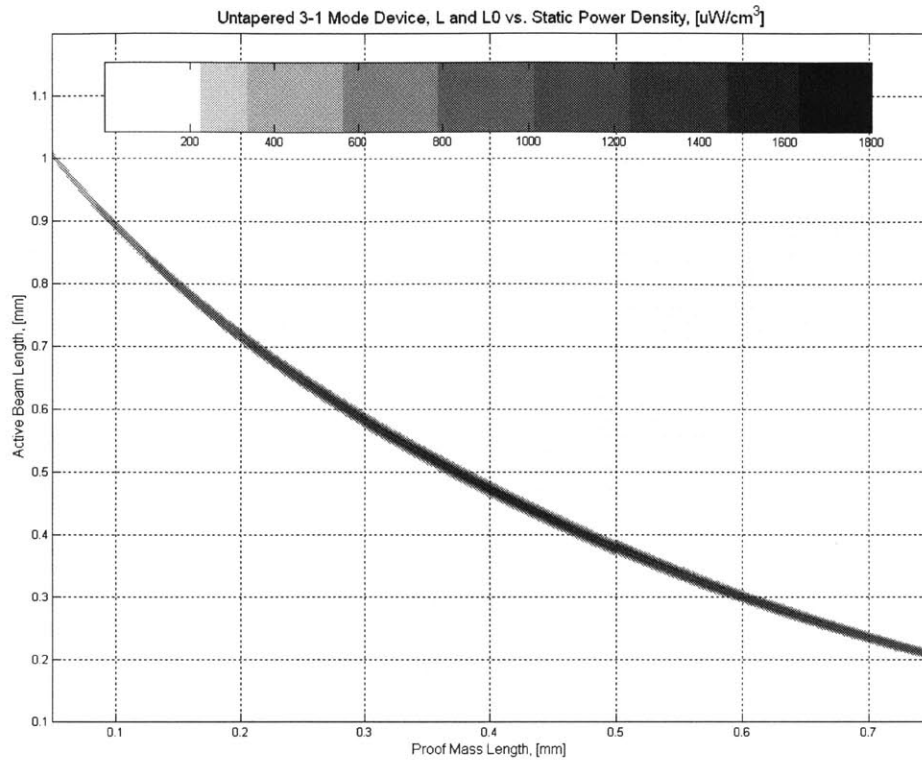


Figure 3.35: Static Power Density Contours for an Untapered {3-1} Mode Bimorph Device

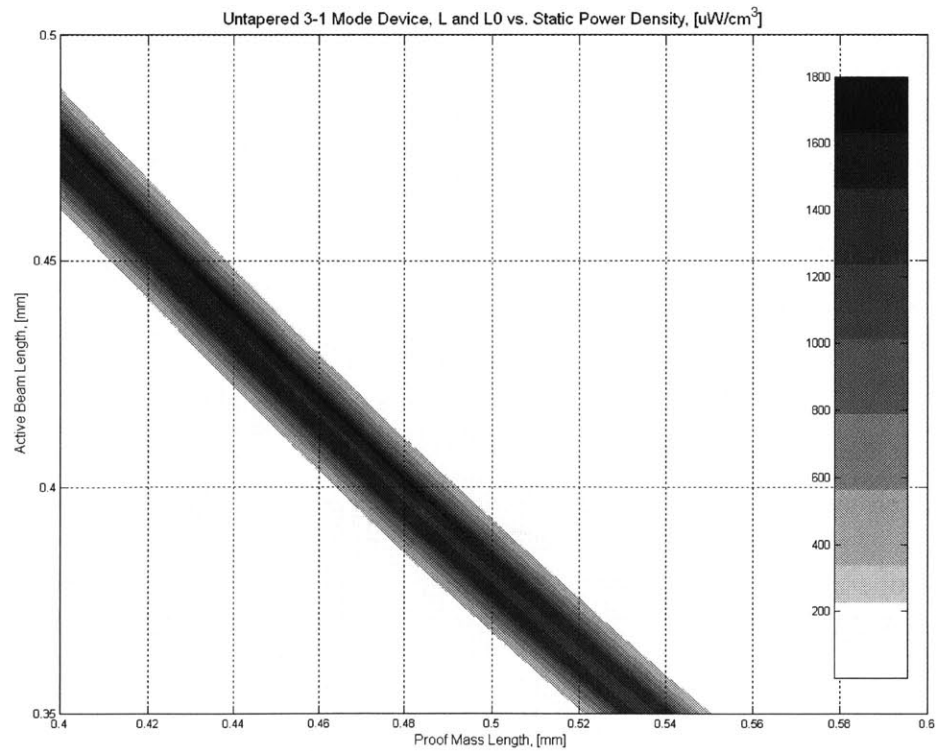


Figure 3.36: Close-Up of Static Power Density Contours for an Untapered {3-1} Mode Bimorph Device

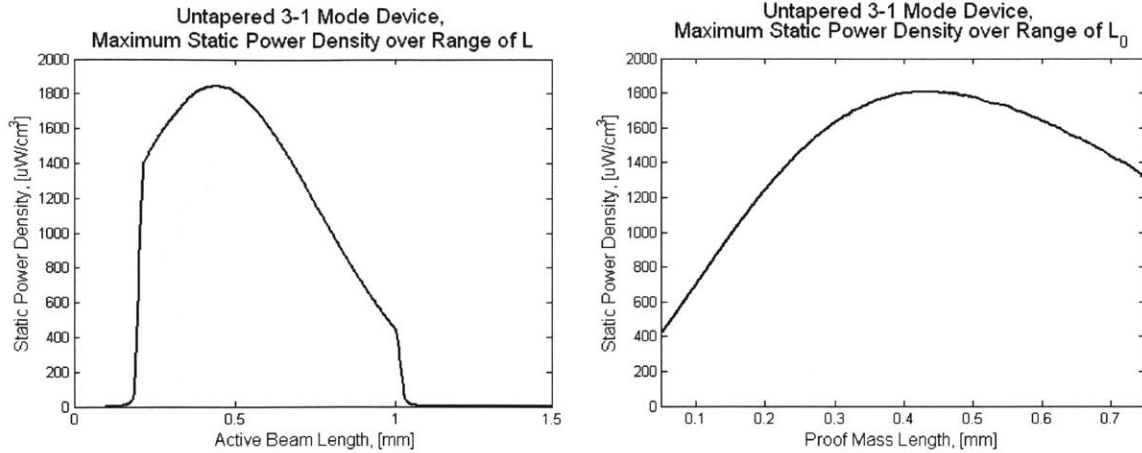


Figure 3.37: Maximum Static Power Density for an Untapered {3-1} Mode Bimorph Device Shown Against L and L_0 Across the Entire Design Space

The maximum static power density predicted for a {3-1} Mode bimorph device in this design space is $1851 \mu\text{W}/\text{cm}^3$, with a geometry of roughly $L \approx 0.45 \text{ mm}$ and $L_0 \approx 0.425 \text{ mm}$, as seen in Figure 3.37. Note that as with the {3-3} Mode unimorph space, this is the same geometry as a device optimized for pure power output.

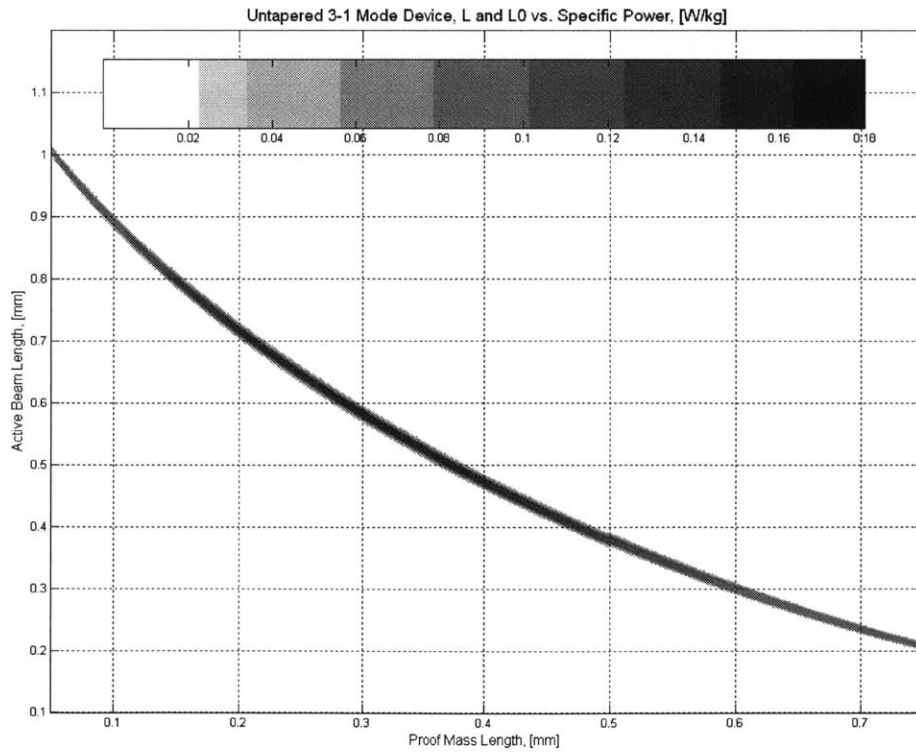


Figure 3.38: Specific Power Contours for an Untapered {3-1} Mode Bimorph Device

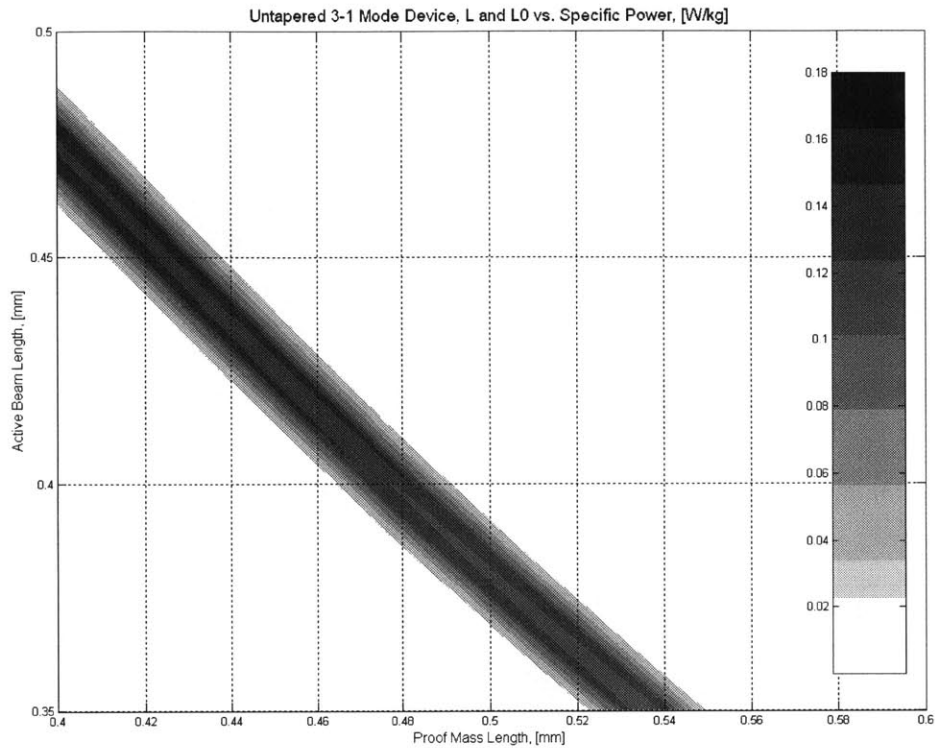


Figure 3.39: Close-Up of Specific Power Contours for an Untapered {3-1} Mode Bimorph Device

Lastly, normalizing by device mass instead of by volume gives the following specific power devices in this design space (see Figures 3.38 and 3.39). Looking at L and L_0 along the above contours for specific power (Figure 3.40) we see that the maximum specific power from a device with this input in this design space is 0.19W/kg with $L \approx 0.6\text{ mm}$ and $L_0 \approx 0.3\text{ mm}$:

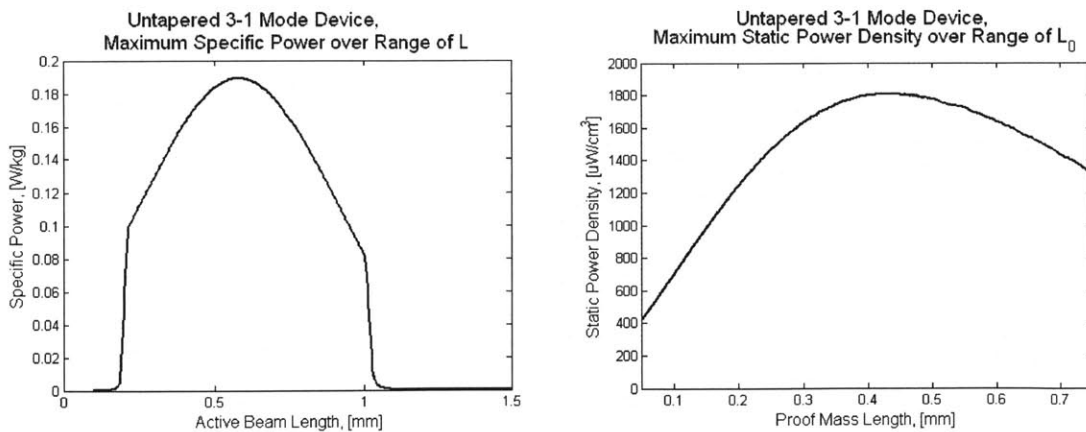


Figure 3.40: Maximum Specific Power for an Untapered {3-1} Mode Bimorph Device Shown Against L and L_0 Across the Entire Design Space

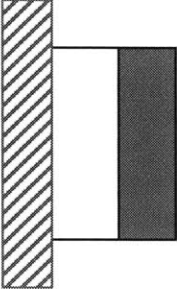
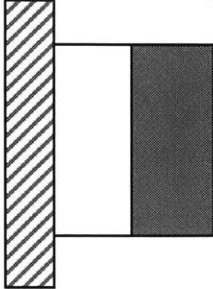
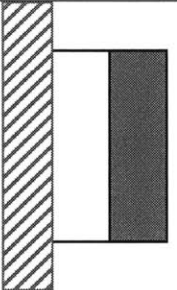
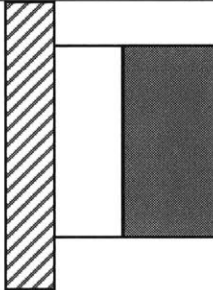
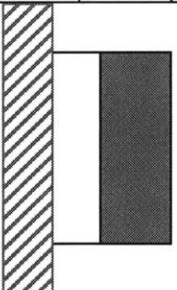
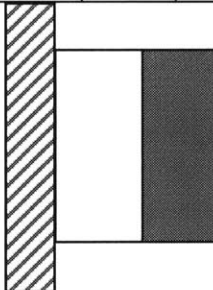
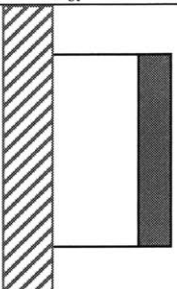
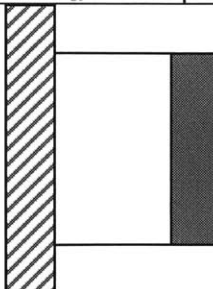
As was done with the {3-3} Mode unimorph, maximum strain was assessed for all optimum devices in this section. With a maximum of $66.5\mu\epsilon$, all of the devices considered in this section are also sufficiently robust to be potentially practical in real application.

3.5.4 Uniform Beam Optimization Results and Conclusions

In the above sections, two basic MEMS un-tapered beam geometries were considered, a {3-3} Mode unimorph device with interdigitated electrodes and one layer of piezoelectric material, and a {3-1} Mode bimorph device with two layers of piezoelectric material each sandwiched with plate electrodes. For both devices, the structural and PZT layer thicknesses, as well as the proof mass height, were set based on previously demonstrated MEMS fabrication and preliminary modeling results. A conservative excitation vibration appropriate for an aircraft structural health monitoring application of 1kHz at just under 4 m/s^2 was chosen and a design space of an active beam length between 0.1mm and 1.5mm and a proof mass length between 0.05mm and 0.5mm for the unimorph (0.05mm to 0.75mm for the bimorph) was defined. Within that space, four power metrics of interest to a device designer were examined: power output, operating and static power densities, and specific power. Each of these metrics drove the device geometry in slightly different ways. A summary table of the resulting “optimum” device geometries is presented in Table 3.7.

It is interesting to note that for pure power output (and static power density), the favored structure is one that is divided nearly in half between active beam area and proof mass. This represents the compromise between the increased strain – and therefore power generation – that results from a large proof mass and the need for sufficient active area of the beam. (Recall that the proof mass is modeled as rigid and thus only the piezoelectric material in the active area of the beam generates power). When the tip displacement becomes detrimental by optimizing against operating power density, more of the device length is taken up by the proof mass, which increases the strain at the root while reducing the overall beam tip deflection. When weight is penalized instead of volume by considering specific power, the design is shifted in the opposite direction. A longer beam with a smaller proof mass results in an overall lighter device that relies on having a larger active piezoelectric area at lower strain. These trends, and this design space technique, can be applied to the design of future piezoelectric energy harvesting devices. In Chapter 4, these same techniques will be applied to a tapered beam geometry, both with and without a tip proof mass.

Table 3.7: Untapered Harvesting Device Optimization Summary

	{3-3} Untapered Unimorphs	{3-1} Untapered Bimorphs
Device Power	 <p>$L = 0.35; L_0 = 0.30; L_t = 0.65$ $P = 0.0051 \mu\text{W}$</p>	 <p>$L = 0.40; L_0 = 0.425; L_t = 0.825$ $P = 0.0089 \mu\text{W}$</p>
Operating Power Density	 <p>$L = 0.25; L_0 = 0.375; L_t = 0.625$ $P_{op} = 536 \mu\text{W}/\text{cm}^3$</p>	 <p>$L = 0.35; L_0 = 0.50; L_t = 0.85$ $P_{op} = 624 \mu\text{W}/\text{cm}^3$</p>
Static Power Density	 <p>$L = 0.35; L_0 = 0.30; L_t = 0.65$ $P_{st} = 1935 \mu\text{W}/\text{cm}^3$</p>	 <p>$L = 0.45; L_0 = 0.425; L_t = 0.875$ $P_{st} = 1852 \mu\text{W}/\text{cm}^3$</p>
Specific Power	 <p>$L = 0.45; L_0 = 0.175; L_t = 0.625$ $P_{sp} = 0.24 \text{ W}/\text{kg}$</p>	 <p>$L = 0.60; L_0 = 0.30; L_t = 0.90$ $P_{sp} = 0.19 \text{ W}/\text{kg}$</p>
<p><i>*All figures approximately to scale of 1'' = 1mm.</i></p>		

In all cases, optima were found within the design spaces considered. The optimum designs for the metrics considered were not at the edges of the space, nor were they strain-limited. This indicates that MEMS-scale devices are actually the devices of choice for this harvesting application. More detailed information about each of the {3-3} Mode untapered unimorph designs presented in Table 3.7 are given in Table 3.8.

Table 3.8: Performance Metrics for {3-3} Mode Untapered Unimorph Optimized Devices

	Optimized for Maximum P_{out}	Optimized for Maximum P_{op}	Optimized for Maximum P_{st}	Optimized for Maximum P_{sp}
L [mm]	0.3156	0.2372	0.3156	0.4472
L_0 [mm]	0.2939	0.3767	0.2939	0.1814
P_{out} [μ W]	0.0051	0.0029	0.0051	0.0043
P_{op} [μ W/cm ³]	380.65	536.0	380.65	268.0
P_{st} [μ W/cm ³]	1935.0	1110.6	1935.0	1541.0
P_{sp} [W/kg]	0.2058	0.0970	0.2058	0.2388
Voltage [V]	0.8949	0.2842	0.8949	0.6536
w_{tip} [μ m]	5.2079	1.1685	5.2079	8.4178
PZT strain, [μ ϵ]	70.75	24.67	70.75	65.013
ω_r [Hz]	959.9	977.5	959.9	963.7
ω_{ar} [Hz]	1000.6	1020.2	1000.6	1000.5
Ω_{OC}	1.0424	1.0437	1.0424	1.0382

4 Modeling and Optimization of Tapered Beam Harvesters

In the previous Chapter, untapered, uniform cross-section beam harvesters with proof masses operating in both the {3-3} and {3-1} Mode were examined for power output, operating and static power density, and specific power. Efficiency, while not explicitly investigated, is optimized at the power generation peaks due to the choice of optimum load resistance that is implemented in the models used. A simple geometric modification that is easily implemented with MEMS fabrication techniques is to taper the beam's footprint so that the width at the tip of the active beam section is not equal to the width at the root. The goal of this modification is to more evenly distribute the strain profile along the beam as compared to an un-tapered beam. The introduction of a proof mass at the end of the un-tapered beams in Chapter 3 had a similar effect (as the moment at the tip of the active beam length is not equal to zero when a proof mass is present). In this section, using a taper instead of a proof mass, and the effect of using both a taper and a proof mass, are examined for {3-3} Mode beams with the same layer structure as described in Table 3.4. As in Chapter 3, the electrode spacing and width were fixed with $p = 16 \mu\text{m}$ and $a = 4 \mu\text{m}$, respectively. The {3-1} Mode was not considered here due to the similarities in operational trends that were seen previously between the {3-1} and {3-3} operation in Chapter 3.

4.1 Tapered {3-3} Mode Beam without a Proof Mass

In the case without a proof mass, it is not necessary to go through the same mode-shape definition that was described for a large proof mass in Section 3.1. Instead, to accurately capture the effect of the changing beam width, a Rayleigh-Ritz procedure was used to approximate the first mode of the tapered structure. The three modes that were combined to find the first tapered mode were simply those for a cantilevered beam:

$$\psi_n(x) = c_n((\cosh(B_n x) - \cos(B_n x)) - s_n(\sinh(B_n x) - \sin(B_n x))) \quad \text{Eq 4-1}$$

Where the constants c_n , s_n and B_n for each mode are defined in the following table [54]:

Table 4.1: Cantilevered Beam Mode Shape Constants for Eq 4-1

	$n = 1$	$n = 2$	$n = 3$
c_n	1	1	1
s_n	0.73410	1.01847	0.99923
B_n	1.8751/L	4.6941/L	7.8548/L

When these modes are combined with a Rayleigh-Ritz procedure, the mode shapes and curvatures are obtained for the approximate first mode of the tapered beam structure as shown in Figure 4.1. The mass and stiffness matrices required to perform this combination are similar to

the scalar equations given in Section 3.1. The terms of the mass matrix (without a proofmass) are given by:

$$M_{ij} = \int_{V_s} \psi_{ri} \psi_{rj} \rho_s dV_s + \int_{V_p} \psi_{ri} \psi_{rj} \rho_p dV_p \quad \text{Eq 4-2}$$

The accompanying stiffness matrix terms are:

$$K_{ij} = \int_{V_s} (-z^2 \psi_{ri}'' \psi_{rj}'') c_s dV_s + \int_{V_p} (-z^2 \psi_{ri}'' \psi_{rj}'') c^E dV_p \quad \text{Eq 4-3}$$

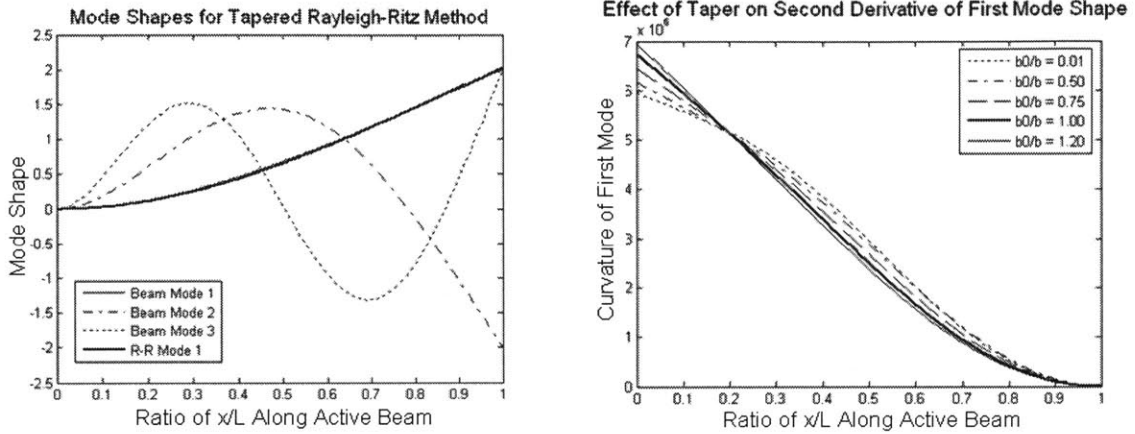


Figure 4.1: Rayleigh-Ritz Results for Tapered Beam without a Proof Mass

The Mode shape shown as the Rayleigh-Ritz first mode is for a taper ratio (tip width, b_0 , over root width, b) of 0.50. Overall, mode shapes were investigated by varying the taper ratio from 0.01 to 1.2 (which corresponds to tip widths from 10% to 120% of the root width). Over this range there was little difference in the actual shape of the first modes between the tapered and un-tapered cases, thus only the 50% case is shown in Figure 4.1. Note that, as can be seen in the second plot in Figure 4.1, the taper does have an effect on the curvature of the beam shape, and therefore on the strain driving power generation in the harvester. However, without a proof mass, no matter what the taper ratio, the curvature goes to zero at the end of the active beam section.

Once the Rayleigh-Ritz process was completed and the combined first mode was determined, the same process that was used for a {3-3} Mode un-tapered beam throughout Chapter 3 was implemented to find the power metrics of interest. Contour and maximum trace plots were generated to explore the design space of a tapered {3-3} Mode beam without a proof mass and are presented below. A summary table is given at the end of this chapter. The input excitation for these studies was the same representative aircraft skin vibration as that used in Chapter 3 of 3.8982 m/s^2 at 1 kHz. As before, the load resistance of the device is tuned to be the optimum for anti-resonant power generation at all points in the design space. The beam width at the root is held constant at 1mm and the tip width is varied from 10% to 120% of the root width. The beam length is varied from 0.5 mm to 1.5 mm.

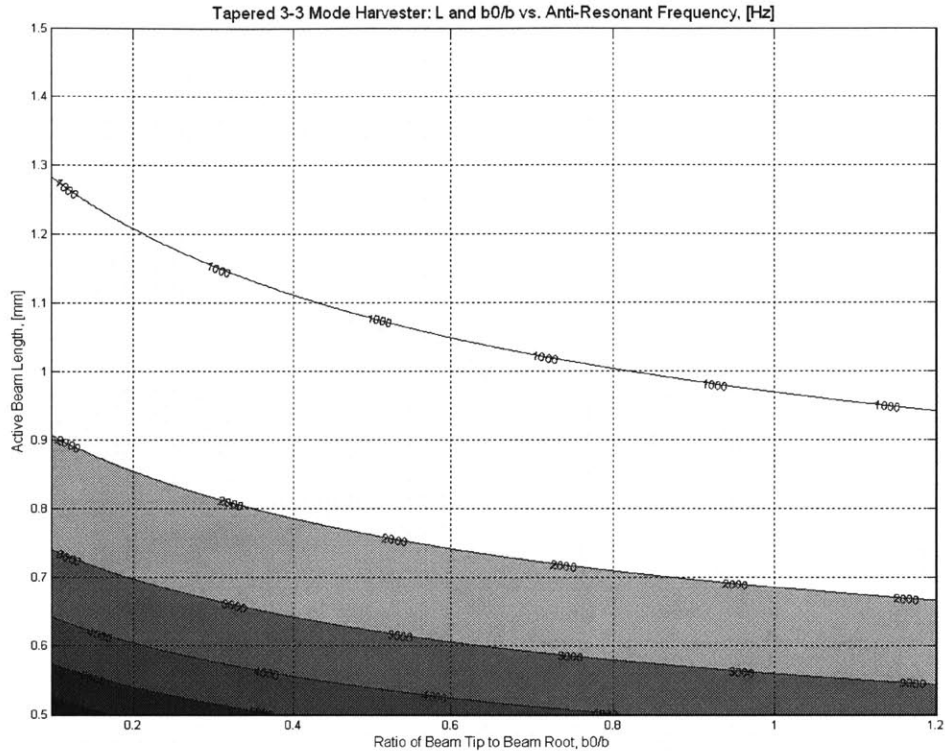


Figure 4.2: Anti-Resonant Frequency Contours for a Tapered {3-3} Unimorph Device, no Proof Mass

The lack of a proof mass results in the overall length of the device needing to be larger than those seen in Chapter 3 in order to have resonant and anti-resonant frequencies aligned with the 1kHz input. The contours in Figure 4.2 are labeled with the anti-resonant frequency of the device in Hz. The horizontal axis is the taper ratio of the device (tip width over root width, b_0/b) while the vertical axis is the active beam length. Since there is no proof mass in this case, the active beam length and the total beam length are the same.

As seen before, the resulting device designs, such as that shown for device power output in Figure 4.3, follow the 1 kHz contour shown in Figure 4.2 fairly tightly. The dual operating peaks first observed for untapered devices in Section 3.5 are seen again in the device power output contours for a tapered device, *e.g.* in Figure 4.3 and Figure 4.4.

The following carpet plots are analogous to those shown in Section 3.5. Instead of plotting a design space of active beam length and proof mass length, in this section beam length is shown on the vertical axis with taper ratio on the horizontal axis. In the next section, proof mass length replaces beam length on the vertical axis and a beam length is fixed for each carpet plot. While the entire space of $0.5\text{mm} < L < 1.5\text{mm}$ and $0.1 < b_0/b < 1.2$ (as shown in Figure 4.2) is calculated for each metric below, some of the design space is trimmed from the plots that follow for ease of use.

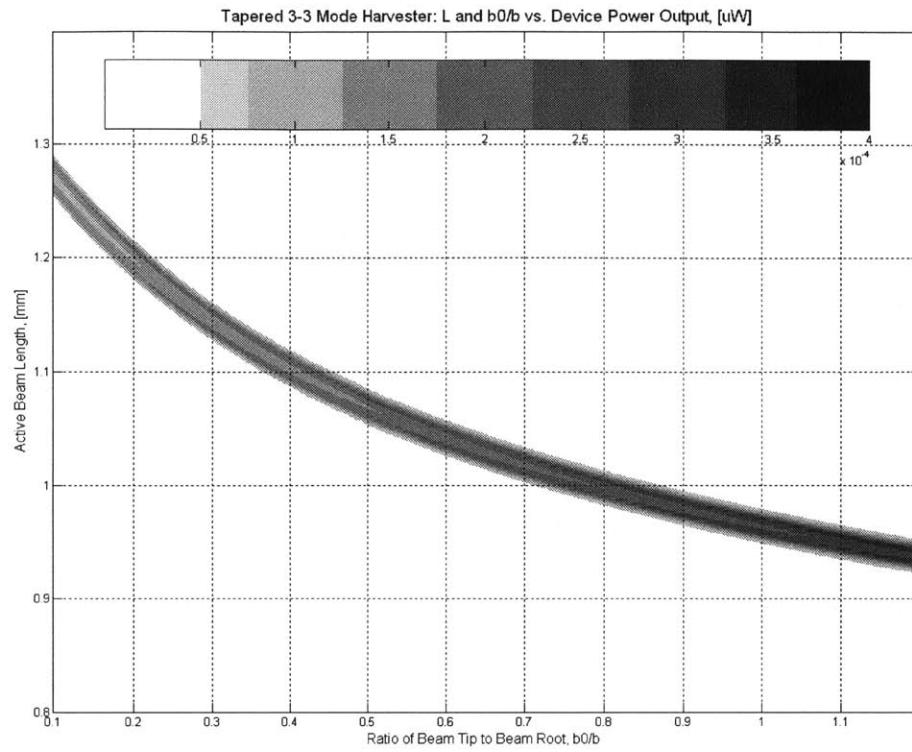


Figure 4.3: Device Power Output Contours for a Tapered {3-3} Mode Unimorph Device, no Proof Mass

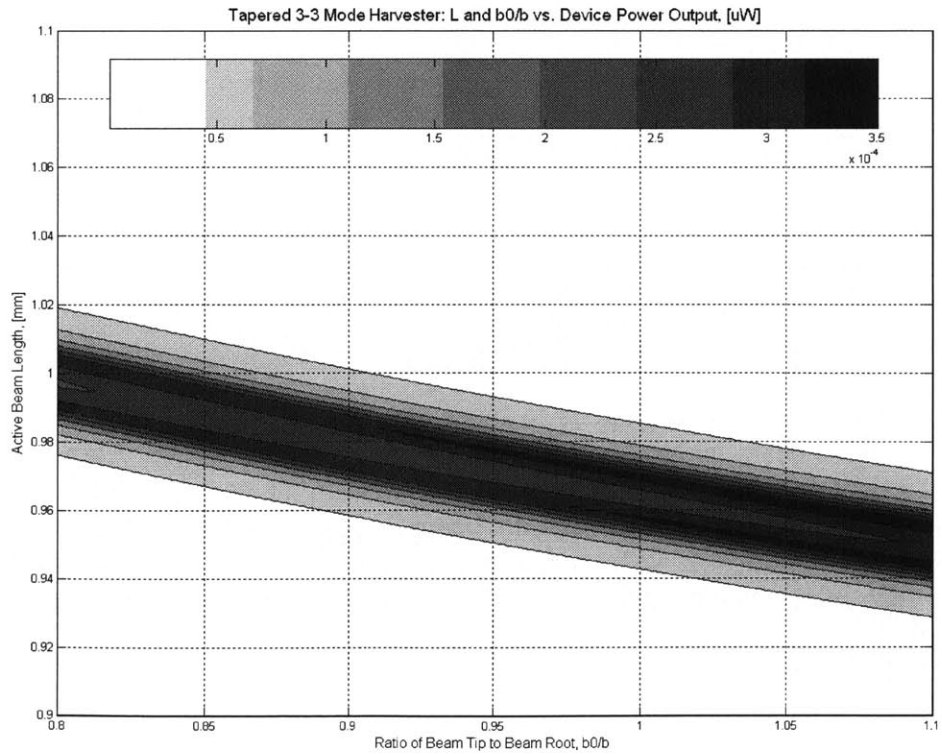


Figure 4.4: Close-Up of Power Output for a Tapered {3-3} Mode Unimorph Device, no Proof Mass

Maximum power generated can be plotted as a function of both taper ratio and beam length over the design space to facilitate finding the optimum device dimensions for power generation. Shown in Figure 4.5, these plots indicate that a wider beam tip width is better for power generation.

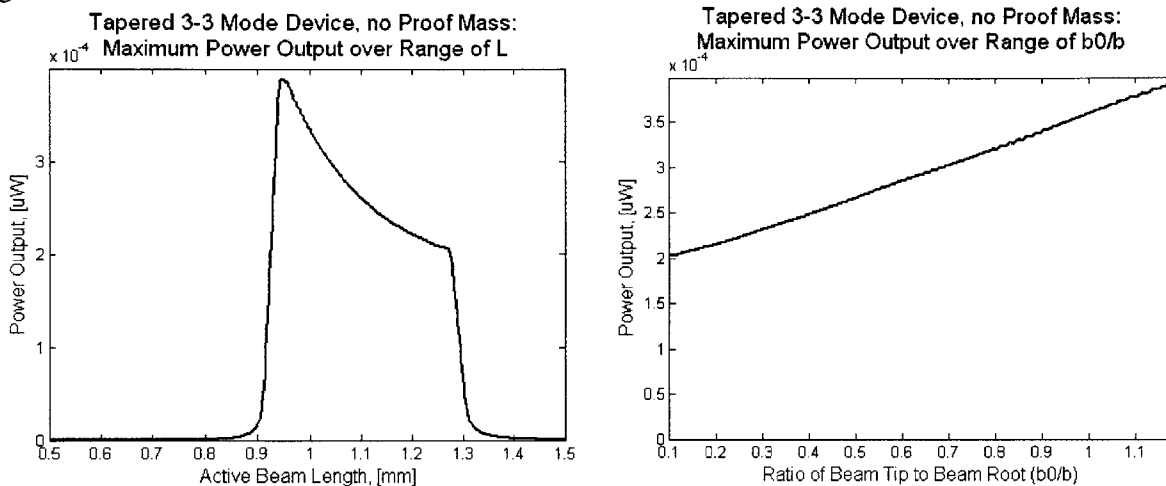


Figure 4.5: Maximum Device Power Output for a Tapered {3-3} Mode Unimorph Device Shown Against Length and Raper Ratio Across the Design Space

From Figure 4.5 it can be seen that the maximum device power output is achieved with a beam length of about $\sim 0.93\text{mm}$ and a taper ratio of ~ 1.2 . This is interpreted as the additional active piezoelectric area achieved by making the beam tip wider than the beam root has more of an effect than the difference in strain profile caused by a smaller beam tip. This results in a single device power generation of roughly $4\text{e-}4 \mu\text{W}$. Note that this is significantly less ($\sim 1/12^{\text{th}}$) than the maximum power that could be produced with an untapered device with a proof mass from this same input. The beam tip was not allowed to be larger than 120% of the beam root width because possible torsional modes were not considered (these modes become more likely as the beam tip gets wider).

The increase in foot print area was not penalized in looking at pure power output above, but as can be seen when looking at operating and static power density, when volume is considered, as in the operating power density contours shown in Figure 4.6, a taper ratio greater than one is no longer advantageous. It should be noted that the method in which device volume, both operating and static, is defined penalizes the empty space on either side of a tapered beam by using a rectangular volume whose width is equal to the greater of the two beam widths (root or tip). This method was chosen for consistency with the untapered geometry performance metrics and because only a single device is considered in each study. With creative microfabrication and packaging, it would be possible to arrange tapered devices such that this “dead space” is utilized, thereby reducing the volume penalty associated with a taper that is seen here. This is left for future work.

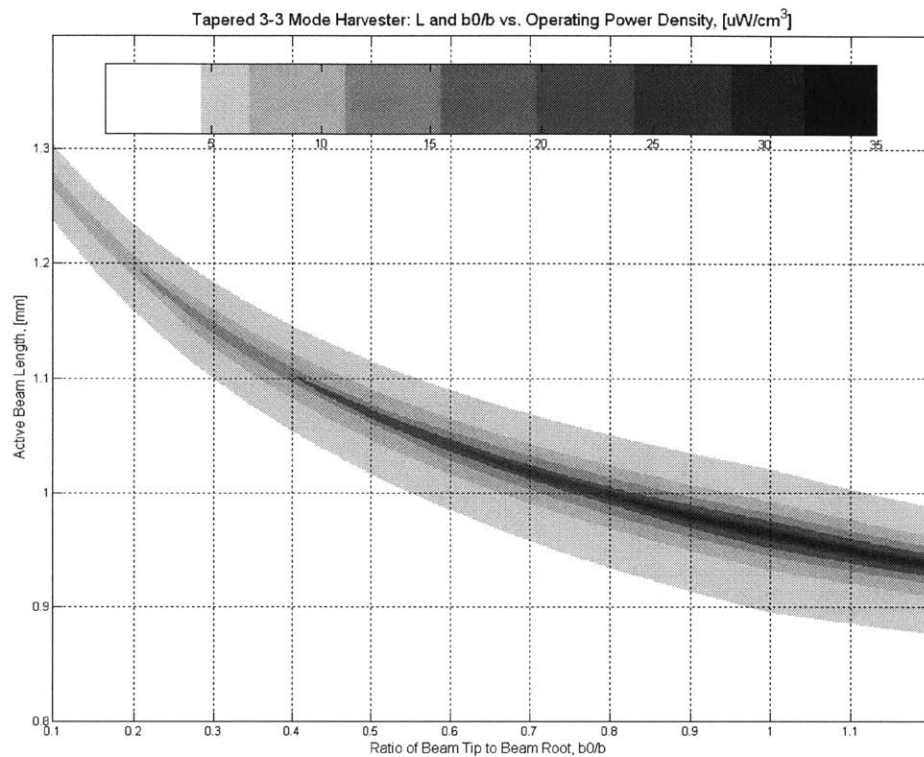


Figure 4.6: Operating Power Density Contours for a Tapered {3-3} Mode Unimorph Device, no Proof Mass

When looking at the close-up of the operating power density in Figure 4.7, the single peak is again observed (as in the untapered {3-1} and {3-3} cases in Chapter 3) due to the compromise of tip displacement and power production that is best achieved when operating between the resonant and anti-resonant frequencies. Recall that while a greater strain, and therefore power production, accompanies a greater tip displacement, the operating volume height is defined as twice the maximum tip displacement of the beam. The design optimized for this objective function balances these two trends by operating between maximum power production peaks.

Traces of operating power as a function of length and taper ratio over the design space are shown in Figure 4.8. From these plots, it is clear that when designing for operating power density, it is no longer advantageous to increase the beam tip width past the beam root width. In fact, viewing the results shown above, an un-tapered beam with a length of about ~ 0.96 mm is the best design in this space for the input considered. This design yields an operating power density of ~ 35 $\mu\text{W}/\text{cm}^3$. Again, this value is much lower ($\sim 1/15^{\text{th}}$) than that which can be achieved with an untapered device with a proof mass.

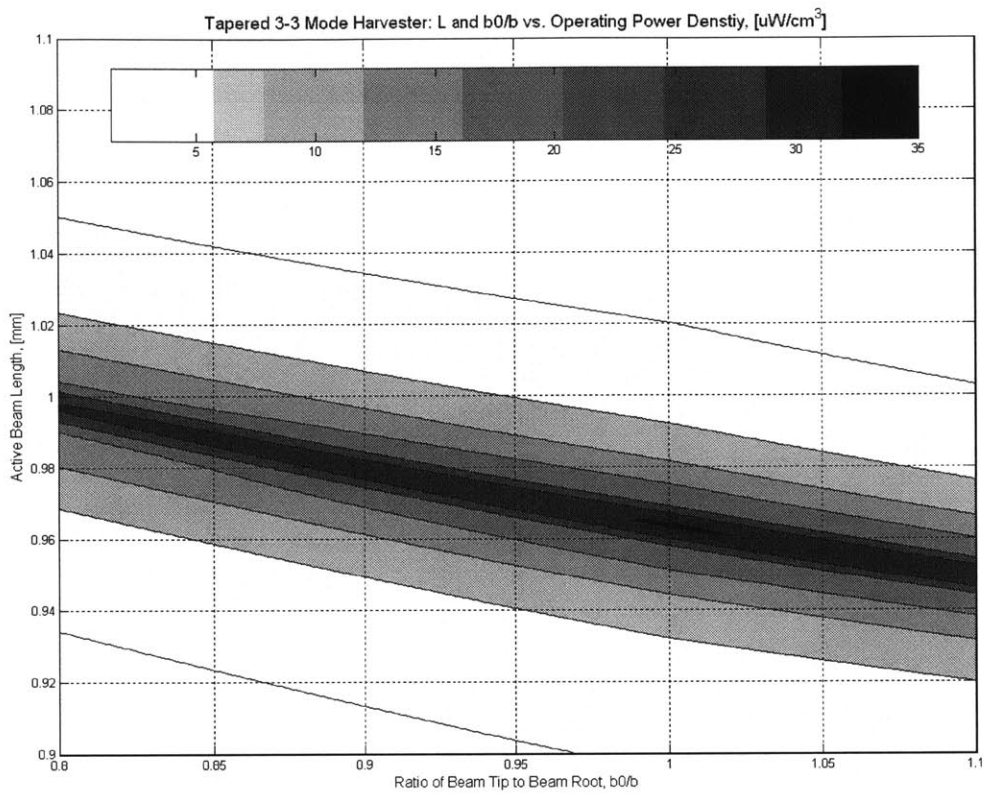


Figure 4.7: Close-Up of Operating Power Density for a Tapered {3-3} Mode Unimorph Device, no Proof Mass

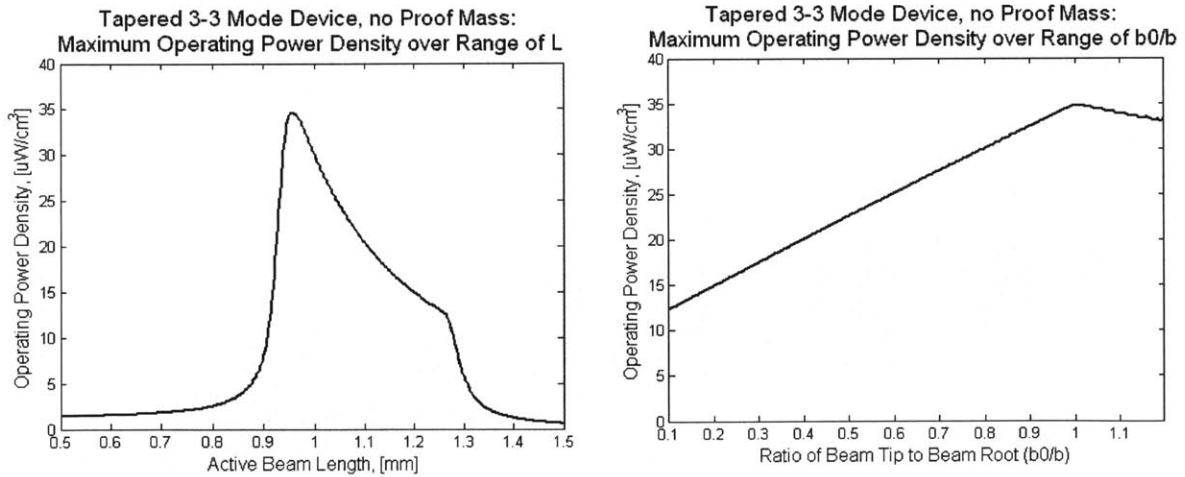


Figure 4.8: Maximum Operating Power Density for a Tapered {3-3} Mode Unimorph Device Shown Against Length and Raper Ratio Across the Design Space

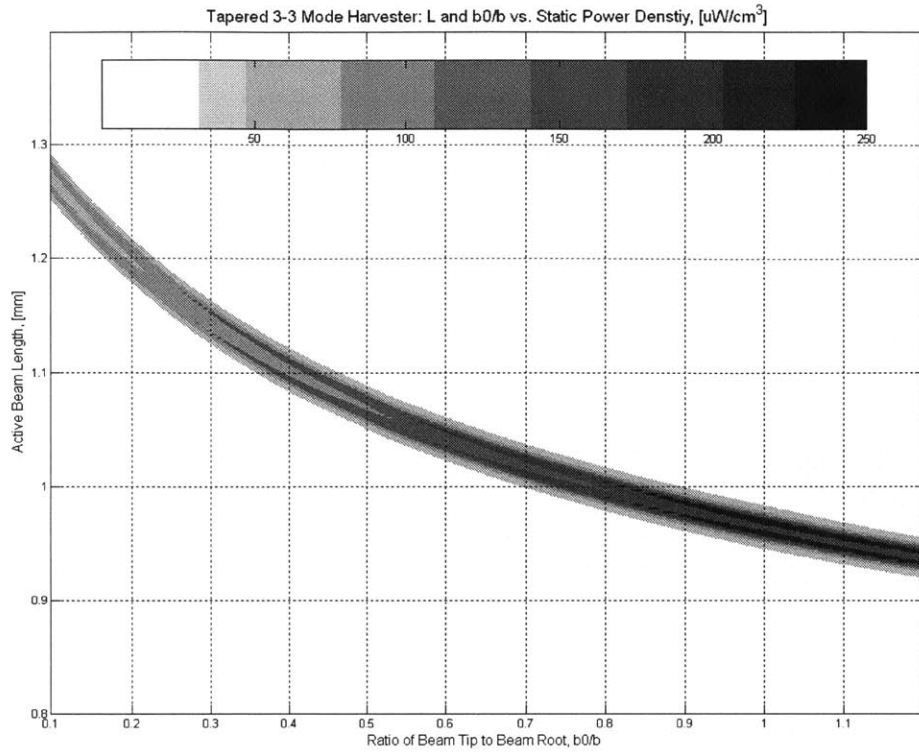


Figure 4.9: Static Power Density Contours for a Tapered {3-3} Mode Unimorph Device, no Proof Mass

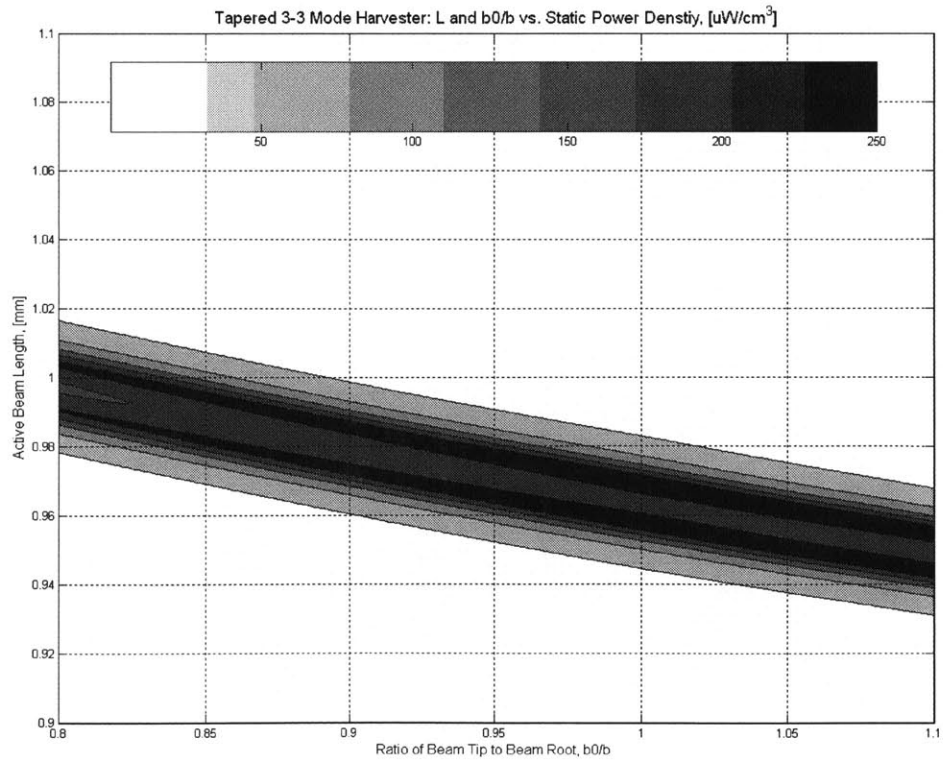


Figure 4.10: Close-Up of Static Power Density Contours for a Tapered {3-3} Mode Unimorph Device, no Proof Mass

As before, static power density contours are shown in Figures 4.9 and 4.10 as this metric is popular in the literature. Recall that operating power density takes into account the entire box of space that is required to give the beam tip full motion when excited, while static power density only includes the volume of the stationary device itself.

As with the un-tapered devices, now that tip deflection does not penalize the metric of interest, both resonant and anti-resonant peaks are clearly visible in Figure 4.11.

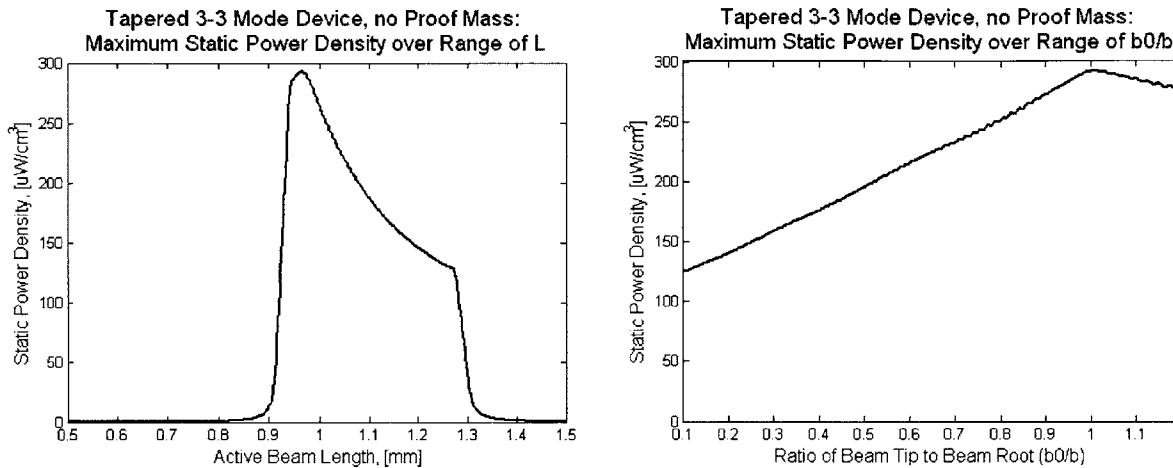


Figure 4.11: Maximum Static Power Density for a Tapered {3-3} Mode Unimorph Device Shown Against Length and Taper Ratio Across the Design Space

From the plots in Figure 4.11, it is clear that once again a uniform device is preferred for static power density design. Similar to the results for operating power density, this is due to the rectangular definition of static volume. The optimal length for a static power density device operating at anti-resonance (0.975 mm) is just longer than that for an operating power density device (0.95 mm). The maximum static power density predicted for the tapered device is 299 $\mu\text{W}/\text{cm}^3$. It is worth noting that while in the un-tapered case the design for power output and static power density were basically the same, in the tapered case, the design for static power density is longer than that for pure power output and the taper ratios of the two cases are different. This is due to the fact that the static power density of a tapered device is penalized due to its inactive volume such that a larger active area results in higher device power generation. The untapered device must be longer than the tapered device in order to maintain an anti-resonant frequency aligned with the input frequency, $\omega = 1$ kHz.

The last of the four metrics that are being investigated here is specific power, or device power output over total device mass. The carpet plot for specific power over the design space is shown in Figure 4.12 with a close-up view shown in Figure 4.13. This metric is interesting in terms of a tapered device, because unlike with volume, which assumes a rectangular space around the device, the device weight with the taper itself. This characteristic turns out to be more significant in the next section where a proof mass is added to the end of a tapered device.

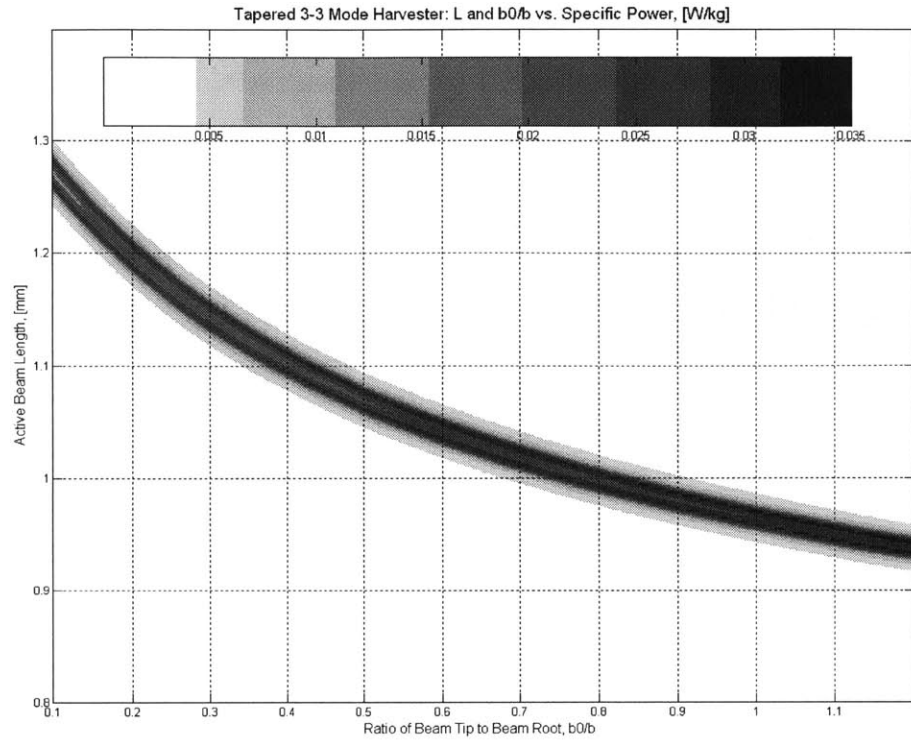


Figure 4.12: Specific Power Contours for a Tapered {3-3} Mode Unimorph Device, no Proof Mass

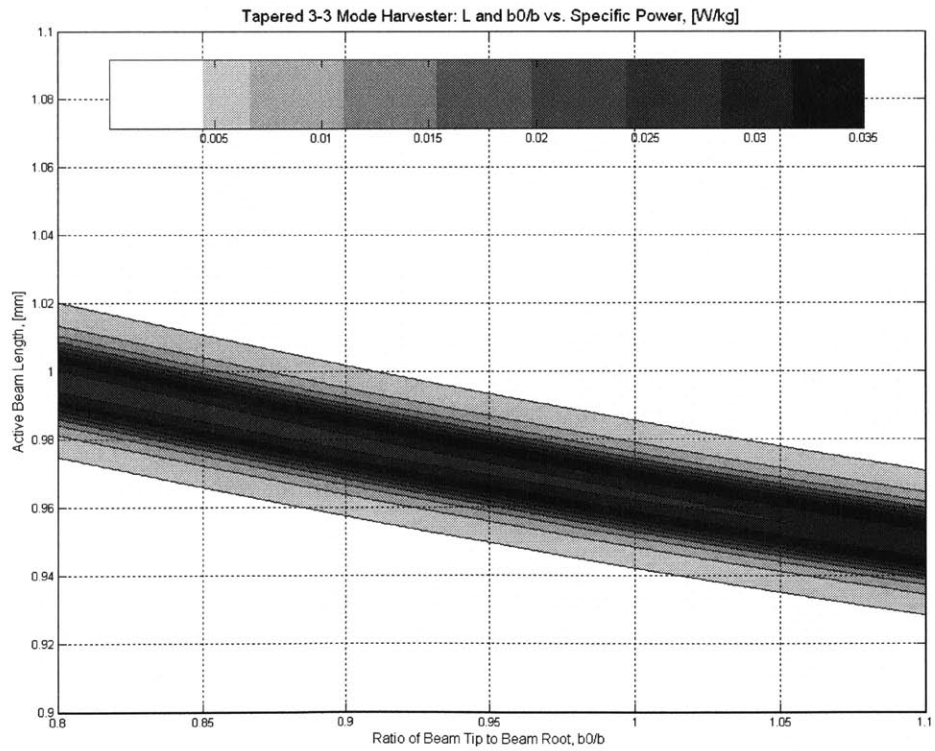


Figure 4.13: Close-Up of Specific Power Contours for a Tapered {3-3} Mode Unimorph Device, no Proof Mass

As with power and static power density, the two operating peaks resulting from tuning the load resistance for power generation are clearly visible when the specific power contour is seen in more detail in Figure 4.13.

Maximum specific power as a function of beam length and taper ratio across the design space is shown in Figure 4.14.

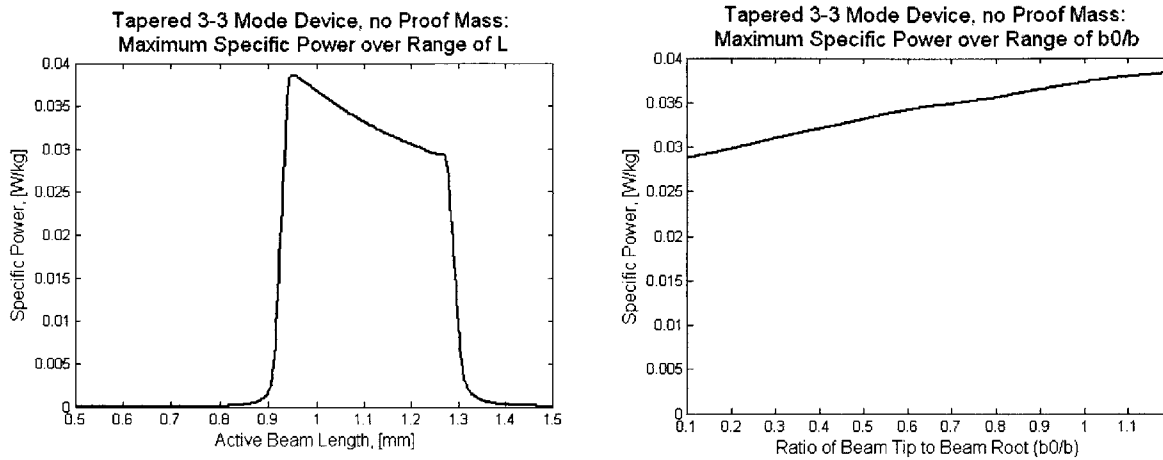


Figure 4.14: Maximum Specific Power for a Tapered {3-3} Mode Unimorph Device Shown Against Length and Raper Ratio Across the Design Space

The curve for specific power as a function of taper ratio is not as strictly linear as those for the other power metrics as this metric is more sensitive to the specific beam geometry in terms of variation in both beam length and taper ratio. Still, the design for maximum specific power closely resembles that for maximum device power output in that the beam tip is 120% the width of the beam root, and the length is 0.93mm. This design gives a predicted specific power of 0.039 W/kg, which is again about an order of magnitude less than the maximum specific power obtained for an untapered device with a proof mass.

4.2 Tapered {3-3} Mode Beam with a Proof Mass

In Section 4.1, a {3-3} Mode device without a proof mass was used to look at just the effect of tapering the beam. Here, a proof mass is added to the end of the beam. The layer structure of the beam is the same as that for all of the {3-3} Mode cases thus far and the input excitation is still considered to be 1 kHz at just under 4m/s^2 . To mitigate the possibility of torsional mode excitation, the proof mass is considered to be the same width as the active beam tip, b_0 .

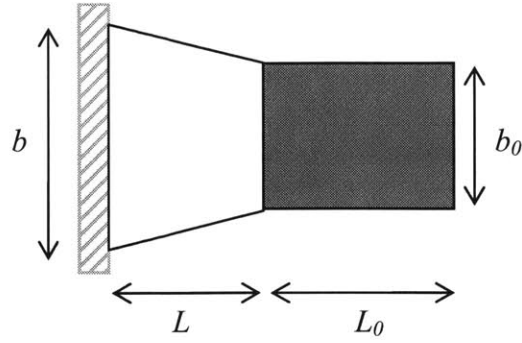


Figure 4.15: Tapered Beam Geometry with Proof Mass

As in the taper analysis without a proof mass done in the previous section, a Rayleigh-Ritz procedure was performed to find an approximate first mode of the tapered structure. The analytical solution for mode shapes that was used in Chapter 3 was reapplied, with the first three instances of the determinant equaling zero being identified and used as the first three modes. The terms in the mass, \mathbf{M} , and stiffness, matrices for the Rayleigh-Ritz procedure are thus determined from the following:

$$M_{ij} = \int_{V_s} \psi_{ri}(x) \psi_{rj} \rho_s dV_s + \int_{V_p} \psi_{ri}(x) \psi_{rj} \rho_p dV_p + m_0 + s_0 + j_0 \quad \text{Eq 4-4}$$

Where the intermediate terms, $m_0 = M_0(\psi_{ri}(L)\psi_{rj}(L))$, represents the inertia of the proof mass, $s_0 = S_0(\psi_{ri}(L))\psi'_{rj}(L) + S_0(\psi_{rj}(L))\psi'_{ri}(L)$, the static moment of the proof mass, and $j_0 = J_0(\psi'_{ri}(L)\psi'_{rj}(L))$, the moment of inertia of the proof mass, and the modes ψ_{ri} are now those from the untapered proof mass analysis of Chapter 3. The stiffness coefficients K_{ij} are again given by Eq 4-3 with these new modes ψ_{ri} .

These modes and the resulting approximate first mode from the Rayleigh-Ritz (R-R) analysis are shown in Figure 4.16. For this chart, the taper ratio was held constant at $b_0/b = 0.5$, the active beam length, L , was set at 0.5mm and the proof mass length, L_0 was held constant at 0.3mm.

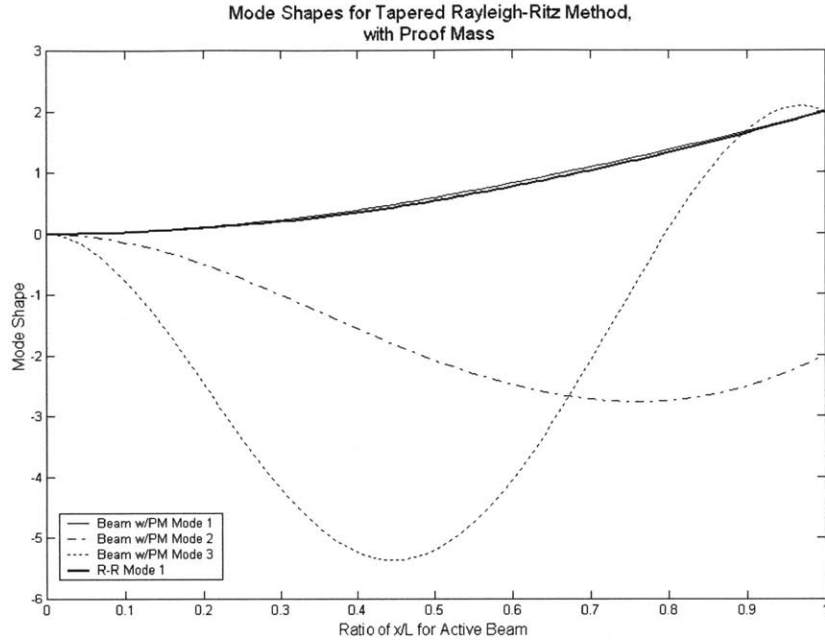


Figure 4.16: Mode Shapes for Rayleigh-Ritz Analysis of a Tapered Beam with a Proof Mass

As was the case with the devices with a taper but no proof mass, the resulting first mode shape is fairly similar to the first mode obtained for a beam with a proof mass without including the taper. The differences come into play when looking at the curvature of the mode shapes, which are shown in Figure 4.17 and Figure 4.18.

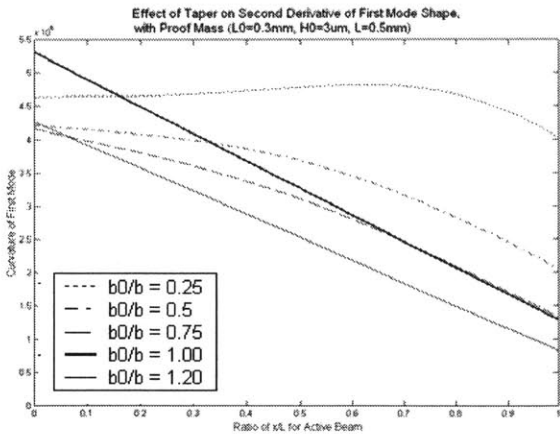


Figure 4.17: Curvature of R-R Mode Shape for Tapered Beam with Proof Mass, varying Taper

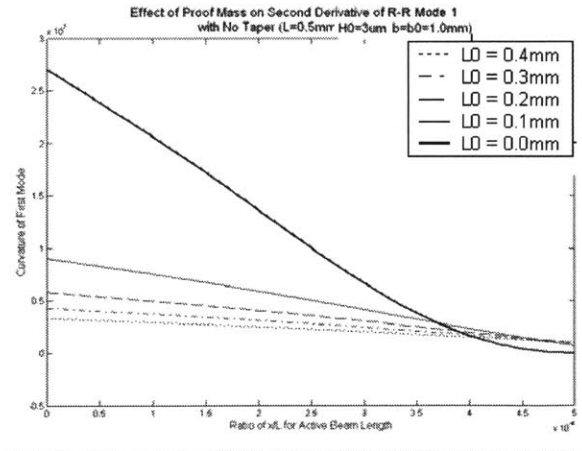


Figure 4.18: Curvature of R-R Mode Shape for Tapered Beam with Proof Mass, varying L_0

As expected, with a proof mass, the curvatures of the first mode shapes do not go to zero at the tip of the active beam length and the addition of a taper results in a more even curvature distribution along the active length of the beam than in the untapered case.

Moving on to the contour plot design tools for this type of device, b is the beam root width and is set at 1mm. The proof mass thickness is again set to $3\mu\text{m}$ and it is made of platinum as in Chapter 3 and its length is L_0 . For the design space investigation done in this section, the active beam length, L , is set at 0.3 mm, 0.5 mm, and 0.7 mm and both b_0/b and L_0 are varied from 0.10 to 1.20, and 0 to 0.5 mm, respectively. The carpet plots shown are for $L=0.5$ mm (unless otherwise noted) as this value represents the middle of the design space. All three values of L are shown on the traces of the maximum for a given metric against either L_0 or b_0/b . If desired for final device design, more values of L could be considered in this same fashion and a three-parameter optimization could be completed using these graphical techniques.

The presence of a proof mass means that an overall shorter active beam length can be employed and still match the anti-resonant frequency to the excitation that has been used throughout of 1 kHz at just under 4 m/s^2 . The layer structure of the beam and the electrodes are again the same as that used for the {3-3} Mode device (see Table 3.4).

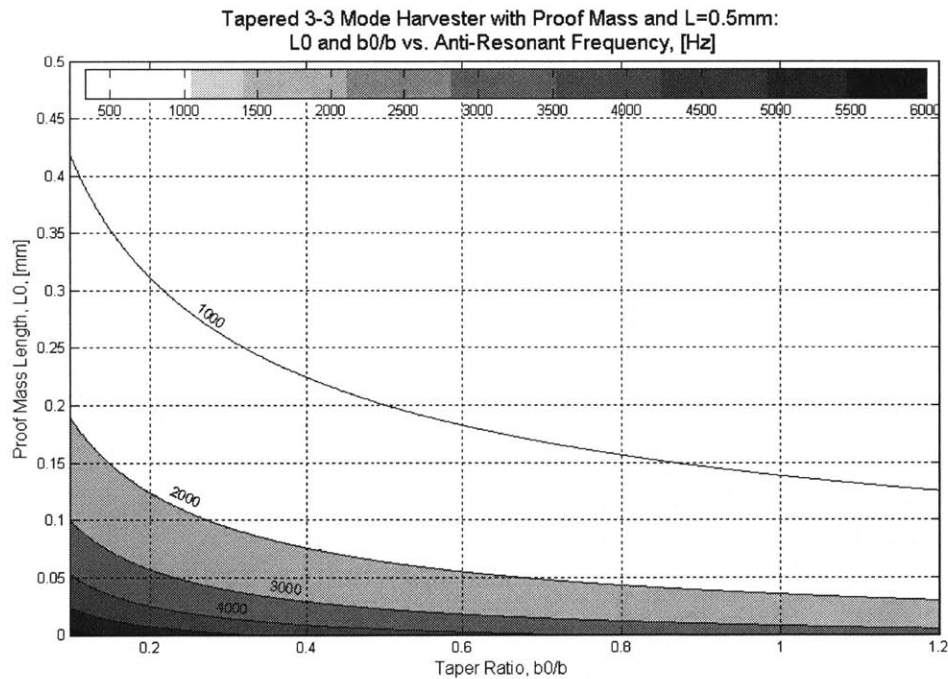


Figure 4.19: Anti-Resonant Frequency Contours for a Tapered {3-3} Unimorph Device with a Proof Mass and L=0.5mm

In Figure 4.19 and the rest of the contour plots in this section, the horizontal axis is the ratio of the beam tip to the beam root and the vertical axis is proof mass length. The numbers on the contours in the anti-resonant plot are the frequency of that contour in Hertz.

Following the same pattern of exploration as in the previous section, power output is the first objective function considered for optimization of a tapered device with a proof mass. The contour plot of device power output over the design space is shown in Figure 4.20 with a closer view of part of the contour in Figure 4.21.

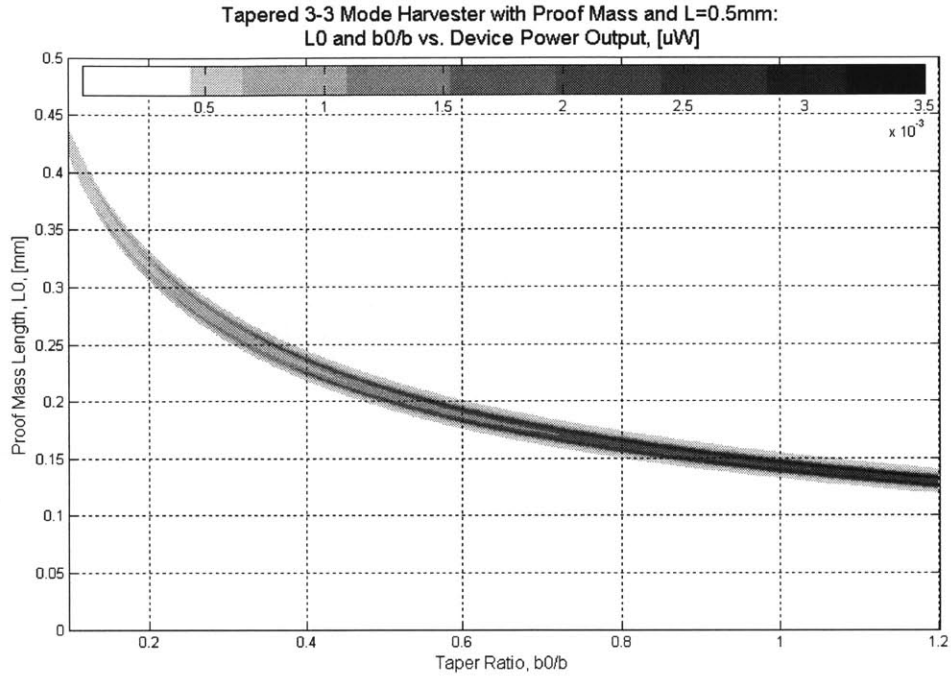


Figure 4.20: Device Power Output Contours for a Tapered {3-3} Mode Unimorph Device, with Proof Mass, $L=0.5\text{mm}$

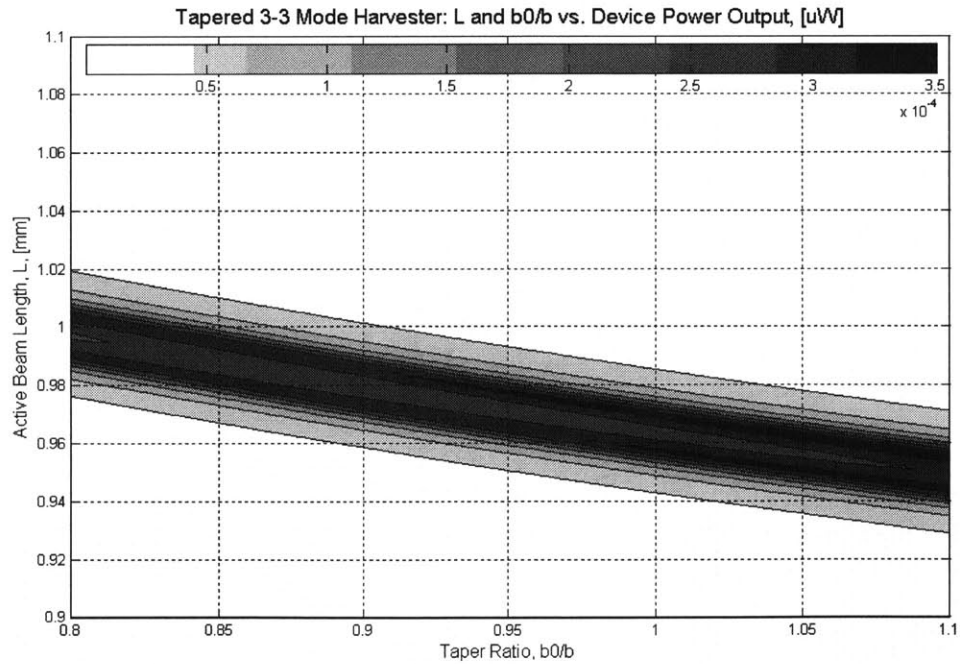


Figure 4.21: Close-Up of Device Power Output Contours for a Tapered {3-3} Mode Unimorph Device with Proof Mass

For comparison, the device power output contours for a device with $L=0.3\text{mm}$ are shown in Figure 4.22. Notice how the shorter beam length results in a larger proof mass in order to still match the input frequency.

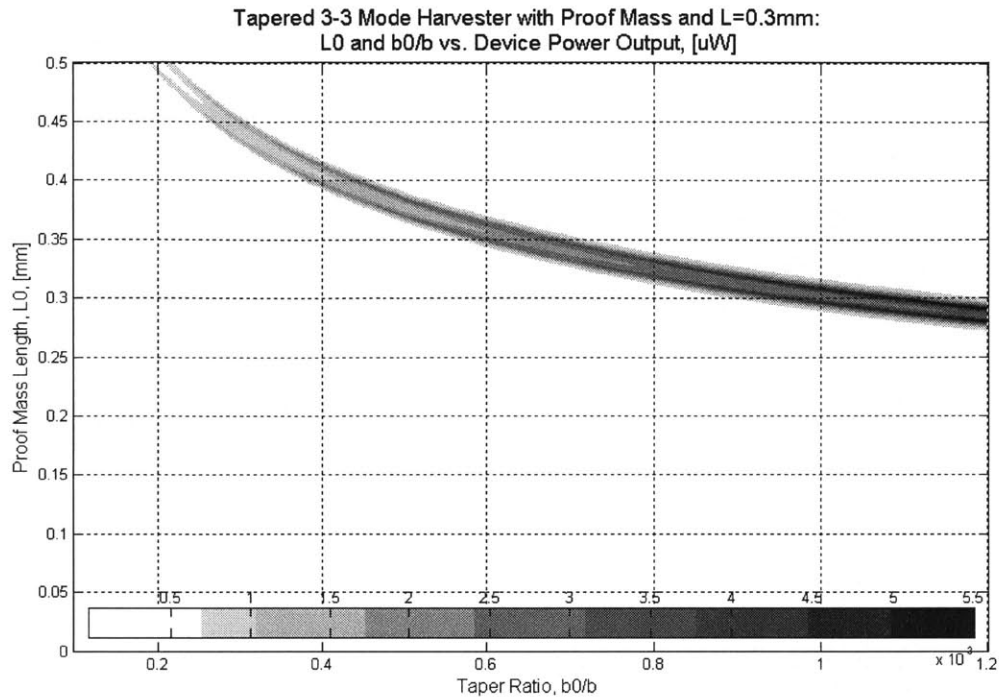


Figure 4.22: Device Power Output Contours for a Tapered {3-3} Mode Unimorph Device, with Proof Mass, $L=0.3\text{mm}$

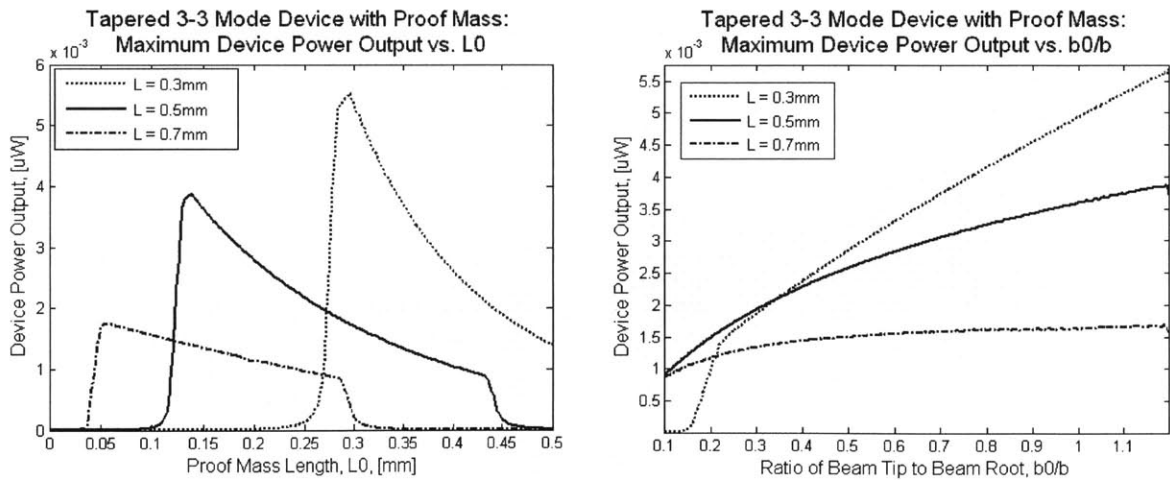


Figure 4.23: Maximum Device Power Output for a Tapered {3-3} Mode Unimorph Device Shown Against Proof Mass and Taper Ratio along Maximum Power Contour

Based on the plots in Figure 4.23, the best design in this space with this input for pure device power output has a length, L of 0.3mm , a proof mass with length, L_0 , of $\sim 0.3\text{mm}$ and a taper ratio of ~ 1.2 . (Recall that the active beam root width is 1.0mm and the proof mass height is $3.0\mu\text{m}$.) This results in a predicted single device power output of $0.0058\mu\text{W}$, ten times that of the best predicted for a taper alone. Given the limited number of active beam lengths considered,

additional optimization would need to be done on all three geometric parameters before a direct comparison to the optimized performance metrics obtained in Section 3.4.2 is meaningful.

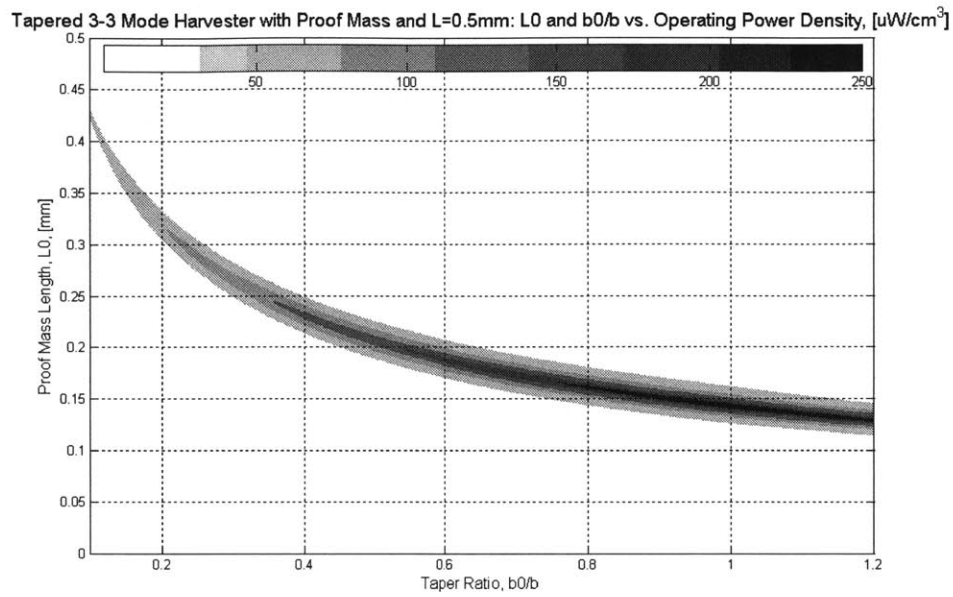


Figure 4.24: Operating Power Density Contours for a Tapered {3-3} Mode Unimorph Device, with a Proof Mass, $L = 0.5\text{mm}$

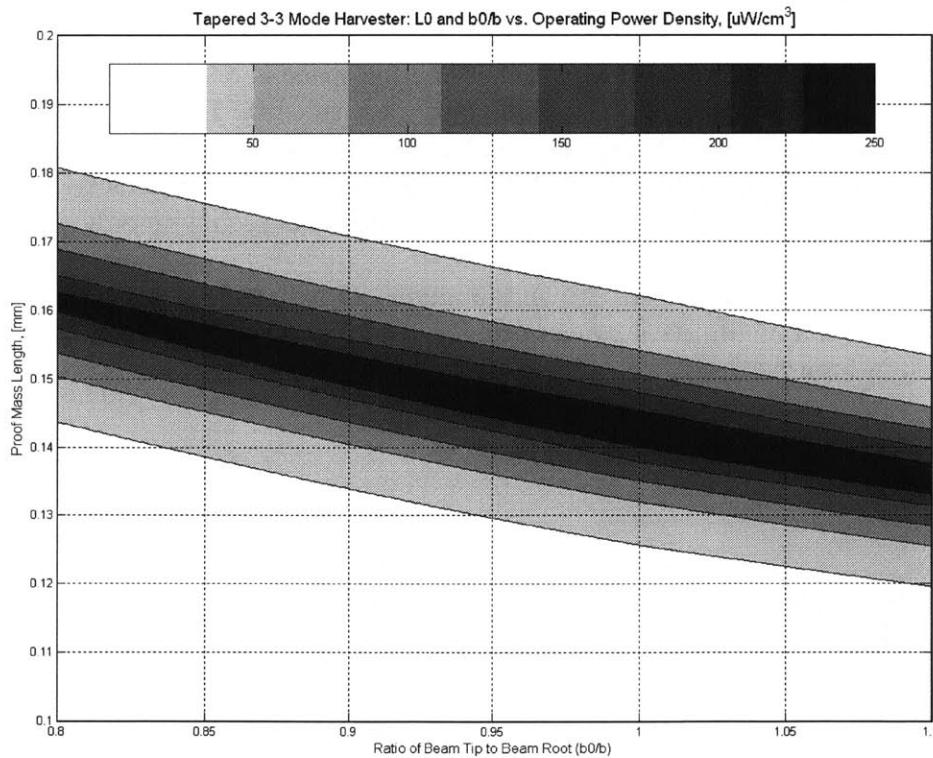


Figure 4.25: Close-Up of Device Power Output Contours for a Tapered {3-3} Mode Unimorph Device, with Proof Mass, $L=0.5\text{mm}$

Carpet plots for operating power density are shown in Figure 4.24 and Figure 4.25. Again, due to the compromise between the volume penalty associated with a large tip displacement and the additional power that can be generated at the two power output peaks, the optimum power density contours reveal only one peak which falls between the two seen when considering the other objective functions.

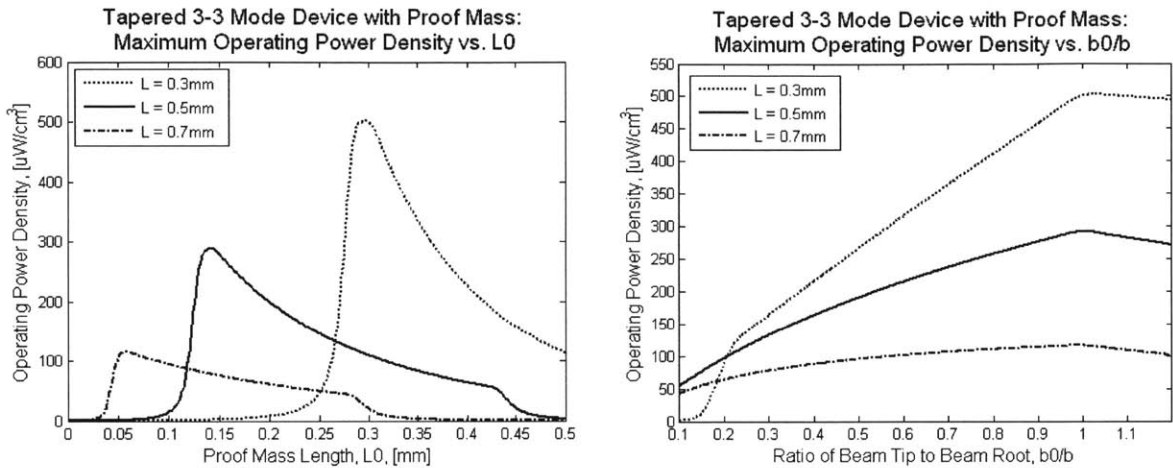


Figure 4.26: Maximum Operating Power Density for a Tapered {3-3} Mode Unimorph Device Shown Against Proof Mass and Taper Ratio along Maximum Power Contour

The optimum device for operating power density in this space is one with an active length, $L = 0.3$ mm , a proof mass of length ~ 0.3 mm and a taper ratio of ~ 1.0 . The tendency for metrics that are based on volume to select towards uniform beams was also seen in the case without a proof mass presented earlier in this Chapter. The predicted operating power density for this device is $503.9 \mu\text{W}/\text{cm}^3$. This is again an order of magnitude greater that seen with only a taper.

The static power density contours are shown in Figure 4.27 with a close-up view of the structure in Figure 4.28. The maximum static power density as a function of proof mass length and taper ratio are shown in Figure 4.29.

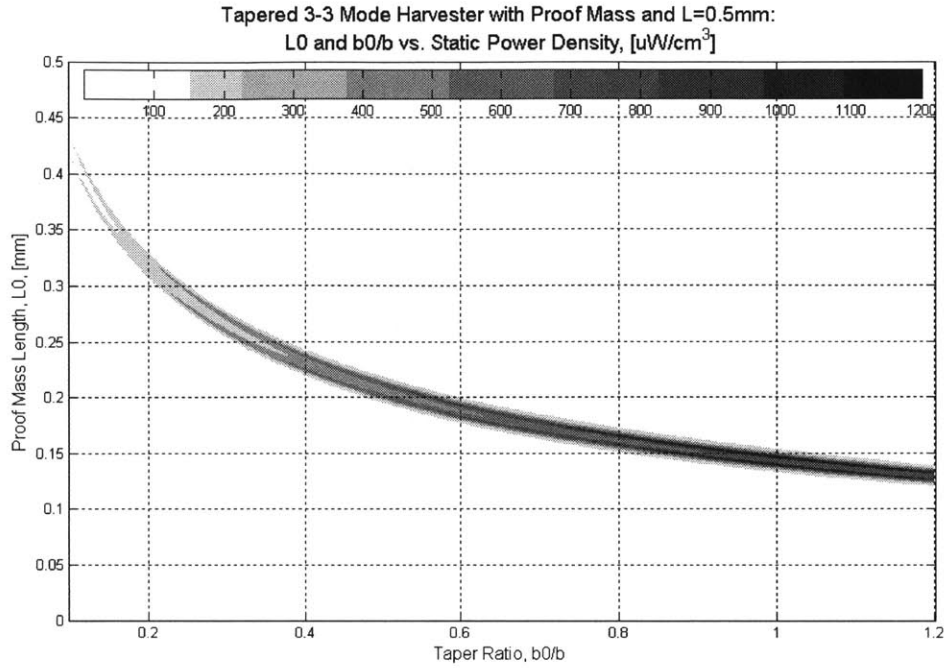


Figure 4.27: Static Power Density Contours for a Tapered {3-3} Mode Unimorph Device, with a Proof Mass, L = 0.5mm

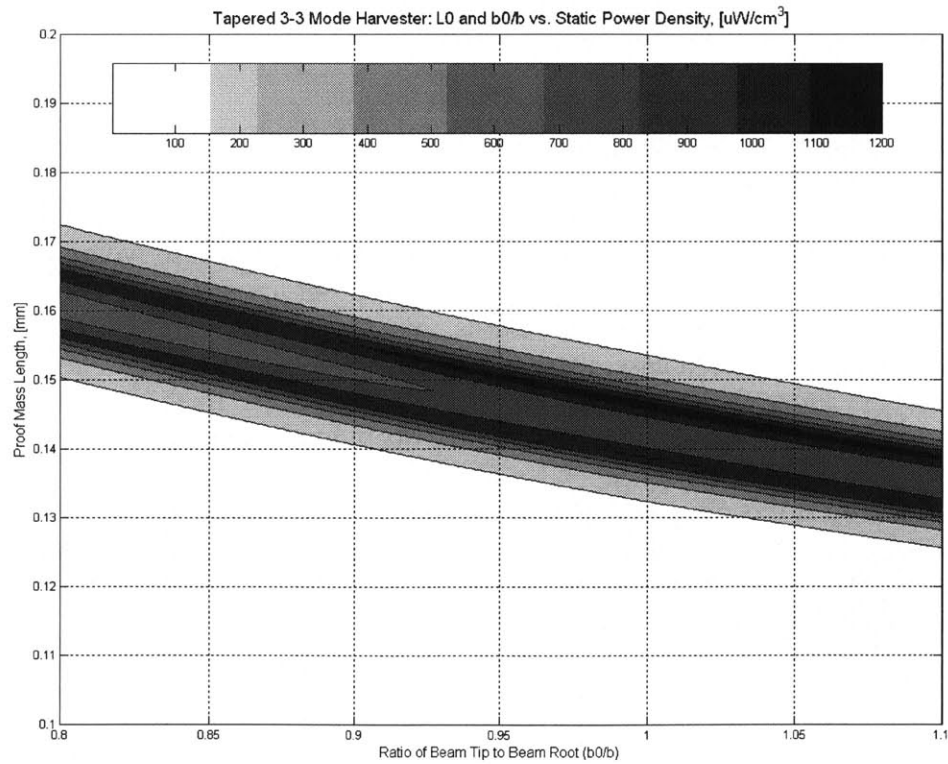


Figure 4.28: Close-Up of Static Power Density Contours for a Tapered {3-3} Mode Unimorph Device with a Proof Mass, L=0.5mm

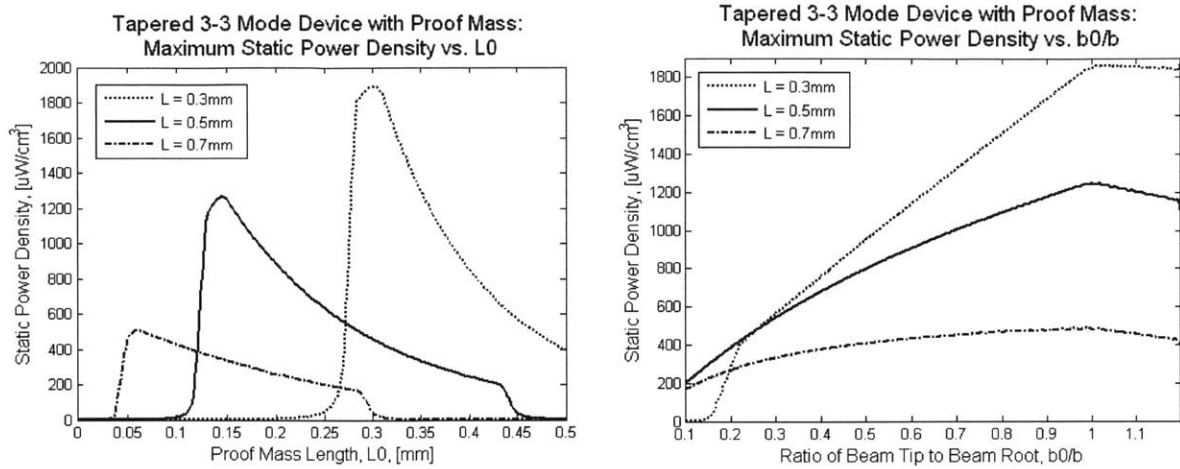


Figure 4.29: Maximum Static Power Density for a Tapered {3-3} Mode Unimorph Device Shown Against Proof Mass and Taper Ratio along Maximum Power Contour

The optimum device designed for static power density in this space is one with an active beam length of 0.3 mm, a proof mass length of ~ 0.3 mm and a beam tip to root ratio of ~ 1.0 , again indicating that when power per unit volume is an important metric, a uniform device is preferable. The predicted static power density for this device is $1897\mu\text{W}/\text{cm}^3$ which is again an order of magnitude greater than the maximum static power density predicted for a device with only a taper.

The last objective function that was considered was specific power for a tapered device with a proof mass. As was mentioned in the previous section, specific power much more closely reflects the presence of a taper as it is based on the mass of the device not on the rectangular volume it occupies. This distinction is particularly important in the case where a proof mass is present on the end of a tapered device. The width of the proof mass is set to the width of the tip of the active beam length, b_0 , and as such there is a direct weight savings to be had by tapering this device. As in the untapered case, there is also an advantage to having a small proof mass. However, since the input frequency and active beam length are fixed, the proof mass must remain large enough to tune the device to the desired operating frequency.

The results of looking at this objective function across the design space are shown in Figure 4.30, with a close-up of the contour structure in Figure 4.31. Maximum specific power as a function of proof mass length and taper ratio across the design space are shown in Figure 4.32 and is used to identify the best design for specific power, within the three choices of $L = 0.3, 0.5$ and 0.7 mm.

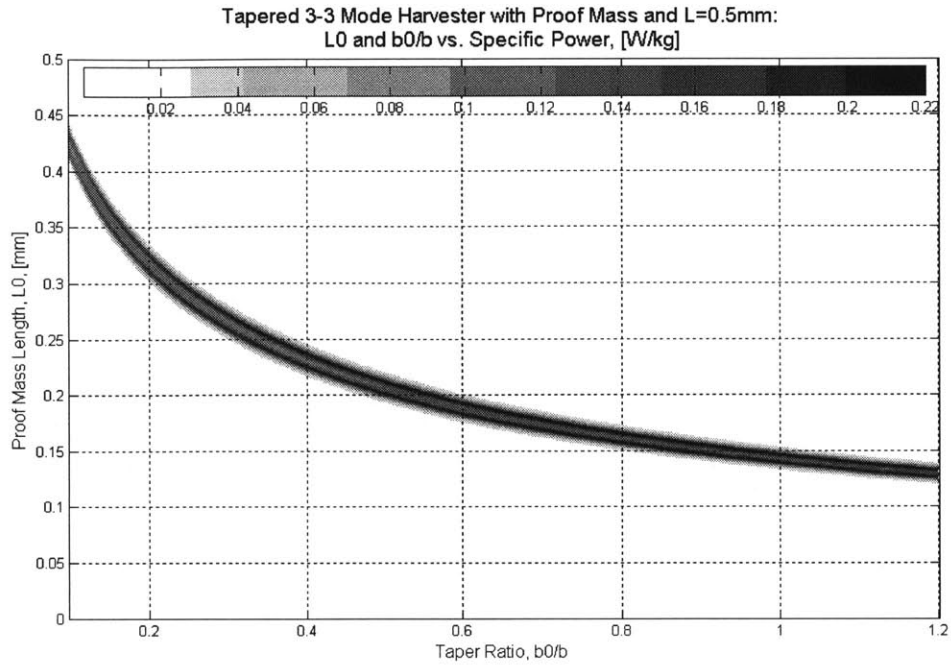


Figure 4.30: Specific Power Contours for a Tapered {3-3} Mode Unimorph Device, with a Proof Mass, $L = 0.5\text{mm}$

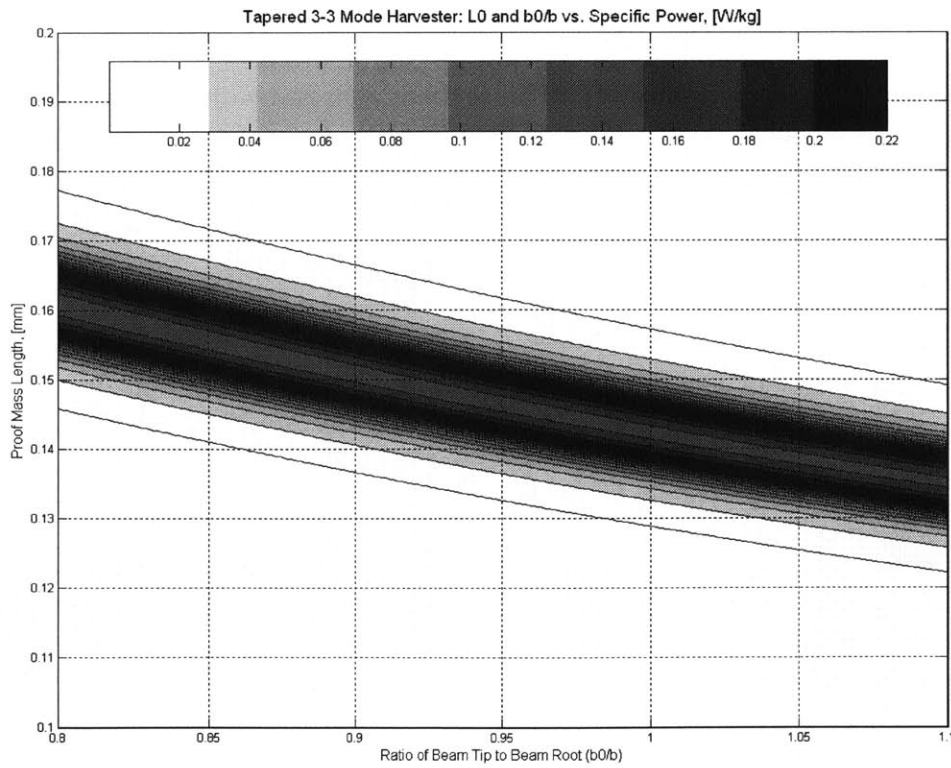


Figure 4.31: Close-Up of Specific Power Contours for a Tapered {3-3} Mode Unimorph Device, with Proof Mass, $L = 0.5\text{mm}$

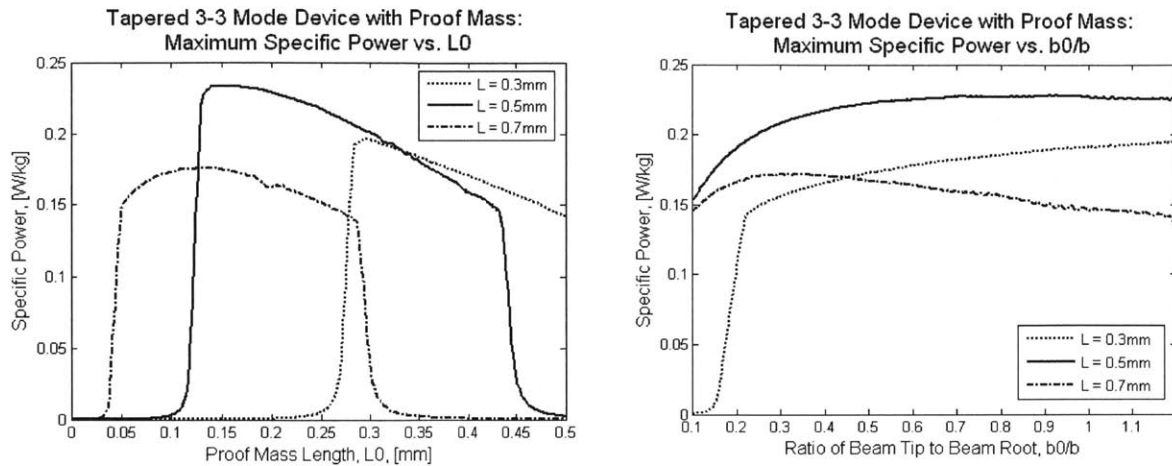


Figure 4.32: Maximum Specific Power for a Tapered {3-3} Mode Unimorph Device Shown Against Proof Mass and Taper Ratio along Maximum Power Contour

From the charts shown in Figure 4.32, a device designed for specific power with a taper and a proof mass in this space would have a length, $L = 0.5$ mm, proof mass length of ~ 0.15 mm, and a taper ratio of ~ 0.8 . (A proof mass on the end of a beam with a taper ratio greater than 1 would be particularly susceptible to torsional excitation and should likely be avoided.) The predicted specific power for this device is 0.23 W/kg, again an order of magnitude greater than that obtainable with a taper alone. It is interesting to note that out of all the objective functions considered for a device that was allowed to taper (both with and without a proof mass) this was the only instance in which a taper ratio less than one was favored. This is due to larger taper ratios reducing the proof mass and thereby lowering its weight penalty.

4.3 Tapered Beam Optimization Results and Conclusions

In this chapter the effect of tapering the harvester, both with and without a proof mass, was investigated. To account for the tapered geometry of the beam, a Rayleigh-Ritz method was employed to find an approximation for the first mode of the structure both with and without a proof mass. Harvester design results of this design study are summarized in Table 4.2.

For a device without a proof mass, a tip width greater than the beam root width was favored due to the increase in active piezoelectric material that it offered for metrics in which volume was not a factor. For both operating and static power density, in which volume is in the denominator of the metric, a uniform beam was preferred. Similar trends emerged for a device with both a taper and a proof mass with the one exception that for specific power, in which device mass is in the denominator, a slight taper is weakly preferred. This allows for a smaller proof mass, which is by far the greatest source of the device mass.

When defining the rectangular operating and static volumes for a single device, as was done in this study, there is no benefit to tapering the beam in terms of operating or static power density. The benefit seen in absolute device power output is one due to the increased active piezoelectric area and is not better than simply increasing entire beam's width if more power is needed. (Caution must be used here as the assumption of a beam geometry breaks down as the device is widened and torsional modes could be introduced if the taper ratio is increased too much.

As a zeroth-order failure assessment of the designs presented in Table 4.2, the maximum strain produced the piezoelectric layer for each of the design spaces considered was calculated. In the design space of a tapered device without a proof mass, the maximum was 18 μ strain. The maximum strain for a tapered device with a proof mass was 83 μ strain. As in the untapered cases in Chapter 3, these values are well below the conservative design maximum of 500 μ strain.

In general, it is recommended that uniform devices with proof masses be pursued in future work due to their simplicity and advantages in terms of power densities. However, for extremely weight-sensitive devices, a designer may elect to go with a slight taper and resulting smaller proof mass as shown in the preceding summary table.

A detailed summary of the performance of the four optimized {3-3} Mode tapered devices with proof masses is given in Table 4.3. When referencing this table, keep in mind that L was fixed to either 0.3mm, 0.5mm or 0.7mm.

Table 4.2: Tapered Harvesting Device Optimization[†] Summary

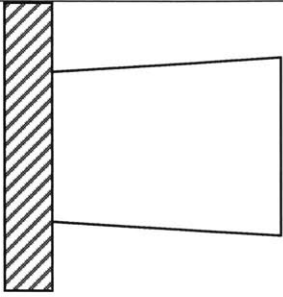
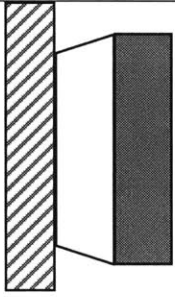
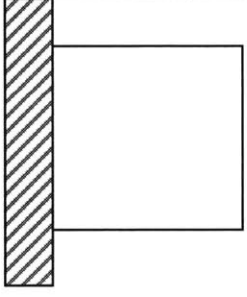
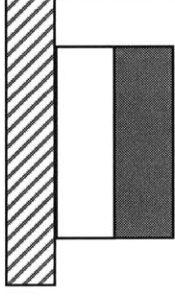
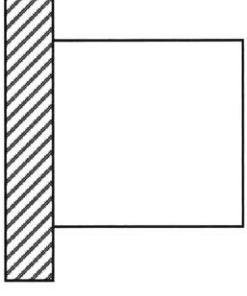
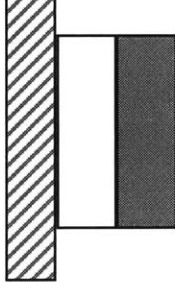
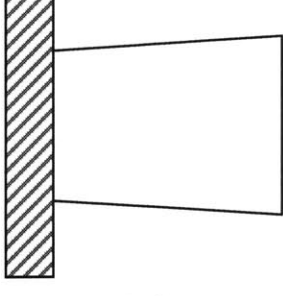
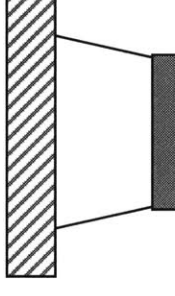
	{3-3} Mode Unimorph Without Proof Mass	{3-3} Mode Unimorph With Proof Mass
Device Power	 <p>$L = 0.93; b_0/b = 1.2$ $P = 4.04e-4 \mu\text{W}$</p>	 <p>$L = 0.3; L_0 = 0.29; b_0/b = 1.2$ $P = 5.80e-3 \mu\text{W}$</p>
Operating Power Density	 <p>$L = 0.96; b_0/b = 1.0$ $P_{op} = 35.28 \mu\text{W}/\text{cm}^3$</p>	 <p>$L = 0.3; L_0 = 0.30; b_0/b = 1.0$ $P_{op} = 503.9 \mu\text{W}/\text{cm}^3$</p>
Static Power Density	 <p>$L = 0.975; b_0/b = 1.0$ $P_{st} = 298.7 \mu\text{W}/\text{cm}^3$</p>	 <p>$L = 0.3; L_0 = 0.30; b_0/b = 1.0$ $P_{st} = 1897.0 \mu\text{W}/\text{cm}^3$</p>
Specific Power	 <p>$L = 0.93; b_0/b = 1.2$ $P_{sp} = 0.0392 \text{ W}/\text{kg}$</p>	 <p>$L = 0.5; L_0 = 0.15; b_0/b = 0.8$ $P_{sp} = 0.2334 \text{ W}/\text{kg}$</p>
<p><i>*All figures approximately to scale of 1'' = 1mm; [†]See Table 4.3.</i></p>		

Table 4.3: Performance Metrics for {3-3} Mode Tapered Unimorph Optimized[†] Devices

	Optimized for Maximum P_{out}	Optimized for Maximum P_{op}	Optimized for Maximum P_{st}	Optimized for Maximum P_{sp}
L [mm]	0.3	0.3	0.3	0.5
L_0 [mm]	0.290	0.301	0.307	0.157
b_0/b	1.2	1.0	1.0	0.878
P_{out} [μ W]	0.0058	0.0031	0.0051	0.0035
P_{op} [μ W/cm ³]	381.6	503.9	385.8	204.2
P_{st} [μ W/cm ³]	1870.6	1177.5	1897.0	1192.5
P_{sp} [W/kg]	0.1975	0.1214	0.1942	0.2334
Voltage [V]	0.8805	0.2518	0.8894	0.5697
w_{tip} [μ m]	5.0405	1.9150	4.8708	9.1749
PZT strain, [μ ϵ]	82.52	29.68	75.35	55.28
ω_r [Hz]	962.9	979.5	961.3	969.35
ω_{ar} [Hz]	1001.2	1019.6	1000.7	1000.6
Ω_{OC}	1.0398	1.0409	1.0409	1.0376

[†]Partial optimization in the case of the tapered beam with a proof mass as only three discrete values of L (active beam length) were considered.

5 Conclusions and Recommendations

The body of work presented in this thesis represents a positive step towards the realization of self sustaining MEMS structural health monitoring sensors for aircraft and other environments where wireless, extended-life devices are desirable. By looking at the design options, and defining performance metrics that are currently of the most interest to the energy harvesting community, placing them in the context of an aircraft vibration spectrum, and developing tools for their further investigation, the foundation has been laid for designing high-performance vibration energy harvesting devices. A summary of the key points and main conclusions from this work follows, along with the author's thoughts on the directions that future work on this topic should take.

5.1 Conclusions and Contributions

Key outcomes of this work can be summarized as follows:

1. The vibration environment of an aircraft that could be expected to be present in one of the main areas of interest for structural health monitoring – and therefore for vibration energy harvesting – was explored. Using MIL STD 810F, an expected excitation that would be received by a device on the empennage of a fighter aircraft was determined to be between 300 and 1000 Hz, with an operating point selected of 3.8991 m/s^2 at 1000 Hz. (The higher frequency was chosen as MEMS devices are more conducive to high frequency design.) The acceleration calculated for this PSD is from aerodynamic excitation only, and is thus conservative as it neglects engine contributions.
2. The literature was surveyed and a set of useful performance metrics – and the device data required to determine them – were compiled. These metrics include power output (μW), operating and static power densities ($\mu\text{W}/\text{cm}^3$), specific power (W/kg), voltage (V) and efficiency ($P_{\text{out}}/P_{\text{in}}$). The metric of most importance will depend on the application at hand. For instance, a highly space-constrained device, such as those embedded in, or mounted on, the skin of an aircraft, might be most sensitive to operating power density and insensitive to total device mass, or specific power. To facilitate comparison and coordination between the various efforts that are ongoing in the field of energy harvesting, research should include not only power output, but device mass, tip displacement, and all of the geometrical parameters (*i.e.* thicknesses and widths) with any report on a device under development. It is also critical that the input vibration – both frequency and acceleration or displacement – be included so that a conversion efficiency can be determined for the device.
3. The theoretical maximum energy conversion efficiency of a piezoelectric cantilevered beam harvester was examined and determined to approach 50%. Half of the energy input into the device from the vibrational excitation is lost due to the various sources of damping within the structure, while half can potentially be harvested electrically as useful

power if the load resistance is properly tuned (at power optimum), at either of the device resonances.

4. The author's investigation of the other energy harvesting work included a detailed review of Roundy *et al.* as published in what is currently the only book on this topic [1]. This review presented in this thesis highlights the importance of allowing for variation in the load resistance with frequency and utilization of both the resonant and anti-resonant frequencies that are characteristic of a piezoelectric device to design for optimal device performance.
5. In an effort to identify all that would be required for the realization of a MEMS structural health monitoring system, power electronics were briefly discussed. This is an area that is receiving attention externally to this particular project, but would do well to be incorporated more integrally with the device design efforts.
6. Previous initial modeling work by du Toit [3 and 5] was built into a design tool that was compared to existing experimental data for verification [3 and 4]. This tool was then used to map a device space bounded by current MEMS fabrication experience and expertise. The vibration input expected from an aircraft empennage (1000Hz at 3.98 m/s^2) was used as the vibration input. Within this space, four different device geometries were explored: Two un-tapered devices with proof masses – one operating in the {3-3} Mode with interdigitated electrodes, and one in the {3-1} Mode, as well as two tapered {3-3} Mode devices, one with a proof mass and one without. For these geometries, beam length, proof mass length and taper ratio (where applicable) were varied over a MEMS design space constrained by fabrication considerations. Other structural parameters, such as layer and proof mass thicknesses, were not varied for two reasons: preliminary investigations showed that the best power production was consistently achievable with the maximum achievable thickness of the PZT layer and proof mass; and a MEMS device with the structural layers used has been manufactured and tested previously [11]. The electrode spacing used for {3-3} Mode device design was also fixed by the resolution obtainable with current MEMS fabrication (mask resolution) constraints and preliminary single parameter investigation into optimal power and voltage production.
7. Four objective functions were defined and investigated across a MEMS-relevant design space for the four geometries considered. The four metrics are power production, operating power density, static power density and specific power. By viewing these metrics graphically across the design space, different optimal device geometries emerged. These tools represent the heart of the contribution of this work: they can be quickly adapted by future device designers to capture the configuration that is most appropriate for their particular application. This effort also illustrated that the metric of interest has a strong effect on the ideal device geometry and as such the application and most important metric need to be considered early in the energy harvester design process.
8. The predicted maximum power densities for the device designs that emerged from this effort were significantly higher than the existing predicted or measured piezoelectric harvester performance data (excepting the Sood [11] device). Operating and static power densities were chosen for comparison due to the size differences between the macro scale

devices that have been tested and the micro-scale device designs considered here. The maximum power densities for a {3-1} bimorph device recorded by du Toit [4] were $263\mu\text{W}/\text{cm}^3$ operating and $397\mu\text{W}/\text{cm}^3$ static. Sodano *et al.* [6] obtained a static power density of $462\mu\text{W}/\text{cm}^3$ from a {3-1} unimorph (no operating power density was available). The predicted maximum operating and static power densities from the {3-1} Mode designs presented here are $629\mu\text{W}/\text{cm}^3$ and $1852\mu\text{W}/\text{cm}^3$, respectively. For {3-3} Mode untapered devices, the maximum operating and static power density predictions are $536\mu\text{W}/\text{cm}^3$ and $1935\mu\text{W}/\text{cm}^3$, respectively. The maximum operating power density was a result of optimizing an untapered {3-1} Mode bimorph MEMS device with a proofmass; the maximum static power density was obtained from the design of an untapered {3-3} Mode unimorph device with a proof mass. (A complete set of maximum optimized performance predictions are given at the end of Chapters 3 and 4.) Note that the global optimum comparisons re. the {3-3} Mode devices with a taper and a proof mass only consider three active beam length and thus are likely suboptimal. If these predictions can be realized in a device, it will represent a significant improvement in performance over existing devices. Additionally, these predictions are conservative, both as a result of the model used (which under-predicts power output at resonance) and because of the conservative input vibration acceleration level considered (which neglected engine vibration).

9. From this design optimization effort, it became clear that the effect of a proof mass was much more prominent and beneficial than the effect of a taper on the device's power output. When device taper was included in the design space, the optimum operating and static power densities occurred at a taper ratio of 1 (an untapered beam). Again, note that this comparison is somewhat limited (see Point 8 above).
10. Durability is a key concern for energy harvesting devices as long-life operation, without maintenance or replacement, is desired. For all cases examined, piezoelectric critical strain was shown to be an order of magnitude below the level at which it would become a design concern. This indicates that the durability of these devices is likely high and that there exists significant margin on the vibration amplitude that can be used for excitation before device damage occurs.
11. There is a strong association between optimizing power output and matching the device operating frequency (resonance or anti-resonance) to the input frequency of the excitation. Within the subset of device geometries that match the desired frequency to the input, optimum geometries were observed, but virtually no power is obtained away from resonance / anti-resonance. This result highlights the importance of characterizing the vibration environment in which a device will operate before setting the geometry of the device.
12. The optimization technique employed is itself an important result of this work. Due to the shape of the objective function surfaces over the design space, with dual operating peaks, small local maxima, and strong frequency dependence, a standard gradient search method of optimization is not effective. Graphically investigating the entire design space proved to be a much more effective and illustrative tool for device design and optimization.

13. Lastly, optima are observed for the power metrics considered within the MEMS scale design spaces considered. This indicates that devices of this scale are desirable for energy harvesting in an aircraft vibration environment.

5.2 *Recommendations for Future Work*

Looking to the future beyond the work presented in this thesis and summarized above, the following are possible directions for future efforts:

1. To facilitate more accurate design and performance predictions, a detailed study of the on-aircraft vibration environment – included engine excitation – needs to be completed and a full, application-based PSD developed.
2. Fabrication of one or more of the optimal designs identified by this modeling effort would provide for further confirmation of this technique and allow for refinement in the microfabrication process. While the author made attempts to reproduce the fabrication efforts found in the literature, these efforts were not successful due largely to high variation in the materials called for, and a lack of specifics in the recorded procedures. Other piezoelectric deposition techniques are currently being explored, but the development of a robust and repeatable fabrication technique is critical in the advance of these devices from concept into service. The piezoelectric material deposition process needs to be refined and the feasibility of depositing large proof masses (3 μ m of platinum was used in this work) needs to be confirmed. While the thickness proposed here is possible, its successful integration into the rest of the fabrication process is key, especially given the strong performance benefits that a proof mass can offer.
3. While the modeling for an untapered device without a proof mass was verified by comparison to experimental data for the {3-1} Mode and validated for the {3-3} Mode of operation, both the effect of adding a proof mass and of tapering the beam need to be verified. This can be accomplished with either macro- or micro-scale experimentation.
4. As mentioned earlier, these harvester devices do not and cannot operate in isolation, and as such, should not be designed that way. Exploration of the power electronics that must accompany these devices needs to be integrated more closely with the device design itself. For instance, instead of depositing a large block of metal for a proof mass, would it be feasible to place a micro-battery or capacitor on the tip of the beam to store the power that is generated? Other questions that need to begin to be answered include how much additional volume will be added to the device by the power electronics and packaging, how the device will be connected to the power electronics (packaging), and what impact these considerations may have on device geometry parameters such as electrode spacing and thickness. Also, the optimum design assumes an optimum load resistance – the effect of the total electrical load (*e.g.*, batteries) needs to be understood and a technique needs to be developed to allow the system to be tuned to the optimum electrical configuration for power generation.

5. In addition to the power electronics, thought must be given to the manner in which these devices will be integrated into the aircraft structure. Current options include affixing the device and its accompanying sensor and transmitter to the skin of the aircraft externally with an adhesive patch or embedding it directly into the composite structure. The first raises concern over the bonding of the device to the skin for both duty cycle survival and (if desired) accurate strain data acquisition. The second potentially requires a much smaller device and raises the issue of effectively introducing inclusions into the composite structure. For both the additional testing and analysis that would have to be done to embed the devices directly into the composite and the appeal of the ability to retrofit an existing fleet with this technology, an external patch system is currently more desirable and feasible.
6. Since the investigation of a tapered device (with the rectangular volume definition used in this work) showed that such a design modification has little advantage (none if operating or static power density is of primary importance), other potential device geometries could be investigated. Perhaps the simplest is dovetailing tapered devices for tighter volumetric packing – this would allow for a different volume definition based on multiple devices and thus a re-evaluation of the potential power density advantage of a tapered device. The basic technique applied in this work for device exploration could be extended to other geometries in a fairly straight-forward fashion. The coefficients in the governing equations (such as mass, damping, capacitance and coupling) and mode shapes would need to be redefined for each case, but otherwise the approach is robust to various geometries. One device geometry that has been proposed is that of a spiral beam design, but the current rectangular beam geometry is however appealing due to the simple MEMS fabrication processes that it facilitates. Any new design will need to take into consideration the fabrication process as well as any potential power gains.
7. The under prediction of peak power production first observed by du Toit [3 and 4], remains relatively unexplored. Possible additions to the modeling effort that might increase the accuracy of the power predicted at resonance include considering higher mode excitations, different types of modal excitation (*i.e.* torsional), and any contributions from shear strain or potential non-linearity that might be present in the device or piezoelectric material.
8. Global, full three-variable (active beam length, taper ratio and proof mass length) optimization for a tapered device with a proof mass needs to be conducted, expanding on the discrete optimization presented in this work.

6 References

1. S. Roundy, P. K. Wright and J. M. Rabaey. *Energy Scavenging for Wireless Sensor Networks*. Kluwer Academic Publishers, Norwell, MA, 2004.
2. S. Roundy, P. K. Wright, J. Rabaey, "A Study of Low Level Vibrations as a Power Source for Wireless Sensor Nodes", *Computer Communications*, vol 26, 2003, p1131-1144.
3. N. E. du Toit, "Modeling and Design of a MEMS Piezoelectric Vibration Energy Harvester", Master of Science Thesis, MIT Department of Aeronautics and Astronautics, 2005.
4. N. E. du Toit and B. L. Wardle, "Experimental Verification of Models for Microfabricated Piezoelectric Vibration Energy Harvesters", AIAA-2006-1792, *47th AIAA Structures, Dynamics, and Materials Conference*, Newport, RI, May 1-4, 2006.
5. N. E. du Toit, B. L. Wardle, S.-G. Kim, "Design Considerations for MEMS-Scale Piezoelectric Mechanical Vibration Energy Harvesters", *Integrated Ferroelectrics*, 71: 121-160, 2005.
6. H. A. Sodano, G. Park, D.J. Inman, "Estimation of Electric Charge Output for Piezoelectric Energy Harvesting", *Strain*, vol 40, 2004, p49-58.
7. C. D. Richards, M. J. Anderson, D. F. Bahr, R. F. Richards, "Efficiency of Energy Conversion for Devices containing a Piezoelectric Component", *Journal of Micromechanics and Microengineering*, vol. 14, 2004, p717-721.
8. H. A. Sodano, D. J. Inman, G. Park, "A Review of Power Harvesting from Vibration Using Piezoelectric Materials", *The Shock and Vibration Digest*, vol. 36, no. 3, May 2004, p197-205.
9. H. A. Sodano, J. L. Lloyd, D. J. Inman, "An Experimental Comparison Between Several Active Composite Actuators for Power Generation", *Smart Structures and Materials 2004: Integrated Systems*, ed. A. B. Flatau, Proc. Of SPIE Vol 5390, p370-378.
10. P. Glynne-Jones, S. P. Beeby, N. M. White, "Towards a Piezoelectric Vibration-Powered Microgenerator", *IEEE Proceedings*, vol. 148, no. 2, March 2001, p68-72.
11. R. Sood, Y. B. Jeon, J.-h. Jeong and S. G. Kim, "Piezoelectric Micro Power Generation for Energy Harvesting", *Proceedings of Hilton Head 2004: A Solid State Sensor, Actuator and Microsystems Workshop*, June 2004.
12. J. Skinner, A. Olson, D. Bahr, C. Richards, R. Richards, "A Piezoelectric Membrane Generator for MEMS Power", AIAA 2002-5742, *NanoTech 2002*, 9-12 September 2002, Houston, TX.

13. M. Umeda, K. Nakamura, S. Ueha, "Analysis of Transformation of Mechanical Impact Energy to Electrical Energy Using a Piezoelectric Vibrator", *Japanese Journal of Applied Physics*, vol. 35, p3267-3273.
14. S. Meninger, J. O. Mur-Miranda, R. Amirtharajah, A. P. Chandrakasan, J. H. Lang, "Vibration-to-Electric Energy Conversion", *IEEE Transaction on Very Large Scale Integration (VLSI) Systems*, vol. 9, no. 1, February 2001, p64-76.
15. J. A. Paradiso, T. Starner, "Energy Scavenging for Mobile and Wireless Electronics", *Pervasive Computing*, Jan-March 2005, p18-26.
16. E. O. Torres, G. A. Rincon-Mora, "Harvesting Ambient Energy", *Electrical Engineering Times*, 8/29/2005, Issue 1386, p62-64.
17. G. K. Ottman, H. F. Hofmann, A. C. Bhatt, G. A. Lesieutre, "Adaptive Piezoelectric Energy Harvesting Circuit for Wireless Remote Power Supply", *IEEE Transactions on Power Electronics*, vol. 17, no. 5, Sept 2002.
18. A. Sinha, A. Chandrakasan, "Dynamic Power Management in Wireless Sensor Networks", *IEEE Design and Test of Computers*, March-April, 2001, p62-74.
19. R. Min, M Bhardwaj, S.-H. Cho, N. Ickes, E. Shih, A. Sinha, A. Wang, A. Chandrakasan, "Energy-Centric Enabling Technologies for Wireless Sensor Networks", *IEEE Wireless Communications*, August 2002, p28-39.
20. A. Chandrakasan, R. Min, M. Bhardwaj, S.-H. Cho, A. Wang, "Power Aware Wireless Microsensor Systems", *ESSCIRC 2002*, p47-54.
21. A. Chandrakasan, R. Amirtharajah, S. Cho, J. Goodman, G. Konduri, J. Kulik, W. Rabiner, A. Wang, "Design Considerations for Distributed Microsensor Systems", *IEEE Custom Integrated Circuits Conference*, 1999, p279-286.
22. C. C. Enz, A. El-Hoiydi, J.-D. Decotignie, V. Periris, "WiseNET: An Ultralow-Power Wireless Sensor Network Solution", *IEEE Computer*, August 2004, p62-70.
23. W. R. Heinzelman, A. Chandrakasan, "Energy-Efficient Communication Protocol for Wireless Microsensor Networks", *Proceedings of the 33rd Hawaii International Conference on System Sciences*, 2000, p1-10.
24. D. M. Ryan, R. M. LaFollette, L. Salmon, "Microscopic Batteries for Micro ElectroMechanical Systems (MEMS)", *Proceedings of the 32nd Intersociety Energy Conversion Engineering Conference*, 1997, p77-82.
25. J. B. Bates, G. R. Gruzalski, C. F. Luck, "Rechargeable Solid State Lithium Microbatteries", *Proceedings of Micro Electro Mechanical Systems, IEEE*, February 7-10, 1993, p82-86.
26. D. R. Sadoway, A. M. Mayes, "Portable Power: Advanced Rechargeable Lithium Batteries", *MRS Bulletin*, August 2002, p590-596.

27. S. C. Mui, P. E. Trapa, B. Huang, P. P. Soo, M. I. Lozow, T. C. Wang, R. E. Cohen, A. N. Mansour, S. Mukerjee, A. M. Mayes, D. R. Sadoway, "Block Copolymer-Templated Nanocomposite Electrodes for Rechargeable Lithium Batteries", *Journal of The Electrochemical Society*, vol. 149, no. 12, 2002, pA1610-A1615.
28. A.-V. G. Ruzette, P. P. Soo, D. R. Sadoway, A. M. Mayes, "Melt-Formable Block Copolymer Electrolytes for Lithium Rechargeable Batteries", *Journal of The Electrochemical Society*, vol. 148, no. 6, 2001, pA537-A543.
29. H. A. Sodano, G. Park, D. J. Leo, D. J. Inman, "Use of piezoelectric energy harvesting devices for charging batteries", *Smart Structures and Materials 2003: Smart Senso Technology and Measurement Systems*, SPIE vol 5050, 2003, p101-108.
30. C. D. E. Lakeman, P. F. Fleig, J. L. Degreeff, "Integrated Power for Microsystems", *CANEUS 2004 – Conference on Micro-Nano-Technologies*, November 1-5, 2004, Monterey, CA, AIAA 2004-6733.
31. G. J. Pottie, W. J. Kaiser, "Wireless Integrated Network Sensors", *Communications of the ACM*, vol. 43, no. 5, May 2000, p51-58.
32. R. Min, M. Bhardwaj, S.-H. Cho, E. Shih, A. Sinha, A. Wang, A. Chandrakasan, "Low-Power Wireless Sensor Networks", *Proceedings of the 14th International Conference on VLSI Design*, January 3-7, 2001, p205-210.
33. K. Römer, F. Mattern, "The Design Space of Wireless Sensor Networks", *IEEE Wireless Communications*, December 2004, p54-61.
34. E. H. Callaway, Jr., *Wireless Sensor Networks: Architectures and Protocols*. Aurbach Publications, Boca Raton, Florida, 2004.
35. C. Hautamaki, S. Zurn, S. C. Mantell, D. L. Polla, "Experimental Evaluation of MEMS Strain Sensors Embedded in Composites", *Journal of Microelectromechanical Systems*, vol. 8, no. 3, September 1999, p272-279.
36. A. Mehra, X. Zhang, A. A. Ayón, I. A. Waitz, M. A. Schmidt, C. M. Spadaccini, "A Six-Wafer Combustion System for a Silicon Micro Gas Turbine Engine", *Journal of Microelectromechanical Systems*, vol. 9, no. 4, Dec. 2000, p517-527.
37. M. Stordeur, I. Stark, "Low Power Thermoelectric Generator – self-sufficient energy supply for microsystems", *16th International Conference on Thermoelectrics, IEEE*, 1997, p575-577.
38. S. Whalen, M. Thompson, D. Bahr, C. Richards, R. Richards, "Design, fabrication and testing of the P3 micro heat engine", *Sensors and Actuators*, A 104, 2003, p290-298.
39. N. G. Elvin, A. A. Elvin, M. Spector, "A self-powered mechanical strain energy sensor", *Smart Materials and Structures*, vol. 10, 2001, p293-299.

40. H. Bai, M. Atiquzzaman, D. Lilja, "Wireless Sensor Network for Aircraft Health Monitoring", *Proceedings of the First International Conference on Broadband Networks (BROADNETS)*, August 12, 2004.
41. W.-T. Park, R. N. Candler, S. Kronmueller, M. Lutz, A. Partridge, G. Yama, T. W. Kenny, "Wafer-Scale Encapsulation of Micromachined Accelerometers", *Proceedings of the 12th International Conference on Solid State Sensors, Actuators and Microsystems*, Boston, June 8-12, 2003, 1903-1906.
42. J. P. Lynch, A. Partridge, K. H. Law, T. W. Kenny, A. S. Kiremidjian, E. Carryer, "Design of Piezoresistive MEMS-Based Accelerometer for Integration with Wireless Sensing Unit for Structural Monitoring", *Journal of Aerospace Engineering*, vol. 16, no. 3, July 1, 2003, p108-114.
43. M. Renaud, T. Sterken, P. Fiorini, R. Puers, K. Baert, C. van Hoof, "Scavenging Energy from Human Body: Design of a Piezoelectric Transducer", *The 13th International Conference on Solid-State Sensors, Actuators and Microsystems*, Seoul, Korea, June 5-9, 2005, p784-787.
44. N. Sato, H. Ishii, M. Urano, T. Sakata, J. Terada, H. Morimura, S. Shigematsu, K. Kudou, T. Kamei, K. Machida, "Novel MEMS Power Generator with Integrated Thermoelectric and Vibrational Devices", *The 13th International Conference on Solid-State Sensors, Actuators and Microsystems*, Seoul, Korea, June 5-9, 2005, p295-298.
45. V. Leonov, P. Fiorini, S. Sedky, T. Torfs, C. Van Hoof, "Thermoelectric MEMS Generators as a Power Supply for a Body Area Network", *The 13th International Conference on Solid-State Sensors, Actuators and Microsystems*, Seoul, Korea, June 5-9, 2005, p291-294.
46. R. T. Borno, M. M. Maharbiz, "A Distributed Actuation Method Based on Young-Laplace Forces", *The 13th International Conference on Solid-State Sensors, Actuators and Microsystems*, Seoul, Korea, June 5-9, 2005, p125-128.
47. MIL-STD-810, 1 January 2000, Annex C, Method 514.5, p514.4C 1-11.
48. R. M. Kent, D. A. Murphy, "Health Monitoring System Technology Assessments – Cost Benefits Analysis", Jan. 2000, NASA/CR-2000-209848.
49. Jane's Aero-Engines, <http://jae.janes.com/public/jae/index.shtml>, as accessed on May 16, 2005.
50. C. Boller, "Ways and options for aircraft structural health management" *Smart Materials and Structures*, vol. 10, 2001, p432-440.
51. M. Lin and F-K Chang, "The manufacture of composite structures with a built-in network of piezoceramics", *Composites Science and Technology*, vol. 62, 2002, p919-939.
52. J. W. Lincoln, R. A. Melliore, "Economic Life Determination for a Military Aircraft", *Journal of Aircraft*, vol. 36, no. 5, Sept.-Oct. 1999, p737-742.

53. L. Molent, B. Aktepe, "Review of fatigue monitoring of agile military aircraft", *Fatigue Fract Engng Mater Stuct*, vol. 23, 2000, p767-785.
54. J. W. Tedesco, W. G. McDougal, and C. A. Ross, "Structural Dynamics Theory and Applications," Addison Wesley Longman, 1999.
55. S. Scherrer, D. G. Plumlee, A. J. Moll, "Energy Scavenging Device in LTCC Materials", *WMED*, IEEE, 2005, p77-78.

7 Appendix A: Optimization Harvester Models: MATLAB Code

The mathematical models used to generate the optimization results presented in Chapters 3 and 4 are given here for reference and future adaptation. Matlab 7.0 was used to run the following code and the carpet plots shown were generated with the `contourf` function.

A.1 Untapered {3-3} Mode Harvester Model with Proof Mass

This specific case is for the {3-3} Mode MEMS unimorph discussed in Section 3.4.2.

```
%%%%%%%%%%%%%%%%%%%%%%%%%%%%%%%%%%%%%%%%%%%%%%%%%%%%%%%%%%%%%%%%%%%%%%%%%%
%UNIMORPH UNTAPERED BEAM - 33 OPERATION
%A. Mracek based on work of N. duToit
%%%%%%%%%%%%%%%%%%%%%%%%%%%%%%%%%%%%%%%%%%%%%%%%%%%%%%%%%%%%%%%%%%%%%%%%%%

% input parameters
Zeta_m = 0.005;
freqin = 1e3; %input vibration frequency in Hz
om_b_ref = freqin*2*pi; % input vibration frequency in rad/s
ddW_b_ref = 9.81*sqrt(freqin*1.579e-4);

% Piezo material properties
eval('pzt_5a_mat_prop');

% assign relevant material properties for current configuration
% plate configuration
cE33 = sE11/(sE11*sE33-sE13^2);
e31 = (sE11*d33-sE13*d31)/(sE11*sE33-sE13^2);
e33 = e31;
Eps_S_33 = Eps_T_33-(sE33*d31^2-
2*sE13*d31*d33+sE11*d33^2)/(sE11*sE33-sE13^2);
KS33 = Eps_S_33/Eps_0;

% parameter assignment
c_E = cE33;
e_m = e33;
Eps_S = Eps_S_33;

% Material properties for layers
% PZT
E_pzt_p = c_E; % PZT plate stiffness
rho_pzt = rho_p;

% platinum
```

```

E_pt = 170e9; % Pt - MEMSnet.org
rho_pt = 21440; % MatWeb.com
nu_pt = 0.39;
E_pt_p = E_pt/(1-nu_pt^2); % plate modulus

% titanium
E_ti = 110e9; % Ti - MEMSnet.org
rho_ti = 4510; % MEMSnet.org
nu_ti = 0.34;
E_ti_p = E_ti/(1-nu_ti^2); % plate modulus

% silicon
E_si = 112.4e9; %www.matweb.com
rho_si = 2329;
nu_si = 0.28;
E_si_p = E_si/(1-nu_si^2); % plate modulus

% SiNx
E_sinx = 313e9; %Noel's Sood analysis
rho_sinx = 3000;
nu_sinx = 0.30;
E_sinx_p = E_sinx/(1-nu_sinx^2); % plate modulus

% SiO2
E_sio2 = 69e9; %Noel's Sood analysis
rho_sio2 = 2300;
nu_sio2 = 0.15;
E_sio2_p = E_sio2/(1-nu_sio2^2); % plate modulus

% ZrO2
E_zro2 = 244e9; %Noel's Sood analysis
rho_zro2 = 6000;
nu_zro2 = 0.27;
E_zro2_p = E_zro2/(1-nu_zro2^2); % plate modulus

%%%%%%%%%%%%%%%%%%%%%%%%%%%%%%%%%%%%%%%%%%%%%%%%%%%%%%%%%%%%%%%%%%%%%%%%
% Define parameters
% device parameters:
Lmin = 0.1e-3;
Lmax = 1.5e-3;
Lrange = [Lmin:(Lmax-Lmin)/500:Lmax];
Lrange = 0.2652e-3
for ll=1:length(Lrange)
L = Lrange(ll)
b = 1.0e-3 % beam width in m
% specify thicknesses
t_pzt = 0.5e-6;
t_zro2 = 0.05e-6; %fixed by process
t_si = 0; %no Si layer used
t_sinx = 0.4e-6;
t_sio2 = 0.1e-6;
%electrode parameters

```

```

t_pt = 0.2e-6;
t_ti = 0.02e-6 ; %
p = 16e-6; %pitch = spacing between electrode centers
a = 4e-6; %width of electrodes

%%%%%%%%%%%%%%%%%%%%%%%%%%%%%%%%%%%%%%%%%%%%%%%%%%%%%%%%%%%%%%%%%%%%%%%%
% Define parameters for mass at the end
L0min = 0.05e-3;
L0max = 0.5e-3;
L0range = [L0min:(L0max-L0min)/500:L0max];
for lo = 1:length(L0range)
L0 = L0range(lo) % length of proof mass
b0 = b;
H0 = 3e-6; % height of the mass w/o middle pt layer
rho_0 = rho_pt; ;

%Calculate taper slope:
taper = 0.5*(b0-b)/L;
fparea = 2*0.5*L*b + b0*L; %foot print area of the beam, not
including the proof mass

%Create width matrix:
xstep = L/100;
xx = (0:xstep:L);
for jj = 1:length(xx)
    bx(jj) = b + 2*taper*xx(jj);
end

for jj = 1:length(bx)
    elecA(jj) = 0.5;
end

% Specify layers
t_l = [t_sinx t_sio2 t_zro2 t_pzt t_ti t_pt]; %set up for
Si base with pzt then electrode
E_l = [E_sinx_p E_sio2_p E_zro2_p E_pzt_p E_ti_p E_pt_p];
rho_l = [rho_sinx rho_sio2 rho_zro2 rho_pzt rho_ti rho_pt] ;

totalthick= sum(t_l);

% determine the neutral axis
for jj = 1: length(bx) %sum over beam length
    for ii = 1: length(t_l) %sum over beam thickness
        if ii == 1
            zb_l(ii) = t_l(ii)/2;
        else
            zb_l(ii) = zb_l(ii-1) + t_l(ii-1)/2 + t_l(ii)/2;
        end % if
        EAzb(ii,jj) = zb_l(ii)*t_l(ii)*bx(jj)*E_l(ii);
        EA(ii,jj) = t_l(ii)*bx(jj)*E_l(ii);
    end
end

```

```

end % for
EAzbsum = sum(EAzb);
EAsum = sum(EA);
zb(jj)=EAzbsum(jj)/EAsum(jj); %note: zb is constant with x b/c the
b(x) in EA divides out
end

%%%%%%%%%%%%%%%%%%%%%%%%%%%%%%%%%%%%%%%%%%%%%%%%%%%%%%%%%%%%%%%%%%%%%%%%
% useful parameters
ind_pzt = 4; %update if changing layers under pzt
%zp_max = zb_l(ind_pzt)+t_pzt/2-zb; from uniform case
zp_max = max(zb_l(ind_pzt)+t_pzt/2-zb); % max piezo distance
from neutral axis set manually
%zp_ave = abs(zb_l(ind_pzt)-zb); from uniform case
zp_ave = abs(zb_l(ind_pzt)-mean(zb)); % distance between neutral
axis and middle of piezo element
t_t = sum(t_l);
%%%%%%%%%%%%%%%%%%%%%%%%%%%%%%%%%%%%%%%%%%%%%%%%%%%%%%%%%%%%%%%%%%%%%%%%

% determine the moment of inertia and effective EI for each layer
for jj = 1: length(bx)
for ii = 1:ind_pzt
I_l(ii,jj) = 1/12*bx(jj)*t_l(ii)^3 +
t_l(ii)*bx(jj)*(zb_l(ii)-zb(jj))^2;
end % for ii
for ii = (ind_pzt+1):length(t_l) %modify for fractional area
coverage of electrodes
I_l(ii,jj) = 1/12*(bx(jj)*elecA(jj))*t_l(ii)^3 +
t_l(ii)*(bx(jj)*elecA(jj))*(zb_l(ii)-zb(jj))^2;
end
I_sx = sum(I_l,1);

for ii=1:length(t_l)
EI_l(ii,jj) = E_l(ii)*I_l(ii,jj);
end
EI_sx = sum(EI_l,1);
E_effx(jj) = EI_sx(jj)/I_sx(jj); % effective young's modulus as a
function of x
end

% effective density, NOT a function of x
rho_c = 0;
for ii = 1:length(t_l)
rho_c = rho_c+t_l(ii)*rho_l(ii);
end % for ii
rho_c = rho_c/t_t;

% mass per length as a function of x
for jj = 1:length(bx)
m(jj) = rho_c*bx(jj)*t_t;
end

```

```

% determine the mass per length for the Proof Mass
%proof mass assumed uniform in x
m0      =  b0*(rho_c*t_t + rho_0*H0);
CG_m    =  (rho_c*t_t*b0*zb(length(bx)) +
rho_0*H0*b0*(t_t+H0/2))/(rho_c*t_t + rho_0*H0);
ox      =  L0/2;          % depends on the beam config
oy      =  CG_m-zb(length(bx)); % distance from CG of mass to
neutral axis

% determine proof mass effective parameters for modal analysis
M0      =  m0*L0;
%M0_    =  M0/(m*L); (from uniform case)
M0_     =  M0/(mean(m)*L);
% determine the static moment
S0      =  M0*ox;
%S0_    =  S0/(m*L^2); (from uniform case)
S0_     =  S0/(mean(m)*L^2);
% determine the moment of inertia of the mass
for ii=1:length(t_l)
    Iz(ii) = rho_l(ii)*b0*(1/12*L0*t_l(ii)^3 + t_l(ii)*L0*(zb_l(ii)-
CG_m)^2);
    Ix(ii) = rho_l(ii)*b0*(1/12*t_l(ii)*L0^3);
end
IzM     =  rho_0*b0*(1/12*L0*H0^3 + H0*L0*(t_t+H0/2-CG_m)^2);
IxM     =  rho_0*b0*(1/12*H0*L0^3);
Iyy     =  sum(Iz) + sum(Ix) + IzM + IxM;
I0      =  Iyy+M0*(ox^2+oy^2);
%I0_    =  I0/(m*L^3); (from uniform case)
I0_     =  I0/(mean(m)*L^3);

%calculate static deflection of beam:
for jj=1:length(xx)
    %from point load:
    stdef1(jj) = (M0*9.81*xx(jj)^2)/(6*EI_sx(jj))*(3*L-xx(jj));
    %from moment:
    stdef2(jj) = (S0*xx(jj)^2)/(2*EI_sx(jj));
    %superposition:
    stdefT(jj)=stdef1(jj)+stdef2(jj);
end
staticdef = stdefT(length(xx));

%%%%%%%%%%%%%%%%%%%%%%%%%%%%%%%%%%%%%%%%%%%%%%%%%%%%%%%%%%%%%%%%%%%%%%%%
% for the specific configuration - modal parameters
% find the value for Beta1
x       =  [0.0:0.05:2.0];
% x = lambda bar; narrow range after successive runs

for ii=1:length(x)
    A11(ii) =  (sinh(x(ii))+sin(x(ii))) + I0_*x(ii)^3*(-
cosh(x(ii))+cos(x(ii))) + S0_*x(ii)^2*(-sinh(x(ii))+sin(x(ii)));
    A12(ii) =  (cosh(x(ii))+cos(x(ii))) + I0_*x(ii)^3*(-sinh(x(ii))-
sin(x(ii))) + S0_*x(ii)^2*(-cosh(x(ii))+cos(x(ii)));

```

```

    A21(ii) = (cosh(x(ii))+cos(x(ii))) + M0_*x(ii)^1*( sinh(x(ii))-
sin(x(ii))) + S0_*x(ii)^2*( cosh(x(ii))-cos(x(ii)));
    A22(ii) = (sinh(x(ii))-sin(x(ii))) + M0_*x(ii)^1*( cosh(x(ii))-
cos(x(ii))) + S0_*x(ii)^2*( sinh(x(ii))+sin(x(ii)));
    % determine the determinant
    DET(ii) = A11(ii)*A22(ii)-A12(ii)*A21(ii);
end

if sign(DET(1)) == 1
    Ind = find(DET<0);
elseif sign(DET(1)) == -1
    Ind = find(DET>0);
end
if numel(Ind)==0
    pickmetric = 0;
    disp('error with Ind')
    return
end

Inda = Ind(1);
Gamma_ = x(Inda); % this is Beta*L

% help narrow x search to improve accuracy:
x = [Gamma_*0.8:0.0001:Gamma_*1.2]; % x = lambda bar; narrow range
after successive runs

for ii=1:length(x)
    A11(ii) = (sinh(x(ii))+sin(x(ii))) + I0_*x(ii)^3*(-
cosh(x(ii))+cos(x(ii))) + S0_*x(ii)^2*(-sinh(x(ii))+sin(x(ii)));
    A12(ii) = (cosh(x(ii))+cos(x(ii))) + I0_*x(ii)^3*(-sinh(x(ii))-
sin(x(ii))) + S0_*x(ii)^2*(-cosh(x(ii))+cos(x(ii)));
    A21(ii) = (cosh(x(ii))+cos(x(ii))) + M0_*x(ii)^1*( sinh(x(ii))-
sin(x(ii))) + S0_*x(ii)^2*( cosh(x(ii))-cos(x(ii)));
    A22(ii) = (sinh(x(ii))-sin(x(ii))) + M0_*x(ii)^1*( cosh(x(ii))-
cos(x(ii))) + S0_*x(ii)^2*( sinh(x(ii))+sin(x(ii)));
    % determine the determinant
    DET(ii) = A11(ii)*A22(ii)-A12(ii)*A21(ii);
end

if sign(DET(1)) == 1
    Ind = find(DET<0);
elseif sign(DET(1)) == -1
    Ind = find(DET>0);
end
if numel(Ind)==0
    pickmetric = 0;
    disp('error with Ind')
    return
end

Inda = Ind(1);
Gamma_ = x(Inda); % this is Beta*L

```

```

%now proceed with more exact Gamma_:
Allused=A11(Inda);
A12used=A12(Inda);
A21used=A21(Inda);
A22used=A22(Inda);

B1 = Gamma_/L;
c1 = 1; % arbitrary constant - Cancels out when determining
the displacement and other parameters
s1 = A12(Inda)/A11(Inda);

% natural freq acc to modal analysis
om_n_a = B1^2*sqrt(mean(EI_sx)/(rho_c*t_t*fparea));

f = om_n_a/2/pi;

%%%%%%%%%%%%%%%%%%%%%%%%%%%%%%%%%%%%%%%%%%%%%%%%%%%%%%%%%%%%%%%%%%%%%%%%
% calculate coefficient matrices:
Phi_L = c1*((cosh(B1*L)-cos(B1*L))-s1*(sinh(B1*L)-sin(B1*L)));
dPhi_L = c1*B1*((sinh(B1*L)+sin(B1*L))-s1*(cosh(B1*L)-
cos(B1*L)));
ddPhi_0 = c1*B1^2*((cosh(B1*0)+cos(B1*0))-
s1*(sinh(B1*0)+sin(B1*0)));

for jj = 1:length(xx)
    Tsilx(jj) = c1*((cosh(B1*xx(jj))-cos(B1*xx(jj))) -
s1*(sinh(B1*xx(jj))-sin(B1*xx(jj))));
    ddTsilx(jj) = c1*((B1^2*cosh(B1*xx(jj))+B1^2*cos(B1*xx(jj))) -
s1*(B1^2*sinh(B1*xx(jj))+B1^2*sin(B1*xx(jj))));
end

%Mass matrix:
for ii = 1:length(t_l)
    for jj = 1:length(bx)
        Mint(ii,jj) = bx(jj)*t_l(ii)*rho_l(ii)*Tsilx(jj)^2*xstep;
    end
    M_l(ii) = sum(Mint(ii,:));
end
for jj=1:length(xx)
    Msum(jj) = sum(Mint(:,jj)/xstep);
end
M1 = sum(M_l) + M0*Phi_L^2 + 2*S0*Phi_L*dPhi_L + I0*dPhi_L^2; %
effective mass

%Stiffness matrix:
for jj = 1:length(xx)
    for ii = 1:length(t_l)
        Kint(ii,jj) = E_l(ii)*I_l(ii,jj)*ddTsilx(jj)^2*xstep;
    end
    Kx(jj) = sum(Kint(:,jj)/xstep);

```

```

end
K1 = sum(Kx.*xstep);

%Coupling matrix
for jj=1:length(bx)
    Thetax(jj) = t_pzt*bx(jj)*zp_ave*e_m*ddTsilx(jj)*(1/(p-
a))*xstep;
    Thetax2(jj) = Thetax(jj)/xstep;
end %for jj (length)
Theta = sum(Thetax);
%Capacitance matrix
for jj = 1:length(bx)
    Cpx(jj) = t_pzt*bx(jj)*Eps_S*(1/(p-a)^2)*xstep;
    Cpx2(jj) = Cpx(jj)/xstep;
end %for jj (length)
Cp = sum(Cpx);

Ke_2 = Theta^2/(K1*Cp);

%Input matrix adjusted to account for proof mass
for jj = 1:length(xx)
    Bf_int(jj) = rho_c*t_t*bx(jj)*Tsilx(jj)*xstep;
    Bfx(jj) = Bf_int(jj)/xstep;
end
Bf = sum(Bf_int) + M0*Phi_L + 1/2*M0*dPhi_L*(2*L+L0);

% estimate the natural frequency acc to lumped model
om_n = sqrt(K1/M1);
%om = om_n*sqrt(1+Ke_2);
%OM = om/om_n;
OM = om_b_ref/om_n; %want to make sure that the OM reflects off-
optimum operation

% adjust the virbation amplitude to the reference frequency:
%ddW_b = sqrt(ddW_b_ref^2*om_n/om_b_ref);

ddW_b = ddW_b_ref; %keeping input the same, represented off-
resonance earlier

% Analyse the system
% calculate the sc and oc resonance freq ratios
OM_oc = sqrt(1+Theta^2/(K1*Cp));
r_opt = (OM_oc^4 + (4*Zeta_m^2-2)*OM_oc^2 + 1)/(OM_oc^6 +
(4*Zeta_m^2-2*(1+Theta^2/(K1*Cp)))*OM_oc^4 +
(1+Theta^2/(K1*Cp))^2*OM_oc^2);
Re_opt_oc = sqrt(r_opt);
Rl_opt_oc = round(Re_opt_oc/(Cp*om_n));
OM_sc = 1;
r_opt = (OM_sc^4 + (4*Zeta_m^2-2)*OM_sc^2 + 1)/(OM_sc^6 +
(4*Zeta_m^2-2*(1+Theta^2/(K1*Cp)))*OM_sc^4 +
(1+Theta^2/(K1*Cp))^2*OM_sc^2);
Re_opt_sc = sqrt(r_opt);

```



```

Rl_opt_sc = round(Re_opt_sc/(Cp*om_n));
Rl_opt_df = Rl_opt_oc-Rl_opt_sc;

% Specify open circuit optimum resistance
Rl = Rl_opt_oc;
Re = Rl*Cp*om_n;

% Next these coefficients calculate the response of the system
den = sqrt( (1 - (1 + 2*Zeta_m*Re)*OM^2 )^2 + ( (2*Zeta_m +
(1+Theta^2/(K1*Cp))*Re)*OM - Re*OM^3 )^2 );
Z = (Bf/K1*sqrt(1+Re^2*OM^2))*ddW_b / den;
W_tip = Phi_L*Z;
Rot_tip = dPhi_L*Z;
Str_m = -zp_max*ddPhi_0*Z;
Vp = (Bf/(K1*Cp)*Re*Theta*OM)*ddW_b / den;
Pout = ((Bf^2/K1^2)*Theta^2*OM^2*om_n*(1/Cp)*Re)*ddW_b^2 /
den^2;
Ip = Pout/Vp;

Re_opt_f = sqrt((OM^4 + (4*Zeta_m^2-2)*OM^2 + 1)/(OM^6 +
(4*Zeta_m^2-2*(1+Theta^2/(K1*Cp)))*OM^4 +
(1+Theta^2/(K1*Cp))^2*OM^2));
Rl_opt_f = Re_opt_f/(Cp*om_n);
den_opt = sqrt( (1 - (1 + 2*Zeta_m*Re_opt_f)*OM^2 )^2 + (
(2*Zeta_m + (1+Theta^2/(K1*Cp))*Re_opt_f)*OM(ii) - Re_opt_f*OM^3 )^2
);
Z_opt = Bf/K1*sqrt(1+(Re_opt_f*OM)^2)*ddW_b / den_opt;
W_tip_opt = Phi_L*Z_opt;
Rot_tip_opt = dPhi_L*Z_opt;
Str_m_opt = -zp_max*ddPhi_0*Z_opt;
Vp_opt = Bf/(K1*Cp)*Re_opt_f*Theta*OM(ii)*ddW_b / den_opt;
Pout_opt = ((Bf/K1*Theta*OM*ddW_b)^2*om_n*(1/Cp)*Re_opt_f) /
den_opt^2;
I_opt = Pout_opt/Vp_opt;

%output data:
opvolume = (2*max(abs(W_tip_opt)) +
H0*cos(max(abs(Rot_tip_opt))+L0*sin(max(abs(Rot_tip_opt))))*(L+L0)*(m
ax(b,b0))*1e6; % approximate volume in cm^3
%volume = 2*max(abs(W_tip_opt))*L*(max(b,b0))*1e6; % approximate
volume in cm^3
P_dens_op = (Pout_opt/1e-6)/opvolume;
volmm3 = opvolume*1e3;
volstatic = (staticdef + t_t + H0) * (L + L0) * max(bx) *1e6;
footprint = (L+L0)*(max(b,b0))*1e6;
P_dens_st = (max(Pout_opt(:))/1e-6)/volstatic;
beammass = rho_c*mean(bx)*t_t*L ;
pmmass = rho_0*H0*b0*L0+ rho_c*bx(length(bx))*t_t*L0;
devicemass = rho_c*mean(bx)*t_t*L + rho_c*bx(length(bx))*t_t*L0 +
rho_0*H0*b0*L0;

```

```
om_r(ll,lo) = om_n/2/pi;
om_ar(ll,lo) = om_n/2/pi*OM_oc;
OM_ocout=OM_oc;
Pout_out(ll,lo) =(Pout_opt)*1e6;
Popdens(ll,lo) =P_dens_op;
Pstdens(ll,lo) =P_dens_st;
SpecificPower(ll,lo) = Pout_opt/devicemass;
maxustrain(ll,lo)=abs(Str_m_opt)/1e-6;
maxV(ll,lo)=abs(Vp_opt);
maxuA(ll,lo)=abs(I_opt)/1e-6;
wtip(ll,lo)=abs(W_tip_opt)*1e6;

end
end
```

A.2 Untapered {3-1} Mode Harvester Model with Proof Mass

This specific case is for the {3-1} Mode MEMS bimorph discussed in Section 3.4.3.

```

%%%%%%%%%%%%%%%%%%%%%%%%%%%%%%%%%%%%%%%%%%%%%%%%%%%%%%%%%%%%%%%%%%%%%%%%
%BIMORPH UNTAPERED BEAM - 31 OPERATION
%A. Mracek based on work of N. du Toit
%%%%%%%%%%%%%%%%%%%%%%%%%%%%%%%%%%%%%%%%%%%%%%%%%%%%%%%%%%%%%%%%%%%%%%%%

% input parameters
Zeta_m = 0.005;
freqin = 1000; %input vibration frequency in Hz
om_b_ref = freqin*2*pi; % input vibration frequency in rad/s
ddW_b_ref = 9.81*sqrt(freqin*1.579e-4); %input vibration amplitude
from psd (valid 300<freqin<1000 Hz)

% Piezo material properties
eval('pzt_5a_mat_prop');

% assign relevant material properties for current configuration
% plate configuration

cE11 = sE11/(sE11^2-sE12^2);
e31 = d31/(sE11+sE12);
Eps_S_33 = Eps_T_33-2*d31^2/(sE11+sE12);
KS33 = Eps_S_33/Eps_0;

% parameter assignment
c_E = cE11;
%c_E = 66e9
e_m = e31;
Eps_S = Eps_S_33;

% Material properties for layers
% PZT
E_pzt_p = c_E; % PZT plate stiffness
rho_pzt = rho_p;

% platinum
E_pt = 170e9; % Pt - MEMSnet.org
rho_pt = 21440; % MatWeb.com
nu_pt = 0.39;
E_pt_p = E_pt/(1-nu_pt^2); % plate modulus

% titanium
E_ti = 110e9; % Ti - MEMSnet.org
rho_ti = 4510; % MEMSnet.org
nu_ti = 0.34;
E_ti_p = E_ti/(1-nu_ti^2); % plate modulus

```

```

% silicon
E_si = 112.4e9; %www.matweb.com
rho_si = 2329;
nu_si = 0.28;
E_si_p = E_si/(1-nu_si^2); % plate modulus

% SiNx
E_sinx = 313e9; %Noel's Sood analysis
rho_sinx = 3000;
nu_sinx = 0.30;
E_sinx_p = E_sinx/(1-nu_sinx^2); % plate modulus

% SiO2
E_sio2 = 69e9; %Noel's Sood analysis
rho_sio2 = 2300;
nu_sio2 = 0.15;
E_sio2_p = E_sio2/(1-nu_sio2^2); % plate modulus

% ZrO2
E_zro2 = 244e9; %Noel's Sood analysis
rho_zro2 = 6000;
nu_zro2 = 0.27;
E_zro2_p = E_zro2/(1-nu_zro2^2); % plate modulus

% structure
E_s = 100e9; % matweb
%rho_s = 6750; % measured
rho_s = 7165; % measured
%nu_s = 0.35; % mat web
nu_s = 0;
E_s_p = E_s/(1-nu_s^2); % plate modulus

%%%%%%%%%%%%%%%%%%%%%%%%%%%%%%%%%%%%%%%%%%%%%%%%%%%%%%%%%%%%%%%%%%%%%%%%
%%
% Define parameters
Lmin = 0.1e-3;
Lmax = 1.5e-3;
Lrange = [Lmin:(Lmax-Lmin)/500:Lmax];
for ll=1:length(Lrange)
%L = 0.5e-3 % length in m
L = Lrange(ll)
b = 1.0e-3; % beam width in m, OPT PARAM
% specify thicknesses
t_pzt = 0.5e-6;
t_zro2 = 0.05e-6; %fixed by process
t_si = 0.5e-6;
t_sinx = 0.4e-6;
t_sio2 = 0.1e-6;
%electrode parameters
t_pt = 0.2e-6;

```

```

t_ti      = 0.02e-6 ; %fixed, not from optimization code

%%%%%%%%%%%%%%%%%%%%%%%%%%%%%%%%%%%%%%%%%%%%%%%%%%%%%%%%%%%%%%%%%%%%%%%%
%%
% Define parameters for mass at the end
L0min = 0.05e-3;
L0max = 0.5e-3;
L0range = [L0min:(L0max-L0min)/500:L0max];
for lo = 1:length(L0range)
L0 = L0range(lo)          % length of proof mass

b0 = b;
H0 = 3e-6;          % height of the mass w/o middle pt layer,
constrained by fabrication
rho_0 = rho_pt;

%Calculate taper slope:
taper = 0.5*(b0-b)/L;
fparea = 2*0.5*L*b + b0*L; %foot print area of the beam, not
including the proof mass

%Create width matrix:
xstep = L/100;
xx = (0:xstep:L);
for jj = 1:length(xx)
    bx(jj) = b + 2*taper*xx(jj);
end
%plot(xx,bx/2)
%hold on
%plot(xx,-bx/2)
%hold off
%effective fractional area of electrode pads, assuming 10um each side
of beam:

% Specify layers
t_l = [t_pt  t_ti  t_pzt  t_ti  t_pt  t_si  t_pt  t_ti
t_pzt  t_ti  t_pt];
E_l = [E_pt_p E_ti_p E_pzt_p E_ti_p E_pt_p E_si_p E_pt_p
E_ti_p E_pzt_p E_ti_p E_pt_p];
rho_l = [rho_pt rho_ti rho_pzt rho_ti rho_pt rho_si rho_pt
rho_ti rho_pzt rho_ti rho_pt];

totalthick= sum(t_l);

% determine the neutral axis
for jj = 1: length(bx) %sum over beam length
    for ii = 1: length(t_l) %sum over beam thickness
        if ii == 1
            zb_l(ii) = t_l(ii)/2;
        else

```

```

        zb_l(ii)      =  zb_l(ii-1) + t_l(ii-1)/2 + t_l(ii)/2;
% zb of individual layers from ground
    end % if
        EAzb(ii,jj) =  zb_l(ii)*t_l(ii)*bx(jj)*E_l(ii);
        EA(ii,jj)   =  t_l(ii)*bx(jj)*E_l(ii);
    end % for
    EAzbsum = sum(EAzb);
    EAsum   = sum(EA);
    zb(jj) = EAzbsum(jj)/EAsum(jj); %note: zb is constant with x b/c the
b(x) in EA divides out
end

```

```

%%%%%%%%%%%%%%%%%%%%%%%%%%%%%%%%%%%%%%%%%%%%%%%%%%%%%%%%%%%%%%%%%%%%%%%%
% useful parameters
ind_pzt = 9;          %update if changing layers under pzt
%zp_max = zb_l(ind_pzt)+t_pzt/2-zb; from uniform case
zp_max = max(zb_l(ind_pzt)+t_pzt/2-zb);      % max piezo distance
from neutral axis set manually
%zp_ave = abs(zb_l(ind_pzt)-zb);      from uniform case
zp_ave = abs(zb_l(ind_pzt)-mean(zb));      % distance between neutral
axis and middle of piezo element
t_t = sum(t_l);
%%%%%%%%%%%%%%%%%%%%%%%%%%%%%%%%%%%%%%%%%%%%%%%%%%%%%%%%%%%%%%%%%%%%%%%%

```

```

% determine the moment of inertia and effective EI for each layer
for jj = 1: length(bx)
    for ii = 1:length(t_l)
        I_l(ii,jj) = 1/12*bx(jj)*t_l(ii)^3 +
t_l(ii)*bx(jj)*(zb_l(ii)-zb(jj))^2;
        I_sx = sum(I_l,1);
        EI_l(ii,jj) = E_l(ii)*I_l(ii,jj);
    end
    EI_sx = sum(EI_l,1);
    E_effx(jj) = EI_sx(jj)/I_sx(jj); % effective young's modulus as a
function of x
end

```

```

% effective density, NOT a function of x
rho_c = 0;
for ii = 1:length(t_l)
    rho_c = rho_c+t_l(ii)*rho_l(ii);
end % for ii
rho_c = rho_c/t_t;

```

```

% mass per length as a function of x
for jj = 1:length(bx)
    m(jj) = rho_c*bx(jj)*t_t;
end

```

```

% determine the mass per length for the Proof Mass

```

```

%proof mass assumed uniform in x
m0      =   b0*(rho_c*t_t + rho_0*H0);
CG_m    =   (rho_c*t_t*b0*z_b(length(bx)) +
rho_0*H0*b0*(t_t+H0/2))/(rho_c*t_t + rho_0*H0);
ox      =   L0/2;          % depends on the beam config
oy      =   CG_m-z_b(length(bx));    % distance from CG of mass to
neutral axis

% determine proof mass effective parameters for modal analysis
M0      =   m0*L0;
%M0_    =   M0/(m*L); (from uniform case)
M0_     =   M0/(mean(m)*L);
% determine the static moment
S0      =   M0*ox;
%S0_    =   S0/(m*L^2); (from uniform case)
S0_     =   S0/(mean(m)*L^2);
% determine the moment of inertia of the mass
for ii=1:length(t_l)
    Iz(ii) = rho_l(ii)*b0*(1/12*L0*t_l(ii)^3 + t_l(ii)*L0*(z_b_l(ii)-
CG_m)^2);
    Ix(ii) = rho_l(ii)*b0*(1/12*t_l(ii)*L0^3);
end
IzM     =   rho_0*b0*(1/12*L0*H0^3 + H0*L0*(t_t+H0/2-CG_m)^2);
IxM     =   rho_0*b0*(1/12*H0*L0^3);
Iyy     =   sum(Iz) + sum(Ix) + IzM + IxM;
I0      =   Iyy+M0*(ox^2+oy^2);
%I0_    =   I0/(m*L^3); (from uniform case)
I0_     =   I0/(mean(m)*L^3);

%calculate static deflection of beam:
for jj=1:length(xx)
    %from point load:
    stdef1(jj) = (M0*9.81*xx(jj)^2)/(6*EI_sx(jj))*(3*L-xx(jj));
    %from moment:
    stdef2(jj) = (S0*xx(jj)^2)/(2*EI_sx(jj));
    %superposition:
    stdefT(jj)=stdef1(jj)+stdef2(jj);
end
staticdef = stdefT(length(xx));

%%%%%%%%%%%%%%%%%%%%%%%%%%%%%%%%%%%%%%%%%%%%%%%%%%%%%%%%%%%%%%%%%%%%%%%%
% for the specific configuration - modal parameters
% find the value for Beta1
%x      =   [0.25:0.005:0.5];
x       =   [0.0:0.005:2.0]; % x = lambda bar; narrow range after
successive runs

for ii=1:length(x)
    A11(ii) = (sinh(x(ii))+sin(x(ii))) + I0_*x(ii)^3*(-
cosh(x(ii))+cos(x(ii))) + S0_*x(ii)^2*(-sinh(x(ii))+sin(x(ii)));
    A12(ii) = (cosh(x(ii))+cos(x(ii))) + I0_*x(ii)^3*(-sinh(x(ii))-
sin(x(ii))) + S0_*x(ii)^2*(-cosh(x(ii))+cos(x(ii)));

```

```

        A21(ii) = (cosh(x(ii))+cos(x(ii))) + M0_*x(ii)^1*( sinh(x(ii))-
sin(x(ii))) + S0_*x(ii)^2*( cosh(x(ii))-cos(x(ii)));
        A22(ii) = (sinh(x(ii))-sin(x(ii))) + M0_*x(ii)^1*( cosh(x(ii))-
cos(x(ii))) + S0_*x(ii)^2*( sinh(x(ii))+sin(x(ii)));
        % determine the determinant
        DET(ii) = A11(ii)*A22(ii)-A12(ii)*A21(ii);
end

if sign(DET(1)) == 1
    Ind = find(DET<0);
elseif sign(DET(1)) == -1
    Ind = find(DET>0);
end
if numel(Ind)==0
    pickmetric = 0;
    disp('error with Ind')
    return
end
Inda = Ind(1);
Gamma_ = x(Inda) ; % this is Beta*L
%disp(['BetaL = ', num2str(Gamma_)]);
%clear x;

B1 = Gamma_/L;
c1 = 1; % arbitrary constant - Cancels out when determining
the displacement and other parameters
s1 = A12(Inda)/A11(Inda);

% natural freq acc to modal analysis
om_n_a = B1^2*sqrt(EI_sx/(rho_c*t_t*fparea));

f = om_n_a/2/pi;

%%%%%%%%%%%%%%%%%%%%%%%%%%%%%%%%%%%%%%%%%%%%%%%%%%%%%%%%%%%%%%%%%%%%%%%%
% calculate coefficient matrices:
Phi_L = c1*((cosh(B1*L)-cos(B1*L))-s1*(sinh(B1*L)-sin(B1*L)));
dPhi_L = c1*B1*((sinh(B1*L)+sin(B1*L))-s1*(cosh(B1*L)-
cos(B1*L)));
ddPhi_0 = c1*B1^2*((cosh(B1*0)+cos(B1*0))-
s1*(sinh(B1*0)+sin(B1*0)));

for jj = 1:length(xx)
    Tsilx(jj) = c1*( (cosh(B1*xx(jj))-cos(B1*xx(jj))) -
s1*(sinh(B1*xx(jj))-sin(B1*xx(jj))));
    ddTsilx(jj) = c1*( (B1^2*cosh(B1*xx(jj))+B1^2*cos(B1*xx(jj))) -
s1*(B1^2*sinh(B1*xx(jj))+B1^2*sin(B1*xx(jj))));
end

%Mass matrix:
for ii = 1:length(t_l)
    for jj = 1:length(bx)

```



```

        Mint(ii,jj) = bx(jj)*t_l(ii)*rho_l(ii)*Tsilx(jj)^2*xstep;
    end
    M_l(ii) = sum(Mint(ii,:));
end
for jj=1:length(xx)
    Msum(jj) = sum(Mint(:,jj))/xstep;
end
M1 = sum(M_l) + M0*Phi_L^2 + 2*S0*Phi_L*dPhi_L + I0*dPhi_L^2; %
effective mass

%Stiffness matrix:
for jj = 1:length(xx)
    for ii = 1:length(t_l)
        Kint(ii,jj) = E_l(ii)*I_l(ii,jj)*ddTsilx(jj)^2*xstep;
    end
    Kx(jj) = sum(Kint(:,jj))/xstep;
end
K1 = sum(Kx.*xstep);

%Coupling matrix
for jj=1:length(bx)
    Thetax(jj) = bx(jj)*zp_ave*e_m*ddTsilx(jj)*xstep;
    Thetax2(jj) = Thetax(jj)/xstep;
end %for jj (length)
Theta = sum(Thetax);
%Capacitance matrix
for jj = 1:length(bx)
    Cpx(jj) = (bx(jj)*Eps_S/t_pzt)*xstep;
    Cpx2(jj) = Cpx(jj)/xstep;
end %for jj (length)
Cp = sum(Cpx);

Ke_2 = Theta^2/(K1*Cp);

%Input matrix adjusted to account for proof mass
for jj = 1:length(xx)
    Bf_int(jj) = rho_c*t_t*bx(jj)*Tsilx(jj)*xstep;
    Bfx(jj) = Bf_int(jj)/xstep;
end
Bf = sum(Bf_int) + M0*Phi_L + 1/2*M0*dPhi_L*(2*L+L0);

% estimate the natural frequency acc to lumped model
om_n = sqrt(K1/M1);
%om = om_n*sqrt(1+Ke_2);
%OM = om/om_n;

OM = om_b_ref/om_n; %want to make sure that the OM reflects off-
optimum operation
ddW_b = ddW_b_ref;

% Analyse the system
% calculate the sc and oc resonance freq ratios

```

```

OM_oc      = sqrt(1+Theta^2/(K1*Cp));
r_opt     = (OM_oc^4 + (4*Zeta_m^2-2)*OM_oc^2 + 1)/(OM_oc^6 +
(4*Zeta_m^2-2*(1+Theta^2/(K1*Cp)))*OM_oc^4 +
(1+Theta^2/(K1*Cp))^2*OM_oc^2);
Re_opt_oc = sqrt(r_opt);
Rl_opt_oc = round(Re_opt_oc/(Cp*om_n));
OM_sc     = 1;
r_opt     = (OM_sc^4 + (4*Zeta_m^2-2)*OM_sc^2 + 1)/(OM_sc^6 +
(4*Zeta_m^2-2*(1+Theta^2/(K1*Cp)))*OM_sc^4 +
(1+Theta^2/(K1*Cp))^2*OM_sc^2);
Re_opt_sc = sqrt(r_opt);
Rl_opt_sc = round(Re_opt_sc/(Cp*om_n));
Rl_opt_df = Rl_opt_oc-Rl_opt_sc;

% Specify open circuit optimum resistance:
Rl = Rl_opt_oc;
Re = Rl*Cp*om_n;

% Next calculate the response of the system
den = sqrt( (1 - (1 + 2*Zeta_m*Re)*OM^2 )^2 + ( (2*Zeta_m +
(1+Theta^2/(K1*Cp))*Re)*OM - Re*OM^3 )^2 );
Z = (Bf/K1*sqrt(1+Re^2*OM^2))*ddW_b / den;
W_tip = Phi_L*Z;
Rot_tip = dPhi_L*Z;
Str_m = -zp_max*ddPhi_0*Z;
Vp = (Bf/(K1*Cp)*Re*Theta*OM)*ddW_b / den;
Pout = ((Bf^2/K1^2)*Theta^2*OM^2*om_n*(1/Cp)*Re)*ddW_b^2 /
den^2;
Ip = Pout/Vp;

Re_opt_f = sqrt((OM^4 + (4*Zeta_m^2-2)*OM^2 + 1)/(OM^6 +
(4*Zeta_m^2-2*(1+Theta^2/(K1*Cp)))*OM^4 +
(1+Theta^2/(K1*Cp))^2*OM^2));
Rl_opt_f = Re_opt_f/(Cp*om_n);
den_opt = sqrt( (1 - (1 + 2*Zeta_m*Re_opt_f)*OM^2 )^2 + (
(2*Zeta_m + (1+Theta^2/(K1*Cp))*Re_opt_f)*OM - Re_opt_f*OM^3 )^2 );
Z_opt = Bf/K1*sqrt(1+(Re_opt_f*OM)^2)*ddW_b / den_opt;
W_tip_opt = Phi_L*Z_opt;
Rot_tip_opt = dPhi_L*Z_opt;
Str_m_opt = -zp_max*ddPhi_0*Z_opt;
Vp_opt = Bf/(K1*Cp)*Re_opt_f*Theta*OM*ddW_b / den_opt;
Pout_opt = ((Bf/K1*Theta*OM*ddW_b)^2*om_n*(1/Cp)*Re_opt_f) /
den_opt^2;
I_opt = Pout_opt/Vp_opt;

%output data:
opvolume = (2*max(abs(W_tip_opt)) +
H0*cos(max(abs(Rot_tip_opt))+L0*sin(max(abs(Rot_tip_opt))))*(L+L0)*(m
ax(b,b0))*1e6; % approximate volume in cm^3
%volume = 2*max(abs(W_tip_opt))*L*(max(b,b0))*1e6; % approximate
volume in cm^3

```

```

P_dens_op = (Pout_opt/1e-6)/opvolume;
volmm3 = opvolume*1e3;
volstatic = (staticdef + t_t + H0) * (L + L0) * max(bx) *1e6;
footprint = (L+L0)*(max(b,b0))*1e6;
P_dens_st = (max(Pout_opt(:))/1e-6)/volstatic;
beammass = rho_c*mean(bx)*t_t*L ;
pmmass = rho_0*H0*b0*L0+ rho_c*bx(length(bx))*t_t*L0;
devicemass = rho_c*mean(bx)*t_t*L + rho_c*bx(length(bx))*t_t*L0 +
rho_0*H0*b0*L0;

om_r(ll,lo) = om_n/2/pi;
om_ar(ll,lo) = om_n/2/pi*OM_oc;
OM_ocout=OM_oc;
Pout_out(ll,lo) =(Pout_opt)*1e6;
Popdens(ll,lo) =P_dens_op;
Pstdens(ll,lo) =P_dens_st;
SpecificPower(ll,lo) = Pout_opt/devicemass;
maxustrain(ll,lo)=abs(Str_m_opt)/1e-6;
maxV(ll,lo)=abs(Vp_opt);
maxuA(ll,lo)=abs(I_opt)/1e-6;
wtip(ll,lo)=abs(W_tip_opt)*1e6;

end
end

```


A.3 Tapered {3-3} Mode Harvester Model without Proof Mass

This specific case is for the {3-3} Mode MEMS tapered unimorph without a proof mass discussed in Section 4.1.2.

```
%%%%%%%%%%%%%%%%%%%%%%%%%%%%%%%%%%%%%%%%%%%%%%%%%%%%%%%%%%%%%%%%%%%%%%%%%%
%UNIMORPH TAPERED BEAM - 33 OPERATION NO PROOF MASS
%A. Mracek based on work of N. du Toit
%%%%%%%%%%%%%%%%%%%%%%%%%%%%%%%%%%%%%%%%%%%%%%%%%%%%%%%%%%%%%%%%%%%%%%%%%%

% input parameters
Zeta_m = 0.005;
freqin = 1e3 %input vibration frequency in Hz
om_b_ref = freqin*2*pi; % input vibration frequency in rad/s
ddW_b_ref = 9.81*sqrt(freqin*1.579e-4);

% Piezo material properties
eval('pzt_5a_mat_prop');

% assign relevant material properties for current configuration
% plate configuration
cE33 = sE11/(sE11*sE33-sE13^2);
e31 = (sE11*d33-sE13*d31)/(sE11*sE33-sE13^2);
e33 = e31;
Eps_S_33 = Eps_T_33-(sE33*d31^2-
2*sE13*d31*d33+sE11*d33^2)/(sE11*sE33-sE13^2);
KS33 = Eps_S_33/Eps_0;

% parameter assignment
c_E = cE33;
e_m = e33;
Eps_S = Eps_S_33;

% Material properties for layers
% PZT
E_pzt_p = c_E; % PZT plate stiffness
rho_pzt = rho_p;

% platinum
E_pt = 170e9; % Pt - MEMSnet.org
rho_pt = 21440; % MatWeb.com
nu_pt = 0.39;
E_pt_p = E_pt/(1-nu_pt^2); % plate modulus

% titanium
E_ti = 110e9; % Ti - MEMSnet.org
rho_ti = 4510; % MEMSnet.org
nu_ti = 0.34;
```

```

E_ti_p = E_ti/(1-nu_ti^2); % plate modulus

% silicon
E_si = 112.4e9; %www.matweb.com
rho_si = 2329;
nu_si = 0.28;
E_si_p = E_si/(1-nu_si^2); % plate modulus

% SiNx
E_sinx = 313e9; %Noel's Sood analysis
rho_sinx = 3000;
nu_sinx = 0.30;
E_sinx_p = E_sinx/(1-nu_sinx^2); % plate modulus

% SiO2
E_sio2 = 69e9; %Noel's Sood analysis
rho_sio2 = 2300;
nu_sio2 = 0.15;
E_sio2_p = E_sio2/(1-nu_sio2^2); % plate modulus

% ZrO2
E_zro2 = 244e9; %Noel's Sood analysis
rho_zro2 = 6000;
nu_zro2 = 0.27;
E_zro2_p = E_zro2/(1-nu_zro2^2); % plate modulus

%%%%%%%%%%%%%%%%%%%%%%%%%%%%%%%%%%%%%%%%%%%%%%%%%%%%%%%%%%%%%%%%%%%%%%%%

% Define parameters
%device parameters:
Lmin = 0.5e-3;
Lmax = 1.5e-3;
Lrange = [Lmin:(Lmax-Lmin)/300:Lmax];
for ll=1:length(Lrange)
L = Lrange(ll);
b = 1.0e-3 % beam width in m
% specify thicknesses
t_pzt = 0.5e-6;
t_zro2 = 0.05e-6; %fixed by process
t_si = 0; %no Si layer used
t_sinx = 0.4e-6;
t_sio2 = 0.1e-6;
%electrode parameters
t_pt = 0.2e-6;
t_ti = 0.02e-6; %fixed, not from optimization code
p = 16e-6; %pitch = spacing between electrode centers
a = 4e-6; %width of electrodes

%%%%%%%%%%%%%%%%%%%%%%%%%%%%%%%%%%%%%%%%%%%%%%%%%%%%%%%%%%%%%%%%%%%%%%%%

% Define parameters for mass at the end
L0 = 0.0e-3; % NO proof mass
b0min = 0.1*b;

```

```

b0max = 1.2*b;
b0range = [b0min:(b0max-b0min)/500:b0max];
for bb = 1:length(b0range)
b0 = b0range(bb); % breadth of the mass
H0 = 0; % height of the mass w/o middle pt layer
rho_0 = rho_pt; ;

%Calculate taper slope:
taperstore(bb) = 0.5*(b0-b)/L;
taper=taperstore(bb);
fparea = 2*0.5*L*b + b0*L; %foot print area of the beam, not
including the proof mass

%Create width matrix:
xstep = L/100;
xx = (0:xstep:L);
for jj = 1:length(xx)
    bx(jj) = b + 2*taper*xx(jj);
end

for jj = 1:length(bx)
    elecA(jj) = 0.5;
end

% Specify layers
t_1 = [t_sinx t_sio2 t_zro2 t_pzt t_ti t_pt]; %set up for
Si base with pzt then electrode
E_1 = [E_sinx_p E_sio2_p E_zro2_p E_pzt_p E_ti_p E_pt_p];
rho_1 = [rho_sinx rho_sio2 rho_zro2 rho_pzt rho_ti rho_pt];

totalthick= sum(t_1);

% determine the neutral axis
for jj = 1: length(bx) %sum over beam length
    for ii = 1: length(t_1) %sum over beam thickness
        if ii == 1
            zb_1(ii) = t_1(ii)/2;
        else
            zb_1(ii) = zb_1(ii-1) + t_1(ii-1)/2 + t_1(ii)/2;
        end
    end
    % zb of individual layers from ground
    EAzb(ii,jj) = zb_1(ii)*t_1(ii)*bx(jj)*E_1(ii);
    EA(ii,jj) = t_1(ii)*bx(jj)*E_1(ii);
end % for
EAzbsum = sum(EAzb);
EAsum = sum(EA);
zb(jj)=EAzbsum(jj)/EAsum(jj); %note: zb is constant with x b/c the
b(x) in EA divides out
end

```

```

%%%%%%%%%%%%%%%%%%%%%%%%%%%%%%%%%%%%%%%%%%%%%%%%%%%%%%%%%%%%%%%%%%%%%%%%
% useful parameters
ind_pzt = 4; %update if changing layers under pzt
zp_max = zb_l(ind_pzt)+t_pzt/2-zb; from uniform case
zp_max = max(zb_l(ind_pzt)+t_pzt/2-zb); % max piezo distance
from neutral axis set manually
zp_ave = abs(zb_l(ind_pzt)-zb); from uniform case
zp_ave = abs(zb_l(ind_pzt)-mean(zb)); % distance between neutral
axis and middle of piezo element
t_t = sum(t_l);
%%%%%%%%%%%%%%%%%%%%%%%%%%%%%%%%%%%%%%%%%%%%%%%%%%%%%%%%%%%%%%%%%%%%%%%%

% determine the moment of inertia and effective EI for each layer
for jj = 1: length(bx)
    for ii = 1:ind_pzt
        I_l(ii,jj) = 1/12*bx(jj)*t_l(ii)^3 +
t_l(ii)*bx(jj)*(zb_l(ii)-zb(jj))^2;
    end % for ii
    for ii = (ind_pzt+1):length(t_l) %modify for fractional area
coverage of electrodes
        I_l(ii,jj) = 1/12*(bx(jj)*elecA(jj))*t_l(ii)^3 +
t_l(ii)*(bx(jj)*elecA(jj))*(zb_l(ii)-zb(jj))^2;
    end
    I_sx = sum(I_l,1);

    for ii=1:length(t_l)
        EI_l(ii,jj) = E_l(ii)*I_l(ii,jj);
    end
    EI_sx = sum(EI_l,1);
    E_effx(jj) = EI_sx(jj)/I_sx(jj); % effective young's modulus as a
function of x
end

% effective density, NOT a function of x
rho_c = 0;
for ii = 1:length(t_l)
    rho_c = rho_c+t_l(ii)*rho_l(ii);
end % for ii
rho_c = rho_c/t_t;

% mass per length as a function of x
for jj = 1:length(bx)
    m(jj) = rho_c*bx(jj)*t_t;
end

%NO proof mass:
M0 = 0;
S0 = 0;
I0 = 0;

%calculate static deflection of beam:

```



```

for jj=1:length(xx)
    %from point load:
    stdef1(jj) = (M0*9.81*xx(jj)^2)/(6*EI_sx(jj))*(3*L-xx(jj));
    %from moment:
    stdef2(jj) = (S0*xx(jj)^2)/(2*EI_sx(jj));
    %superposition:
    stdefT(jj)=stdef1(jj)+stdef2(jj);
end
staticdef = stdefT(length(xx));

%%%%%%%%%%%%%%%%%%%%%%%%%%%%%%%%%%%%%%%%%%%%%%%%%%%%%%%%%%%%%%%%%%%%%%%%
%%
%define coefficients for first 3 clamped-free traditional beam modes:

c1 = 1;
s1 = 0.73410;
B1 = 1.8751/L;

c2 = 1;
s2 = 1.01847;
B2 = 4.6941/L;

c3 = 1;
s3 = 0.99923;
B3 = 7.8548/L;

%define mode shapes and integrals for first three modes (without p.m.)

Phi1_L = c1*((cosh(B1*L)-cos(B1*L))-s1*(sinh(B1*L)-sin(B1*L)));
dPhi1_L = c1*B1*((sinh(B1*L)+sin(B1*L))-s1*(cosh(B1*L)-
cos(B1*L)));
ddPhi1_0 = c1*B1^2*((cosh(B1*0)+cos(B1*0))-
s1*(sinh(B1*0)+sin(B1*0)));

Phi2_L = c2*((cosh(B2*L)-cos(B2*L))-s2*(sinh(B2*L)-sin(B2*L)));
dPhi2_L = c2*B2*((sinh(B2*L)+sin(B2*L))-s2*(cosh(B2*L)-
cos(B2*L)));
ddPhi2_0 = c2*B2^2*((cosh(B2*0)+cos(B2*0))-
s2*(sinh(B2*0)+sin(B2*0)));

Phi3_L = c3*((cosh(B3*L)-cos(B3*L))-s3*(sinh(B3*L)-sin(B3*L)));
dPhi3_L = c3*B3*((sinh(B3*L)+sin(B3*L))-s3*(cosh(B3*L)-
cos(B3*L)));
ddPhi3_0 = c3*B3^2*((cosh(B3*0)+cos(B3*0))-
s3*(sinh(B3*0)+sin(B3*0)));

for jj = 1:length(xx)
    Tsilx(jj) = c1*((cosh(B1*xx(jj))-cos(B1*xx(jj))) -
s1*(sinh(B1*xx(jj))-sin(B1*xx(jj))));
    ddTsilx(jj) = c1*((B1^2*cosh(B1*xx(jj))+B1^2*cos(B1*xx(jj))) -
s1*(B1^2*sinh(B1*xx(jj))+B1^2*sin(B1*xx(jj))));

```

```

    Tsi2x(jj) = c2*( (cosh(B2*xx(jj))-cos(B2*xx(jj))) -
s2*(sinh(B2*xx(jj))-sin(B2*xx(jj)))));
    ddTsi2x(jj) = c2*( (B2^2*cosh(B2*xx(jj))+B2^2*cos(B2*xx(jj))) -
s2*(B2^2*sinh(B2*xx(jj))+B2^2*sin(B2*xx(jj)))));

    Tsi3x(jj) = c3*( (cosh(B3*xx(jj))-cos(B3*xx(jj))) -
s3*(sinh(B3*xx(jj))-sin(B3*xx(jj)))));
    ddTsi3x(jj) = c3*( (B3^2*cosh(B3*xx(jj))+B3^2*cos(B3*xx(jj))) -
s3*(B3^2*sinh(B3*xx(jj))+B3^2*sin(B3*xx(jj)))));
end

% natural freq of each mode acc to modal analysis
om_n_a1 = sqrt(B1^2*sqrt(mean(EI_sx./m)));
om_n_a2 = sqrt(B2^2*sqrt(mean(EI_sx./m)));
om_n_a3 = sqrt(B3^2*sqrt(mean(EI_sx./m)));

%om_n_a1 = B1^2*sqrt(mean(EI_sx./m));
%om_n_a2 = B2^2*sqrt(mean(EI_sx./m));
%om_n_a3 = B3^2*sqrt(mean(EI_sx./m));

f1 = om_n_a1/2/pi;
f2 = om_n_a2/2/pi;
f3 = om_n_a3/2/pi;

%Mass matrix:
%M11:
for ii=1:length(t_l)
    for jj=1:length(xx)
        Mint11(ii,jj) =
bx(jj)*t_l(ii)*rho_l(ii)*Tsilx(jj)*Tsilx(jj)*xstep;
        Mint12(ii,jj) =
bx(jj)*t_l(ii)*rho_l(ii)*Tsilx(jj)*Tsi2x(jj)*xstep;
        Mint13(ii,jj) =
bx(jj)*t_l(ii)*rho_l(ii)*Tsilx(jj)*Tsi3x(jj)*xstep;
        Mint22(ii,jj) =
bx(jj)*t_l(ii)*rho_l(ii)*Tsi2x(jj)*Tsi2x(jj)*xstep;
        Mint23(ii,jj) =
bx(jj)*t_l(ii)*rho_l(ii)*Tsi2x(jj)*Tsi3x(jj)*xstep;
        Mint33(ii,jj) =
bx(jj)*t_l(ii)*rho_l(ii)*Tsi3x(jj)*Tsi3x(jj)*xstep;
    end
    M_l11(ii) = sum(Mint11(ii,:));
    M_l12(ii) = sum(Mint12(ii,:));
    M_l13(ii) = sum(Mint13(ii,:));
    M_l22(ii) = sum(Mint22(ii,:));
    M_l23(ii) = sum(Mint23(ii,:));
    M_l33(ii) = sum(Mint33(ii,:));
end
%account for proof mass: (Doesn't do anything here but assemble)

```

```

MM(1,1) = sum(M_l11) + M0*Phi1_L*Phi1_L +
S0*(Phi1_L*dPhi1_L+Phi1_L*dPhi1_L) + I0*dPhi1_L*dPhi1_L;
MM(1,2) = sum(M_l12) + M0*Phi1_L*Phi2_L +
S0*(Phi1_L*dPhi2_L+Phi2_L*dPhi1_L) + I0*dPhi1_L*dPhi2_L;
MM(1,3) = sum(M_l13) + M0*Phi1_L*Phi3_L +
S0*(Phi1_L*dPhi3_L+Phi3_L*dPhi1_L) + I0*dPhi1_L*dPhi3_L;
MM(2,2) = sum(M_l22) + M0*Phi2_L*Phi2_L +
S0*(Phi2_L*dPhi2_L+Phi2_L*dPhi2_L) + I0*dPhi2_L*dPhi2_L;
MM(2,3) = sum(M_l23) + M0*Phi2_L*Phi3_L +
S0*(Phi2_L*dPhi3_L+Phi3_L*dPhi2_L) + I0*dPhi2_L*dPhi3_L;
MM(3,3) = sum(M_l33) + M0*Phi3_L*Phi3_L +
S0*(Phi3_L*dPhi3_L+Phi3_L*dPhi3_L) + I0*dPhi3_L*dPhi3_L;
MM(2,1) = MM(1,2);
MM(3,1) = MM(1,3);
MM(3,2) = MM(2,3);
MM;

```

```
%Stiffness matrix:
```

```

for jj=1:length(xx)
    for ii=1:length(t_l)
        Kint11(ii,jj) =
E_l(ii)*I_l(ii,jj)*ddTsi1x(jj)*ddTsi1x(jj)*xstep;
        Kx11(jj) = sum(Kint11(:,jj));

        Kint12(ii,jj) =
E_l(ii)*I_l(ii,jj)*ddTsi1x(jj)*ddTsi2x(jj)*xstep;
        Kx12(jj) = sum(Kint12(:,jj));

        Kint13(ii,jj) =
E_l(ii)*I_l(ii,jj)*ddTsi1x(jj)*ddTsi3x(jj)*xstep;
        Kx13(jj) = sum(Kint13(:,jj));

        Kint22(ii,jj) =
E_l(ii)*I_l(ii,jj)*ddTsi2x(jj)*ddTsi2x(jj)*xstep;
        Kx22(jj) = sum(Kint22(:,jj));

        Kint23(ii,jj) =
E_l(ii)*I_l(ii,jj)*ddTsi2x(jj)*ddTsi3x(jj)*xstep;
        Kx23(jj) = sum(Kint23(:,jj));

        Kint33(ii,jj) =
E_l(ii)*I_l(ii,jj)*ddTsi3x(jj)*ddTsi3x(jj)*xstep;
        Kx33(jj) = sum(Kint33(:,jj));

    end
end
KK(1,1) = sum(Kx11);
KK(1,2) = sum(Kx12);
KK(1,3) = sum(Kx13);
KK(2,2) = sum(Kx22);
KK(2,3) = sum(Kx23);
KK(3,3) = sum(Kx33);

```

```

KK(2,1) = KK(1,2);
KK(3,1) = KK(1,3);
KK(3,2) = KK(2,3);
KK;

%now apply R-R method to get actual mode shape:
[V,D] = eig(inv(MM)*KK);
%natural frequencies of first 3 modes:
om_nall(1) = sqrt(D(1,1));
om_nall(2) = sqrt(D(2,2));
om_nall(3) = sqrt(D(3,3));

[ordered_om,i_om]=sort(om_nall);
om_n1 = ordered_om(1);
om_n2 = ordered_om(2);
om_n3 = ordered_om(3);

%coefficients of first mode:
C1 = V(1,i_om(1));
C2 = V(2,i_om(1));
C3 = V(3,i_om(1));

%combine modes 1, 2 and 3 from above to get actual mode shape:
Tsiallx = C1.*Tsi1x + C2.*Tsi2x + C3.*Tsi3x;
ddTsiallx = C1.*ddTsi1x + C2.*ddTsi2x + C3.*ddTsi3x;
Phi_Lall = C1*Phi1_L + C2*Phi2_L + C3*Phi3_L;
dPhi_Lall = C1*dPhi1_L + C2*dPhi2_L + C3*dPhi3_L;
ddPhi_0all = C1*ddPhi1_0 + C2*ddPhi2_0 + C3*ddPhi3_0;

%now recalculate using only first mode found above:

%Mass matrix:
for ii = 1:length(t_l)
    for jj = 1:length(bx)
        Mint(ii,jj) = bx(jj)*t_l(ii)*rho_l(ii)*Tsiallx(jj)^2*xstep;
    end
    M_l(ii) = sum(Mint(ii,:));
end
M1 = sum(M_l) + M0*Phi_Lall^2 + 2*S0*Phi_Lall*dPhi_Lall +
I0*dPhi_Lall^2; % effective mass

%Stiffness matrix:
for ii = 1:length(t_l)
    for jj = 1:length(xx)
        Kint(ii,jj) = E_l(ii)*I_l(ii,jj)*ddTsiallx(jj)^2*xstep;
    end
    K_l(ii) = sum(Kint(ii,:));
end
K1 = sum(K_l);

%Coupling matrix
for jj=1:length(bx)

```

```

    Thetax(jj) = t_pzt*bx(jj)*zp_ave*e_m*ddTsiallx(jj)*(1/(p-
a))*xstep;
end %for jj (length)
Theta = sum(Thetax);

%Capacitance matrix
for jj = 1:length(bx)
    Cpx(jj) = t_pzt*bx(jj)*Eps_S*(1/(p-a)^2)*xstep;
end %for jj (length)
Cp = sum(Cpx);

Ke_2 = Theta^2/(K1*Cp);

%Input matrix adjusted to account for proof mass (again, no effect)
for jj = 1:length(xx)
    Bf_int(jj)=rho_c*t_t*bx(jj)*Tsiallx(jj)*xstep;
end
Bf = sum(Bf_int) + M0*Phi_Lall + 1/2*M0*dPhi_Lall*(2*L+L0);

% estimate the natural frequency acc to lumped model
%om_n = sqrt(K1/M1);
om_n = om_n1;
om = om_n*sqrt(1+Ke_2);
%OM = om/om_n;
OM = om_b_ref/om_n; %want to make sure that the OM reflects off-
optimum operation

% estimate the natural frequency acc to lumped model
Ke_2 = Theta*Theta*inv(K1*Cp);

om = om_n*sqrt(1+Ke_2);
%OM = om/om_n;
OM = om_b_ref/om_n; %want to make sure that the OM reflects off-
optimum operation

% adjust the virbation amplitude to the reference frequency:
%ddW_b = sqrt(ddW_b_ref^2*om_n/om_b_ref);

ddW_b = ddW_b_ref; %keeping input the same, represented off-
resonance earlier

% Analyse the system
% calculate the sc and oc resonance freq ratios
OM_oc = sqrt(1+Theta^2/(K1*Cp));
r_opt = (OM_oc^4 + (4*Zeta_m^2-2)*OM_oc^2 + 1)/(OM_oc^6 +
(4*Zeta_m^2-2*(1+Theta^2/(K1*Cp)))*OM_oc^4 +
(1+Theta^2/(K1*Cp))^2*OM_oc^2);
Re_opt_oc = sqrt(r_opt);
Rl_opt_oc = round(Re_opt_oc/(Cp*om_n));
OM_sc = 1;

```

```

r_opt      = (OM_sc^4 + (4*Zeta_m^2-2)*OM_sc^2 + 1)/(OM_sc^6 +
(4*Zeta_m^2-2*(1+Theta^2/(K1*Cp)))*OM_sc^4 +
(1+Theta^2/(K1*Cp))^2*OM_sc^2);
Re_opt_sc  = sqrt(r_opt);
Rl_opt_sc  = round(Re_opt_sc/(Cp*om_n));
Rl_opt_df  = Rl_opt_oc-Rl_opt_sc;

% Specify open circuit optimum resistance:
Rl = Rl_opt_oc;
Re = Rl*Cp*om_n;

% Next calculate the response of the system
den      = sqrt( (1 - (1 + 2*Zeta_m*Re)*OM^2 )^2 + ( (2*Zeta_m +
(1+Theta^2/(K1*Cp))*Re)*OM - Re*OM^3 )^2 );
Z        = (Bf/K1*sqrt(1+Re^2*OM^2))*ddW_b / den;
W_tip    = Phi_Lall*Z;
Rot_tip  = dPhi_Lall*Z;
Str_m    = -zp_max*ddPhi_0all*Z;
Vp       = (Bf/(K1*Cp)*Re*Theta*OM)*ddW_b / den;
Pout     = ((Bf^2/K1^2)*Theta^2*OM^2*om_n*(1/Cp)*Re)*ddW_b^2 /
den^2;
Ip       = Pout/Vp;

Re_opt_f  = sqrt((OM^4 + (4*Zeta_m^2-2)*OM^2 + 1)/(OM^6 +
(4*Zeta_m^2-2*(1+Theta^2/(K1*Cp)))*OM^4 +
(1+Theta^2/(K1*Cp))^2*OM^2));
Rl_opt_f  = Re_opt_f/(Cp*om_n);
den_opt   = sqrt( (1 - (1 + 2*Zeta_m*Re_opt_f)*OM^2 )^2 + (
(2*Zeta_m + (1+Theta^2/(K1*Cp))*Re_opt_f)*OM - Re_opt_f*OM^3 )^2
);
Z_opt     = Bf/K1*sqrt(1+(Re_opt_f*OM)^2)*ddW_b / den_opt;
W_tip_opt = Phi_Lall*Z_opt;
Rot_tip_opt = dPhi_Lall*Z_opt;
Str_m_opt = -zp_max*ddPhi_0all*Z_opt;
Vp_opt    = Bf/(K1*Cp)*Re_opt_f*Theta*OM*ddW_b / den_opt;
Pout_opt  = ((Bf/K1*Theta*OM*ddW_b)^2*om_n*(1/Cp)*Re_opt_f) /
den_opt^2;
I_opt     = Pout_opt/Vp_opt;

%output data:
opvolume = (2*max(abs(W_tip_opt)) +
H0*cos(max(abs(Rot_tip_opt)))+L0*sin(max(abs(Rot_tip_opt))))*(L+L0)*(m
ax(b,b0))*1e6; % approximate volume in cm^3
%volume = 2*max(abs(W_tip_opt))*L*(max(b,b0))*1e6; % approximate
volume in cm^3
P_dens_op = (Pout_opt/1e-6)/opvolume;
volmm3 = opvolume*1e3;
volstatic = (staticdef + t_t + H0) * (L + L0) * max(bx) *1e6;
footprint = (L+L0)*(max(b,b0))*1e6;
P_dens_st = (max(Pout_opt(:))/1e-6)/volstatic;

```

```

beammass = rho_c*mean(bx)*t_t*L ;
pmmass = rho_0*H0*b0*L0+ rho_c*bx(length(bx))*t_t*L0;
devicemass = rho_c*mean(bx)*t_t*L + rho_c*bx(length(bx))*t_t*L0 +
rho_0*H0*b0*L0;

om_r(ll,bb)          = om_n/2/pi;
om_ar(ll,bb) = om_n/2/pi*OM_oc;
OM_ocout=OM_oc;
Pout_out(ll,bb) =(Pout_opt)*1e6;
Popdens(ll,bb) =P_dens_op;
Pstdens(ll,bb) =P_dens_st;
SpecificPower(ll,bb) = Pout_opt/devicemass;
maxustrain(ll,bb)=abs(Str_m_opt)/1e-6;
maxV(ll,bb)=abs(Vp_opt);
maxuA(ll,bb)=abs(I_opt)/1e-6;
wtip(ll,bb)=abs(W_tip_opt)*1e6;

end
end

```


A.4 Tapered {3-3} Mode Harvester Model with Proof Mass

This specific case is for the {3-3} Mode MEMS tapered unimorph with a proof mass discussed in Section 4.1.3.

```

%%%%%%%%%%%%%%%%%%%%%%%%%%%%%%%%%%%%%%%%%%%%%%%%%%%%%%%%%%%%%%%%%%%%%%%%
%UNIMORPH TAPERED BEAM - 33 OPERATION with PROOF MASS
%A. Mracek based on work of N. du Toit
%%%%%%%%%%%%%%%%%%%%%%%%%%%%%%%%%%%%%%%%%%%%%%%%%%%%%%%%%%%%%%%%%%%%%%%%

%%%%%%%%%%%%%%%%%%%%%%%%%%%%%%%%%%%%%%%%%%%%%%%%%%%%%%%%%%%%%%%%%%%%%%%%
% input parameters
Zeta_m = 0.005;
freqin = 1e3 %input vibration frequency in Hz
om_b_ref = freqin*2*pi; % input vibration frequency in rad/s
ddW_b_ref = 9.81*sqrt(freqin*1.579e-4);

% Piezo material properties
eval('pzt_5a_mat_prop');

% assign relevant material properties for current configuration
% plate configuration
cE33 = sE11/(sE11*sE33-sE13^2);
e31 = (sE11*d33-sE13*d31)/(sE11*sE33-sE13^2);
e33 = e31;
Eps_S_33 = Eps_T_33-(sE33*d31^2-
2*sE13*d31*d33+sE11*d33^2)/(sE11*sE33-sE13^2);
KS33 = Eps_S_33/Eps_0;

% parameter assignment
c_E = cE33;
e_m = e33;
Eps_S = Eps_S_33;

% Material properties for layers
% PZT
E_pzt_p = c_E; % PZT plate stiffness
rho_pzt = rho_p;

% platinum
E_pt = 170e9; % Pt - MEMSnet.org
rho_pt = 21440; % MatWeb.com
nu_pt = 0.39;
E_pt_p = E_pt/(1-nu_pt^2); % plate modulus

% titanium
E_ti = 110e9; % Ti - MEMSnet.org
rho_ti = 4510; % MEMSnet.org

```

```

nu_ti = 0.34;
E_ti_p = E_ti/(1-nu_ti^2); % plate modulus

% silicon
E_si = 112.4e9; %www.matweb.com
rho_si = 2329;
nu_si = 0.28;
E_si_p = E_si/(1-nu_si^2); % plate modulus

% SiNx
E_sinx = 313e9; %Noel's Sood analysis
rho_sinx = 3000;
nu_sinx = 0.30;
E_sinx_p = E_sinx/(1-nu_sinx^2); % plate modulus

% SiO2
E_sio2 = 69e9; %Noel's Sood analysis
rho_sio2 = 2300;
nu_sio2 = 0.15;
E_sio2_p = E_sio2/(1-nu_sio2^2); % plate modulus

% ZrO2
E_zro2 = 244e9; %Noel's Sood analysis
rho_zro2 = 6000;
nu_zro2 = 0.27;
E_zro2_p = E_zro2/(1-nu_zro2^2); % plate modulus

%%%%%%%%%%%%%%%%%%%%%%%%%%%%%%%%%%%%%%%%%%%%%%%%%%%%%%%%%%%%%%%%%%%%%%%%
% Define parameters
%device parameters:
L = 0.3e-3; % also 0.5e-3 and 0.7e-3, in m
b = 1.0e-3 % beam root width in m
% specify thicknesses
t_pzt = 0.5e-6;
t_zro2 = 0.05e-6; %fixed by process
t_si = 0; %no Si layer used
t_sinx = 0.4e-6;
t_sio2 = 0.1e-6;
%electrode parameters
t_pt = 0.2e-6;
t_ti = 0.02e-6; %fixed, not from optimization code
p = 16e-6; %pitch = spacing between electrode centers
a = 4e-6; %width of electrodes

%%%%%%%%%%%%%%%%%%%%%%%%%%%%%%%%%%%%%%%%%%%%%%%%%%%%%%%%%%%%%%%%%%%%%%%%
% Define parameters for mass at the end
L0min = 0.0;
L0max = 0.5e-3;
L0range = [L0min:(L0max-L0min)/500:L0max];
for lo = 1:length(L0range)
L0 = L0range(lo)
b0min = 0.1*b;

```

```

b0max = 1.2*b;
b0range = [b0min:(b0max-b0min)/500:b0max];
for bb = 1:length(b0range)
b0 = b0range(bb) %beam tip (and proof mass) width
H0 = 3e-6; % height of the mass w/o middle pt layer
rho_0 = rho_pt; ;

%Calculate taper slope:
taperstore(bb) = 0.5*(b0-b)/L;
taper=taperstore(bb);
fparea = 2*0.5*L*b + b0*L; %foot print area of the beam, not
including the proof mass

%Create width matrix:
xstep = L/100;
xx = (0:xstep:L);
for jj = 1:length(xx)
    bx(jj) = b + 2*taper*xx(jj);
end

for jj = 1:length(bx)
    elecA(jj) = 0.5;
end

% Specify layers
t_1 = [t_sinx t_sio2 t_zro2 t_pzt t_ti t_pt]; %set up for
Si base with pzt then electrode
E_1 = [E_sinx_p E_sio2_p E_zro2_p E_pzt_p E_ti_p E_pt_p];
rho_1 = [rho_sinx rho_sio2 rho_zro2 rho_pzt rho_ti rho_pt];

totalthick= sum(t_1);

% determine the neutral axis
for jj = 1: length(bx) %sum over beam length
    for ii = 1: length(t_1) %sum over beam thickness
        if ii == 1
            zb_1(ii) = t_1(ii)/2;
        else
            zb_1(ii) = zb_1(ii-1) + t_1(ii-1)/2 + t_1(ii)/2;
        end % if
        EAzb(ii,jj) = zb_1(ii)*t_1(ii)*bx(jj)*E_1(ii);
        EA(ii,jj) = t_1(ii)*bx(jj)*E_1(ii);
    end % for
    EAzbsum = sum(EAzb);
    EAsum = sum(EA);
    zb(jj)=EAzbsum(jj)/EAsum(jj); %note: zb is constant with x b/c the
b(x) in EA divides out
end

```

```

%%%%%%%%%%%%%%%%%%%%%%%%%%%%%%%%%%%%%%%%%%%%%%%%%%%%%%%%%%%%%%%%%%%%%%%%
%%
% useful parameters
ind_pzt = 4; %update if changing layers under pzt
%zp_max = zb_l(ind_pzt)+t_pzt/2-zb; from uniform case
zp_max = max(zb_l(ind_pzt)+t_pzt/2-zb); % max piezo distance
from neutral axis set manually
%zp_ave = abs(zb_l(ind_pzt)-zb); from uniform case
zp_ave = abs(zb_l(ind_pzt)-mean(zb)); % distance between neutral
axis and middle of piezo element
t_t = sum(t_l);
%%%%%%%%%%%%%%%%%%%%%%%%%%%%%%%%%%%%%%%%%%%%%%%%%%%%%%%%%%%%%%%%%%%%%%%%
%%

% determine the moment of inertia and effective EI for each layer
along x
for jj = 1: length(bx)
    for ii = 1:ind_pzt
        I_l(ii,jj) = 1/12*bx(jj)*t_l(ii)^3 +
t_l(ii)*bx(jj)*(zb_l(ii)-zb(jj))^2;
    end % for ii
    for ii = (ind_pzt+1):length(t_l) %modify for fractional area
coverage of electrodes
        I_l(ii,jj) = 1/12*(bx(jj)*elecA(jj))*t_l(ii)^3 +
t_l(ii)*(bx(jj)*elecA(jj))*(zb_l(ii)-zb(jj))^2;
    end
    I_sx = sum(I_l,1);

    for ii=1:length(t_l)
        EI_l(ii,jj) = E_l(ii)*I_l(ii,jj);
    end
    EI_sx = sum(EI_l,1);
    E_effx(jj) = EI_sx(jj)/I_sx(jj); % effective young's modulus as a
function of x
end

% effective density, NOT a function of x
rho_c = 0;
for ii = 1:length(t_l)
    rho_c = rho_c+t_l(ii)*rho_l(ii);
end % for ii
rho_c = rho_c/t_t;

% mass per length as a function of x
for jj = 1:length(bx)
    m(jj) = rho_c*bx(jj)*t_t;
end

% determine the mass per length for the Proof Mass
%proof mass assumed uniform in x
m0 = b0*(rho_c*t_t + rho_0*H0);

```

```

CG_m = (rho_c*t_t*b0*zb(length(bx)) +
rho_0*H0*b0*(t_t+H0/2))/(rho_c*t_t + rho_0*H0);
ox_ = L0/2; % depends on the beam config
oy_ = CG_m-zb(length(bx)); % distance from CG of mass to
neutral axis

% determine proof mass effective parameters for modal analysis
M0 = m0*L0;
%M0_ = M0/(m*L); (from uniform case)
M0_ = M0/(mean(m)*L);
% determine the static moment
S0 = M0*ox;
%S0_ = S0/(m*L^2); (from uniform case)
S0_ = S0/(mean(m)*L^2);
% determine the moment of inertia of the mass
for ii=1:length(t_l)
Iz(ii) = rho_l(ii)*b0*(1/12*L0*t_l(ii)^3 + t_l(ii)*L0*(zb_l(ii)-
CG_m)^2);
Ix(ii) = rho_l(ii)*b0*(1/12*t_l(ii)*L0^3);
end
IzM = rho_0*b0*(1/12*L0*H0^3 + H0*L0*(t_t+H0/2-CG_m)^2);
IxM = rho_0*b0*(1/12*H0*L0^3);
Iyy = sum(Iz) + sum(Ix) + IzM + IxM;
I0 = Iyy+M0*(ox^2+oy^2);
%I0_ = I0/(m*L^3); (from uniform case)
I0_ = I0/(mean(m)*L^3);

%calculate static deflection of beam:
for jj=1:length(xx)
%from point load:
stdef1(jj) = (M0*9.81*xx(jj)^2)/(6*EI_sx(jj))*(3*L-xx(jj));
%from moment:
stdef2(jj) = (S0*xx(jj)^2)/(2*EI_sx(jj));
%superposition:
stdefT(jj)=stdef1(jj)+stdef2(jj);
end
staticdef = stdefT(length(xx));

%%%%%%%%%%%%%%%%%%%%%%%%%%%%%%%%%%%%%%%%%%%%%%%%%%%%%%%%%%%%%%%%%%%%%%%%
%%
% find the mode shapes with the proof mass:
%x = [0.25:0.005:0.5]; % x = lambda bar; narrow range after
successive runs
x = [0.0:0.005:10.0]; % x = lambda bar; narrow range after
successive runs

for ii=1:length(x)
A11(ii) = (sinh(x(ii))+sin(x(ii))) + I0_*x(ii)^3*(-
cosh(x(ii))+cos(x(ii))) + S0_*x(ii)^2*(-sinh(x(ii))+sin(x(ii)));
A12(ii) = (cosh(x(ii))+cos(x(ii))) + I0_*x(ii)^3*(-sinh(x(ii))-
sin(x(ii))) + S0_*x(ii)^2*(-cosh(x(ii))+cos(x(ii)));

```

```

    A21(ii) = (cosh(x(ii))+cos(x(ii))) + M0_*x(ii)^1*( sinh(x(ii))-
sin(x(ii))) + S0_*x(ii)^2*( cosh(x(ii))-cos(x(ii)));
    A22(ii) = (sinh(x(ii))-sin(x(ii))) + M0_*x(ii)^1*( cosh(x(ii))-
cos(x(ii))) + S0_*x(ii)^2*( sinh(x(ii))+sin(x(ii)));
    % find the determinant
    %DET(ii) = A11(ii)*A22(ii)-A12(ii)*A21(ii);
    DET(ii) = det([A11(ii) A12(ii); A21(ii) A22(ii)]);
end

modecount = 1;
sgn(1)=sign(DET(1));
for ii=2:length(DET)
    sgn(ii)=sign(DET(ii));
    if sgn(ii)~=sgn(ii-1);
        Ind(modecount)=ii;
        modecount = modecount + 1;
    end
end

Ind1    = Ind(1);
Gamma1_ = x(Ind1);      % this is Beta*L
Ind2    = Ind(2);
Gamma2_ = x(Ind2);
Ind3    = Ind(3);
Gamma3_ = x(Ind3);
%clear x;

%define coefficients for first 3 clamped-free beam modes:

B1 = Gamma1_/L
c1 = 1; % arbitrary constant - Cancels out when determining the
displacement and other parameters
s1 = A12(Ind1)/A11(Ind1)

B2 = Gamma2_/L
c2 = 1; % arbitrary constant - Cancels out when determining the
displacement and other parameters
s2 = A12(Ind2)/A11(Ind2)

B3 = Gamma3_/L
c3 = 1; % arbitrary constant - Cancels out when determining the
displacement and other parameters
s3 = A12(Ind3)/A11(Ind3)

%define mode shapes and integrals for first three modes (without p.m.
at this point)

Phi1_L    = c1*((cosh(B1*L)-cos(B1*L))-s1*(sinh(B1*L)-sin(B1*L)));
dPhi1_L   = c1*B1*((sinh(B1*L)+sin(B1*L))-s1*(cosh(B1*L)-
cos(B1*L)));
ddPhi1_0  = c1*B1^2*((cosh(B1*0)+cos(B1*0))-
s1*(sinh(B1*0)+sin(B1*0)));

```

```

Phi2_L      = c2*((cosh(B2*L)-cos(B2*L))-s2*(sinh(B2*L)-sin(B2*L)));
dPhi2_L     = c2*B2*((sinh(B2*L)+sin(B2*L))-s2*(cosh(B2*L)-
cos(B2*L)));
ddPhi2_0    = c2*B2^2*((cosh(B2*0)+cos(B2*0))-
s2*(sinh(B2*0)+sin(B2*0)));

```

```

Phi3_L      = c3*((cosh(B3*L)-cos(B3*L))-s3*(sinh(B3*L)-sin(B3*L)));
dPhi3_L     = c3*B3*((sinh(B3*L)+sin(B3*L))-s3*(cosh(B3*L)-
cos(B3*L)));
ddPhi3_0    = c3*B3^2*((cosh(B3*0)+cos(B3*0))-
s3*(sinh(B3*0)+sin(B3*0)));

```

```

for jj = 1:length(xx)
    Tsi1x(jj) = c1*((cosh(B1*xx(jj))-cos(B1*xx(jj))) -
s1*(sinh(B1*xx(jj))-sin(B1*xx(jj))));
    ddTsi1x(jj) = c1*((B1^2*cosh(B1*xx(jj))+B1^2*cos(B1*xx(jj))) -
s1*(B1^2*sinh(B1*xx(jj))+B1^2*sin(B1*xx(jj))));

    Tsi2x(jj) = c2*((cosh(B2*xx(jj))-cos(B2*xx(jj))) -
s2*(sinh(B2*xx(jj))-sin(B2*xx(jj))));
    ddTsi2x(jj) = c2*((B2^2*cosh(B2*xx(jj))+B2^2*cos(B2*xx(jj))) -
s2*(B2^2*sinh(B2*xx(jj))+B2^2*sin(B2*xx(jj))));

    Tsi3x(jj) = c3*((cosh(B3*xx(jj))-cos(B3*xx(jj))) -
s3*(sinh(B3*xx(jj))-sin(B3*xx(jj))));
    ddTsi3x(jj) = c3*((B3^2*cosh(B3*xx(jj))+B3^2*cos(B3*xx(jj))) -
s3*(B3^2*sinh(B3*xx(jj))+B3^2*sin(B3*xx(jj))));
end

```

```

% natural freq of each mode acc to modal analysis
om_n_a1 = sqrt(B1^2*sqrt(mean(EI_sx./m)));
om_n_a2 = sqrt(B2^2*sqrt(mean(EI_sx./m)));
om_n_a3 = sqrt(B3^2*sqrt(mean(EI_sx./m)));

```

```

f1 = om_n_a1/2/pi
f2 = om_n_a2/2/pi
f3 = om_n_a3/2/pi

```

```

%Mass matrix:

```

```

%M11:
for ii=1:length(t_l)
    for jj=1:length(xx)
        Mint11(ii,jj) =
bx(jj)*t_l(ii)*rho_l(ii)*Tsi1x(jj)*Tsi1x(jj)*xstep;
        Mint12(ii,jj) =
bx(jj)*t_l(ii)*rho_l(ii)*Tsi1x(jj)*Tsi2x(jj)*xstep;
        Mint13(ii,jj) =
bx(jj)*t_l(ii)*rho_l(ii)*Tsi1x(jj)*Tsi3x(jj)*xstep;

```

```

        Mint22(ii,jj) =
bx(jj)*t_l(ii)*rho_l(ii)*Tsi2x(jj)*Tsi2x(jj)*xstep;
        Mint23(ii,jj) =
bx(jj)*t_l(ii)*rho_l(ii)*Tsi2x(jj)*Tsi3x(jj)*xstep;
        Mint33(ii,jj) =
bx(jj)*t_l(ii)*rho_l(ii)*Tsi3x(jj)*Tsi3x(jj)*xstep;
    end
    M_l11(ii) = sum(Mint11(ii,:));
    M_l12(ii) = sum(Mint12(ii,:));
    M_l13(ii) = sum(Mint13(ii,:));
    M_l22(ii) = sum(Mint22(ii,:));
    M_l23(ii) = sum(Mint23(ii,:));
    M_l33(ii) = sum(Mint33(ii,:));
end
%account for proof mass:
MM(1,1) = sum(M_l11) + M0*Phi1_L*Phi1_L +
S0*(Phi1_L*dPhi1_L+Phi1_L*dPhi1_L) + I0*dPhi1_L*dPhi1_L;
MM(1,2) = sum(M_l12) + M0*Phi1_L*Phi2_L +
S0*(Phi1_L*dPhi2_L+Phi2_L*dPhi1_L) + I0*dPhi1_L*dPhi2_L;
MM(1,3) = sum(M_l13) + M0*Phi1_L*Phi3_L +
S0*(Phi1_L*dPhi3_L+Phi3_L*dPhi1_L) + I0*dPhi1_L*dPhi3_L;
MM(2,2) = sum(M_l22) + M0*Phi2_L*Phi2_L +
S0*(Phi2_L*dPhi2_L+Phi2_L*dPhi2_L) + I0*dPhi2_L*dPhi2_L;
MM(2,3) = sum(M_l23) + M0*Phi2_L*Phi3_L +
S0*(Phi2_L*dPhi3_L+Phi3_L*dPhi2_L) + I0*dPhi2_L*dPhi3_L;
MM(3,3) = sum(M_l33) + M0*Phi3_L*Phi3_L +
S0*(Phi3_L*dPhi3_L+Phi3_L*dPhi3_L) + I0*dPhi3_L*dPhi3_L;
MM(2,1) = MM(1,2);
MM(3,1) = MM(1,3);
MM(3,2) = MM(2,3);
MM

%Stiffness matrix:
for jj=1:length(xx)
    for ii=1:length(t_l)
        Kint11(ii,jj) =
E_l(ii)*I_l(ii,jj)*ddTsi1x(jj)*ddTsi1x(jj)*xstep;
        Kx11(jj) = sum(Kint11(:,jj));

        Kint12(ii,jj) =
E_l(ii)*I_l(ii,jj)*ddTsi1x(jj)*ddTsi2x(jj)*xstep;
        Kx12(jj) = sum(Kint12(:,jj));

        Kint13(ii,jj) =
E_l(ii)*I_l(ii,jj)*ddTsi1x(jj)*ddTsi3x(jj)*xstep;
        Kx13(jj) = sum(Kint13(:,jj));

        Kint22(ii,jj) =
E_l(ii)*I_l(ii,jj)*ddTsi2x(jj)*ddTsi2x(jj)*xstep;
        Kx22(jj) = sum(Kint22(:,jj));

```



```

        Kint23(ii,jj) =
E_l(ii)*I_l(ii,jj)*ddTsi2x(jj)*ddTsi3x(jj)*xstep;
        Kx23(jj)      = sum(Kint23(:,jj));

        Kint33(ii,jj) =
E_l(ii)*I_l(ii,jj)*ddTsi3x(jj)*ddTsi3x(jj)*xstep;
        Kx33(jj)      = sum(Kint33(:,jj));

    end
end
KK(1,1) = sum(Kx11);
KK(1,2) = sum(Kx12);
KK(1,3) = sum(Kx13);
KK(2,2) = sum(Kx22);
KK(2,3) = sum(Kx23);
KK(3,3) = sum(Kx33);
KK(2,1) = KK(1,2);
KK(3,1) = KK(1,3);
KK(3,2) = KK(2,3);
KK

%now apply R-R method to get actual mode shape:
[V,D] = eig(inv(MM)*KK);
%natural frequencies of first 3 modes:
om_nall(1) = sqrt(D(1,1));
om_nall(2) = sqrt(D(2,2));
om_nall(3) = sqrt(D(3,3));

[ordered_om,i_om]=sort(om_nall);
om_n1 = ordered_om(1)
om_n2 = ordered_om(2)
om_n3 = ordered_om(3)

%coefficients of first mode:
C1 = V(1,i_om(1))
C2 = V(2,i_om(1))
C3 = V(3,i_om(1))

%combine modes 1, 2 and 3 from above to get actual mode shape:
Tsi1allx = C1.*Tsi1x + C2.*Tsi2x + C3.*Tsi3x;
ddTsi1allx = C1.*ddTsi1x + C2.*ddTsi2x + C3.*ddTsi3x;
Phi_Lall = C1*Phi1_L + C2*Phi2_L + C3*Phi3_L;
dPhi_Lall = C1*dPhi1_L + C2*dPhi2_L + C3*dPhi3_L;
ddPhi_0all = C1*ddPhi1_0 + C2*ddPhi2_0 + C3*ddPhi3_0;

%now recalculate using only first mode found above:

%Mass matrix:
for ii = 1:length(t_l)
    for jj = 1:length(bx)
        Mint(ii,jj) = bx(jj)*t_l(ii)*rho_l(ii)*Tsi1allx(jj)^2*xstep;
    end
end

```

```

    M_l(ii) = sum(Mint(ii,:));
end
M1 = sum(M_l) + M0*Phi_Lall^2 + 2*S0*Phi_Lall*dPhi_Lall +
I0*dPhi_Lall^2    % effective mass

%Stiffness matrix:
for ii = 1:length(t_l)
    for jj = 1:length(xx)
        Kint(ii,jj) = E_l(ii)*I_l(ii,jj)*ddTsiallx(jj)^2*xstep;
    end
    K_l(ii) = sum(Kint(ii,:));
end
K1 = sum(K_l)

%Coupling matrix
for jj=1:length(bx)
    Thetax(jj) = t_pzt*bx(jj)*zp_ave*e_m*ddTsiallx(jj)*(1/(p-
a))*xstep;
end %for jj (length)
Theta = sum(Thetax)

%Capacitance matrix
for jj = 1:length(bx)
    Cpx(jj) = t_pzt*bx(jj)*Eps_S*(1/(p-a)^2)*xstep;
end %for jj (length)
Cp = sum(Cpx)

Ke_2 = Theta^2/(K1*Cp)

%Input matrix adjusted to account for proof mass
for jj = 1:length(xx)
    Bf_int(jj)=rho_c*t_t*bx(jj)*Tsiallx(jj)*xstep;
end
Bf = sum(Bf_int) + M0*Phi_Lall + 1/2*M0*dPhi_Lall*(2*L+L0)

% estimate the natural frequency acc to lumped model
%om_n = sqrt(K1/M1);
om_n = om_n1
om = om_n*sqrt(1+Ke_2);
%OM = om/om_n;
OM = om_b_ref/om_n %want to make sure that the OM reflects off-
optimum operation

% estimate the natural frequency acc to lumped model
Ke_2 = Theta*Theta*inv(K1*Cp);

om = om_n*sqrt(1+Ke_2);
%OM = om/om_n;
OM = om_b_ref/om_n; %want to make sure that the OM reflects off-
optimum operation

```

```

% adjust the vibration amplitude to the reference frequency:
%ddW_b = sqrt(ddW_b_ref^2*om_n/om_b_ref);

ddW_b = ddW_b_ref; %keeping input the same, represented off-
resonance earlier

% Analyse the system
% calculate the sc and oc resonance freq ratios
OM_oc = sqrt(1+Theta^2/(K1*Cp));
r_opt = (OM_oc^4 + (4*Zeta_m^2-2)*OM_oc^2 + 1)/(OM_oc^6 +
(4*Zeta_m^2-2*(1+Theta^2/(K1*Cp)))*OM_oc^4 +
(1+Theta^2/(K1*Cp))^2*OM_oc^2);
Re_opt_oc = sqrt(r_opt);
Rl_opt_oc = round(Re_opt_oc/(Cp*om_n));
OM_sc = 1;
r_opt = (OM_sc^4 + (4*Zeta_m^2-2)*OM_sc^2 + 1)/(OM_sc^6 +
(4*Zeta_m^2-2*(1+Theta^2/(K1*Cp)))*OM_sc^4 +
(1+Theta^2/(K1*Cp))^2*OM_sc^2);
Re_opt_sc = sqrt(r_opt);
Rl_opt_sc = round(Re_opt_sc/(Cp*om_n));
Rl_opt_df = Rl_opt_oc-Rl_opt_sc;

% Specify open circuit optimum resistance
Rl = Rl_opt_oc;
Re = Rl*Cp*om_n;

% Next calculate the response of the system
den = sqrt( (1 - (1 + 2*Zeta_m*Re)*OM^2 )^2 + ( (2*Zeta_m +
(1+Theta^2/(K1*Cp))*Re)*OM - Re*OM^3 )^2 );
Z = (Bf/K1*sqrt(1+Re^2*OM^2))*ddW_b / den;
W_tip = Phi_Lall*Z;
Rot_tip = dPhi_Lall*Z;
Str_m = -zp_max*ddPhi_0all*Z;
Vp = (Bf/(K1*Cp)*Re*Theta*OM)*ddW_b / den;
Pout = ((Bf^2/K1^2)*Theta^2*OM^2*om_n*(1/Cp)*Re)*ddW_b^2 /
den^2;
Ip = Pout/Vp;

Re_opt_f = sqrt((OM^4 + (4*Zeta_m^2-2)*OM^2 + 1)/(OM^6 +
(4*Zeta_m^2-2*(1+Theta^2/(K1*Cp)))*OM^4 +
(1+Theta^2/(K1*Cp))^2*OM^2));
Rl_opt_f = Re_opt_f/(Cp*om_n);
den_opt = sqrt( (1 - (1 + 2*Zeta_m*Re_opt_f)*OM^2 )^2 + (
(2*Zeta_m + (1+Theta^2/(K1*Cp))*Re_opt_f)*OM(ii) - Re_opt_f*OM^3 )^2
);
Z_opt = Bf/K1*sqrt(1+(Re_opt_f*OM)^2)*ddW_b / den_opt;
W_tip_opt = Phi_Lall*Z_opt;
Rot_tip_opt = dPhi_Lall*Z_opt;
Str_m_opt = -zp_max*ddPhi_0all*Z_opt;
Vp_opt = Bf/(K1*Cp)*Re_opt_f*Theta*OM(ii)*ddW_b / den_opt;

```

```

Pout_opt      = ((Bf/K1*Theta*OM*ddW_b)^2*om_n*(1/Cp)*Re_opt_f) /
den_opt^2;
I_opt        = Pout_opt/Vp_opt;

%output data:
opvolume = (2*max(abs(W_tip_opt)) +
H0*cos(max(abs(Rot_tip_opt)))+L0*sin(max(abs(Rot_tip_opt))))*(L+L0)*(m
ax(b,b0))*1e6; % approximate volume in cm^3
%volume = 2*max(abs(W_tip_opt))*L*(max(b,b0))*1e6; % approximate
volume in cm^3
P_dens_op = (Pout_opt/1e-6)/opvolume;
volmm3 = opvolume*1e3;
volstatic = (staticdef + t_t + H0) * (L + L0) * max(bx) *1e6;
footprint = (L+L0)*(max(b,b0))*1e6;
P_dens_st = (max(Pout_opt(:))/1e-6)/volstatic;
beammass = rho_c*mean(bx)*t_t*L ;
pmmass = rho_0*H0*b0*L0+ rho_c*bx(length(bx))*t_t*L0;
devicemass = rho_c*mean(bx)*t_t*L + rho_c*bx(length(bx))*t_t*L0 +
rho_0*H0*b0*L0;

om_r(lo,bb) = om_n/2/pi;
om_ar(lo,bb) = om_n/2/pi*OM_oc;
OM_ocout=OM_oc;
Pout_out(lo,bb) =(Pout_opt)*1e6;
Popdens(lo,bb) =P_dens_op;
Pstdens(lo,bb) =P_dens_st;
SpecificPower(lo,bb) = Pout_opt/devicemass;
maxustrain(lo,bb)=abs(Str_m_opt)/1e-6;
maxV(lo,bb)=abs(Vp_opt);
maxuA(lo,bb)=abs(I_opt)/1e-6;
wtip(lo,bb)=abs(W_tip_opt)*1e6;

end
end

```

A.5 Piezoelectric Material Library File

```
% PZT-5A material properties
% from Morgan Electro Ceramic Website

% permittivity
Eps_0   =   8.854e-12;
Eps_T_33 = 1700*Eps_0;
Eps_T_11 = 1730*Eps_0;
Eps_S_33 = 830*Eps_0;
Eps_S_11 = 916*Eps_0;

% piezoelectric constants
d31 = -171e-12;
d33 = 374e-12;
d15 = 584e-12;
g31 = -11.4e-3;
g33 = 24.8e-3;
g15 = 38.2e-3;
e31 = -5.4;
e33 = 15.8;
e15 = 12.3;

% Stiffness matrix
cE11 = 12.1e10;
cE33 = 11.1e10;
cE44 = 2.11e10;
cE66 = 2.26e10;
cE12 = 7.54e10;
cE13 = 7.52e10;

% Compliance
sE11 = 16.4e-12;
sE33 = 18.8e-12;
sE44 = 47.5e-12;
sE66 = 44.3e-12;
sE12 = -5.74e-12;
sE13 = -7.22e-12;

% density
rho_p = 7750;

% coupling coefficients
k31 = -0.334;
k33 = 0.705;
```